



UNIVERSITY
of
OTAGO

Te Whare Wānanga o Otāgo
NEW ZEALAND

**Cell-penetrating peptides for enhanced oral delivery of
nanoformulations**

Sarah Streck

A thesis submitted in the fulfilment of the requirements for the degree of

Doctor of Philosophy

at the University of Otago, Dunedin,

New Zealand.

November 2019

Abstract

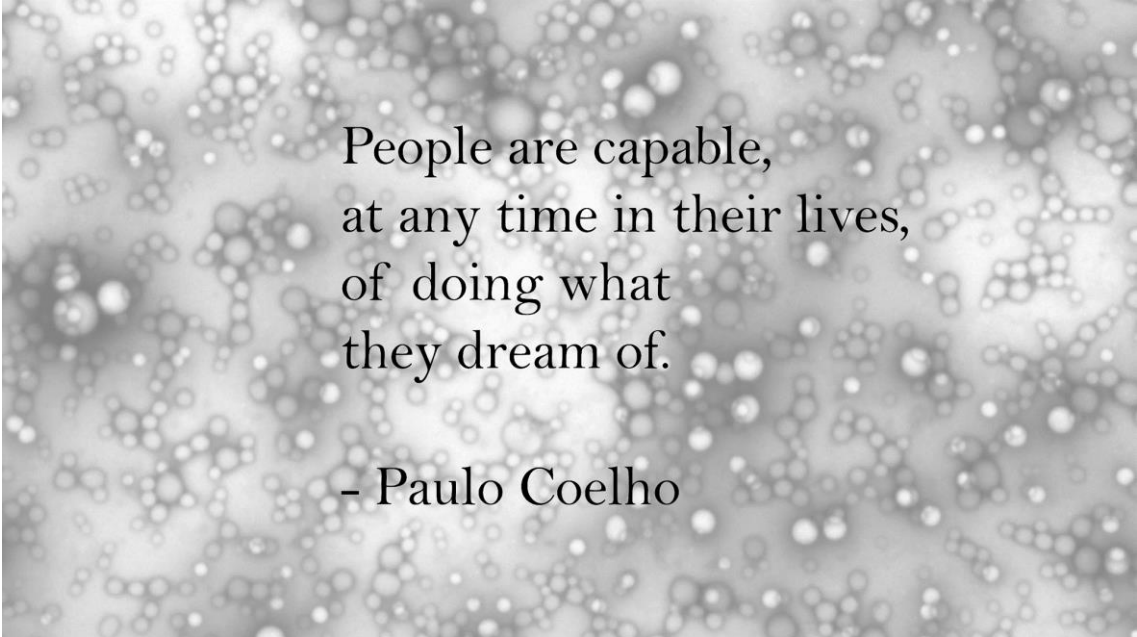
Introduction: Oral drug delivery systems such as polymeric nanoparticles are used to improve therapies that utilize biomacromolecules like proteins and peptides. Surface modifications of polymeric nanoparticles play a crucial role in the interactions with the intestinal epithelium. Cell-penetrating peptides (CPPs) are short cationic amino acid sequences that can be utilized to enhance interactions between polymeric nanoparticles and cells. In this thesis, surface-modified polymeric nanoparticles are prepared using a nanoprecipitation method and a zero-length crosslinking reaction for the covalent conjugation of CPPs to polymeric nanoparticles. Three CPPs with a distinct architecture, namely the short RRH, the long linear TAT and the branched bTAT were exploited. Further, the nanoparticles were characterised and the influence of the CPP architecture on cellular uptake was investigated.

Methods: A bulk nanoprecipitation and a microfluidics method were compared for the formulation of uniform poly-lactic-*co*-glycolic acid (PLGA) nanoparticles using a design of experiments study. CPP-tagged PLGA nanoparticles were formulated using a post-microfluidics and an *in situ* microfluidics conjugation approach developed for the first time. The physiochemical characteristics and morphology of PLGA and CPP-tagged PLGA nanoparticles were analysed with dynamic light scattering, laser Doppler electrophoresis, Fourier-transform infrared spectroscopy and transmission electron microscopy (TEM). The distribution of CPPs on PLGA nanoparticles was further elucidated with small angle X-ray scattering (SAXS) after gold labelling of the CPP-tagged PLGA nanoparticles. PLGA and CPP-tagged PLGA nanoparticles were prepared using a fluorophore-labelled PLGA for *in vitro* cell culture studies. The cell toxicity and interactions of the fluorophore-labelled PLGA and CPP-tagged PLGA nanoparticles with HeLa and Caco-2 cells were investigated using flow cytometry and confocal laser scanning microscopy.

Results: PLGA nanoparticles intended for oral drug delivery and formulated with microfluidics showed a size of 151.2 ± 1.2 nm (PDI 0.149 ± 0.014) and had superior size characteristics in comparison to the bulk nanoprecipitation method resulting in PLGA nanoparticles with a size of 184.0 ± 3.9 nm (PDI 0.110 ± 0.007). The covalent conjugation of CPPs with different architectures tuned the surface charge of CPP-tagged PLGA nanoparticles from negative to slightly positive (-24 to +5 mV). This trend in change of surface charge was observed for both preparation methods, the post-microfluidics and the *in situ* microfluidics conjugation approach. After analysis with TEM and SAXS, it was found that the distribution of CPPs on PLGA nanoparticles depends on the preparation approach. The *in situ* microfluidics conjugation approach showed a distribution of the CPPs throughout the PLGA nanoparticles, whereas the post-microfluidics conjugation approach indicated a surface arrangement of the CPPs on the PLGA nanoparticle surface. *In vitro* cell culture studies using HeLa and Caco-2 cells revealed association rather than uptake of the CPP-tagged PLGA nanoparticles.

Conclusion: Microfluidics and CPPs of different architecture were successfully utilized for the formulation of surface-modified polymeric nanoparticles with a tuneable surface charge. For nanoparticle-cell interactions to occur e.g. at the nano-bio interface, the surface charge of nanoparticles plays a crucial role. Further investigation of nanoparticle-cell interactions can aid to gain a better understanding of how the well-characterised CPP-tagged PLGA nanoparticles presented in this thesis can influence cellular uptake.

To my family



People are capable,
at any time in their lives,
of doing what
they dream of.

- Paulo Coelho

Acknowledgements

It all began on an icy winter day in July 2016 and now a little bit more than three years later I am finishing this thesis. This journey would not have been possible without the constant support and guidance from my supervisor Assoc. Prof. Arlene McDowell and my co-supervisors Prof. Hanne Mørck Nielsen and Prof. Thomas Rades.

First of all, I would like to say thanks to Arlene for her supervision, generous time and motivation over the past years. Looking back at this PhD journey it was so much more than just lab research. I was very fortunate to have had the possibility to demonstrate for undergraduate students, meet professors and researchers, go to conferences, participate in various competitions and learn about what it means to be part of an academic world. All this would not have been possible without Arlene's encouragement and her trust in me that I am capable of doing it. With Arlene's help, I have grown so much as a researcher and on a personal level. I'm very grateful to have had the chance to do my PhD under her supervision here at Otago.

I would like to thank Thomas and Hanne for sharing their enthusiasms and knowledge about research during our countless skype meetings over the past three years and for providing the opportunity to do part of my PhD research in Copenhagen. It was a great experience accompanied by a great summer and the opportunity to see my family and friends. I also want to say thanks to Hanne's Lab group and everyone else on the 4th floor for their support to help me find my way around the lab and department, strawberry cake, ice cream (with strawberries) and shared lunches. Thanks to Ditlev for maintaining the cells and helping me with the *in vitro* experiments.

I would like to express my gratitude to Prof. Ben Boyd for his valuable advice and input on my PhD, the encouragement to get things done, for looking after me at conferences and

hosting me at MIPS. A huge thank you goes to Ben's Lab group for sharing my short stay at the synchrotron with me, great Argentinian and Korean BBQs and a bit of karaoke to make my stay in Melbourne fantastic. In particular, thanks to Linda and Andy for their help with the lab work and writing papers.

Many thanks to Hannah for sharing the long hours we spent in the office and the lab, but also for introducing me to the Vietnamese cuisine. Thanks to Henriette, Sanjay and Alisa for actively taking part in my thesis research and their help with the FTIR analysis, HPLC analysis and *in vitro* studies with our care-intensive cells (aka our babies). I would like to thank Pummy, Bettina, Sumit, and all postgraduates and visiting students for the scientific and sometimes less scientific conversations and for recreational activities outside the School.

I would like to thank Joel Tyndall my facilitator, Sarah Hook, Greg Walker and Natalie Medlicott and all academics, administrative, research and technical staff of the School of Pharmacy for their help. I want to acknowledge the financial support I received from the School of Pharmacy and the Division of Health Sciences.

I would like to thank Dr Torsten Kleffmann and Diana Carne from the Centre for Protein Research, University of Otago for help and advice with MALDI-TOF and the staff from Otago Micro and Nanoscale imaging facility, especially Richard Easingwood for the support and thoughtful TEM training.

Last but not least, I would like to thank my family and friends. My parents, Mum (Mäuschen) and Dad, for letting me go to chase my dream at the other end of the world. Antonio for always being there for me. My brother, Gregor and his boys Neo, Elias and Jona, for their never-ending interest about my adventures in New Zealand. Thanks to my prodrug girls (Kirstin, Karen Janina and Katha) and all my friends in Dunedin, especially Jean, Yim, Som, other Jean, Belinda and Johnson for living with me and distracting me from work.

List of Publications

Refereed journal articles

S. Streck, H. Neumann, H. Mørck Nielsen, T. Rades and A. McDowell (2019). Comparison of bulk and microfluidics methods for the formulation of poly-lactic-*co*-glycolic acid (PLGA) nanoparticles modified with cell-penetrating peptides of different architectures. *International Journal of Pharmaceutics: X*, 1, 100030. [Impact Factor 4.213]

S. Streck, A. J. Clulow, H. Mørck Nielsen, T. Rades, B. J. Boyd and A. McDowell (2019). The distribution of cell-penetrating peptides on polymeric nanoparticles prepared using microfluidics and elucidated with small angle X-ray scattering. *Journal of Colloid and Interface Science*, 555, 438-48. [Impact Factor 6.361]

S. Streck, L. Hong, B. J. Boyd and A. McDowell (2019). Microfluidics for the production of nanomedicines: Considerations for polymer and lipid-based systems. *Pharmaceutical Nanotechnology*, 7, 1-21.

S. Streck, S. Schmidt-Rasmussen Nielsen, D. Birch, T. Rades, N. S. Hatzakis, A. McDowell and H. Mørck Nielsen (manuscript in preparation). Interaction of cell-penetrating peptide-modified polymeric nanoparticles with the nano-bio interface evaluated using single particle tracking. *Bioconjugate Chemistry*

Conference contributions (Oral presentations)

S. Streck, A. J. Clulow, H. Neumann, H. Mørck Nielsen, T. Rades, B. J. Boyd, A. McDowell (2018). The application of light scattering techniques to investigate surface distribution of cell-

penetrating peptides on polymeric nanoparticles. *Globalization of Pharmaceutics Education Network (GPEN) Conference 2018, Singapore*

S. Streck, H. Mørck Nielsen, T. Rades and A. McDowell (2018). MALDI-TOF-MS to investigate covalent binding between cell-penetrating peptides and polymeric nanoparticles. *Centre for Protein Research User Meeting, Department of Biochemistry, University of Otago, Dunedin, New Zealand*

S. Streck, H. Mørck Nielsen, T. Rades and A. McDowell (2016). Nanoformulations decorated with cell-penetrating peptides for enhanced delivery of therapeutics. *School of Pharmacy Research Day, University of Otago, Dunedin, New Zealand*

S. Streck, H. Mørck Nielsen, T. Rades and A. McDowell (2016). Microfluidics: an efficient approach to formulate uniform poly(lactic-co-glycolic) acid nanoparticles. *D4 Conference, Dunedin, New Zealand*

S. Streck, S. Schmidt-Rasmussen Nielsen, D. Birch, T. Rades, N. S. Hatzakis, H. Mørck Nielsen, **A. McDowell** (2019). Does the architecture of cell-penetrating peptides influence cell interactions? *10th International Nanomedicine Conference 2019, Sydney, Australia*

S. Streck, H. Neumann, A. J. Clulow, H. Mørck Nielsen, T. Rades, B. J. Boyd, **A. McDowell** (2018). Designing the arrangement of cell-penetrating peptides on polymeric nanoparticles using microfluidics. *9th International Nanomedicine Conference 2018, Sydney, Australia*

Conference contributions (Poster presentations)

S. Streck, A. J. Clulow, H. Neumann, H. Mørck Nielsen, T. Rades, B. J. Boyd, A. McDowell (2018). Investigation of the surface distribution of the cell-penetrating peptide TAT on polymeric nanoparticles produced with microfluidics. *1st Controlled Release Asia (CRA) Meeting 2018, Singapore*

S. Streck, H. Mørck Nielsen, T. Rades, B. J. Boyd and A. McDowell (2018). Probing the surface characteristics of polymeric nanoparticles decorated with cell-penetrating peptides. *31st Australian colloid and surface science student conference (ACSSSC) 2018, Warrnambool, Australia*

S. Streck, H. Mørck Nielsen, T. Rades and A. McDowell (2017). Designing CPP-tagged PLGA nanoparticles using microfluidics. *Drug Delivery Australia Conference 2017, Wollongong, Australia*

S. Streck, A. Goutach, A. J. Clulow, H. Mørck Nielsen, T. Rades, B. J. Boyd and **A. McDowell** (2019). Microfluidics for the Formulation of Polymeric Nanoparticles Functionalized with Cell-Penetrating Peptides to Enhance Delivery of Biomacromolecules. *CRS Annual Meeting 2019, Valencia, Spain*

Awards

Division of Health Sciences International Engagement Grant, University of Otago (\$2,000.00), August 2017

Bursary to attend D4 Conference 2016, Dunedin New Zealand, November 2016

Selected and sponsored GPEN student representative from the University of Otago

Table of Contents

Abstract	ii
Acknowledgements	v
List of Publications	vii
Table of Contents.....	x
List of Figures	xv
List of Tables.....	xx
List of Abbreviations	xxii
1 Chapter One.....	25
1.1 Nanoparticles as oral drug delivery systems.....	26
1.2 Polymeric delivery systems.....	27
1.2.1 Poly(lactic-co-glycolic acid).....	28
1.3 Preparation of polymeric nanoparticles.....	30
1.3.1 Bulk preparation methods.....	30
1.3.2 Nanoprecipitation.....	34
1.3.3 Microfluidics.....	37
1.3.3.1 Types of microfluidics mixer.....	38
1.3.3.2 Optimisation of size and charge of polymeric nanoparticles.....	41
1.4 Modifications of polymeric nanoparticles.....	44
1.4.1 Influence of size on cellular uptake and biodistribution.....	45
1.4.2 Effective surface charge.....	46
1.4.3 Surface modification.....	47
1.5 Cell-penetrating peptides.....	49
1.5.1 Classification and specific properties of CPPs.....	49
1.5.1.1 Sequence-modified cell-penetration peptides.....	52
1.5.2 Interactions between cell-penetrating peptides and cells.....	55

1.5.3	Association of cell-penetrating peptides with cargos	59
1.6	Thesis aims	63
2	Chapter Two	65
2.1	Introduction	66
2.1.1	Design of experiments	66
2.1.2	Design of experiments for bulk and microfluidics preparation of nanoparticles..	69
2.1.3	Optimisation of size of polymeric nanoparticles	71
2.1.4	Conjugation of biomacromolecules and polymers	73
2.1.5	Chapter aims	77
2.2	Materials.....	78
2.3	Methods	79
2.3.1	Design of experiments to optimize the preparation of PLGA nanoparticles using a bulk nanoprecipitation method.....	79
2.3.2	Preparation of polymeric nanoparticles using microfluidics	80
2.3.3	Design of experiments study for microfluidics preparation of PLGA nanoparticles	81
2.3.4	Bulk nanoprecipitation method for preparation of PLGA nanoparticles.....	82
2.3.5	Microfluidics method for the preparation of PLGA nanoparticles.....	83
2.3.6	Preparation of surface-modified PLGA nanoparticles.....	83
2.3.7	Mass spectrometry assessment of cell-penetrating peptides.....	84
2.3.8	Characterization of PLGA and CPP-tagged PLGA nanoparticles.....	85
2.3.9	Investigation of covalent binding between CPPs and PLGA conjugates	85
2.3.10	Conjugation efficiency of CPPs tagged to PLGA nanoparticles	86
2.3.11	Validation of RP-HPLC method for CPPs.....	87
2.3.12	Statistical analysis	88
2.4	Results and Discussion	89

2.4.1	Optimal PLGA and stabilizer concentration for the formulation of PLGA nanoparticles determined by design of experiments (DoE).....	89
2.4.2	Tuning the size and polydispersity of PLGA nanoparticles using microfluidics and design of experiments	91
2.4.3	Quality assessment of cell-penetrating peptides	94
2.4.4	Characterization of PLGA nanoparticles	96
2.4.5	Investigation of binding between CPPs and PLGA polymer.....	100
2.4.6	Characteristics of CPP-tagged PLGA nanoparticles depends on the CPP architecture.....	101
2.4.7	Validation of RP-HPLC methods	104
2.4.8	Conjugation efficiency of CPPs with different architectures on PLGA nanoparticles	108
2.5	Conclusion.....	111
3	Chapter Three.....	112
3.1	Introduction	113
3.1.1	Characterisation of polymeric nanoparticles using small angle X-ray scattering.	113
3.1.2	Imaging of nanoparticles to reveal morphology	118
3.1.3	Functionalisation of polymeric nanoparticles using microfluidics.....	120
3.1.4	Chapter aims	123
3.2	Materials.....	124
3.3	Methods.....	124
3.3.1	<i>In situ</i> microfluidics conjugation for the preparation of CPP-tagged PLGA nanoparticles and Au-labelled CPP-tagged nanoparticles	124
3.3.2	Conjugation efficiency of CPPs after <i>in situ</i> microfluidics preparation of CPP-tagged PLGA nanoparticles	126
3.3.3	Post-microfluidics conjugation for the preparation of CPP-tagged PLGA nanoparticles and Au-labelled CPP-tagged PLGA nanoparticles.....	127

3.3.4	Characterization of nanoformulations.....	127
3.3.5	Transmission electron microscopy	127
3.3.6	Small angle X-ray scattering.....	128
3.3.7	Statistical analysis	128
3.4	Results and Discussion	129
3.4.1	Conjugation approaches for preparation of CPP-tagged PLGA nanoparticles.....	129
3.4.2	Characteristics of CPP-tagged PLGA nanoparticles depends on the CPP architecture.....	129
3.4.3	Conjugation efficiency of CPPs with different architecture on PLGA nanoparticles	132
3.4.4	Characterization of Au-labelled CPP-tagged PLGA nanoparticles	133
3.4.5	TEM micrographs show the distribution of CPP on PLGA nanoparticles	135
3.4.6	Investigation of CPP distribution on PLGA nanoparticles using SAXS	139
3.4.7	Structural distribution of CPPs	144
3.5	Conclusion.....	146
4	Chapter Four	147
4.1	Introduction	148
4.1.1	Interactions of nanoparticles at the nano-bio interface	148
4.1.2	The intestinal epithelium as a barrier for nanoparticle uptake.....	152
4.1.3	Chapter aims	158
4.2	Materials.....	159
4.3	Methods	160
4.3.1	Preparation of CPP-tagged PLGA-FPR nanoparticles using microfluidics ...	160
4.3.2	Characterization of CPP-tagged PLGA-FPR nanoparticles	160
4.3.3	Culturing of HeLa and Caco-2 cells	161
4.3.4	Toxicity of nanoformulations in HeLa and Caco-2 cells.....	162

4.3.5	Cell integrity of Caco-2 cell monolayer.....	163
4.3.6	Uptake of nanoparticles using flow cytometry for HeLa and Caco-2 cells	163
4.3.7	Qualitative cell uptake study using confocal laser scanning microscopy for HeLa and Caco-2 cells	165
4.3.8	Statistical analysis	166
4.4	Results and Discussion	167
4.4.1	Characterization of CPP-tagged PLGA-FPR nanoparticles	167
4.4.1.1	Physicochemical properties of nanoparticles in ultra-pure water	167
4.4.1.2	Physicochemical properties of nanoparticles in cell culture buffer	169
4.4.2	Interaction of nanoformulations with HeLa cells	172
4.4.2.1	Cell viability of HeLa cells	172
4.4.2.2	Quantification of cellular uptake of nanoparticles in HeLa cells	175
4.4.2.3	Qualification of cellular uptake of nanoparticles in HeLa cells	177
4.4.3	Interaction of nanoformulations with Caco-2 cells.....	181
4.4.3.1	Cell viability and cell integrity of Caco-2 cells	181
4.4.3.2	Quantification of cellular uptake of nanoparticles in Caco-2 cells.....	184
4.4.3.3	Qualification of cellular uptake in Caco-2 cells	189
4.5	Conclusion.....	192
5	Chapter Five.....	194
5.1	Introduction and general summary	195
5.2	Application of research in the wider research area	196
5.3	Future direction: Defining the surface of nanoparticles.....	199
5.4	Future direction: Improvement of <i>in vitro</i> studies	202
	References.....	204
	Appendix	226

List of Figures

Figure 1.1. Structure and reaction of cyclic monomers used for the synthesis of PLGA and the structure of monomers after hydrolysis of the PLGA polymer (Avgoustakis, 2008; Makadia and Siegel, 2011).....	29
Figure 1.2. Schematic description of w/o/w double emulsion solvent evaporation (A) and o/w single emulsion solvent evaporation (B) method for the preparation of polymeric nanoparticles (Crucho and Barros, 2017).	32
Figure 1.3. Schematic of the bulk nanoprecipitation method for the preparation of polymeric nanoparticles (A) and assembly of polymeric nanoparticles (B) during preparation using the nanoprecipitation method (Crucho and Barros, 2017; Karnik <i>et al.</i> , 2008).....	35
Figure 1.4. Illustration of the flow pattern of fluids in different microfluidic devices used for the formulation of nanoparticles. (A) 2D and (B) 3D hydrodynamic flow-focusing microchannel, (C) droplet-based microchannel and (D) microchannel with a staggered herringbone mixer (SHM) channel design (Streck <i>et al.</i> , 2019c).....	39
Figure 1.5. The influence of size, charge and surface modification on the physicochemical properties of polymeric nanoparticles (Fenton <i>et al.</i> , 2018; Torchilin, 2014). CPPs = cell-penetrating peptides, PEG = polyethylene glycol.	47
Figure 1.6. Classification of cell-penetrating peptides after modification of their sequence by adding branches, dimers, scaffolds and creating networks and dendrimers (Angeles-Boza <i>et al.</i> , 2010; Brock <i>et al.</i> , 2018; Eggimann <i>et al.</i> , 2014; Foerg <i>et al.</i> , 2007; Jeong <i>et al.</i> , 2016; Saleh <i>et al.</i> , 2010; Yoo <i>et al.</i> , 2017; Zhao <i>et al.</i> , 2014a). CPP = cell-penetrating peptide.	53
Figure 1.7. Cellular uptake mechanisms of cell-penetrating peptides adapted from Guidotti <i>et al.</i> (2017) with permission from Elsevier.	56
Figure 1.8. Possible cell-penetrating peptide cargos and schematic of non-covalent (A) and covalent (B) interactions between polymeric nanoparticles and CPPs (Guidotti <i>et al.</i> , 2017; Streck <i>et al.</i> , 2019c) (With permission from Elsevier). CPP = cell-penetrating peptide.....	60
Figure 2.1. Schematic representations of two-level factorial design (A), central composite design (B) and Box-Behnken design (C) for three different input factors (Hanrahan and Lu, 2006; Mandenius and Brundin, 2008).	68
Figure 2.2. Influence of input factors on the output responses for the preparation of PLGA nanoparticles using a bulk nanoprecipitation method (Bairagi <i>et al.</i> , 2018; Patel <i>et al.</i> , 2016; Sonam <i>et al.</i> , 2014; Tefas <i>et al.</i> , 2015; Vuddanda <i>et al.</i> , 2015; Yadav and Sawant, 2010). PDI = polydispersity index, EE = encapsulation efficiency.	69

Figure 2.3. Generalized correlation between microfluidics-related parameters and the size of the resulting polymeric nanoparticles formulated with PLGA (10 mg/mL, co-polymer ratio 75:25 and 50:50) and PEG-PLGA (10 to 30 mg/mL) (Lim <i>et al.</i> , 2014a; Min <i>et al.</i> , 2014; Morikawa <i>et al.</i> , 2018). Arrows indicate an increase in flow rate or flow rate ratio (Streck <i>et al.</i> , 2019c).....	72
Figure 2.4. Schematic of maleimide reaction (A), EDC/sulfo-NHS zero-length crosslinking reaction (B) and streptavidin-biotin affinity reaction (C) for the surface conjugation of nanoparticles (Hermanson, 2013c; Nam <i>et al.</i> , 2002; Xu <i>et al.</i> , 2013a).	75
Figure 2.5. Illustration of the architecture of the short (RRH), the long linear (TAT) and the branched CPP (bTAT: modified TAT backbone and three RRH branches). Amino acid single letter codes have been used for each peptide (R = arginine, H = histidine, G = glycine, K = lysine, Q = glutamine) (Streck <i>et al.</i> , 2019a).	79
Figure 2.6. Microfluidic cartridge used for the NanoAssemblr [®] Benchtop Device (A) and depth profile of herringbone feature (B) found within the microchannel (not to scale). Schematic of herringbone feature was adapted from Belliveau <i>et al.</i> (2012). The SHM section of the microchannel is 2.5 cm long and can hold a volume of 0.0004 mL.	81
Figure 2.7. Response surface plots for the size (nm) (A) and polydispersity index (PDI) (B) of nanoparticles as a function of PLGA and PVA concentration for preparation of PLGA nanoparticles using the bulk nanoprecipitation method (Streck <i>et al.</i> , 2019a).....	90
Figure 2.8. Response surface plots for the responses size (A) and PDI (B) as a function of the total flow rate (mL/min) and the flow rate ratio (aqueous:organic) for preparation of PLGA nanoparticles using the microfluidics method (Streck <i>et al.</i> , 2019b).....	92
Figure 2.9. Mass spectra of the RRH (A), TAT (B) and bTAT (C) obtained with matrix assisted laser desorption ionisation-time of flight mass spectrometry analysis.....	95
Figure 2.10. Transmission electron micrographs of unmodified PLGA (A) and TAT-tagged PLGA nanoparticles (B) prepared using a bulk nanoprecipitation method and unmodified PLGA (C), RRH- (D), TAT- (E) and bTAT-tagged PLGA nanoparticles (F) prepared using the microfluidics method (Streck <i>et al.</i> , 2019a).	99
Figure 2.11. Fourier-transform infrared spectra of PLGA polymer, the individual cell-penetrating peptides (RRH, TAT, bTAT) and PLGA-CPP conjugates (Streck <i>et al.</i> , 2019a).	100
Figure 2.12. Size, polydispersity index (A) and zeta potential (B) of PLGA nanoparticles and CPP-tagged PLGA nanoparticles with different concentrations of CPPs (RRH, TAT, bTAT), prepared using the post-microfluidics conjugation approach. Size is displayed as circles and	

triangles represent polydispersity (Streck <i>et al.</i> , 2019a). Data are means \pm SD ($n = 3$ independent batches). * p -value < 0.05 for the comparison of CPP-tagged PLGA nanoparticles with PLGA nanoparticles, ns = not significant.	102
Figure 2.13. Representative RP-HPLC chromatograms of RRH (100 $\mu\text{g/mL}$) (A), TAT (100 $\mu\text{g/mL}$) (B) and bTAT (100 $\mu\text{g/mL}$) (C) eluted with the individual RP-HPLC methods for each CPP.	105
Figure 3.1. Schematic of the sample set up for small angle X-ray scattering with the detection of scattering patterns (A) and a small angle X-ray scattering plot showing information about the sample structure deduced from the scattering curve (B) (Li <i>et al.</i> , 2016; Luo <i>et al.</i> , 2019b). 2θ = scattering angle, $I(q)$ = scattering intensity, q = scattering vector.	115
Figure 3.2. Functionalisation of polymeric nanoparticles using a pre-microfluidics (A) (Kamaly <i>et al.</i> , 2016; Liu <i>et al.</i> , 2010; Valencia <i>et al.</i> , 2013), an <i>in situ</i> microfluidics (B) or a post-microfluidics (C) (Kolishetti <i>et al.</i> , 2010) conjugation approach (Streck <i>et al.</i> , 2019c).	121
Figure 3.3. Comparison of the <i>in situ</i> microfluidics (A) and the post-microfluidics (B) conjugation approaches for the formulation of Au-labelled CPP-tagged PLGA nanoparticles. Label-free CPP-tagged PLGA nanoparticles (i) and Au-labelled CPP-tagged PLGA nanoparticles (ii) were produced using the <i>in situ</i> microfluidics (A) conjugation approach. The microchannel diagram, with the red box indicating the herringbone structure, was modified from Belliveau <i>et al.</i> (2012) (Streck <i>et al.</i> , 2019b). SHM = staggered herringbone mixer, ACN = acetonitrile.	126
Figure 3.4. Size, polydispersity (A) and zeta potential (B) of PLGA nanoparticles and CPP-tagged PLGA nanoparticles with different concentrations of the CPPs (RRH, TAT and bTAT), prepared using the <i>in situ</i> microfluidics conjugation approach. Size is displayed as circles and triangles represent polydispersity. Data are means \pm SD ($n = 3$ independent batches). * p -value < 0.05 for the comparison of CPP-tagged PLGA nanoparticles with PLGA nanoparticles, ns = not significant.	131
Figure 3.5. Representative micrographs of Au-labelled RRH-tagged PLGA nanoparticles prepared using the post-microfluidics (A) and the <i>in situ</i> microfluidics conjugation approach (B) (Streck <i>et al.</i> , 2019b).	135
Figure 3.6. Transmission electron micrograph of Au-labelled RRH-tagged PLGA nanoparticles (A) and inserts of free individual AuNPs (1) and a RRH-tagged PLGA nanoparticle with surface-bound AuNPs (2). The hexagonal formation of the AuNPs is	

indicated by the red dashed line and the red arrows indicate how the distance between AuNPs was measured (Streck <i>et al.</i> , 2019b).....	137
Figure 3.7. Representative micrographs of Au-labelled TAT- and bTAT-tagged PLGA nanoparticles prepared using the post-microfluidics (A, C) and the <i>in situ</i> microfluidics conjugation approach (B, D).	138
Figure 3.8. Small angle X-ray scattering profiles of AuNPs (black data points) and PLGA nanoparticles tagged with CPPs of different architectures (RRH, TAT and bTAT) (red data points). Panels A-C show Au-labelled CPP-tagged PLGA nanoparticles prepared with the post-microfluidics conjugation approach (purple data points) and panels D-F were produced using the <i>in situ</i> microfluidics conjugation approach (green data points) (Streck <i>et al.</i> , 2019b). AuNPs = gold nanoparticles and MF = microfluidics.	141
Figure 3.9. Schematic overview of proposed CPP distribution of Au-labelled CPP-tagged PLGA nanoparticles and the corresponding distribution of label-free CPP-tagged PLGA nanoparticles prepared using a post-microfluidics conjugation (A) or an <i>in situ</i> microfluidics conjugation (B) approach (Streck <i>et al.</i> , 2019b). NP = nanoparticle.	145
Figure 4.1. Schematic representation of the <i>in vitro</i> Sedimentation, Diffusion, Dissolution, and Dosimetry model applied to polymeric nanoparticles including the sedimentation and diffusion of the drug-loaded polymeric nanoparticles (A), the dissolution of the polymer and drug release (B) and the interaction/uptake of drug/nanoparticles at the cell surface (C) (Thomas <i>et al.</i> , 2018).....	151
Figure 4.2. Cell viability of HeLa cells after 1 h incubation with PLGA-FPR and CPP-tagged PLGA-FPR nanoparticles prepared using the post-microfluidics (A) or <i>in situ</i> microfluidics (B) conjugation approach and CPP solutions with different concentrations (C). The black line indicates 100% as negative control. Data are means \pm SEM ($n = 3$). NPs = nanoparticles. .	174
Figure 4.3. Fluorescence intensity measured in HeLa cells after 1 h incubation with different dilutions of PLGA-FPR and CPP-tagged PLGA-FPR nanoparticles prepared using the post-microfluidics (A) or the <i>in situ</i> microfluidics (B) conjugation approach. Control cells were incubated with cell culture buffer. Data are means \pm SEM ($n = 3$). * p -value < 0.05 for comparison between PLGA-FPR and TAT-tagged PLGA-FPR nanoparticles. NPs = nanoparticles.....	177
Figure 4.4. Confocal images of HeLa cells incubated for 1 h with PLGA-FPR (A), RRH- (B), TAT- (C) and bTAT-tagged PLGA-FPR nanoparticles (D) prepared using the post-microfluidics conjugation approach.	179

Figure 4.5. Confocal images of HeLa cells incubated for 1 h with PLGA-FPR (A), RRH- (B), TAT- (C) and bTAT-tagged PLGA-FPR nanoparticles (D) prepared using the <i>in situ</i> microfluidics conjugation approach.	180
Figure 4.6. Cell viability graphs of Caco-2 cells after 2 h incubation with PLGA-FPR and CPP-tagged PLGA-FPR nanoparticles prepared using the post-microfluidics conjugation approach (A) and CPP solutions with different concentrations (B). The black line indicates 100% as negative control. Data are means \pm SEM ($n = 3$). NPs = nanoparticles.	183
Figure 4.7. Uptake of PLGA-FPR and CPP-tagged PLGA-FPR nanoparticles prepared using the post-microfluidics conjugation approach in Caco-2 cells after incubation for different time points (0.5, 2 and 6 h) (A) and cell viability assessed with propidium iodide staining (B). Data are means \pm SEM ($n = 3$). NPs = nanoparticles.	186
Figure 4.8. Comparison of uptake of PLGA-FPR and CPP-tagged PLGA-FPR nanoparticles after heparin treatment and no heparin treatment in Caco-2 cells after incubation for 2 h. Cells were either washed with heparin (20 μ g/mL in DPBS, pH 7.4) or washed with DPBS (pH 7.4) without heparin. Data are means \pm SEM ($n = 3$). * p -value < 0.05 for comparison between samples prepared with or without heparin treatment. NPs = nanoparticles.	188
Figure 4.9. Representative confocal images of Caco-2 cell monolayer incubated for 2 h with PLGA-FPR (A), RRH- (B), TAT- (C) and bTAT-tagged PLGA-FPR nanoparticles (D) prepared using the post-microfluidics conjugation approach. The white arrow is pointing towards red fluorescence of PLGA-FPR nanoparticles or CPP-tagged PLGA-FPR nanoparticles.	190

List of Tables

Table 1.1. Summary of bulk preparation methods for the formulation of polymeric nanoparticles. PLGA = poly (lactic- <i>co</i> -glycolic acid), PCL = poly(ϵ -caprolactone), PLA = poly-L-lactic acid, PLLA-PEG = poly-L-lactic acid-poly (ethylene glycol), w/o = water/oil, w/o/w = water/oil/water.....	31
Table 1.2. Summary of cell-penetrating peptides commonly used in pharmaceutical research.	51
Table 2.1. Input parameters for the DoE study to optimize the formulation of PLGA nanoparticles using a bulk nanoprecipitation method (Streck <i>et al.</i> , 2019a).....	80
Table 2.2. Input parameters for the DoE study for the formulation of PLGA nanoparticles using microfluidics (Streck <i>et al.</i> , 2019b). FRR = flow rate ratio, TFR = total flow rate.	82
Table 2.3. Summary of results for the statistical analysis of the size and polydispersity index models for the bulk nanoprecipitation method to produce PLGA nanoparticles (Streck <i>et al.</i> , 2019a).	91
Table 2.4. Summary of results for the statistical analysis of the size and polydispersity index models for the microfluidics method to produce PLGA nanoparticles (Streck <i>et al.</i> , 2019b).	94
Table 2.5. Characterization of PLGA and TAT-tagged PLGA nanoparticles prepared with the optimized parameters for the bulk nanoprecipitation method and with the microfluidics method (Streck <i>et al.</i> , 2019a). Data are means \pm SD ($n = 3$ independent batches). * p -value < 0.05 in comparison to the respective bulk method.	97
Table 2.6. Measured concentration ($\mu\text{g/mL}$), coefficient of variation (CV, %) and accuracy of standard curves obtained for the validation of RP-HPLC methods for RRH, TAT and bTAT. Data are means \pm SD ($n = 3$).	106
Table 2.7. Measured concentration ($\mu\text{g/mL}$), coefficient of variation (CV, %) and accuracy for intra- and inter-day values of quality control samples of RRH, TAT and bTAT for the validation of RP-HPLC methods. Data are means \pm SD ($n = 3$). QC = quality control sample.	107
Table 2.8. The limit of quantification and the limit of detection for the three different RP-HPLC assays to quantify the concentration of each of the CPPs (Streck <i>et al.</i> , 2019a).	108
Table 2.9. Conjugation efficiencies and the equivalent concentrations of the CPPs tagged to PLGA nanoparticles (NPs) using different concentrations of CPPs prepared with a post-microfluidics conjugation approach (Streck <i>et al.</i> , 2019a). Data are means \pm SD ($n = 3$ independent batches). * p -value < 0.05 in comparison to the conjugation efficiency of 8.6 mM TAT.	110

Table 3.1 Conjugation efficiencies and the equivalent concentration of the CPPs tagged to PLGA nanoparticles (NPs) using different concentrations of CPPs prepared with the <i>in situ</i> microfluidics conjugation approach. Data are means \pm SD ($n = 3$ independent batches). * $p < 0.05$ in comparison to the CPP concentration of 10 and 50 mM RRH, * ^a $p < 0.05$ in comparison to the CPP concentration of 2.9 and 5.7 mM TAT, * ^b $p < 0.05$ in comparison to the CPP concentration of 8.6 mM TAT.....	133
Table 3.2. Characterization of Au-labelled CPP-tagged PLGA nanoparticles used for transmission electron microscopy and small angle X-ray scattering analysis prepared using the <i>in situ</i> microfluidics or post-microfluidics conjugation approach (Streck <i>et al.</i> , 2019b). Data are means \pm SD ($n = 3$). * $p < 0.05$ in comparison to bTAT-tagged PLGA NPs prepared with the <i>in situ</i> microfluidics conjugation approach.....	134
Table 4.1. Chemical inhibitors of <i>in vitro</i> uptake pathways categorized based on their influence on polymeric nanoparticle internalization. +, ++, and +++ represent low, medium and high influence on nanoparticle internalization.	156
Table 4.2. Characterization of PLGA-FPR and CPP-tagged PLGA-FPR nanoparticles in ultra-pure water prepared using the post-microfluidics or the <i>in situ</i> microfluidics conjugation approach. Data are mean \pm SD ($n = 3$).	168
Table 4.3. Conjugation efficiencies and the equivalent concentration of CPPs tagged to PLGA-FPR nanoparticles using the post-microfluidics and the <i>in situ</i> microfluidics conjugation approach. Data are mean \pm SD ($n = 3$).	169
Table 4.4. Characterization of PLGA-FPR and CPP-tagged PLGA-FPR nanoparticles in cell culture buffer for <i>in vitro</i> studies in HeLa cells prepared using the post-microfluidics and the <i>in situ</i> microfluidics conjugation approach. Data are mean \pm SD ($n = 6$).	171
Table 4.5. Characterization of PLGA-FPR and CPP-tagged PLGA-FPR nanoparticles in cell culture buffer for <i>in vitro</i> studies in Caco-2 cells prepared using the post-microfluidics conjugation approach. Data are mean \pm SD ($n = 6$).	171

List of Abbreviations

ACN	Acetonitrile
ADME	Absorption-Distribution-Metabolism-Excretion
ANOVA	Analysis of variance
ATP	Adenosine triphosphate
AuNPs	Gold nanoparticles
BSA	Bovine serum albumin
bTAT	Branched TAT
CLSM	Confocal laser scanning microscopy
CPP	Cell-penetrating peptide
CV	Coefficient of variation
dfTat	Dimeric and fluorescent Tat
DLS	Dynamic light scattering
DMEM	Dulbecco's Modified Eagle Medium
DMSO	Dimethyl sulfoxide
DoE	Design of experiments
DPBS	Dulbecco's Phosphate Buffered Saline
D ₂ O/H ₂ O	Deuterated water/Water
EDC	N-(3-dimethylaminopropyl)-N-ethylcarbodiimide hydrochloride
EDTA	Ethylenediaminetetraacetic acid
EMEM	Eagle's Minimal Essential Medium
FBS	Fetal bovine serum
FPR	Fluorescent dye FPR648
FTIR	Fourier-transform infrared
GIT	Gastrointestinal tract
GnRH	Gonadotropin releasing hormone
HBSS	Hank's balanced salt solution
HEPES	2-[4-(2-hydroxyethyl)piperazin-1-yl]ethanesulfonic acid
HFF	Hydrodynamic flow-focusing
IDSS	<i>In vitro</i> Sedimentation, Diffusion and Dosimetry
ISD3	<i>In vitro</i> Sedimentation, Diffusion, Dissolution, and Dosimetry
IU	International unit
LOD	Limit of detection
LOQ	Limit of quantification

MALDI-TOF	Matrix assisted laser desorption ionisation-time of flight
MLR	Multiple linear regression
MPS	Mononuclear phagocytic system
MTS	3-(4,5-Dimethylthiazol-2-yl)-5-(3-carboxymethoxyphenyl)-2-(4-sulfophenyl)-2H-tetrazolium
MS	Mass spectrometry
MWCO	Molecular weight cut off
NHS	N-hydroxysulfosuccinimide
NP	Nanoparticle
PCL	Poly(ϵ -caprolactone)
PDI	Polydispersity index
PECA	Poly(ethyl-cyanoacrylate)
PEG	Polyethylene glycol
PES/PMS	Phenazine ethosulfate/Phenazine methosulfate
PGA	Poly glycolic acid
PLA	Poly lactic acid
PLLA-PEG	Poly-L-lactic acid-polyethylene glycol
PLGA	Poly(lactic- <i>co</i> -glycolic acid)
PLS	Partial least square regression
QCs	Quality controls
Re	Reynolds number
RES	Reticuloendothelial system
RGD	Argininyglycyl aspartic acid
RP-HPLC	Reverse phase-high performance liquid chromatography
RRH	Arginine-arginine-histidine
siRNA	Small interfering RNA
SANS/SAXS	Small angle neutron/X-ray scattering
SD	Standard deviation
SEM	Standard error of the mean
SHM	Staggered herringbone mixer
SLD	Scattering length density
Sulfo-NHS	Sulfo-N-hydroxysulfosuccinimide
TAT	Trans-activating transcriptional activator
TATp-D	Dimeric branched Tat peptide
TEER	Transepithelial electrical resistance

TEM	Transmission electron microscopy
TFA	Trifluoroacetic acid
WAXS	Wide angle X-ray scattering

Chapter One

General Introduction

Part of this Chapter has been published as:

S. Streck, L. Hong, B. J. Boyd and A. McDowell (2019). Microfluidics for the production of nanomedicines: Considerations for polymer and lipid-based systems. *Pharmaceutical Nanotechnology*, 7, 1-21.

1.1 Nanoparticles as oral drug delivery systems

The metric scale categorizes materials according to their dimensions, and pharmaceutical research utilizes both micro- and nano-sized particles for application in delivering therapeutic compounds to patients. Micro- and nanoparticles are used as drug delivery systems for the treatment of cancer (Derakhshandeh *et al.*, 2007; Dong *et al.*, 2019; Jaimes-Aguirre *et al.*, 2017), diabetes (Sharma *et al.*, 2015), bacterial infections (Sonam *et al.*, 2014), for vaccine delivery (Bailey *et al.*, 2017; Kaneko *et al.*, 2018) or as diagnostic agents (Zhu *et al.*, 2019). The term ‘nano’ refers to structures between 1 and 100 nm, but nanoparticles more commonly include structures of up to 1000 nm in one dimension (Farokhzad and Langer, 2009). The application of nanoparticles for drug delivery via the oral route of administration is a simple approach and results in good patient compliance since self-administration of the drug delivery system is convenient for the patient (Date *et al.*, 2016).

For therapeutic applications, proteins and peptides are often referred to as biopharmaceuticals or biomacromolecules and they are of interest due to their high efficiency, low toxicity and good tolerance after administration (Malhaire *et al.*, 2016; Thwala *et al.*, 2017). The main challenge for oral delivery of proteins and peptides, however, is their fragility in the gastrointestinal tract (GIT) (Malhaire *et al.*, 2016). There are three main hurdles biomacromolecules encounter before reaching the cell surface where uptake into the body can occur. These hurdles are (i) the changes in pH that occur throughout the GIT and alter the ionisation status of the molecules, (ii) the presence of enzymes in the lumen and within epithelial cells that can degrade biomacromolecules and (iii) the mucus layer covering the apical surface of the epithelium that acts as a diffusion barrier to absorption (Kristensen and Nielsen, 2016). In addition, the physicochemical characteristics of biomacromolecules including a high

molecular weight, hydrophilicity and enzymatic instability contribute to a low oral bioavailability (< 1%) and poor permeability after oral administration (Bourganis *et al.*, 2017; Date *et al.*, 2016; Thwala *et al.*, 2017).

A strategy to overcome low bioavailability and physicochemical instability is the encapsulation of biomacromolecules in drug delivery systems. Drug delivery systems are a diverse group of carriers including liposomes (Kastner *et al.*, 2015), micelles (Capretto *et al.*, 2012), lipid-polymer hybrid nanoparticles (Kim *et al.*, 2012) and polymeric nanoparticles (Jaimes-Aguirre *et al.*, 2017). Nanoparticles can be used to shield proteins and peptides against the harsh environment in the GIT and to assist the transport of therapeutics across the intestinal epithelium (Malhaire *et al.*, 2016). Polymeric nanoparticles are characterised by prolonged stability in an acidic environment, low toxicity and targeted delivery abilities (Lee *et al.*, 2016). Three key advantages of polymeric nanoparticles as an oral drug delivery system have been identified. The encapsulation of drug in polymeric nanoparticles improves the bioavailability of the drug (Bobo *et al.*, 2016), and facilitates controlled release of encapsulated drug from the polymer matrix (Banik *et al.*, 2016; Jaimes-Aguirre *et al.*, 2017). A third advantage is that surface modification increases the stability of the polymeric nanoparticles in *in vitro* and *in vivo* conditions and the targeting of specific tissue as the site of action for the encapsulated drug (Banik *et al.*, 2016; Torchilin, 2014).

1.2 Polymeric delivery systems

Polymeric materials for production of nanoparticles for drug delivery can be obtained from natural sources like albumin, alginate and chitosan or can be of synthetic origin (Zhang *et al.*, 2013). Synthetic polymers can be divided into biodegradable polymers like poly(ϵ -

caprolactone) and poly(lactic-co-glycolic acid) (PLGA) and non-degradable polymers such as polyacrylates (Zhang *et al.*, 2013). The polymer used for the formation of nanoparticles has a major influence on the physicochemical characteristics of the formulated polymeric nanoparticles and needs to be chosen carefully to suit the needs of the application (Bobo *et al.*, 2016). The focus of this thesis is on PLGA as a biodegradable polymer for oral drug delivery systems due its biocompatibility and low toxicity and the approval of the polymer for human applications by the FDA (Food and Drug Administration US) and EMA (European Medicine Agency) (Danhier *et al.*, 2012; Masood, 2016).

1.2.1 *Poly(lactic-co-glycolic acid)*

A copolymer is defined by the presence of two different monomer units repeating in the polymer chain (Scott and Penlidis, 2017). The physicochemical characteristics of copolymers depend on the incorporated monomers and show a wide range of characteristics due to the combination of individual monomer properties (Scott and Penlidis, 2017). From a chemical point of view, PLGA is a copolymer (Masood, 2016), but more commonly in scientific publications it is referred to as a polymer and this nomenclature will also apply for this thesis.

The PLGA polymer consists of two monomers, namely lactic acid and glycolic acid, and can be synthesised by direct polycondensation of the monomers or ring-opening polymerisation of the cyclic diesters lactide and glycolide (Figure 1.1) (Avgoustakis, 2008). Poly lactic acid (PLA) is a hydrophobic polymer due to methyl side groups in the molecule and provides a slow rate of degradation over the period of weeks (Makadia and Siegel, 2011; Steinbach *et al.*, 2016). Poly glycolic acid (PGA) on the other hand is a hydrophilic polymer and shows faster degradation because of hydrolytic instability (Makadia and Siegel, 2011). In

a physiological environment, PLGA is degraded through hydrolysis of the ester bonds (Figure 1.1) and the monomers are further metabolized via the Krebs cycle, which leads to minimal systemic toxicity (Avgoustakis, 2008; Danhier *et al.*, 2012).

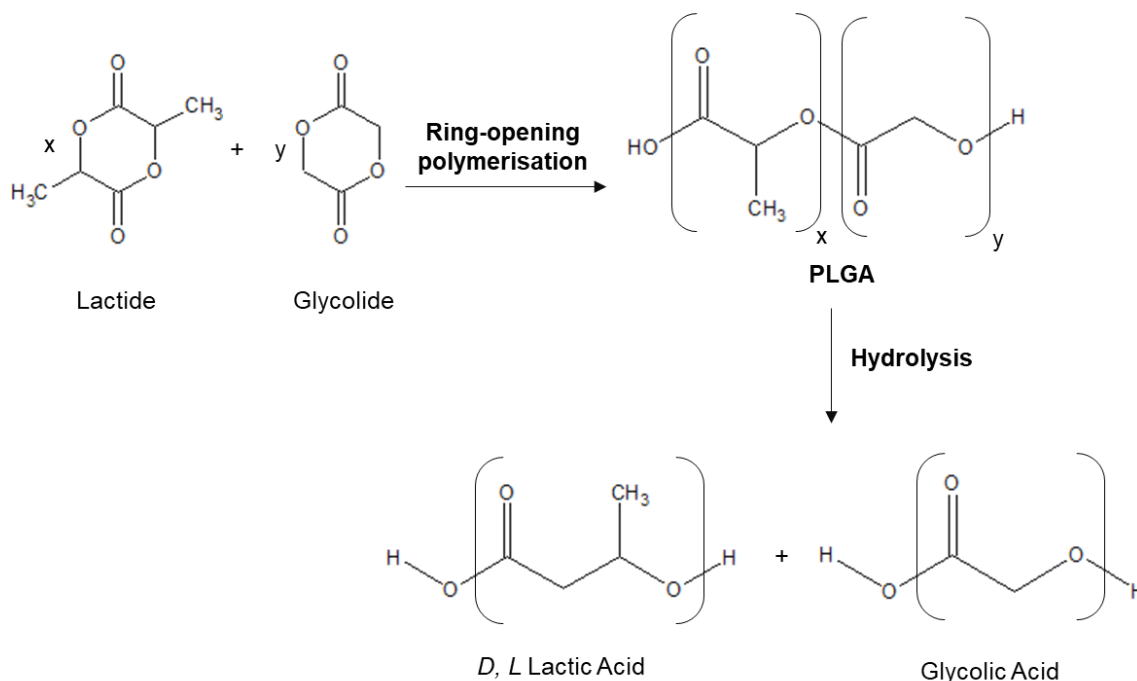


Figure 1.1. Structure and reaction of cyclic monomers used for the synthesis of PLGA and the structure of monomers after hydrolysis of the PLGA polymer (Avgoustakis, 2008; Makadia and Siegel, 2011).

The characteristics of the PLGA polymer, including degradation rate and solubility, are influenced by the molecular weight and ratio of the monomers, the end-group (either acid or ester-end groups) on the monomer as well as the shape of the polymer chain (Makadia and Siegel, 2011; Park *et al.*, 2019). A higher molecular weight PLGA and a higher amount of lactic acid units result in slower degradation of the polymer (Park, 1995; Wu and Wang, 2001). In particular, the solubility of PLGA depends on the ratio of lactic acid and glycolic acid monomers. With an increasing number of lactic acid monomers and a decreasing number of

glycolic acid monomers, the physicochemical characteristics change from being soluble in fluorinated solvents to common organic solvents like acetone (Park *et al.*, 2019).

1.3 Preparation of polymeric nanoparticles

Polymeric nanoparticles formulated with the PLGA polymer can increase the systemic absorption after oral administration of small molecular weight drugs with different structures and hydrophilicities as well as larger molecules like insulin, heparin and vaccines (Mante *et al.*, 2016). Efficient production of nanoparticles for drug delivery applications is increasingly important to ensure that the benefits of these delivery systems are translated from ‘bench to bedside’.

1.3.1 Bulk preparation methods

The formulation of nanoparticles is commonly performed with bulk preparation methods, which use volumes between 5 and 50 mL in an appropriate vessel (Babos *et al.*, 2018; Haggag *et al.*, 2018). There are a number of preparation methods like dialysis, interfacial polymerisation, salting out and spray-drying that are less frequently used for the preparation of nanoparticles (Allemann *et al.*, 1993; Draheim *et al.*, 2015; Kafka *et al.*, 2009; Kostag *et al.*, 2010). Reasons for the infrequent use of these methods include the requirement of special equipment, extensive washing, long production time (days) and unwanted side products. In this Chapter, the focus is on the most common preparation methods including emulsion solvent evaporation, nanoprecipitation, nanoemulsions and supercritical fluids for the formulation of polymeric nanoparticles (Table 1.1).

Table 1.1. Summary of bulk preparation methods for the formulation of polymeric nanoparticles. PLGA = poly (lactic-*co*-glycolic acid), PCL = poly(ϵ -caprolactone), PLA = poly-L-lactic acid, PLLA-PEG = poly-L-lactic acid-poly (ethylene glycol), w/o = water/oil, w/o/w = water/oil/water.

Preparation method	Polymer	Advantages	Disadvantages	Reference
Emulsion solvent evaporation (w/o or w/o/w)	PLGA, PLGA-PEG	Encapsulation of hydrophobic and hydrophilic drugs	High energy use Time consuming Expensive	(Babos <i>et al.</i> , 2018; Haggag <i>et al.</i> , 2018; Vaidya <i>et al.</i> , 2019)
Nanoprecipitation /Solvent displacement	PLGA, PCL	Small quantity of organic solvent	Encapsulation: hydrophobic drugs > hydrophilic drugs	(Jara <i>et al.</i> , 2018; Vuddanda <i>et al.</i> , 2015)
Nanoemulsion – phase inversion composition (PIC)	PLGA	Mild operation conditions (temperature), scale-up of production	High concentration of surfactant	(Feiner-Gracia <i>et al.</i> , 2018; Homs <i>et al.</i> , 2018; Sharma <i>et al.</i> , 2013)
Supercritical fluid – supercritical anti-solvent technique	PLA, PLLA-PEG, PLGA	Environmentally friendly, low residual solvent, mild operation conditions (temperature, pressure)	Nanoparticle size > 300 nm Broad size distribution	(Kalani and Yunus, 2012; Zabihi <i>et al.</i> , 2014; Zhao <i>et al.</i> , 2014b)

The most common bulk method for the production of PLGA nanoparticles is the emulsification-based, double emulsion solvent evaporation method (Haque *et al.*, 2018). Applying the water/oil/water (w/o/w) double emulsion solvent evaporation method (Figure 1.2A), the polymer is dissolved in a water-miscible or immiscible organic solvent like chloroform, dichloromethane or ethyl acetate and a primary emulsion in aqueous solution is formed by high-energy sonication or homogenization (Haggag *et al.*, 2018; Haque *et al.*, 2018). The primary emulsion, water/oil (w/o), is then added dropwise to an aqueous solution containing stabilizer like polysorbate-80 or polyvinyl alcohol (PVA) (Jeevanandam *et al.*, 2016; Masood, 2016). For the production of the double emulsion, high-energy sonication or homogenization is applied and the secondary double emulsion is left for solvent removal at

room temperature resulting in formation of polymeric nanoparticles by solidification of the polymer (Arshad *et al.*, 2015; Haggag *et al.*, 2018; Haque *et al.*, 2018). The high-speed sonication or homogenization and the related energy that is introduced to form the emulsion represents a crucial step in order to obtain particles in the nano-scale size range (Quintanar-Guerrero *et al.*, 1998). In addition, Haque *et al.* (2018) stated that the emulsification-based method is influenced by the grade and concentration of the polymer, the concentration of stabilizer, the volume of the aqueous and organic phases and the vessel geometry. An alternative to this method is the single emulsion solvent evaporation method, which can be used to encapsulate hydrophobic or poorly water soluble drugs (Sharma *et al.*, 2016; Vaidya *et al.*, 2019). Using a single emulsion evaporation method, a w/o emulsion of polymer/drug mixture in an aqueous surfactant solution is produced by high-speed sonication or homogenization before solvent removal as described above (Figure 1.2B) (Sharma *et al.*, 2016; Zu *et al.*, 2019).

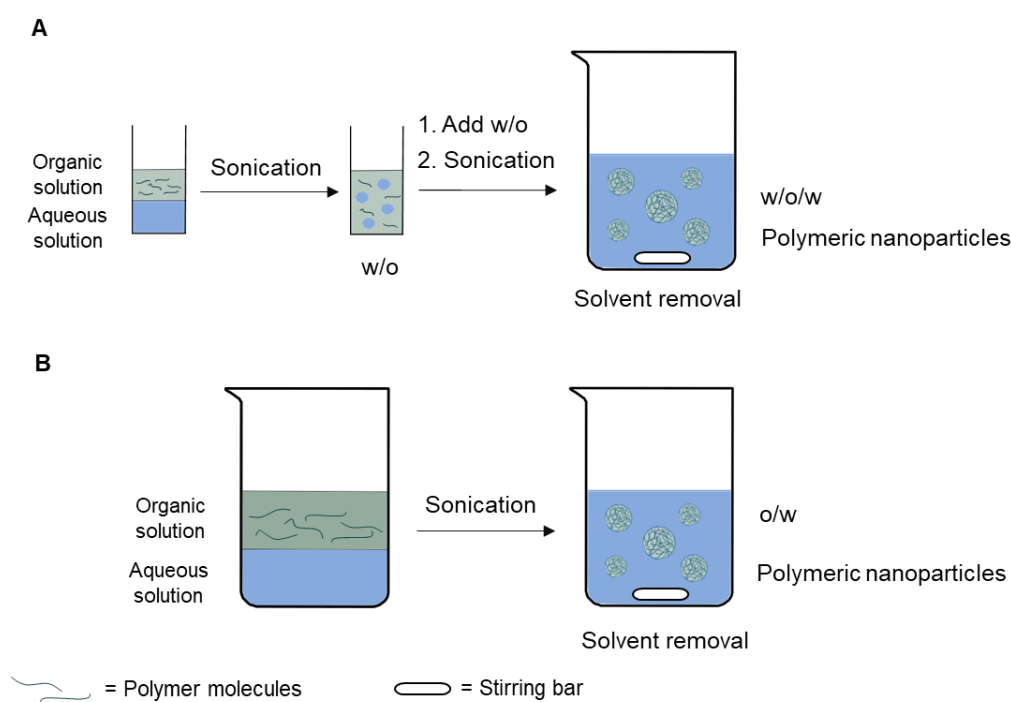


Figure 1.2. Schematic description of w/o/w double emulsion solvent evaporation (A) and o/w single emulsion solvent evaporation (B) method for the preparation of polymeric nanoparticles (Crucho and Barros, 2017).

Nanoemulsions have a droplet size of 20-200 nm and can be used for the production of polymeric nanoparticles with a size below 60 nm (Feiner-Gracia *et al.*, 2018; Homs *et al.*, 2018). In order to produce nanoemulsions, high-energy methods like sonication and high-pressure homogenization can be applied (Homs *et al.*, 2018). Alternatively, low-energy methods, such as the phase inversion composition method, where nanoemulsions are produced by changing the solvent composition at a constant temperature can be used (Fornaguera *et al.*, 2015; Homs *et al.*, 2018). High-energy methods are cost-inefficient due to the use of high levels of energy, whereas low-energy methods can produce small and uniform droplets by stirring as they utilize the internal chemical energy of the system (Caldero *et al.*, 2011; Solans and Solé, 2012). Nanoparticles are then obtained from the nanoemulsion by solvent removal under reduced pressure or continuous stirring (Caldero *et al.*, 2011; Feiner-Gracia *et al.*, 2018).

Another approach for the formation of nanoparticles utilizes supercritical fluids for the production of polymeric nanoparticles (Table 1.1) (Zabihi *et al.*, 2014). Using the supercritical anti-solvent technique, supercritical CO₂ is introduced under pressure into the organic polymer solution, which is in a high-pressure tank containing liquid CO₂ that acts as an anti-solvent (Zhao *et al.*, 2014b). Under these conditions, the velocity of the supercritical CO₂ breaks the polymer solution apart and droplets are formed (Zhao *et al.*, 2014b). The quick mass transfer between the supercritical CO₂ and organic solvent results in supersaturation and precipitation of the polymeric precursor to form nanoparticles (Kalani and Yunus, 2012; Zhao *et al.*, 2014b).

All of the methods described rely on residual solvent removal by magnetic stirring or under reduced pressure before collection of nanoparticles (Masood, 2016; Sharma *et al.*, 2016).

The collected nanoparticles are then washed at least twice using centrifugation with either centrifugation at high speed or ultra-centrifugation and dialysis (Masood, 2016).

1.3.2 Nanoprecipitation

Nanoprecipitation, also known as solvent displacement (Bairagi *et al.*, 2018; Fessi *et al.*, 1989), is the second most commonly used method for the formulation of polymeric nanoparticles (Table 1.1 and Figure 1.3A). The method was first described by Fessi *et al.* (1989) and since then has been optimised and adapted for the production of polymeric nanoparticles with a small size (< 300 nm) and to encapsulate both hydrophobic and hydrophilic drugs (Bilati *et al.*, 2005). Using nanoprecipitation, nanoparticles are prepared by the dropwise addition of an organic solution of the polymer to an aqueous solution while the mixture is agitated (Derakhshandeh *et al.*, 2007). Suitable water-miscible organic solvents for use in the nanoprecipitation method include acetone, acetonitrile, ethanol and dimethylsulfoxide (Bilati *et al.*, 2005). The aqueous phase usually contains ionic and non-ionic surfactants like PVA and pluronics (Tefas *et al.*, 2015). After addition of the organic solvent to the aqueous phase, an emulsification process takes place due to agitation of the solutions and a colloidal dispersion with nanodroplets is formed (Derakhshandeh *et al.*, 2007). The nanodroplets are unstable and interfacial tension is decreased due to the rapid diffusion of the organic solvent towards the aqueous phase (Derakhshandeh *et al.*, 2007). This process is further supported by the addition of a surfactant added to the aqueous phase (Derakhshandeh *et al.*, 2007). The added surfactant acts as a stabilizer and reduces the interfacial tension between the organic and aqueous phase of the colloidal dispersion (Tefas *et al.*, 2015). Turbulence at the interface between the aqueous and organic phase due to differences of the interfacial tension are described by the Marangoni effect (Derakhshandeh *et al.*, 2007; Fessi *et al.*, 1989). The Marangoni effect is a result of

variations in flow, diffusion and surface tension occurring at the interface of the two miscible solvents (Bilati *et al.*, 2005). Diffusion of the organic solvent reduces the local solubility of the polymer at the interface between the organic solvent and the aqueous phase resulting in nanoparticle formation due to precipitation of the polymer (Jara *et al.*, 2018; Yadav and Sawant, 2010).

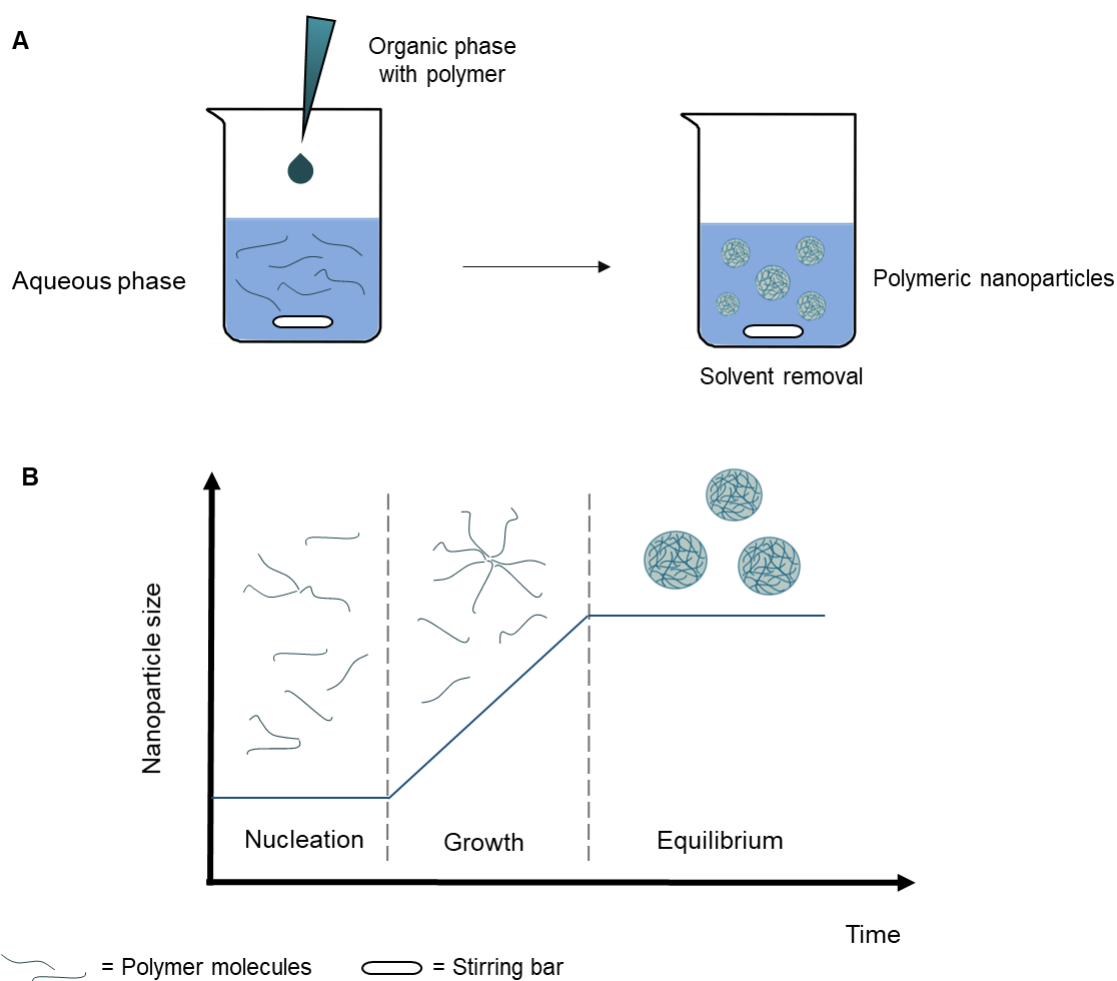


Figure 1.3. Schematic of the bulk nanoprecipitation method for the preparation of polymeric nanoparticles (A) and assembly of polymeric nanoparticles (B) during preparation using the nanoprecipitation method (Crucho and Barros, 2017; Karnik *et al.*, 2008).

After precipitation of the polymer, the formation of nanoparticles is described by classical nucleation theory, which is divided into three stages (i) nucleation, (ii) growth and (iii)

equilibrium (Figure 1.3B) (Jara *et al.*, 2018). Nucleation occurs when a local supersaturation of the polymer is achieved, meaning the concentration of the polymer is higher than its solubility (Jara *et al.*, 2018). During the nucleation phase, nuclei of dissolved polymer molecules are formed and can undergo a growth reaction with the addition of further polymer molecules (Lepeltier *et al.*, 2014). The last stage, equilibrium, is described by the formation of stable nanoparticles (Karnik *et al.*, 2008). In order to formulate small and uniform nanoparticles, the nucleation and growth processes need to be separated in time so that a high nucleation rate can yield a high number of small nuclei (Jara *et al.*, 2018; Lince *et al.*, 2008). The supersaturation state is influenced and controlled by the polymer concentration, type of solvent and removal time, mixing energy and type of mixing (Jara *et al.*, 2018). Further, the addition of surfactants is crucial as they act as a stabilizer to avoid aggregation after formation of monodisperse polymeric nanoparticles (Derakhshandeh *et al.*, 2007; Tefas *et al.*, 2015; Vuddanda *et al.*, 2015).

Even though the nanoprecipitation method is a simple preparation method (Jara *et al.*, 2018; Yadav and Sawant, 2010) and can be performed with basic laboratory equipment, the physical process behind the formation of the polymeric nanoparticles is complex. The advantages and disadvantages of the nanoprecipitation method are summarised in Table 1.1. The main limitation of the nanoprecipitation method is the aggregation of nanoparticles and the low reproducibility of the method (Jara *et al.*, 2018). In order to overcome the limitations of the nanoprecipitation method, an optimisation of the method is necessary and can be performed using design of experiments (DoE). The principles of a DoE study are described in detail in the introduction for Chapter 2. An optimised nanoprecipitation method can be used to formulate uniform nanoparticles, yield higher encapsulation efficiency and drug loading and reduce costs and production times (Jara *et al.*, 2018).

Each of the methods described up to this point are used for the preparation of polymeric nanoparticles and suitable for the encapsulation of hydrophilic and hydrophobic drugs, but the main drawback of these methods is the variation in particle size from batch-to-batch. A recent advance in the production of nanoparticles is the use of microfluidics as a promising technique to improve the formulation of nanoparticles.

1.3.3 *Microfluidics*

There are a plethora of nanoparticle carriers that have been developed for drug delivery, however, successful translation to a therapeutic product is often limited by the ability to consistently produce optimized, uniform nanoparticles with the potential for scale up of the manufacturing process under GMP (good manufacturing practice) conditions (Valencia *et al.*, 2012). The application of microfluidic approaches can address the limitations of traditional bulk production methods. Microfluidics makes use of intersecting microchannels, which enable nanolitre volumes of fluids to be mixed homogeneously or contacted in a precisely controlled environment (Khan *et al.*, 2015; Whitesides, 2006). While a wide range of microchannel configurations and flow types are used to prepare nanoparticles, a very common chemical process for the nanoparticle preparation in these devices is an ‘anti-solvent approach’. Here, the organic solution containing nanoparticle precursor components and the aqueous solution are introduced into the microfluidic device at a pre-determined flow rate and flow rate ratio between aqueous and organic reagents (Donno *et al.*, 2017; Kolishetti *et al.*, 2010). The flow rate is the combined speed of the fluids within the microchannel and the flow rate ratio is the ratio between the two solvent streams in the microfluidic device. Flow rate and flow rate ratio are discussed in more detail in Chapter 2, Section 2.1.3. Mixing the organic solution with the anti-solvent (most often the aqueous solution) induces precipitation of the precursor

components as nanoparticles (Valencia *et al.*, 2010). The advantages of microfluidic devices include high reproducibility, control over the mixing process, the possibility of automation and the mixing of fluids at high speed (Kang *et al.*, 2005; Williams *et al.*, 2008), enabling the rapid production of nanoparticles. The key improvement of using a microfluidic device instead of a bulk, macro-scale reaction vessels for the production of nanomedicines is the potential for formulation of uniform nanoparticles (Jafarifar *et al.*, 2017).

1.3.3.1 Types of microfluidics mixer

The mixing of small volumes of fluids in a microfluidic channel can be achieved using devices with a range of different designs. There is a great variety of commercially available microfluidic devices and individual microfluidic devices can be designed and manufactured with soft lithography in the laboratory to suit specific production requirements. The most commonly used microchannel design is hydrodynamic flow-focusing (HFF). HFF devices can have a planar 2D geometry or a 3D geometry (Figure 1.4A and B) (Othman *et al.*, 2015) and can be used for the formulation of a variety of nanoparticles made of PLGA (Bramosanti *et al.*, 2017; Kang *et al.*, 2013; Ortiz de Solorzano *et al.*, 2016) and other polymers (Laulicht *et al.*, 2008; Liu *et al.*, 2015; Min *et al.*, 2014). In microfluidic devices, interfacial forces between the fluids are dominant and diffusion-related mass transfer of the molecules is limited to the interface between the fluids, which leads to greater control over the mixing process (Jahn *et al.*, 2004; Whitesides, 2006). With the 2D geometry device, fluids are injected concurrently through three inlets. A central stream of a water-miscible organic solvent containing the nanoparticle precursor components and drug is focussed horizontally by lateral fluid streams of the aqueous anti-solvent introduced perpendicular to the central stream (Figure 1.4A) (Kang *et al.*, 2013). In a 2D HFF device, nanoparticle aggregation can occur at the wall of the

microfluidic channel (Figure 1.4A, cross section) and interfere with the ability to control the size of nanoparticles and also increase internal pressure in the device by blocking the microchannel (Kang *et al.*, 2013; Othman *et al.*, 2015). However, by using a 3D HFF device a more efficient mixing can be achieved because the solvent stream, introduced through a capillary, is surrounded by the anti-solvent stream, avoiding aggregation of the polymer at the walls of the microchannel (Figure 1.4B) (Kang *et al.*, 2013; Lim *et al.*, 2014a; Othman *et al.*, 2015).

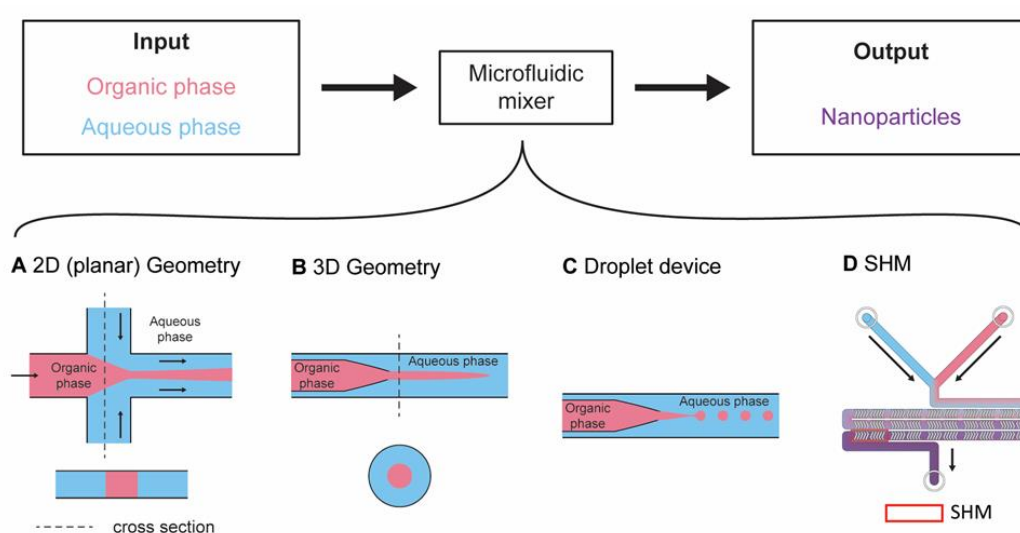


Figure 1.4. Illustration of the flow pattern of fluids in different microfluidic devices used for the formulation of nanoparticles. (A) 2D and (B) 3D hydrodynamic flow-focusing microchannel, (C) droplet-based microchannel and (D) microchannel with a staggered herringbone mixer (SHM) channel design (Streck *et al.*, 2019c).

A second common design that can be used for microfluidic mixing is a droplet-based microfluidic system (Figure 1.4C). With this approach, emulsion droplets are formed by using two immiscible fluids, e.g. water and oil, and a capillary microfluidic device (Utada *et al.*, 2007; Wang *et al.*, 2011). Single, uniform droplets are generated when coaxial flow is induced by reducing the diameter of the inner capillary, which is embedded in the outer capillary (Utada *et*

al., 2007). The formed droplets have a spherical shape due to surface tension and act as a micro-reactor for the formulation of nanoparticles in the emulsion (Wang *et al.*, 2011). This approach can be used for the formulation of polymeric nanoparticles, nanocrystals and liposomes (Wang *et al.*, 2011).

Finally, passive mixers can be incorporated as a structural element within the microchannel to induce a turbulent flow of the fluids (Capretto *et al.*, 2013). One of the most common passive mixers in microfluidic devices is the staggered herringbone mixer (SHM) (Du *et al.*, 2010; Stroock *et al.*, 2002). The SHM is described as an in-groove pattern in the microchannel with an asymmetric herringbone shape (Figure 1.4D) (Du *et al.*, 2010; Stroock *et al.*, 2002). The topology of the SHM disturbs the laminar flow of the fluids within the microchannel, causing mixing of fluids through chaotic advection (Du *et al.*, 2010). The main advantages of the SHM are the simplicity of the manufacturing process and the ability to achieve complete mixing of fluids at a low Reynolds number (Re) (Du *et al.*, 2010). The Re is a physical measurement of the viscous and inertial forces of fluids within a channel (Capretto *et al.*, 2013). At low Re, laminar flow is present and the fluids flow in a parallel pattern (Capretto *et al.*, 2013). In contrast, turbulences have a high Re and fluctuations and vortices of the fluids occur in these situations (Capretto *et al.*, 2013). Microvortices are able to increase the yield (g/hour) of nanoparticle formulations due to rapid convective mixing of the solvent and anti-solvent in the microchannel (Kim *et al.*, 2012). Other structural elements including a mixing spiral to create microvortices (Feng *et al.*, 2017; Sun *et al.*, 2015; Zhang *et al.*, 2015) or a zigzag mixer can be added as passive mixers to the microchannel to reduce the mixing time (Valencia *et al.*, 2010).

As mentioned earlier for the bulk preparation of nanoparticles, residual solvent removal is required before further use of polymeric nanoparticles produced with microfluidics e.g. in *in vitro* cell culture studies. Processes like solvent removal with or without reduced pressure (Leung and Shen, 2018; Ortiz de Solorzano *et al.*, 2016), filtration through a 0.2 μm membrane (Donno *et al.*, 2017; Kolishetti *et al.*, 2010), ultrafiltration (Kolishetti *et al.*, 2010), centrifugal filtration (Lim *et al.*, 2014b), centrifugation (Xie and Smith, 2010) or ultra-centrifugation (Amoyav and Benny, 2018) are applied individually or in combination to remove residual solvents.

Scaling up the production of nanoparticles is necessary to formulate a sufficient amount of nanoparticles for *in vivo* studies and clinical applications (Baby *et al.*, 2017). The parallelization of 8-25 microfluidic channels can increase the productivity of nanoparticle production from 0.084 g/h to 75 g/h depending on the microfluidic device (Lim *et al.*, 2014a; Min *et al.*, 2014; Toth *et al.*, 2017). Other strategies to scale up the production of nanoparticles include increasing the flow rate or designing the microchannel to have a greater depth to increase the sample volume and yield (Baby *et al.*, 2017; Liu *et al.*, 2015).

1.3.3.2 *Optimisation of size and charge of polymeric nanoparticles*

The size of nanoparticles plays a crucial role in determining the therapeutic efficacy and biodistribution (Zhigaltsev *et al.*, 2012), and generally small uniform nanoparticles are desirable, particularly for intravenous drug application. Uniform and small nanoparticles can be obtained with a microfluidic approach and are characterized by a low polydispersity and a narrow size range (Capretto *et al.*, 2013; Karnik *et al.*, 2008). Further, a uniform nanoparticle

size is advantageous for consistent release of encapsulated drugs, prediction of biodistribution and cellular uptake of nanoparticles (Xie and Smith, 2010).

In order to influence the size of polymeric nanoparticles, sample-related parameters, like molecular weight and concentration of the polymer, organic solvents, surfactant concentration and channel dimensions can be varied to influence the size of polymeric nanoparticles prepared using microfluidics. For example, an increase in size from 25 to 220 nm for polymeric nanoparticles formulated with polyethylene glycol-poly(lactic-*co*-glycolic) acid (PEG-PLGA) polymer was found when the molecular weight of the PLGA polymer was increased from 10 to 95 K (Kang *et al.*, 2013; Lim *et al.*, 2014a; Min *et al.*, 2014; Valencia *et al.*, 2013). Similarly, an increase in concentration of the PEG-PLGA polymer from 5 to 50 mg/mL led to an increase in size of the resulting nanoparticles (Amoyav and Benny, 2018; Kang *et al.*, 2013; Karnik *et al.*, 2008; Lim *et al.*, 2014a) and a similar observation was made for the PLGA polymer (Bramosanti *et al.*, 2017; Karnik *et al.*, 2008; Xu *et al.*, 2017). However, there are limits to these polymer characteristics in order to yield high quality nanoparticles. This is illustrated in a study by Min *et al.* (2014) who reported aggregation when PEG-PLGA with high molecular weight PLGA (PEG_{5k}-PLGA_{55k}) and at a high concentration (50 mg/mL) were used in combination with a low flow rate ratio (7:3, aqueous:organic) and low flow rates (< 0.08 mL/min). A possible reason for aggregation is that at low flow rates, the Re is low, diffusive mixing is less efficient and aggregation of the non-precipitated polymer can occur (Min *et al.*, 2014). This demonstrates that several factors need to be considered to operate a microfluidic device without losing control over the size of nanoparticles and to avoid blocking of the microchannel (Liu *et al.*, 2010). From the studies performed to date, it seems that the influence of polymer concentration is more predominant than the influence of molecular weight in determining the size of the resulting polymeric nanoparticles (Lim *et al.*, 2014a).

The organic solvent used to dissolve the polymer also influences the size of polymeric nanoparticles. In comparison to polymeric nanoparticles formulated with dimethyl sulfoxide (DMSO) as an organic solvent, smaller polymeric nanoparticles below 150 nm were obtained when acetonitrile or acetone were used (Bramosanti *et al.*, 2017; Chiesa *et al.*, 2018). The reason proposed for this was that the higher viscosity of DMSO reduced the flow of the fluids at the interface between the aqueous and organic solutions in the microfluidic device, resulting in an increase in nanoparticle size (Bramosanti *et al.*, 2017; Chiesa *et al.*, 2018).

The charge carried by polymeric nanoparticles is a key property that can influence *in vivo* performance and is determined by the functional groups present on the polymers that comprise the nanoparticles. Modification to the polymer end group can be used to influence the surface charge of polymeric nanoparticles. For example, by mixing neutral PEG with a methoxy (-OCH₃) end group with negatively charged PEG comprising a carboxyl (-COOH) end group, the surface charge of nanoparticles was tuned between -5 and -20 mV (Valencia *et al.*, 2013).

Incorporation of stabilizers including PVA, sodium cholate or Tween[®]80 in the aqueous anti-solvent for use in microfluidics can influence the size of PLGA nanoparticles and the encapsulation efficiency of drugs (Morikawa *et al.*, 2018). The highest encapsulation efficiency of 18% for curcumin-loaded PLGA nanoparticles was achieved with 1% (w/v) PVA (Morikawa *et al.*, 2018). However, the nanoparticles showed a large size of around 200 nm. In contrast, nanoparticles formulated with sodium cholate or Tween[®]80 had an encapsulation efficiency below 15% and a size below 120 nm (Morikawa *et al.*, 2018). Amoyav and Benny (2018) also investigated the influence of PVA on the size of PLGA-PEG nanoparticles and found that

smaller nanoparticles with a size of 130 nm were produced with increasing concentrations of PVA from 0.5 to 2% (w/v). Surfactants such as PVA are needed to reduce the interfacial tension between the fluids and avoid aggregation of the newly formed nanoparticles (Amoyav and Benny, 2018).

Baby *et al.* (2017) investigated the influence of the microchannel characteristics, width (y-dimension) and depth (z-dimension), of a 2D HFF device on the size of PEG-PLGA nanoparticles. The size of PEG-PLGA_{55K} nanoparticles increasing to 107 nm when the width of the microchannel was increased from 20 to 100 μm . Further, an increased depth of the microchannel, 200 μm in comparison to 50 μm , decreased the size of the formulated nanoparticles by 40 nm at a flow rate ratio of 0.8 (Baby *et al.*, 2017).

Microfluidics is an efficient approach to tune the size of nanoparticles by altering sample-related parameters. In addition, the physicochemical characteristics of polymeric nanoparticles such as surface charge and decoration can be altered to enhance nanoparticle-cell interaction.

1.4 Modifications of polymeric nanoparticles

The potential of nanoparticles to be effective drug carriers depends on their physiochemical properties, which determine interactions with the human body including cellular uptake, biodistribution and clearance (Banik *et al.*, 2016; Griffin *et al.*, 2016; von Roemeling *et al.*, 2017). Further, the biodistribution of polymeric nanoparticles depends on several characteristics of the drug delivery system including size, charge, surface modifications and the surface density of ligands (Farokhzad and Langer, 2009).

1.4.1 Influence of size on cellular uptake and biodistribution

As discussed earlier, the size of nanoparticles is influenced by the components used in their production such as the type of polymer (e.g. PLGA, chitosan) and surfactant (e.g. PVA) and by the selected preparation method (Banik *et al.*, 2016; He *et al.*, 2010; Partikel *et al.*, 2019). The preferred pathway of cellular uptake is determined by the size of the nanoparticles, with smaller nanoparticles having a greater chance of uptake in comparison to larger nanoparticles (Griffin *et al.*, 2016). Nanoparticles with a size under 1 μm are internalized via phagocytosis and nanoparticles with a size under 200 nm can enter the cell via endocytosis (Sharma *et al.*, 2015). He *et al.* (2012) showed higher uptake of methyl methacrylate-chitosan nanoparticles with a size of 300 nm in comparison to nanoparticles with a size of 600 or 1000 nm in a Caco-2 cell monoculture and co-culture with Raji B cells. An explanation for this size-dependent behaviour is that with a larger size, the number of available pathways for uptake into cells is reduced (He *et al.*, 2012). Endocytic uptake pathways for nanoparticles include the clathrin-dependent and caveolae-dependent pathways as well as macropinocytosis (Dausend *et al.*, 2008), which are further discussed in Section 1.5.2. In a similar study, PLGA nanoparticles with a size of 170 nm showed greater uptake in Caco-2 cells in comparison to PLGA nanoparticles with a size above 300 nm (Gaumet *et al.*, 2009), indicating that the size of polymeric nanoparticles is crucial to enhance cellular uptake.

In addition, the size of polymeric nanoparticles influences their elimination from the body. The main routes for elimination of nanoparticles include the kidneys, the lymphatic system and the reticuloendothelial system (RES) (Griffin *et al.*, 2016; von Roemeling *et al.*, 2017). The RES, more frequently referred to as the mononuclear phagocytic system (MPS), is the system responsible for the removal of nanoparticles from the blood vessels by macrophages

(Alexander-Bryant *et al.*, 2013). Nanoparticles circulating in the bloodstream are recognised by proteins called opsonins (Alexander-Bryant *et al.*, 2013). These proteins bind to the nanoparticle surface and make the particles available to be taken up by macrophages and further transported to liver and spleen (Alexander-Bryant *et al.*, 2013; Danhier *et al.*, 2012). Nanoparticles with a size above 200 nm are likely to be removed by the MPS, whereas smaller nanoparticles under 100 nm and with hydrophilic characteristics show fewer interactions with the MPS and can avoid elimination (Alexander-Bryant *et al.*, 2013). Nanoparticles with a size between 40-60 nm can exit blood vessels via fenestrated capillaries in the kidneys and in the intestine (Siafaka *et al.*, 2016). The pores in the renal fenestrated endothelium are up to 100 nm in diameter and particles with a smaller size can pass through (von Roemeling *et al.*, 2017). The route of elimination through the lymphatic system applies to nanoparticles with a size of 600 nm or more and clearance occurs through liver and spleen (Bobo *et al.*, 2016; Siafaka *et al.*, 2016).

1.4.2 *Effective surface charge*

The degree of surface charge associated with nanoparticles influences the stability of the nanoparticles and thus their tendency to aggregate. Polymeric nanoparticles form a stable suspension if their zeta potentials are lower than -30 mV or higher than +30 mV, since the aggregation of nanoparticles is reduced due to electrostatic repulsion between the nanoparticles (Sonam *et al.*, 2014; Tefas *et al.*, 2015; Vasconcelos *et al.*, 2015). Depending on the design of the nanoparticles, their surface charge is able to influence the electrostatic interactions with the gastrointestinal mucus (Griffin *et al.*, 2016). Mucin, a mucus protein, can immobilise charged nanoparticles because of hydrophobic interactions (Lundquist and Artursson, 2016). Nanoparticles with a surface charge between -10 and +10 mV show fewer interactions with the

cell membrane, whereas positively charged nanoparticles ($> +15$ mV) can help to improve the internalization due to the interactions with the negatively charged cell membrane (He *et al.*, 2010; Lundquist and Artursson, 2016). After internalization, positively charged nanoparticles are also able to avoid degradation via lysosomes and locate in the perinuclear regions of cells (Danhier *et al.*, 2012; Frohlich, 2016).

1.4.3 Surface modification

The surface of nanoparticles can be modified and approaches such as the addition of PEG (Partikel *et al.*, 2019), coating with chitosan (Cole *et al.*, 2018) and attachment of ligands (Bartheldyova *et al.*, 2018) are used (Figure 1.5).

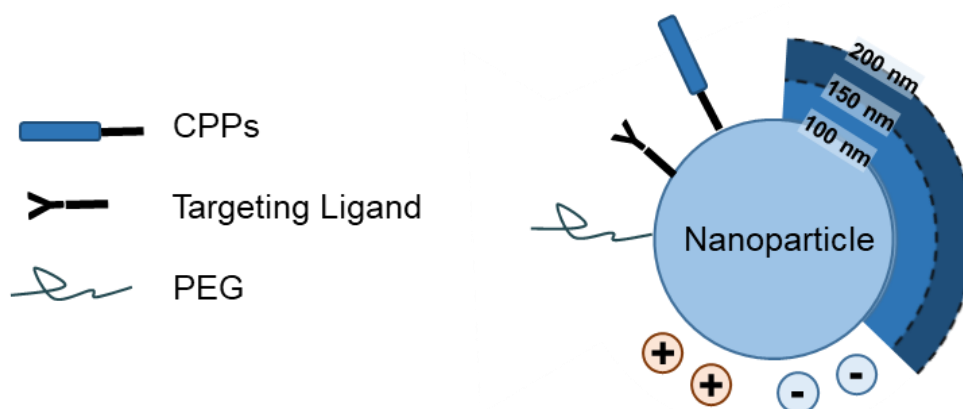


Figure 1.5. The influence of size, charge and surface modification on the physicochemical properties of polymeric nanoparticles (Fenton *et al.*, 2018; Torchilin, 2014). CPPs = cell-penetrating peptides, PEG = polyethylene glycol.

Modification of nanoparticles with PEG attached to the nanoparticle wall is beneficial to achieve a longer blood circulation in order to increase the half-life of the nanoformulations in the bloodstream (Danhier *et al.*, 2012). The molecular weight and density of PEG chains on the nanoparticle surface influence the absorption of proteins leading to an inhibition of the

opsonisation process and the delayed clearance of the modified nanoparticles (Pelaz *et al.*, 2015; von Roemeling *et al.*, 2017). In addition, PEG decoration can enhance the mucus permeability, by preventing aggregation and reducing degradation of the nanoparticles (Griffin *et al.*, 2016).

The surface of polymeric nanoparticles can be modified by coating the nanoparticles with a charged polymer. The coating of polymeric nanoparticles is based on an electrostatic interaction between the negatively charged nanoparticles and the positively charged chitosan (Czuba *et al.*, 2018). The blood circulation time of chitosan-coated polymeric nanoparticles is improved by hindrance of protein binding to the surface of the nanoparticles and prevention of phagocytic uptake (Abouelmagd *et al.*, 2015). After oral administration, the chitosan coating can act as a permeation enhancer due to the mucoadhesive properties of chitosan and by opening tight junctions between epithelial cells and increasing uptake (Cole *et al.*, 2018; Lopes *et al.*, 2016; Sheng *et al.*, 2015).

Surface modification of nanoparticles with specific ligands, including proteins like transferrin and glycoprotein 1b and polysaccharides like hyaluronic acid, are advantageous for targeted delivery of drugs into epithelial, endothelial and cancer cells, respectively (Bartheldyova *et al.*, 2018; Xu *et al.*, 2013a; Zhu *et al.*, 2016b). Active targeting is achieved by binding of surface-modified nanoparticles to specific and overexpressed receptors on target cells or by extending the residence time and uptake (Danhier *et al.*, 2012; Date *et al.*, 2016).

1.5 Cell-penetrating peptides

Cell-penetrating peptides (CPPs) are membrane-permeable peptides with positive charges, dictated by the number of arginine and lysine amino acids in the peptide sequence (Jafari *et al.*, 2015; Lonn and Dowdy, 2015). CPPs are short amino acid sequences of 30 amino acids or less and also called protein transduction domains or Trojan peptides and show potential to enhance the delivery of cargos (Huang *et al.*, 2013; Jafari *et al.*, 2015; Lukanowska *et al.*, 2013; Zhang *et al.*, 2016). CPPs are characterised by the ability to cross cell membranes, such as the blood brain barrier and intestinal membrane, while also mediating the uptake of cargos due to the strong affinity of the CPPs to the lipid bilayer of cells (Feiner-Gracia *et al.*, 2018; Su *et al.*, 2009; Zhu *et al.*, 2016a). The translocation ability applies to the CPP on their own but also for conjugates of the CPPs with different cargos like polymeric nanoparticles (Feiner-Gracia *et al.*, 2018; Vasconcelos *et al.*, 2015), liposomes (Shi *et al.*, 2019), protein-based nanoparticles (van Oppen *et al.*, 2019), macromolecules such as peptides, proteins (Kristensen *et al.*, 2015), small interfering RNA (siRNA) and plasmid DNA (Künnapuu *et al.*, 2019; Zhang *et al.*, 2019) and fluorophores (Trehin *et al.*, 2004). CPP conjugates have been studied for the treatment of asthma, cardiovascular diseases, inflammation, cancer and stroke (Jones *et al.*, 2005).

1.5.1 Classification and specific properties of CPPs

CPPs can be classified into different categories depending on the focus of the classification (Table 1.2). Commonly CPPs are classified based on their physicochemical properties and divided in cationic, amphipathic and hydrophobic CPPs (Jafari *et al.*, 2015). Further, CPPs are categorised by the origin of the peptide and can be either derived from natural proteins, chimeric combination of two different peptide motifs or synthesised as artificial

sequences of amino acids (Jafari *et al.*, 2015; Zhu *et al.*, 2016a). The number of charges in the CPP sequence influences the penetration abilities of CPPs; with a comparatively small amount of positive charges leading to reduced cell internalization. In contrast, a high amount of positive charges can induce toxicity (Lonn and Dowdy, 2015).

CPPs that are commonly used for drug delivery include TAT, polyarginine, penetratin and Xentry. The highly positively charged TAT is the most studied CPP and is derived from the human immunodeficiency virus trans-activating transcriptional activator (TAT) protein (Trehin *et al.*, 2004). The translocation abilities of the TAT protein were discovered by Green and Lowenstein as well as Frankel and Pabo in 1988 (Frankel and Pabo, 1988; Green and Loewenstein, 1988). Later, Vives *et al.* (1997) identified that the amino acid residues number 48-60 (GRKKRRQRRRPPQ) showed cell internalization on their own. The number of arginine residues in the CPP sequence influences the transduction ability of the highly positively charged arginine-rich CPPs to deliver small molecules. Synthetic CPPs with 6 to 12 arginine residues were found to achieve an efficient translocation into mouse macrophages and human skin fibroblasts (Futaki *et al.*, 2001; van Oppen *et al.*, 2019). Further, polyarginines showed higher efficiency for the internalization in comparison to polyhistidines and polylysines (Mitchell *et al.*, 2000). Some CPPs are of special interest due to the fact that the peptide has been shown to have specific features in addition to translocation abilities. Penetratin (Table 1.2) can cross the blood brain barrier (Xia *et al.*, 2012) and Xentry (Table 1.2) can permeate into cancer cells such as HepG2 cells to deliver siRNA, which express syndecans, a group of heparan sulphate proteoglycans on the cell surface (Montrose *et al.*, 2014b; Patel *et al.*, 2019).

Table 1.2. Summary of cell-penetrating peptides commonly used in pharmaceutical research.

Name	Parent protein	Origin	Properties	Sequence	Cargos	References
TAT (48-57)	Human immunodeficiency virus-1 transcriptional activator protein	Protein derived	Cationic	GRKKRRQRRR	Nanoparticles, protein	(Frankel and Pabo, 1988; Green and Loewenstein, 1988)
Penetratin (43-58)	<i>Drosophila antennapedia</i> homeodomain	Protein derived	Amphipathic	16-mer RQIKIWFQNRRMKWKK	Protein, oligopeptides, oligonucleotides	(Clayton <i>et al.</i> , 2006; Derossi <i>et al.</i> , 1996)
Polyarginine (R₆₋₁₂)	N/A	Synthetic	Cationic	RRRRRRRR	Nanoparticles, protein	(Ryser and Hancock, 1965)
Transportan	Mastoparan (full sequence) and galanin (N-terminal sequence)	Chimeric	Amphipathic	21-mer GWTLSAGYLLGKINLK- -ALAAALAKKIL	Drug molecules	(Pooga <i>et al.</i> , 1998; Ruczyński <i>et al.</i> , 2019)
Xentry	X-protein of the hepatitis B virus	Protein derived	Hydrophobic	LCLRPGV	Protein	(Montrose <i>et al.</i> , 2014a; Patel <i>et al.</i> , 2019)

Over the years, additional categories for the classification of CPPs have emerged and include antimicrobial, activatable and cyclic CPPs. For example, transportan (Table 1.2) shows antimicrobial activity against Gram-positive and Gram-negative bacteria, which makes it attractive for conjugation with antibiotic drugs (Ruczyński *et al.*, 2019). Antimicrobial peptides have similar characteristics as CPPs, but a higher number of lysine residues in the sequence is beneficial for uptake into bacteria (Bahnsen *et al.*, 2013). Another class of CPPs are ‘activatable CPPs’, which are designed to release the functional CPP sequence from a polyanionic peptide after activation by enzymes (Farkhani *et al.*, 2014). Activatable CPPs are primarily used in cancer research and can be utilized for the visualisation of enzyme reactions by releasing imaging probes (Farkhani *et al.*, 2014). The CPP sequence plays a role in the cellular uptake and a modification of the amino acid sequence to form cyclic CPPs is believed to enhance the delivery capacity of CPPs and promote cellular uptake efficiency (Amoura *et al.*, 2019; Patel *et al.*, 2019). A cyclic structure is formed by disulphide bonds between cysteine residues after introduction to the amino acid sequence at the N- and C-terminal ends (Amoura *et al.*, 2019; Patel *et al.*, 2019). Cellular uptake, expressed as an increase in fluorescence in HeLa cells, of conjugates between cyclic R₈ or TAT and the green fluorescence protein increased by 6-9 fold in comparison to the linear amino acid sequences of the CPPs (Patel *et al.*, 2019).

1.5.1.1 Sequence-modified cell-penetration peptides

Optimisation of the CPP sequence is of great research interest and several studies have shown a positive impact on cell internalization when branched CPPs are used. Limitations of linear CPPs include a low translocation efficiency, low target specificity and instability in the physiological environment (Monreal *et al.*, 2015). Modification of the CPP sequence results in new classes of CPPs with a variety of different architectures (Figure 1.6).

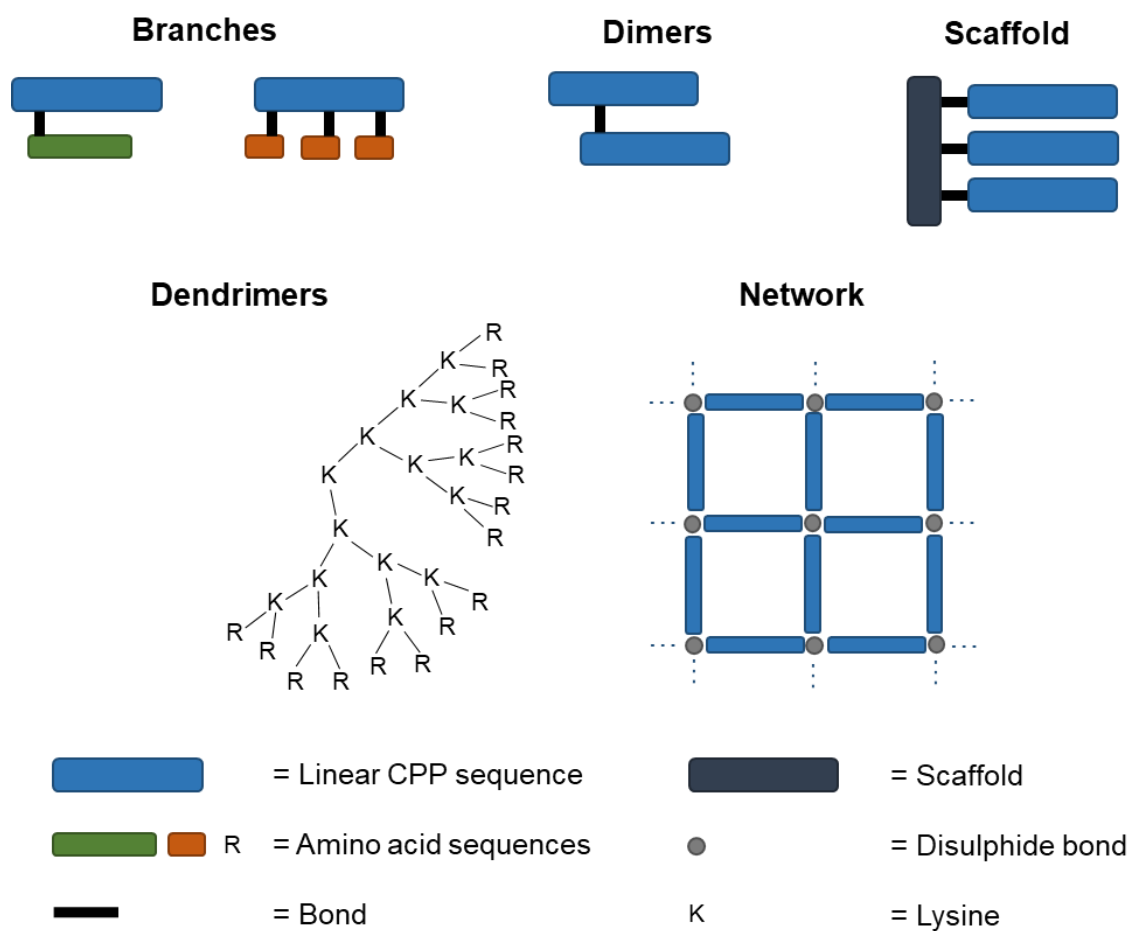


Figure 1.6. Classification of cell-penetrating peptides after modification of their sequence by adding branches, dimers, scaffolds and creating networks and dendrimers (Angeles-Boza *et al.*, 2010; Brock *et al.*, 2018; Eggimann *et al.*, 2014; Foerg *et al.*, 2007; Jeong *et al.*, 2016; Saleh *et al.*, 2010; Yoo *et al.*, 2017; Zhao *et al.*, 2014a). CPP = cell-penetrating peptide.

New strategies to increase the number of positive charges associated with CPPs include the synthesis of more complex CPP analogues with additional cationic groups. The dimerization of CPPs (Figure 1.6) showed improvements in cellular uptake, endosomal escape and cytotoxicity (Erazo-Oliveras *et al.*, 2014; Monreal *et al.*, 2015). For example, the fluorescently labelled dimeric branched TAT peptide (TATp-D) led to an improved cellular uptake in HeLa cells, with a six- to seven-fold increase in fluorescence intensity compared to linear TAT at concentrations of 0.25 μM (Monreal *et al.*, 2015). Another dimeric and fluorescent TAT (dfTAT) showed the ability of efficient cytosol delivery of a cell-impermeable

fluorophore after co-administration to HeLa cells (Erazo-Oliveras *et al.*, 2014). Further, the dimerization of the sC18 peptide (derived from the antimicrobial parent protein CAP 18), increased the fluorescence intensity of the sC18 dimer in HT-29-MTX-E12 cells (further referred to as HT-29 cells) by 10-fold in comparison to a linear sC18 (Hoyer *et al.*, 2012). In addition, the dimeric TAT-based CPPs, TATp-D and dfTAT, did not show cytotoxicity in HeLa at concentrations between 5-50 μM and concentrations of the sC18 dimer up to 50 μM did not show cytotoxicity in HT-29 cells (Erazo-Oliveras *et al.*, 2014; Hoyer *et al.*, 2012; Monreal *et al.*, 2015).

The CPP sequence can be modified by the introduction of side branches, formation of dendrimers, linkage of CPPs sequences via disulphide bonds and attachment of the CPP sequence to a peptide scaffold (Figure 1.6). Side branches can either be single or multiple branches and can consist of specific amino acid sequences or can be non-natural amino acid sequences, depending on the application (Foerg *et al.*, 2007; Saleh *et al.*, 2010). The formation of G1 to G3 dendrimers based on CPP sequences can increase the charges in the outer region of the peptide sequence (Zhao *et al.*, 2014a). A G3 dendrimer based on TAT with short dipeptide branches showed higher cell penetration, lower cytotoxicity in HeLa cells and better human serum stability in comparison to the linear CPP (Eggimann *et al.*, 2014). Cysteine can be used to link to CPPs via disulphide bonds when adjacent cysteine residues are present in the CPP sequence. A branched TAT network made through disulphide bonds showed improved gene delivery ability and cyto-compatibility compared to the linear peptide TAT (Jeong *et al.*, 2016; Yoo *et al.*, 2017). CPPs can be conjugated to a peptide scaffold containing lysine or cysteine amino acids in order to achieve a branched structure (Angeles-Boza *et al.*, 2010; Brock *et al.*, 2018). The peptide scaffold further serves for the conjugation of a fluorescent dye for detection purposes (Angeles-Boza *et al.*, 2010; Brock *et al.*, 2018). Trimers of TAT on a

peptide scaffold showed locally increased concentrations (Angeles-Boza *et al.*, 2010), and more efficient endocytosis in comparison to the monomeric TAT (Brock *et al.*, 2018). It is worth noting that these trimers of TAT on a peptide scaffold were only non-toxic to HeLa cells at concentrations below 3 μM (Angeles-Boza *et al.*, 2010; Brock *et al.*, 2018).

1.5.2 *Interactions between cell-penetrating peptides and cells*

CPPs have been studied for more than thirty years, starting with the discovery of TAT in 1988; however, their detailed cellular uptake mechanisms as drug delivery systems are still not completely understood. Initially, it was believed that direct penetration was the main route for CPPs into cells but with further investigations also endocytosis was found as a pathway for CPP uptake (Silva *et al.*, 2019). The cellular uptake of CPPs is proposed to occur via non-endocytic pathways or endocytic pathways (Birch *et al.*, 2018b) and is influenced by the structure and concentration of the CPP, the delivery cargo, the bond with the delivery cargo, the detection label, temperature, cell type and lipid composition of the cell membrane (Cardoso *et al.*, 2012; Hoyer *et al.*, 2012; Hu *et al.*, 2019; Hyrup Møller *et al.*, 2015; Klein *et al.*, 2017; Patel *et al.*, 2019). A rapid uptake or direct transduction through the cell membrane is observed when cells are incubated with higher concentration of CPPs due to a higher local concentrations of the CPPs on the cell membrane (Brock, 2014; Pan *et al.*, 2016).

The different models proposed for CPP uptake are based on the general assumption that the mechanism for translocation is through interactions between the positively charged CPPs and the negatively charged phosphate groups of the cell membrane (Hu *et al.*, 2019). Specifically, the guanidinium ion that is present in arginine-rich CPP sequences interacts with the negatively charged functional groups on phospholipids, monosaccharides and proteins

present in the cell membrane (Borrelli *et al.*, 2018; Su *et al.*, 2009). A study by Su *et al.* (2009) showed the importance of arginine and lysine amino acids in the CPP sequence by investigating the distance between penetratin and phospholipids, indicating a close contact of arginine and lysine with the phospholipids. More recently, molecular simulations also showed strong attraction between CPPs and phospholipids, which is needed for translocation through the lipid-rich cell bilayer (Gao *et al.*, 2019).

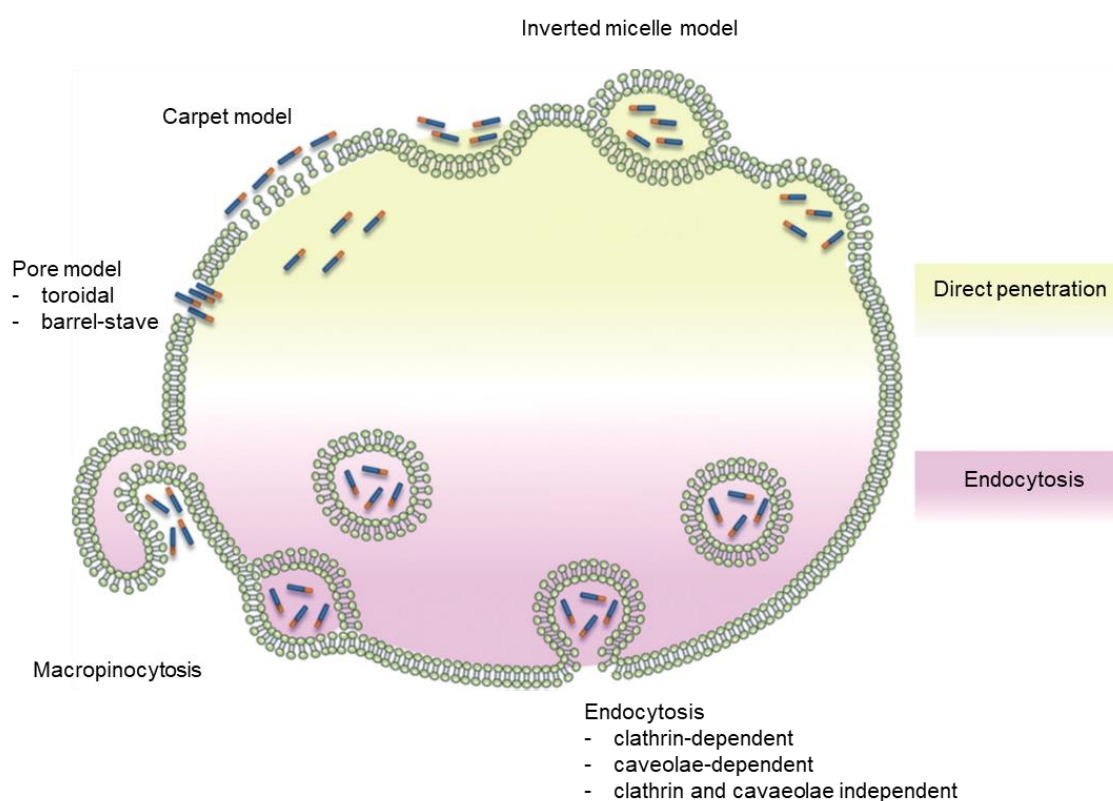


Figure 1.7. Cellular uptake mechanisms of cell-penetrating peptides adapted from Guidotti *et al.* (2017) with permission from Elsevier.

The non-endocytic pathways (direct translocation) include uptake in an energy independent manner via the inverted micelle, the carpet model or the pore model (Figure 1.7) (Derossi *et al.*, 1996; Koren and Torchilin, 2012). The inverse micelle model is based on the formation of an inverse micelle within the cell membrane, which incorporates the peptides on

the outside of the cell and releases the peptides on the inside of the cell (Su *et al.*, 2009). The carpet model is described by the adsorption of CPPs to the outer layer of the cell membrane in a parallel orientation (Binder and Lindblom, 2003; Clayton *et al.*, 2006; Su *et al.*, 2009). With the presence of the CPPs on the surface of the cell membrane, the transmembrane electric field between the outer and inner membrane is disturbed resulting in the permeation of the CPP through the leakier cell membrane (Binder and Lindblom, 2003; Su *et al.*, 2009). After translocation of the CPP, an equilibrium of the CPP concentration between the outside and the inside of the cell supports the stabilization of the transmembrane electric field (Binder and Lindblom, 2003). The carpet model was reported for penetratin and arginine-rich CPPs (Alves *et al.*, 2008). Two kinds of pores, barrel-stave and toroidal, are induced by CPPs (Clayton *et al.*, 2006). In the barrel-stave pore model, CPP monomers aggregate and form a bundle where the hydrophobic regions interact with the lipid compartments of the cell membrane and the hydrophilic regions of the bundle produce an aqueous pore (Clayton *et al.*, 2006). In contrast, the toroidal pore model relies on direct interactions of the hydrophilic and charged regions of the CPPs with the phospholipid head groups of the cell membrane (Clayton *et al.*, 2006).

To better understand the interactions on a molecular level, molecular simulation between a cell membrane model and CPPs are used (Gao *et al.*, 2019; Hu *et al.*, 2019). Molecular dynamic simulation of octa-arginine with a small hydrophilic cargo showed that the lifetime of a formed water pore within the membrane is longer and translocation of CPPs and cargo increased when the linker length is half the membrane thickness (Hu *et al.*, 2019). It is important to consider that linkers between CPPs and cargos can influence the cellular selectivity and linkers should be biodegradable (Hu *et al.*, 2019). The direct penetration mechanisms are preferred by CPPs with small cargos, whereas CPPs with larger cargos (peptides and proteins) prefer to enter the cell via endocytosis (Brock, 2014; Patel *et al.*, 2019).

Endocytosis mechanisms including clathrin-dependent, caveolae-dependent, clathrin independent and caveolae independent uptake as well as macropinocytosis can be utilized by CPPs (Figure 1.7) (Gump *et al.*, 2010; Koren and Torchilin, 2012). For the clathrin-dependent endocytosis, clathrin coat protein complexes are expressed on the cell surface and binding of molecules induces endocytosis (Xu *et al.*, 2013b). Caveolae appear as invaginations on the cell surface and after binding to the cell surface molecules get trapped and internalised (Pelkmans and Helenius, 2002). Macropinocytosis relies on the formation of membrane ruffles, which are able to fold back towards the cell membrane entrapping fluids and nanoparticles located on the cell surface (Reifarh *et al.*, 2018; Xu *et al.*, 2013b). Cellular uptake via macropinocytosis is initiated by electrostatic interactions of the positively charged and arginine-rich CPPs with negatively charged molecules on the cell membrane (Gump *et al.*, 2010). The internalization of CPPs via endocytosis results in the formation of endosomes containing the CPPs (Jones, 2007). Therefore, after endocytosis it is important for the CPPs to escape the endosome in order to avoid degradation and to deliver the cargo (Silva *et al.*, 2019). Possible mechanisms include release through endosomal acidification or interaction of the CPPs with the endosomal membrane (Fischer *et al.*, 2004; Silva *et al.*, 2019).

Apart from the uptake pathway of CPPs, there are three crucial steps to consider for successful internalization. First, the CPP needs to bind to the components of the cell membrane and secondly the binding needs to be followed by the absorption through the hydrophobic cell membrane. Lastly, a breakage of the bond between the cell membrane and the CPP needs to occur in order to release the CPP into the cytoplasm (Hercé *et al.*, 2014). These steps are crucial for a translation of CPPs from *in vitro* and *in vivo* studies to clinical studies and the development of commercial products.

The number of CPPs in the clinic and in clinical trials is low due to a limited understanding of the molecular mechanisms for the uptake of CPPs into cells (Gao *et al.*, 2019; Klein *et al.*, 2017). CPPs are captured in endosomes after endocytosis and the low cytoplasmic delivery efficiency, as well as the low bioavailability and selectivity, make translation to the clinic difficult (Klein *et al.*, 2017). Clinical trials are mainly reported for CPP-drug conjugates and the reasons for discontinuing clinical trials include low stability and poor efficiency of CPPs *in vivo* and toxicity introduced by excipients (Habault and Poyet, 2019). For the efficient delivery of CPPs and cargos into cells, it is crucial to understand the uptake mechanisms and localization processes within the cells and ensure the functionality of the cargo is protected until it reaches the site of action (Huang *et al.*, 2015).

1.5.3 Association of cell-penetrating peptides with cargos

The association of CPPs with cargo includes either a physical mixture of both components or formation of a covalent bond between CPP and cargo (Figure 1.8) (Liu *et al.*, 2013). Both approaches, non-covalent and covalent conjugation, aim to increase the delivery efficiency of cargos and are used for a variety of different cargos (Huang *et al.*, 2015).

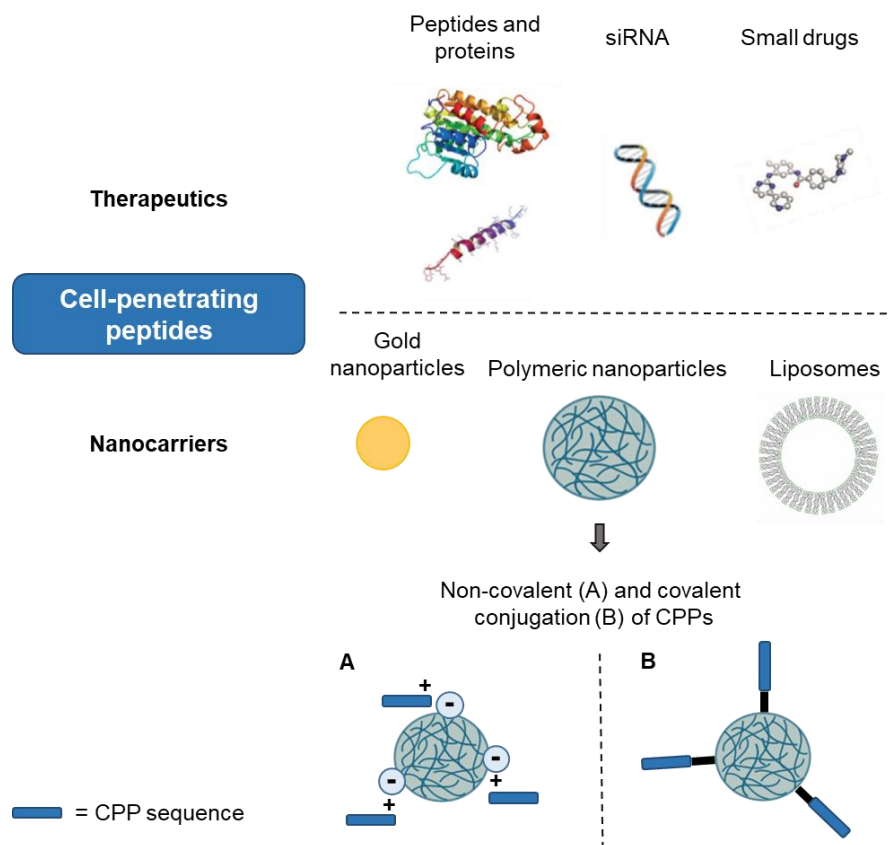


Figure 1.8. Possible cell-penetrating peptide cargos and schematic of non-covalent (A) and covalent (B) interactions between polymeric nanoparticles and CPPs (Guidotti *et al.*, 2017; Streck *et al.*, 2019c) (With permission from Elsevier). CPP = cell-penetrating peptide.

Using a physical mixture, CPPs and cargos are co-administered in order to enhance the cellular interactions of the cargo (Bu *et al.*, 2015). The main non-covalent binding approaches include electrostatic interactions and the formation of ionic complexes between anionic and cationic molecules or streptavidin-biotin interactions and metal-affinity interactions between CPPs and cargos (Huang *et al.*, 2015). Electrostatic interaction based on opposite charges can be formed between CPPs and macromolecules as well as polymeric nanoparticles and CPPs (Figure 1.8A) (Bu *et al.*, 2015; Liu *et al.*, 2013). CPPs were found to enhance absorption of biomarcomolecules (e.g. insulin) by co-administration with excess concentrations of CPPs (Kamei *et al.*, 2009). Using electrostatic interactions, CPPs should be present in excess to ensure binding to oppositely charged cargos. Any potential instability of the physical mixture

also needs to be considered due to interactions with competing ions in the GIT (Liu *et al.*, 2013). Further, CPPs have been used for *in vivo* gene and protein delivery after complexation or condensation of CPPs with siRNA or antigens and studies in mice have shown that these CPP delivery systems were able to inhibit the influenza virus replication and reduced tumour growth of lung epithelial cells that were transformed with human papillomavirus (Shahbazi and Bolhassani, 2018; Zhang *et al.*, 2019). Electrostatic interactions between negatively charged PLA or PLGA nanoparticles and positively charged CPPs can enhance the delivery of CPP/messenger RNA polyplexes and encapsulated drugs (Bu *et al.*, 2015; Cai *et al.*, 2017; Coolen *et al.*, 2019).

The covalent linkage between CPPs and cargos depends on the cargo that is bound to the CPP. Proteins and peptides are most commonly conjugated to CPPs by gene fusion utilizing bacterial expression of recombinant fusion peptides between CPPs and therapeutic peptides or proteins (Kristensen *et al.*, 2015). For the conjugation of drug molecules, proteins and fluorescent dyes for tracking of CPP-cargo formulations, chemical reactions like click chemistry reactions are used (Patel *et al.*, 2009; Ruczyński *et al.*, 2019; Trehin *et al.*, 2004). Other binding strategies for cargos to CPPs include covalent linkage via hydrazine and disulphide bonds (Hu *et al.*, 2019). The linkage of small molecules to the CPP sequence should preferably leave amino acids towards the C-terminus protonated, in order to preserve the activity of CPP and cargo, the uptake abilities, and to avoid unwanted toxicity (Ruczyński *et al.*, 2019). Covalent conjugation between CPPs and the above mentioned cargos results in well-defined molecules and enables predictions of the chemical structure and the activity of the conjugates (Kristensen *et al.*, 2015; Patel *et al.*, 2019). Recent studies have shown that the position of the conjugation in the CPPs sequence is crucial since this influences if a compound shows biological activity e.g. against bacteria (Patel *et al.*, 2019).

Different bioconjugation reactions can be used to functionalize polymeric nanoparticles with CPPs. A covalent linkage between CPPs and nanoparticles can be produced by bioconjugation reactions between polymers and CPPs (Figure 1.8B). Typical bioconjugation reactions are the formation of a thiol-maleimide bond by thiol-amine coupling (Nam *et al.*, 2002; Steinbach *et al.*, 2016; Xia *et al.*, 2012) and formation of an amide bond by carbodiimide conjugation (Egusquiaguirre *et al.*, 2015). Arginine-rich CPPs are well-established for the surface modification of polymeric nanoparticles or inorganic nanoparticles and less frequently for the surface modification of liposomes (Figure 1.8) (Bartczak and Kanaras, 2011; Gullotti and Yeo, 2012; Shi *et al.*, 2019). As part of the introduction to Chapter 2, these reactions will be explained in more detail (Section 2.1.4).

To confirm surface modification, surface charge is frequently used to assess the conjugation of polymeric nanoparticles with CPPs (Coolen *et al.*, 2019; Moku *et al.*, 2019). Changes in surface charge from a negative surface charge of unmodified polymeric nanoparticles to a slightly negative or positive surface charge can indicate successful conjugation of CPPs, depending on the exact composition of the nanoparticle formulation with CPPs (Gartziandia *et al.*, 2016; Liu *et al.*, 2013; Xu *et al.*, 2013a). Additionally, techniques including Fourier-transform infrared spectroscopy (FTIR), nuclear magnetic resonance and X-ray photoelectron spectroscopy (XPS) are used to investigate covalent binding (Bu *et al.*, 2015; Liu *et al.*, 2013; Xia *et al.*, 2012). For example, using XPS the elemental composition of the modified nanoparticles is investigated and the presence of nitrogen indicates the modification of the surface with CPPs (Liu *et al.*, 2013; Xia *et al.*, 2012). FTIR spectroscopy will be discussed further in Section 2.1.4.

Surface modification of polymeric nanoparticles to enhance delivery of encapsulated macromolecules is a prudent approach that does not alter the bioactivity of the encapsulated macromolecule (Jain and Jain, 2015; Liu *et al.*, 2013). CPPs have been conjugated to the surface of polymeric nanoparticles to increase cellular uptake via the ocular and oral routes of drug administration (Chiu *et al.*, 2015; Vasconcelos *et al.*, 2015; Zhu *et al.*, 2016a). In this thesis, the focus is on microfluidics for the preparation of polymeric nanoparticles and the conjugation of CPPs with different architecture to alter the surface properties of polymeric nanoparticles and exploit the influence of the CPP architecture on cellular uptake.

1.6 Thesis aims

Despite the vast amount of research conducted in pharmaceutical formulation science, there is still a need for the improvement of drug delivery systems to successfully translate the research from bench to bedside. Therefore, the overall aim of this thesis was to design, characterise and evaluate an oral drug delivery system with polymeric nanoparticles decorated with CPPs of different architectures for the ability to enhance cellular uptake.

The use of microfluidics for the formulation of polymeric nanoparticles results in the preparation of small and uniform nanoparticles with a good reproducibility. Here, a traditional bulk method and a microfluidics method were compared to investigate if microfluidics is advantageous over a traditional bulk approach for the formulation of PLGA nanoparticles (Chapter 2). Further, the conjugation of CPPs with different architecture to the surface of PLGA nanoparticles leads to a change in the physicochemical properties of the nanoparticles. Therefore, PLGA nanoparticles were modified with CPPs of different architecture using the post-microfluidics conjugation approach and the influence of the CPP architecture on the

physicochemical properties such as size and surface charge of the CPP-tagged PLGA nanoparticles was studied (Chapter 2).

To gain a better understanding of the surface modification and distribution of CPPs on PLGA nanoparticles a second preparation method, an *in situ* microfluidics conjugation approach, for the formulation of the CPP-tagged PLGA nanoparticles was designed. The translation of the conjugation reaction from a post-microfluidics to an *in situ* microfluidics conjugation approach should change the CPP distribution on PLGA nanoparticles. The influence of CPP architecture and the conjugation approach on the distribution of CPPs on PLGA nanoparticles were elucidated with transmission electron microscopy and small angle X-ray scattering (Chapter 3).

To investigate the cellular uptake and interactions of CPP-tagged PLGA nanoparticles with the nano-bio interface, *in vitro* studies with two different cell lines were performed. CPP-tagged PLGA nanoparticles are expected to show greater cellular uptake than unmodified PLGA nanoparticles due the surface modification with CPPs. Further, the role of the CPP architecture on the internalization of PLGA nanoparticles was investigated (Chapter 4).

Chapter Two

Formulation and characterisation of poly-lactic-co-glycolic acid (PLGA) nanoparticles modified with cell-penetrating peptides of different architectures

Parts of this Chapter have been published as:

S. Streck, H. Neumann, H. Mørck Nielsen, T. Rades and A. McDowell (2019). Comparison of bulk and microfluidics methods for the formulation of poly-lactic-co-glycolic acid (PLGA) nanoparticles modified with cell-penetrating peptides of different architectures. *International Journal of Pharmaceutics: X*, 1, 100030.

S. Streck, A. J. Clulow, H. Mørck Nielsen, T. Rades, B. J. Boyd and A. McDowell (2019). The distribution of cell-penetrating peptides on polymeric nanoparticles prepared using microfluidics and elucidated with light scattering techniques. *Journal of Colloid and Interface Science*, 555, 438-448.

S. Streck, L. Hong, B. J. Boyd and A. McDowell (2019). Microfluidics for the production of nanomedicines: Considerations for polymer and lipid-based systems. *Pharmaceutical Nanotechnology*, 7, 1-21.

2.1 Introduction

The physicochemical characteristics of drug delivery systems depend on the preparation method and optimization of preparation-related parameters supports the design of well-defined nanoparticles. Further, surface modifications of polymeric nanoparticles are crucial to increase interactions with cells and the utilization of CPPs for this purpose is described in this Chapter.

2.1.1 Design of experiments

Experimental research carried out in the pharmaceutical sciences often follows a ‘trial and error’ approach (Singh *et al.*, 2011a; Singh *et al.*, 2011b). Using ‘trial and error’ methods means that one variable is adjusted at the time and incrementally, whereas all other parameters remain constant (Singh *et al.*, 2011a; Singh *et al.*, 2011b). The main drawback of applying this approach to the formulation of drug delivery systems is that the true optimum of the input factors may not be able to be identified (Singh *et al.*, 2011a; Singh *et al.*, 2011b). In addition, optimization based on changing one variable at the time does not guarantee that the relation and dependency of the input factors on the output response of the process can be shown. The DoE approach is a powerful alternative used to design experiments efficiently and to show the effect of input factors alone and in combination on the output responses.

DoE is described as finding mathematical relations between various input factors and an output response of a process or system (Mandenius and Brundin, 2008). The applications of DoE studies are broad and include biotechnological processes such as antioxidant extraction from plants (*Sonchus oleraceus* L.) (Ou *et al.*, 2014), enzyme production in relation to the composition of bacteria culture media and pharmaceutical technology processes such as the formulation of nanoparticles (Hanrahan and Lu, 2006). In general, a specific software, e.g.

MODDE, Design-Expert or Mini-Tab, is used to analyse the defined input factors and output responses simultaneously to predict an experimental scheme (Bairagi *et al.*, 2018; Kastner *et al.*, 2014; Patel *et al.*, 2016; Singh *et al.*, 2011a). The use of a DoE for optimisation of a process is greatly supported by advantages including the requirement of only a small number of experiments, minimized experimental bias, and an environmentally friendly and cost-effective aspect due to better use of resources, materials and time (Singh *et al.*, 2011a; Singh *et al.*, 2011b). However, there are also disadvantages, which need to be addressed to make sure the DoE is performed correctly. The disadvantages of a DoE, including a lack of process knowledge and inappropriate selection of variables, need to be overcome by judging the process in question critically (Mandenius and Brundin, 2008). However, when used correctly, DoE can contribute to the investigated process by giving direction to the optimal parameters with a minimum number of experiments and variation of more than one variable at the time.

After definition of the input factors and output responses, a mathematical design for the performance of the DoE study is selected. The applied designs for the DoE commonly include two- or three-level factorial (Derakhshandeh *et al.*, 2007; Vuddanda *et al.*, 2015), central composite (Water *et al.*, 2015) and Box Behnken designs (Figure 2.1) (Bairagi *et al.*, 2018; Patel *et al.*, 2016). The aim is to identify the input factors that have a significant influence on the output response (Bairagi *et al.*, 2018). The experiments are performed in a random order to decrease the appearance of systematic errors and to avoid that expectations about the results of the experiment are likely to influence the experimenter (Mandenius and Brundin, 2008). In addition, the gathering of triplicate data at a specific centre point allows the determination of the experimental error when the same experimental parameters are used. The mathematical models to analyse the obtained output responses include a multiple linear regression (MLR) or a partial least square regression (PLS) model. The MLR model is used for processes that show

a relationship between the independent input factors and one output response (Kastner *et al.*, 2014). The PLS model is used if a correlation between one or more input factors in the process are found (Mandenius and Brundin, 2008). The generated mathematical models are evaluated by either one-way analysis of variance (ANOVA) for the comparison of groups or two-way ANOVA to investigate the effect of separate factors and identify any interactive effects (Hanrahan and Lu, 2006). In addition, the relationship between the input factors and output responses can be visualized graphically to support the explanation of the relationships (Vuddanda *et al.*, 2015). The data can either be shown in a 3D response surface plot or a 2D contour plot (Singh *et al.*, 2011a; Singh *et al.*, 2011b). Both plots show the correlation and interactions between the independent input factors and their influence on the output response (Bairagi *et al.*, 2018; Vuddanda *et al.*, 2015). In particular, mathematical trends of the input factors shown in the response surface plot allow determination of the optimal settings for the experiment (Yadav and Sawant, 2010).

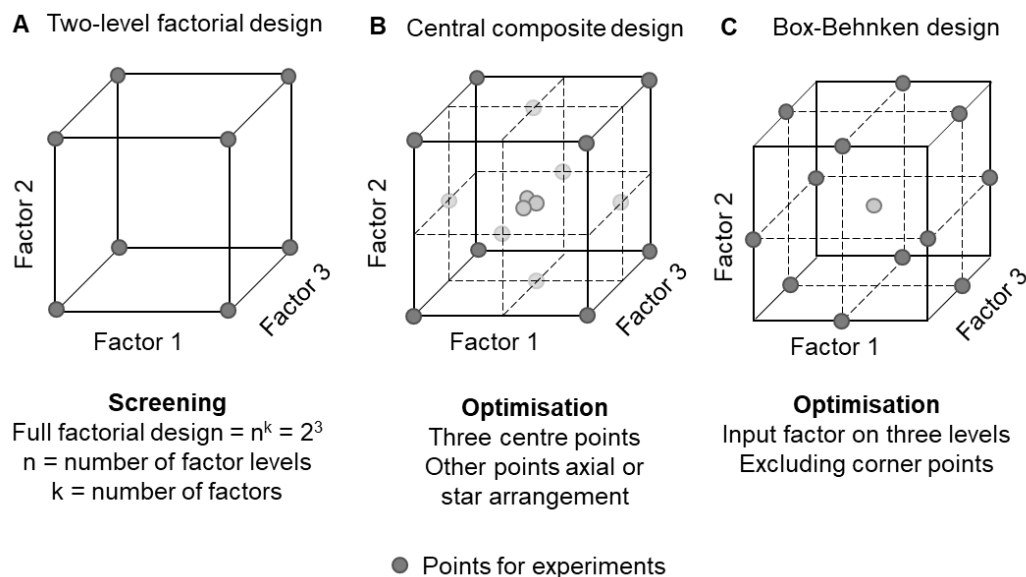


Figure 2.1. Schematic representations of two-level factorial design (A), central composite design (B) and Box-Behnken design (C) for three different input factors (Hanrahan and Lu, 2006; Mandenius and Brundin, 2008).

2.1.2 Design of experiments for bulk and microfluidics preparation of nanoparticles

Previous studies have utilized a DoE approach to optimise the nanoprecipitation method for the preparation of polymeric PLGA nanoparticles. In a bulk method, the relevant input factors identified by DoE approaches include the concentration of the polymer, the concentration and kind of surfactant, the ratio between organic and aqueous phase, and the addition of a co-solvent to the aqueous phase (Figure 2.2) (Bozkir and Saka, 2005; Derakhshandeh *et al.*, 2007; Patel *et al.*, 2016; Sonam *et al.*, 2014; Vuddanda *et al.*, 2015; Yadav and Sawant, 2010). The output responses include size, polydispersity index (PDI) and zeta potential of the polymeric nanoparticles as well as the drug encapsulation efficiency (EE) (Figure 2.2) (Bairagi *et al.*, 2018; Bozkir and Saka, 2005; Derakhshandeh *et al.*, 2007; Patel *et al.*, 2016; Sonam *et al.*, 2014; Yadav and Sawant, 2010).

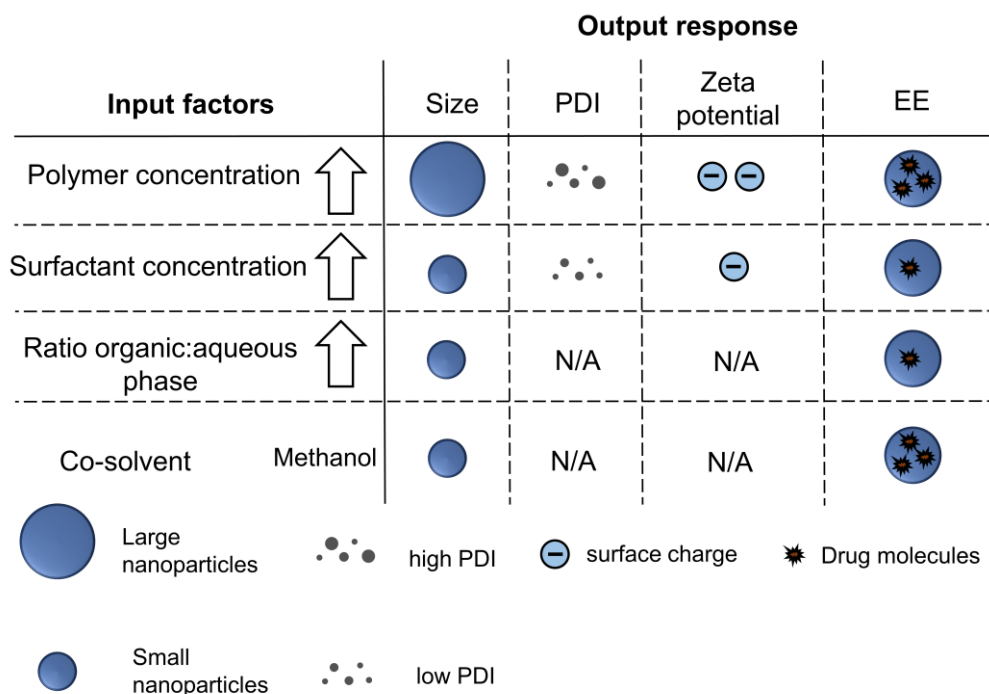


Figure 2.2. Influence of input factors on the output responses for the preparation of PLGA nanoparticles using a bulk nanoprecipitation method (Bairagi *et al.*, 2018; Patel *et al.*, 2016; Sonam *et al.*, 2014; Tefas *et al.*, 2015; Vuddanda *et al.*, 2015; Yadav and Sawant, 2010). PDI = polydispersity index, EE = encapsulation efficiency.

Size and PDI of PLGA nanoparticles are influenced by the concentration of the polymer, with a higher polymer concentration having a positive effect on size leading to the formation of larger PLGA nanoparticles (Patel *et al.*, 2016; Sonam *et al.*, 2014; Tefas *et al.*, 2015; Vuddanda *et al.*, 2015). The viscosity of the organic solution is increased with higher polymer concentrations, slowing down the diffusion of the dissolved polymer from the coarse emulsion droplets towards the aqueous phase, and increasing the chance of collision between nanoparticles in the organic phase resulting in the formation of larger nanoparticles (Patel *et al.*, 2016; Sonam *et al.*, 2014; Tefas *et al.*, 2015). Further, size and PDI of PLGA nanoparticles are decreased with higher surfactant concentrations due to the reduction of the interfacial tension between the aqueous and organic phase (Patel *et al.*, 2016; Sonam *et al.*, 2014). With a higher ratio of aqueous to organic solution, the formulation of smaller PLGA nanoparticles is achieved as coalescence of organic solvents droplets in the aqueous phase can be prevented (Patel *et al.*, 2016; Sonam *et al.*, 2014). The surface charge of PLGA nanoparticles is found to be more negative with higher concentrations of the PLGA polymer used (Tefas *et al.*, 2015), whereas higher surfactant concentrations resulted in PLGA nanoparticles with a less negative zeta potential (Bairagi *et al.*, 2018; Tefas *et al.*, 2015). Finally, a higher polymer and surfactant concentration as well as the addition of a co-solvent increases the encapsulation efficiency of hydrophilic (Patel *et al.*, 2016; Yadav and Sawant, 2010) and hydrophobic drugs (Bairagi *et al.*, 2018; Sonam *et al.*, 2014).

As described in Chapter 1, a variety of microfluidic devices have been used for the preparation of polymeric nanoparticles, micelles, nanogels and liposomes (Capretto *et al.*, 2012; Chiesa *et al.*, 2018; Kastner *et al.*, 2014; Water *et al.*, 2015). However, there have been few DoE studies performed on the optimisation of microfluidic methods for the preparation of nanoparticles. The used designs include full factorial designs (Capretto *et al.*, 2012; Chiesa *et*

al., 2018) and a central composite design (Water *et al.*, 2015) to evaluate the influence of microfluidics-related parameters on nanoparticle size and drug encapsulation. The production of PLGA nanoparticles and liposomes using a SHM was optimised using a DoE (Chiesa *et al.*, 2018; Kastner *et al.*, 2014). Both, PLGA nanoparticles and liposomes showed a size ≤ 200 nm at higher flow rate ratios (5:1) between the aqueous and organic phase (Chiesa *et al.*, 2018; Kastner *et al.*, 2014). The same correlation between size and flow rate ratio was found for polymeric micelles prepared with a 2D HFF device (Capretto *et al.*, 2012). Encapsulation of poorly soluble drugs in liposomes and peptides in hydrophilic nanogels has been reported to be higher at flow rates around 2 mL/min (Kastner *et al.*, 2014; Water *et al.*, 2015). The above-mentioned examples of DoE studies for the bulk and microfluidic methods show that the optimisation of method-related parameters is crucial for the preparation of nanoparticles. The method-related parameters have an influence on size, polydispersity and encapsulation efficiency of drugs in the nanoparticles and thus define the suitability of formulated nanoparticles as drug delivery systems.

2.1.3 Optimisation of size of polymeric nanoparticles

The microfluidics-related parameters; flow rate and flow rate ratio have an impact on the size of polymeric nanoparticles produced with microfluidics and general considerations are discussed below.

The flow rate is described as the combined speed of the fluids within the microchannel. Generally, an increase in flow rate of the fluids within the microchannel leads to the formation of polymeric nanoparticles with a size between 40 and 160 nm depending on the microfluidic device utilized (Figure 2.3) (Lim *et al.*, 2014b; Min *et al.*, 2014; Morikawa *et al.*, 2018). This

effect is predominantly noticeable for polymeric nanoparticles formulated with concentrations between 10 and 30 mg/mL of the biodegradable polymer PEG-PLGA with a specific molecular weight (PEG_{5k}-PLGA_{55k}) (Min *et al.*, 2014) and for PLGA polymers with different monomer ratios (75/25 and 50/50) (Amoyav and Benny, 2018; Morikawa *et al.*, 2018). Faster flow rates are advantageous due to rapid mixing within the microchannel (Min *et al.*, 2014) and assists with the homogenous nucleation of the polymer at low polymer concentrations. Amoyav and Benny (2018) formulated small nanoparticles with a size of 40 nm at a flow rate of 0.7 mL/min using a 2D HFF microfluidic device. In addition, at faster flow rates the mixing time of the fluids is below the aggregation time of the polymer and blocking of the microchannel due to aggregation of the polymer is reduced (Lim *et al.*, 2014a; Min *et al.*, 2014). Taken together, these influences mean that faster flow rates give rise to smaller nanoparticles.

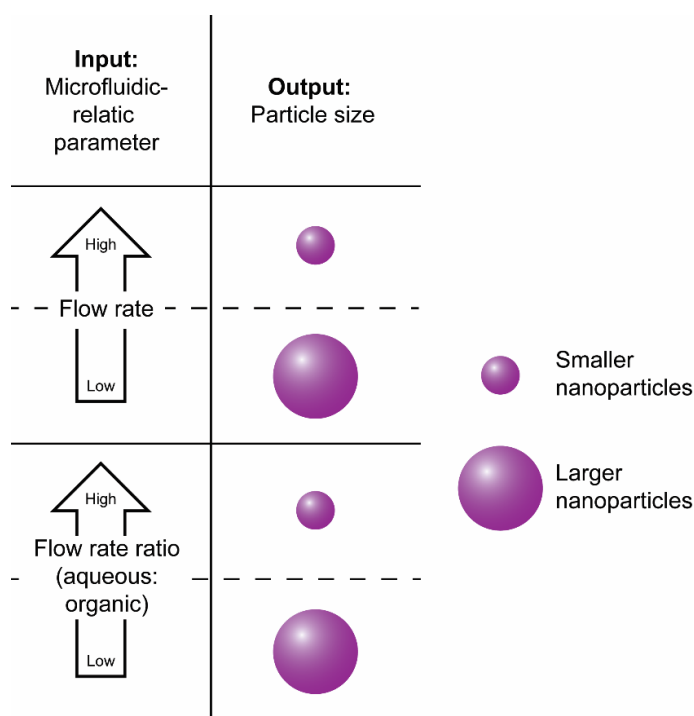


Figure 2.3. Generalized correlation between microfluidics-related parameters and the size of the resulting polymeric nanoparticles formulated with PLGA (10 mg/mL, co-polymer ratio 75:25 and 50:50) and PEG-PLGA (10 to 30 mg/mL) (Lim *et al.*, 2014b; Min *et al.*, 2014; Morikawa *et al.*, 2018). Arrows indicate an increase in flow rate or flow rate ratio (Streck *et al.*, 2019c).

The flow rate ratio is described as the ratio between the two solvent streams (anti-solvent or aqueous phase and organic solution) in the microfluidic device and can have a significant influence on the size distribution of polymeric nanoparticles. Polymeric nanoparticles prepared using HFF microfluidic devices with PEG_{5k}-PLGA_{10-27k} (Lim *et al.*, 2014a) and PLGA (Bramosanti *et al.*, 2017) showed a decrease in size when the amount of anti-solvent was 20 to 50 times larger than the amount of organic polymer solution (Figure 2.3) (Bramosanti *et al.*, 2017; Lim *et al.*, 2014a; Liu *et al.*, 2015). The decrease in size at higher flow rate ratios was attributed to the reduced width of the organic solvent stream and diffusive mixing occurring in a more controlled way (Liu *et al.*, 2015). Most of the microfluidics studies for the preparation of PLGA or PEG-PLGA nanoparticles have been performed based on a ‘trial and error’ approach. The utilization of a DoE approach aids in simultaneously evaluating the influence of microfluidics-related parameters on the formulation of PLGA nanoparticles. The DoE study performed in this thesis contributes to a better understanding of the parameters required to produce nanoparticles with a size below 200 nm. This has not yet been described in the published literature for PLGA (50:50).

2.1.4 Conjugation of biomacromolecules and polymers

Bioconjugation reactions are defined by the formation of a covalent bond between two compounds through the use of reactive crosslinking reagents (Hermanson, 2013a). Crosslinkers are molecules that exploit reactive groups of compounds to facilitate the conjugation reaction (Hermanson, 2013a). Common bioconjugation reactions between polymeric nanoparticles and proteins or peptides include the maleimide reaction, the EDC/sulfo-NHS zero-length crosslinking reaction and streptavidin-biotin affinity reaction (Yadav *et al.*, 2011). The maleimide reaction requires the presence of a thiol group (often a free cysteine) in the protein

or peptide sequence and a maleimide moiety on the polymer (Cox *et al.*, 2019; Gullotti and Yeo, 2012). The thiol group reacts with the maleimide moiety and forms a thioether bond (Figure 2.4A) (Yadav *et al.*, 2011). The EDC/sulfo-NHS reaction is a zero-length crosslinking reaction where a covalent bond between two compounds is formed directly without any bridging groups (Hermanson, 2013c). This reaction is especially suitable for the conjugation of peptides to nanoparticles due to the solubility of the reagents EDC and sulfo-NHS in the aqueous environment and the maintenance of the native structure of biomacromolecules in this environment (Totaro *et al.*, 2016; Yadav *et al.*, 2011). For the zero-length crosslinking reaction, the carboxyl group of the polymer is activated with EDC and sulfo-NHS to form a sulfo-reactive ester intermediate that can react with a primary amine present in the N-terminus or side chain of the peptide sequence to form a covalent amide bond (Figure 2.4B) (Hermanson, 2013c; Yadav *et al.*, 2011). One disadvantage is the formation of side products including EDC-urea, anhydrides of o-acylisourea and N-acylisourea, which are competing with the formation of the desired amide bond if EDC is used in excess (Hermanson, 2013c; Totaro *et al.*, 2016). The streptavidin-biotin affinity reaction is based on the strong affinity of streptavidin to biotin and is a non-covalent bioconjugation reaction (Figure 2.4C) (Hermanson, 2013b; Yadav *et al.*, 2011). The main advantage of this bioconjugation reaction is that the affinity of streptavidin to biotin is not influenced by the conjugation to other proteins or labels (Hermanson, 2013b; Yadav *et al.*, 2011).

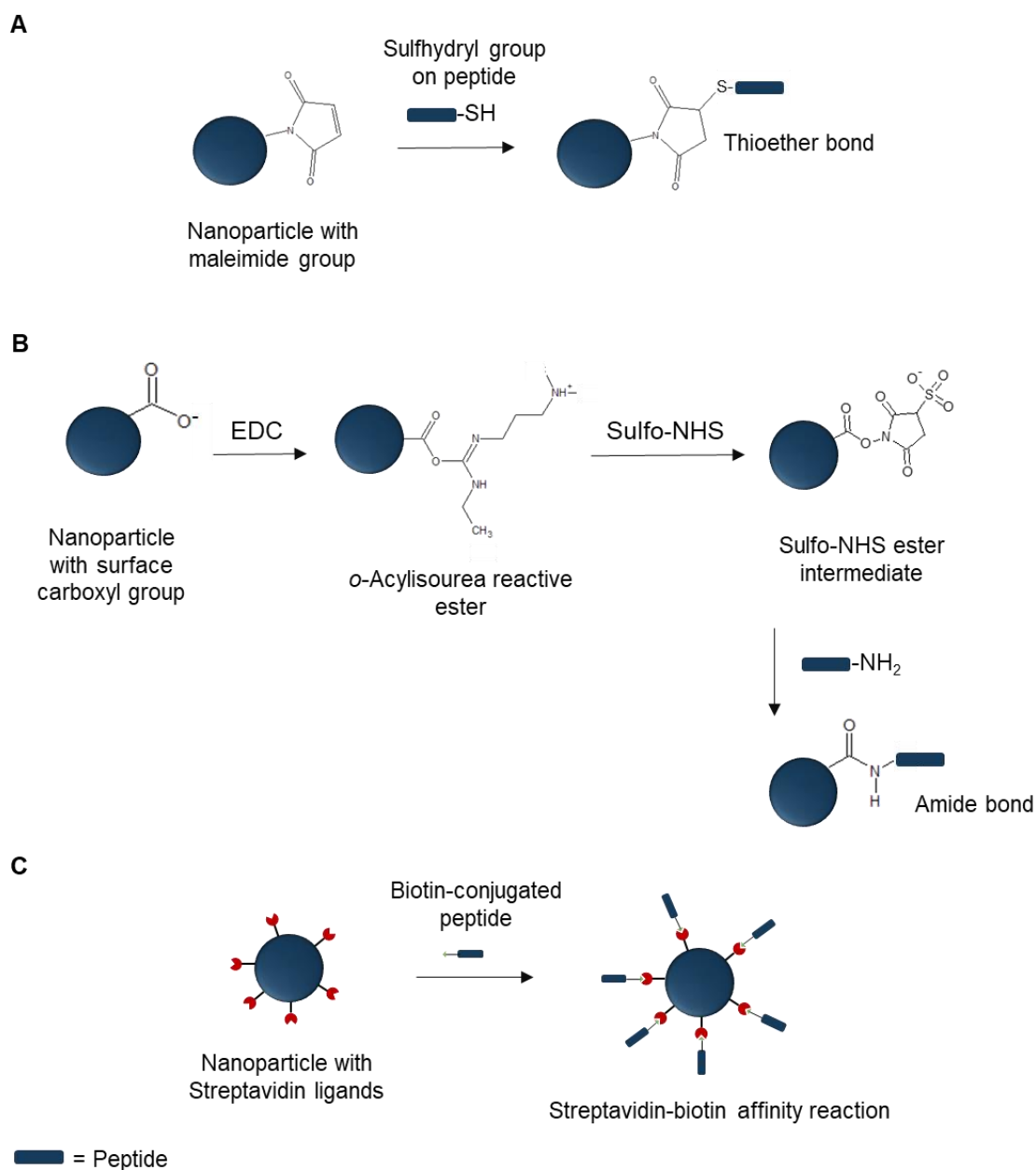


Figure 2.4. Schematic of maleimide reaction (A), EDC/sulfo-NHS zero-length crosslinking reaction (B) and streptavidin-biotin affinity reaction (C) for the surface conjugation of nanoparticles (Hermanson, 2013c; Nam *et al.*, 2002; Xu *et al.*, 2013a).

Surface modifications via a covalent linkage are preferred over adsorption interactions since protein or ligand desorption can be prevented and the loss of targeting ability is avoided (Cox *et al.*, 2019). The covalent bond has two main advantages; (i) the selectivity of binding

is improved and (ii) the displacement of surface proteins by serum proteins after *in vivo* administration or during purification process is prevented (Cox *et al.*, 2019).

Mass spectrometry (MS) can be used for identification analysis of a wide range of compounds. The combination of MS with the soft ionisation method matrix assisted laser desorption ionisation (MALDI) and a time of flight (TOF) detector is an analytical tool for the characterisation of peptides, proteins polymers and biomolecules with a large molecular weight (Bilati *et al.*, 2005; Kafka *et al.*, 2011). Using MALDI-TOF, MS samples are co-crystallised with excess of matrix before the sample matrix mixture is activated by laser energy to achieve vaporisation (Kafka *et al.*, 2011). In the gas phase, proton transfer from the matrix to the sample results in single charge ions that are analysed by the detector according to their velocity depending on their mass to charge ratio (Kafka *et al.*, 2011). The qualitative analysis of peptides with MALDI-TOF MS offers high sensitivity, a small sample amount and rapid sample preparation in addition to the analysis of a wide mass range (Bilati *et al.*, 2005). Previously, MALDI-TOF MS was used successfully to investigate the conjugation between the poly(ethyl-cyanoacrylate) nanoparticles (PECA) and the gonadotropin releasing hormone (GnRH) analogue, D-Lys⁶-GnRH, showing that ethyl-cyanoacrylate monomer units were co-polymerised with the D-Lys⁶-GnRH via histidine residues in the peptide sequence (Kafka *et al.*, 2009).

The successful conjugation of biomacromolecules to polymeric nanoparticles can be analysed using Fourier-transform infrared (FTIR) spectroscopy. FTIR spectroscopy uses infrared radiation to measure the wavelength and intensity of the absorbed radiation by a sample (Kong and Yu, 2007). Using attenuated total reflectance (ATR)-FTIR, the infrared beam passes

through a Germanium or ZnSe crystal, which is optically dense and has a high reflection index (Shai, 2013). The crystal supports internal reflectance of the infrared beam, which can leave the crystal and penetrate into the sample to a depth of 0.5-5 μm (Shai, 2013). With FTIR, the type of chemical bond (single or double) and the quality of the bond vibration (stretch or bend) can be assessed (Shai, 2013). The amide I bond vibration between 1700-1600 cm^{-1} is primarily related to the C=O stretch within the peptide sequence (Kong and Yu, 2007; Shai, 2013). In the wavenumber range between 1575-1480 cm^{-1} the amide II bond vibration is located, which is related to the in-plane NH-bending and CN stretching of molecules/peptides/proteins (Kong and Yu, 2007). Infra-red radiation absorbed by amide bonds leads to a total amount of nine characteristics bands in peptides and proteins, with the amide I and II vibrations being the most prominent ones (Kong and Yu, 2007).

2.1.5 *Chapter aims*

In this Chapter, the preparation of polymeric nanoparticles using a traditional bulk method and a microfluidics method is highlighted. The two preparation methods were optimised using a DoE approach and compared to evaluate the uniformity of the formulated PLGA nanoparticles. Further, PLGA nanoparticles prepared with the microfluidics method were surface-modified with CPPs of different architectures (Figure 2.5), to alter their physicochemical properties. The three CPPs have a distinct architecture, namely a short, a long linear and a branched architecture. The modified nanoparticles were characterized for their suitability as a drug delivery system to enhance uptake after oral administration.

2.2 Materials

Poly(DL-lactide-*co*-glycolide) (PLGA) 50:50, ester terminated, MW 15,980 Da, was supplied by Durect Lactel (Cupertino, CA, USA). Acetonitrile (ACN) (HPLC grade) was supplied by Merck (Darmstadt, Germany). Mowiol[®] 4-88 (polyvinyl alcohol, PVA, MW 31,000), 2-[4-(2-hydroxyethyl)piperazin-1-yl]ethanesulfonic acid (HEPES) (purity > 99.5%), N-(3-dimethylaminopropyl)-N-ethylcarbodiimide hydrochloride (EDC) (purity > 98%), trifluoroacetic acid (TFA, HPLC grade, purity > 99%), GRKKRRQK(RRH)K(RRH)K(RRH) (bTAT, custom synthesized, MW 2661.2 Da, purity > 95%), α -cyano-4-hydroxycinnamic acid (purity \geq 99%) and ammonium phosphate were purchased from Sigma–Aldrich (St. Louis, MO, USA). Snake Skin[™] dialysis tubing (10 kDa MWCO) and sulfo-N-hydroxysulfosuccinimide (sulfo-NHS) were purchased from Thermo Fisher Scientific Australia Pty (Scoresby, Australia). The peptides RRH (MW 467.3 Da, purity > 98%) and GRKKRRQRRR (TAT (48-57), MW 1396.7 Da, purity > 98%) were custom synthesized by GLS (Shanghai, China) and used as supplied. Distilled, ultra-pure water was produced using a Milli-Q[®] Water Millipore Purification System (Billerica, MA, USA).

In this work, CPPs with three different architectures were designed for conjugation to PLGA nanoparticles to be able to investigate how the architecture of the CPPs influences cell uptake (Figure 2.5). The short RRH was chosen due to previous work that showed 30% increase in cellular uptake in Caco-2 cells when RRH was conjugated to PECA nanoparticles in comparison to unmodified PECA nanoparticles (Chiu *et al.*, 2015). The long linear CPP was the widely investigated TAT peptide and the third CPP was custom designed and is subsequently referred to as branched TAT (bTAT). It has a modified TAT backbone with three RRH side branches (Figure 2.5).

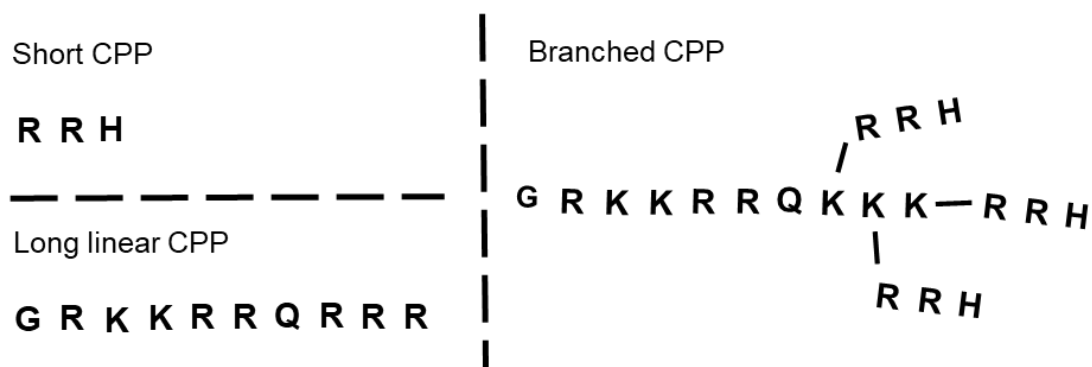


Figure 2.5. Illustration of the architecture of the short (RRH), the long linear (TAT) and the branched CPP (bTAT: modified TAT backbone and three RRH branches). Amino acid single letter codes have been used for each peptide (R = arginine, H = histidine, G = glycine, K = lysine, Q = glutamine) (Streck *et al.*, 2019a).

2.3 Methods

2.3.1 Design of experiments to optimize the preparation of PLGA nanoparticles using a bulk nanoprecipitation method

A DoE study was used to identify the optimal concentration of PLGA and PVA as well as the stirring time for the bulk nanoprecipitation method. The influence of stirring speed on the physicochemical nanoparticle characteristics was not investigated in the DoE study due to technical restrictions and the stirring speed was set to a constant value of 400 rpm. MODDE GO 12 software (Umetrics, Umeå, Sweden) was used for the design and analysis of the experiments. After definition of the input parameters, a two-level full factorial design with a centre point for objective screening was used to define parameters for the individual experiments (Table 2.1). The selected response parameters for the PLGA nanoparticles were size and PDI. For the validation of how well the model fits the data (R^2) and to validate the ability to predict new data (Q^2), an ANOVA was performed. Further, statistical testing included testing the regression model for significance to obtain a probability value (p), and a lack of fit

test to estimate the error of the model. The statistical parameters were obtained at a 95% confidence interval.

Table 2.1. Input parameters for the DoE study to optimize the formulation of PLGA nanoparticles using a bulk nanoprecipitation method (Streck *et al.*, 2019a).

Parameters	Level		
	-1	0	1
PLGA concentration (mg/mL in ACN)	2	13.5	25
PVA concentration (% (w/v))	0.5	2.75	5
Stirring time (h)	0.5	2.25	4

2.3.2 Preparation of polymeric nanoparticles using microfluidics

PLGA nanoparticles were prepared using a NanoAssemblr[®] Benchtop Device (Precision NanoSystems, Vancouver, Canada) and the associated proprietary software. The microchannel had a width of 200 μm and a height of 79 μm and was embedded in the microfluidic cartridge (Figure 2.6A). The cartridge was made of propylene, viton and cyclic olefin copolymer and had dimensions of 6.6 \times 5.5 \times 0.8 cm (L \times W \times H). The microchannel had two inlets in a Y-shaped configuration for the aqueous and organic solutions and was staggered in multiple layers to achieve a serpentine configuration of the microchannel. Another feature of the microchannel was the asymmetric in-floor herringbone groove at the bottom of the microchannel, which induced a transverse flow in the microchannel (Stroock *et al.*, 2002). The herringbone feature was 50 μm thick and 31 μm high and orientated at a 45° angle to the length of the microchannel (Figure 2.6B) (Stroock *et al.*, 2002; Zhigaltsev *et al.*, 2012). The NanoAssemblr[®] Benchtop Device contained two syringe pumps to control the total flow rate and flow rate ratio of the aqueous and organic solutions.

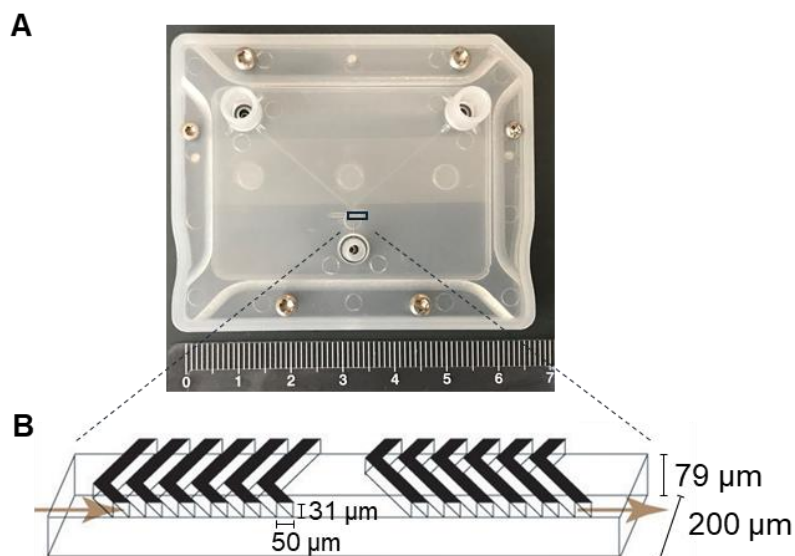


Figure 2.6. Microfluidic cartridge used for the NanoAssemblr[®] Benchtop Device (A) and depth profile of herringbone feature (B) found within the microchannel (not to scale). Schematic of the herringbone feature was adapted from Belliveau *et al.* (2012). The SHM section of the microchannel is 2.5 cm long and can hold a volume of 0.0004 mL.

2.3.3 Design of experiments study for microfluidics preparation of PLGA nanoparticles

For the preparation of PLGA nanoparticles using microfluidics, a DoE study was used to screen for factors that influenced the size distribution and PDI of the resulting nanoparticles. A two-level full factorial design with a centre point was chosen to investigate the factors total flow rate and flow rate ratio at three different levels (-1, 0, 1) (Table 2.2). The concentration of the organic PLGA solution in ACN and the concentration of the aqueous PVA solution were kept constant at 10 mg/mL (in ACN) and 2% (w/v), respectively (Table 2.2). After preparation, the PLGA nanoparticle suspension was dialyzed overnight against ultra-pure water using a regenerated cellulose membrane with a 10 kDa MWCO.

The experimental data were fitted with a MLR model using the MODDE GO 12 software. Interaction terms were determined by the addition of two-factor interactions to the model to investigate a beneficial contribution to the model quality. The response surface plots

were generated using the MODDE GO software and used for interpretation of the data. One-way ANOVA was performed to validate how the model fits the data (R^2) and to validate the ability to predict new data (Q^2). In addition, the regression of the model was tested for significance and the probability value p was obtained. A lack of fit test was performed to estimate the errors in the model. The statistical parameters were obtained at a 95% confidence interval.

Table 2.2. Input parameters for the DoE study for the formulation of PLGA nanoparticles using microfluidics (Streck *et al.*, 2019b). FRR = flow rate ratio, TFR = total flow rate.

Parameters	Concentration		
PLGA concentration (mg/mL in ACN)	10		
PVA concentration (% (w/v))	2		
	Levels		
	-1	0	1
FRR (aqueous:organic)	1:1	6.5:1	12:1
TFR (mL/min)	2	7	12

2.3.4 Bulk nanoprecipitation method for preparation of PLGA nanoparticles

PLGA nanoparticles were prepared using a bulk nanoprecipitation method based on the description by Fessi *et al.* (1989) and optimised using DoE (Section 2.3.1). Briefly, an organic PLGA solution (10 mg/mL in ACN) was added dropwise to a beaker containing 10 mL PVA (2% w/v in ultra-pure water) and the solvent was evaporated during magnetic stirring (400 rpm) for 2 h and 15 min. The resulting PLGA nanoparticles were washed twice with ultra-pure water by centrifugation at 17,900 g for 10 min at room temperature and stored as suspension in ultra-pure water at 4°C until required with a maximum storage time of 7 days. Preliminary results showed that size, PDI and zeta potential of PLGA nanoparticles did not change over a storage time of 7 days at 4°C (Day 0: 144 ± 2 nm, 0.135 ± 0.001 , -21 ± 2 mV; Day 7: 147 ± 5 nm, 0.198

± 0.065 , -21 ± 2 mV). PLGA nanoparticles were stored in aqueous solution, while stirring to avoid sedimentation if immediate use was restricted by equipment availability.

2.3.5 *Microfluidics method for the preparation of PLGA nanoparticles*

PLGA nanoparticles were prepared using the NanoAssemblr[®] Benchtop Device with the optimised setting from the DoE (Section 2.3.3). The aqueous PVA solution (2% w/v) was mixed with the organic PLGA solution (10 mg/mL in ACN) at a flow rate ratio (aqueous:organic) of 6:1 and a total flow rate of 10 mL/min. PLGA nanoparticles were dialyzed overnight against ultra-pure water at room temperature using Snake Skin[™] dialysis tubing (10 kDa MWCO) and stored as suspension in ultra-pure water at 4°C until required with a maximum storage time of 7 days.

2.3.6 *Preparation of surface-modified PLGA nanoparticles*

Prior to the surface modification, PLGA nanoparticles suspensions produced with the bulk nanoprecipitation or the microfluidics method (Section 2.3.4 and 2.3.5) were dialyzed overnight against ultra-pure water at room temperature using Snake Skin[™] dialysis tubing (10 kDa MWCO).

A zero-length crosslinking reaction for the conjugation of CPPs to the surface of PLGA nanoparticles was adapted from Egusquiaguirre *et al.* (2015) with some modifications. Briefly, 500 μ L of the PLGA nanoparticle suspension was diluted with HEPES buffer (0.025 M, pH 6.4) to 1.5 mL and the nanoparticle suspension was gently stirred while adding 250 μ L EDC (1.5 mM in ultra-pure water) and 250 μ L sulfo-NHS (2 mM in ultra-pure water). The stirring continued for 30 min at room temperature, before the solution was separated by ultra-

centrifugation at 42,800 *g* for 15 min at 4°C. The pellet, containing the activated nanoparticles, was re-suspended and diluted with HEPES buffer (0.025 M, pH 6.4) to a volume of 1.1 mL. To this suspension, 100 µL of the CPP solutions with varying concentrations of RRH (10, 50 and 75 mM), TAT (2.9, 5.7, and 8.6 mM) and bTAT (4.5 mM and 6 mM) were added. The mixture was left to incubate overnight at 4°C and was then separated by ultra-centrifugation at 42,800 *g* for 15 min at 4°C. The supernatant was aspirated and kept at 4°C until RP-HPLC analysis and the nanoparticle pellet was stored at 4°C until required with a maximum storage time of 7 days.

2.3.7 *Mass spectrometry assessment of cell-penetrating peptides*

MALDI-TOF MS was used to analyse the three different CPPs; RRH, TAT and bTAT. CPPs were dissolved in 2 µL ultra-pure water and diluted with ACN to achieve concentrations of 0.5 mg/mL. The organic CPPs solutions were mixed with freshly prepared α -cyano-4-hydroxycinnamic acid (10 mg/mL with 1 µL 1 M ammonium phosphate and 1 µL 10% (v/v) TFA in ACN) matrix at a ratio of 2:1 (matrix:sample) before spotting on the Opti-TOF™ Sample Plate (Applied Biosystems, Framingham, MA, USA). After the spots were air dried, the sample plate was inserted into the Applied Biosystems/MDS SCIEX 4800 MALDI TOF/TOF™ Analyzer and analysed in a positive ion reflector mode with 1000 shots per sample spot. A calibration was performed using the calibrations spots on the sample plate of 5 peptides with different *m/z* (Insulin B chain *m/z* 3494.651, ACTH 18-39 *m/z* 2465.199, angiotensin II *m/z* 1046.542, P14R *m/z* 1533.858 and bradykinin 1-7 *m/z* 757.400).

2.3.8 *Characterization of PLGA and CPP-tagged PLGA nanoparticles*

Dynamic light scattering (DLS) was used to measure the Z-average diameter and PDI of the nanoparticles (Malvern[®] Nano ZS, Model Zen 3600, Malvern Instruments, Malvern, UK) equipped with a 633 nm laser and 173° detection optics. Laser Doppler electrophoresis was used to measure zeta potential of the nanoparticles with the same instrument. All samples were diluted to an appropriate concentration and triplicate measurements from three individual batches were taken.

The morphologies of the PLGA and CPP-tagged PLGA nanoparticles, prepared using the bulk nanoprecipitation method and the microfluidics method, were investigated using transmission electron microscopy (TEM). First, the carbon film on a 300 mesh copper grid was made hydrophilic by glow discharge in air (Aebi and Pollard, 1987). Afterwards, 10 μL of the PLGA nanoparticle suspension was placed on the grid for 1 min and excess suspension was blotted before the grid was washed twice with ultra-pure water and stained to contrast the specimen with phosphotungstic acid (1% w/v, pH 6.8). The samples were viewed on a Philips CM100 BioTWIN TEM (Philips Electron Optics, Eindhoven, The Netherlands) and the micrographs were recorded using a MegaView3 camera (Soft Imaging System, Münster, Germany).

2.3.9 *Investigation of covalent binding between CPPs and PLGA conjugates*

To investigate any interactions between the CPPs and PLGA, FTIR spectra of PLGA polymer, CPPs and PLGA-CPP conjugates were recorded with a Varian 3100 FTIR (Varian, Palo Alto, CA, USA) using transmission mode and compared. The spectra were obtained at wavenumbers between 400-4000 cm^{-1} with 64 scans per sample and a resolution of 4 cm^{-1} . The

PLGA-CPP conjugates were prepared using the zero-length crosslinking reaction. PLGA polymer was dissolved in ACN (10 mg/mL) and to a 1 mL solution of the polymer, 250 μ L EDC (1.5 mM in ultra-pure water) and 250 μ L of sulfo-NHS (2 mM in ultra-pure water) were added. The mixture was gently stirred on a magnetic stirring plate for 30 min and then precipitated by adding 3 mL of ultra-pure water and separated by centrifugation at 3220 g for 20 min at 8 °C (Karve *et al.*, 2011). The supernatant was removed and the pellet re-suspended in ACN. 200 μ L of CPP solutions (50 mM RRH, 8.6 mM TAT and 4.5 mM bTAT HEPES (0.025 M, pH 6.4)) were added and incubated while gently stirred at room temperature for 30 min. The PLGA-CPP conjugates were precipitated again as described above and the pellet was dissolved in ACN at a 1:10 ratio (v/v).

The PLGA polymer was dissolved in ACN at a concentration of 10 mg/mL and the CPPs were dissolved in 20 μ L ultra-pure water and then diluted with ACN to the intended concentration (50 mM RRH, 8.6 mM TAT and 4.5 mM bTAT) before analysis.

2.3.10 Conjugation efficiency of CPPs tagged to PLGA nanoparticles

The conjugation efficiency of the CPPs to the nanoparticles was obtained indirectly from the amount of CPPs remaining in the supernatant. The supernatant was collected after overnight incubation of the activated nanoparticles with the different concentrations of the three CPPs as described in Section 2.3.6.

CPP concentrations in the supernatant were quantified with validated RP-HPLC methods using the Agilent series 1200 HPLC system (Agilent Technologies, Santa Clara, CA, USA) with a reverse phase column (HiChrom ultrasphere 5 ODS, 250 \times 4.6 mm, 5 μ m particle size, 300 Å pore size (HiChrom, Theale, UK)) and a UV detector (G1314B) at wavelengths

between 214-220 nm. The aqueous mobile phase contained 0.1% (v/v) TFA in ultra-pure water and the organic mobile phase contained 0.1% (v/v) TFA in ACN. The CPPs in the supernatant were eluted by gradient (0 to 7% over 25 min for RRH, 0 to 13% over 37 min for TAT and 12 to 22% over 25 min for bTAT) at a flow rate of 0.6 mL/min. The CPP concentration was quantified using peak integration and an individual standard curve was produced for each CPP.

Equation (2-1) was used to calculate the conjugation efficiency of the different CPPs used in the study. The conjugation efficiency was obtained by calculating the difference between the total concentration of CPPs added to the nanoparticle suspension and the measured concentration of CPPs in the supernatant after conjugation.

$$\text{Conjugation efficiency (\%)} = \frac{\text{Total conc. CPP} - \text{Measured conc. CPP}}{\text{Total conc. CPP}} \times 100\% \quad (2-1)$$

2.3.11 Validation of RP-HPLC method for CPPs

A stock solution of RRH (1 mg/mL), TAT (1 mg/mL) and bTAT (1 mg/mL) was prepared daily and divided into two aliquots for the preparation of an independent set of standards and for the quality control samples (QCs). In order to obtain a standard curve, stock solutions were diluted with HEPES buffer (0.025 M, pH 6.45) to concentrations within the range of the standard curve (RRH: 50-1000 $\mu\text{g/mL}$, TAT: 100-1000 $\mu\text{g/mL}$ and bTAT: 50-750 $\mu\text{g/mL}$). The QCs were prepared with HEPES buffer (0.025 M, pH 6.45) at three different concentrations of 75, 250 and 750 $\mu\text{g/mL}$; 200, 450 and 900 $\mu\text{g/mL}$ and 75, 350 and 600 $\mu\text{g/mL}$ for RRH, TAT and bTAT, respectively. The validation was carried out over three subsequent days with multiple injections of the QCs within one day. The analysis of the validation included linearity of the standard curve, the inter- and intra-day precision and accuracy and sensitivity.

For the evaluation of the RP-HPLC methods of the CPPs, the coefficient of variance and the accuracy were calculated using Equations 2-2 and 2-3, respectively.

$$\text{Coefficient of variance (\%)} = \frac{\text{SD of sample concentration}}{\text{Mean sample concentration}} \times 100 \quad (2-2)$$

$$\text{Accuracy (\%)} = \frac{\text{Mean sample concentration}_{\text{measured}}}{\text{Standard concentration}} \times 100 \quad (2-3)$$

The limit of quantification (LOQ) is characterised by a detector response 10 times as high as the noise level and the limit of detection (LOD) is characterised by a detector response 3.3 times as high as the noise level. The LOD and LOQ were calculated using Equations 2-4 and 2-5 (FDA, 1997).

$$\text{LOD} = \frac{(10 * \text{Standard deviation of } y\text{-intercept})}{\text{slope}} \quad (2-4)$$

$$\text{LOQ} = \frac{(3.3 * \text{Standard deviation of } y\text{-intercept})}{\text{slope}} \quad (2-5)$$

2.3.12 Statistical analysis

All experiments were performed in triplicate and results are presented as mean \pm standard deviation (SD). Statistical analysis for the DoEs was performed using one-way ANOVA with MODDE GO 12 software. Comparisons between single groups were made by performing a Student's *t* test. The reported *p*-values were considered statistically significant at $p < 0.05$.

2.4 Results and Discussion

2.4.1 *Optimal PLGA and stabilizer concentration for the formulation of PLGA nanoparticles determined by design of experiments (DoE)*

The size of nanoparticles plays a crucial role in cellular uptake and formulation of PLGA nanoparticles, with a size below 200 nm facilitating cellular uptake via endocytosis (Sharma *et al.*, 2015). In a DoE study, the influence of PLGA concentration, stabilizer concentration and stirring time on the size and PDI of PLGA nanoparticles was investigated. The size and PDI of formulated PLGA nanoparticles obtained at the different levels of the input factors are summarized in Appendix I. A response surface plot was used for model interpretation and represents the combined effect of alterations of the input factors on the output response (Bairagi *et al.*, 2018; Yadav and Sawant, 2010). The response surface plot obtained for the size of PLGA nanoparticles prepared using a bulk nanoprecipitation method showed that a low concentration of PVA ($\geq 2\%$) and a low concentration of PLGA (< 15 mg/mL) were advantageous for the production of PLGA nanoparticles with a size of approximately 150 nm (Figure 2.7A). The significant factors influencing the size of PLGA nanoparticles were the concentration of PLGA polymer, the concentration of PVA and the interaction term PLGA*PVA. Stirring time was found to have no significant influence on the size and PDI of PLGA nanoparticles and a stirring time of 2 h and 15 min, equal to the centre point of the DoE, was selected for the preparation of PLGA nanoparticles. With increasing concentrations of PLGA and PVA, size increased to approximately 200 nm. This observation was similar to other studies that reported an increase in nanoparticle size of PLGA nanoparticles when increased concentrations of PLGA (Sonam *et al.*, 2014; Tefas *et al.*, 2015) and PVA (Patel *et al.*, 2016; Sonam *et al.*, 2014) were used.

The PDI of the formulated PLGA nanoparticles was highly dependent on the PLGA concentration and was not influenced by the PVA concentration (Figure 2.7B). The response surface plot showed that the PDI of PLGA nanoparticles formulated using the bulk nanoprecipitation method was the lowest between 10 to 22 mg/mL of the PLGA polymer and increased towards higher PDI values outside of this PLGA concentration range. This is in contrast to the literature, reporting increased PDI values with increasing polymer concentrations due to the formation of larger emulsion droplets (Patel *et al.*, 2016). The PDI indeed increased with PLGA polymer concentrations above 20 mg/mL, but also at concentrations below 5 mg/mL of the PLGA polymer, which might be due to the instability of the formed PLGA nanoparticles at the low polymer concentration and subsequent nanoparticle aggregation (Figure 2.7B).

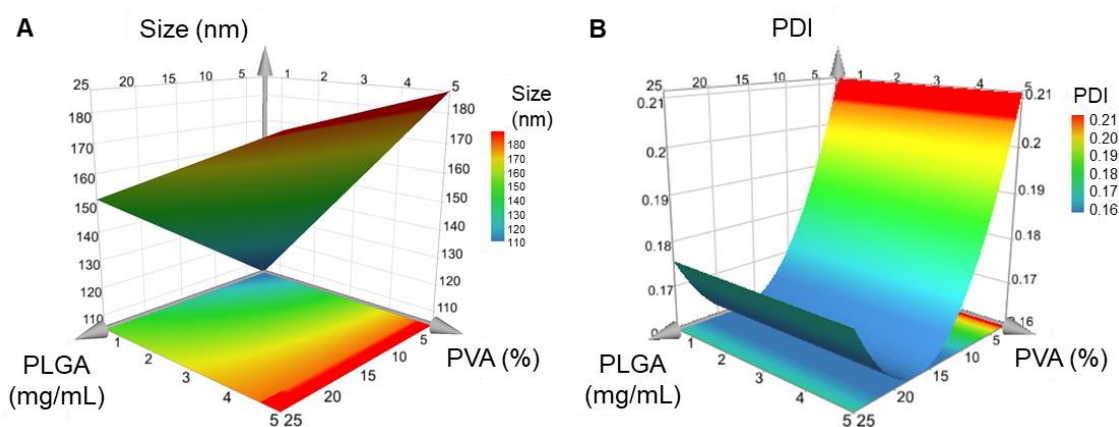


Figure 2.7. Response surface plots for the size (nm) (A) and polydispersity index (PDI) (B) of nanoparticles as a function of PLGA and PVA concentration for preparation of PLGA nanoparticles using the bulk nanoprecipitation method (Streck *et al.*, 2019a).

The PLS model of size and PDI for the formulation of PLGA nanoparticles was analysed with ANOVA to describe the quality of the model (Table 2.3). The values for R^2 and Q^2 (Table 2.3) were above the recommended values from the literature ($R^2 > 0.75$, $Q^2 > 0.60$) (Mandenius and Brundin, 2008) and provide support that the models of size and PDI produced with a bulk

nanoprecipitation method were able to fit the data and can be used to predict new data. The p -values for the regression of the models were < 0.05 and lack of fit p -values were either above or approximating 0.25, indicating that both models were significant and statistically good at a 95% confidence interval.

Table 2.3. Summary of results for the statistical analysis of the size and polydispersity index models for the bulk nanoprecipitation method to produce PLGA nanoparticles (Streck *et al.*, 2019a).

	R²	Q²	Regression	Lack of fit	Significant
Size	0.963	0.806	> 0.001	0.442	Yes
Polydispersity index	0.869	0.763	0.006	0.234	Yes

The response surface plots for size and PDI of the experimental data were used to select the parameters to produce optimized nanoformulations. The selected optimized parameters from the response surface plot for further experiments were a PLGA concentration of 10 mg/mL and a PVA concentration of 2% (w/v).

2.4.2 *Tuning the size and polydispersity of PLGA nanoparticles using microfluidics and design of experiments*

A DoE study was used to optimize the size and PDI of PLGA nanoparticles based on the microfluidics parameters total flow rate and flow rate ratio (aqueous:organic). The size and PDI of formulated PLGA nanoparticles obtained at the different levels of the input factors are summarized in Appendix II. To investigate the influence of flow rate ratio on the size and PDI of PLGA nanoparticles, the data were fitted with a MLR model to obtain the response surface plots (Mandenius and Brundin, 2008). The response surface plots showed the relationship between the input parameters, flow rate ratio and total flow rate, and the response in size and PDI of the PLGA nanoparticles (Figure 2.8). Data analysis with MODDE 12 GO software

further confirmed the significant factors for size and PDI were the flow rate ratio and the interaction term flow rate ratio*flow rate ratio. Specifically, the interaction term flow rate ratio*flow rate ratio revealed that the ratio between the aqueous and organic solutions used for the preparation of the PLGA nanoparticles is of high importance for both size and PDI. The response surface plots showed that at higher flow rate ratio (12:1), the PLGA nanoparticles had a smaller size, whereas at lower flow rate ratio (2:1), the PLGA nanoparticles showed an increase in size (Figure 2.8A). The PDI was also highly dependent on the flow rate ratio, showing an increasing PDI with higher flow rate ratio (Figure 2.8B).

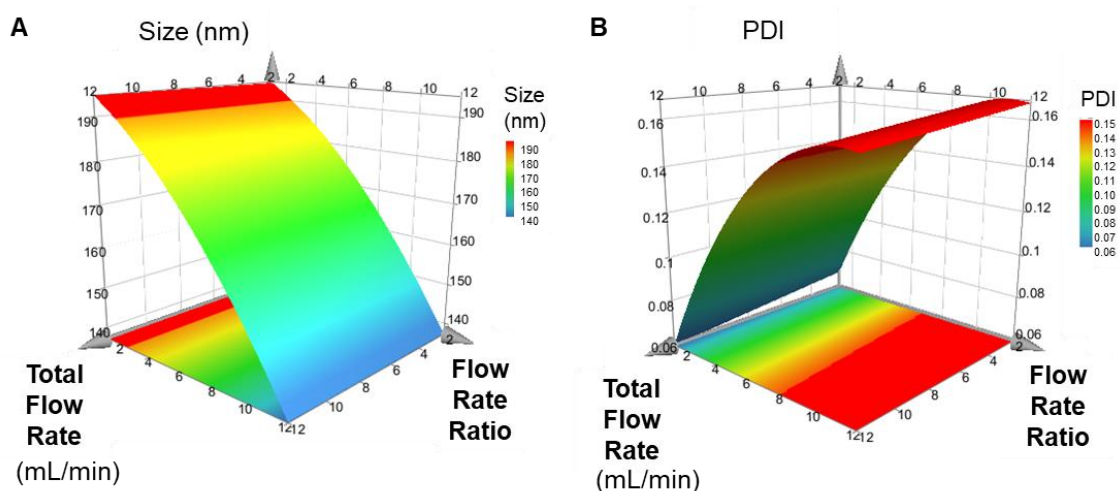


Figure 2.8. Response surface plots for the responses size (A) and PDI (B) as a function of the total flow rate (mL/min) and the flow rate ratio (aqueous:organic) for preparation of PLGA nanoparticles using the microfluidics method (Streck *et al.*, 2019b).

Therefore, the size and PDI of PLGA nanoparticles formulated with the NanoAssembl[®] Benchtop Device depends strongly on the flow rate ratio between the aqueous and the organic solutions. Higher flow rate ratio leads to a greater proportion of the aqueous solution with the organic solution being constantly diluted during mixing in the microchannel. This is advantageous for the formation of uniform nanoparticles because the polymer molecules precipitate whilst isolated from each other. Here, the observed PDI increases from 0.060 to

0.150 with higher flow rate ratio, however, since the PDI values are low and indicated a monodisperse nanoparticle size distribution, this effect was minimal. A DoE study with liposomes comprising phospholipids prepared using the NanoAssemblr[®] Benchtop Device revealed that flow rate ratio had the largest impact on the size of the liposomes prepared (Kastner *et al.*, 2014). Similarly, Chiesa *et al.* (2018) reported that the flow rate ratio had a major influence on the size of PLGA nanoparticles formulated using a PLGA polymer with a monomer ratio of 75:25 (lactic acid:glycolic acid) and the NanoAssemblr[®] Benchtop Device.

One-way ANOVA was used to identify the statistical significance of the model to describe size and PDI. The R^2 and Q^2 values were calculated to determine how well the model fits the data and if the model is able to predict new data, respectively. The results of the one-way ANOVA (Table 2.4) revealed that the models were able to fit the experimental data. The R^2 and Q^2 values for both models were higher than the recommended values from the literature (Mandenius and Brundin, 2008). In addition, the regression p -values for both models are below 0.05 indicating the significance of the models (Table 2.4). The lack of fit test showed that the p -values were greater than 0.05 for both models and that the models had no statistical error (Table 2.4). All statistical analysis for the size and PDI models were performed at a 95% confidence interval. Overall, the models were highly accurate and had a good reliability and robustness. Consequently, the models were used for the selection of parameters to further prepare PLGA nanoparticles using microfluidics. A total flow rate of 10 mL/min and a flow rate ratio of 6:1 was found to yield PLGA nanoparticles with a size of 150 nm and a PDI below 0.150 and these parameters were used for the subsequent preparation of PLGA nanoparticles.

Table 2.4. Summary of results for the statistical analysis of the size and polydispersity index models for the microfluidics method to produce PLGA nanoparticles (Streck *et al.*, 2019b).

	R²	Q²	Regression	Lack of fit	Significant
Size	0.994	0.992	< 0.001	0.052	Yes
Polydispersity index	0.929	0.907	0.012	0.499	Yes

2.4.3 Quality assessment of cell-penetrating peptides

The quality of the CPPs obtained from external sources was confirmed using MALDI-TOF MS. The mass spectrum of the short CPP RRH showed the main RRH peak at a mass to charge ratio (m/z) of 468.2, which is equivalent to the theoretical molecular weight of RRH (Figure 2.9A). The main peaks of the long linear CPP TAT and the branched CPP bTAT were observed in the mass spectra with m/z of 1396.9 and 2661.7, respectively, which were equivalent to their theoretical molecular weight (Figure 2.9B and C). Therefore, the three CPPs meet the required quality and were used for further studies.

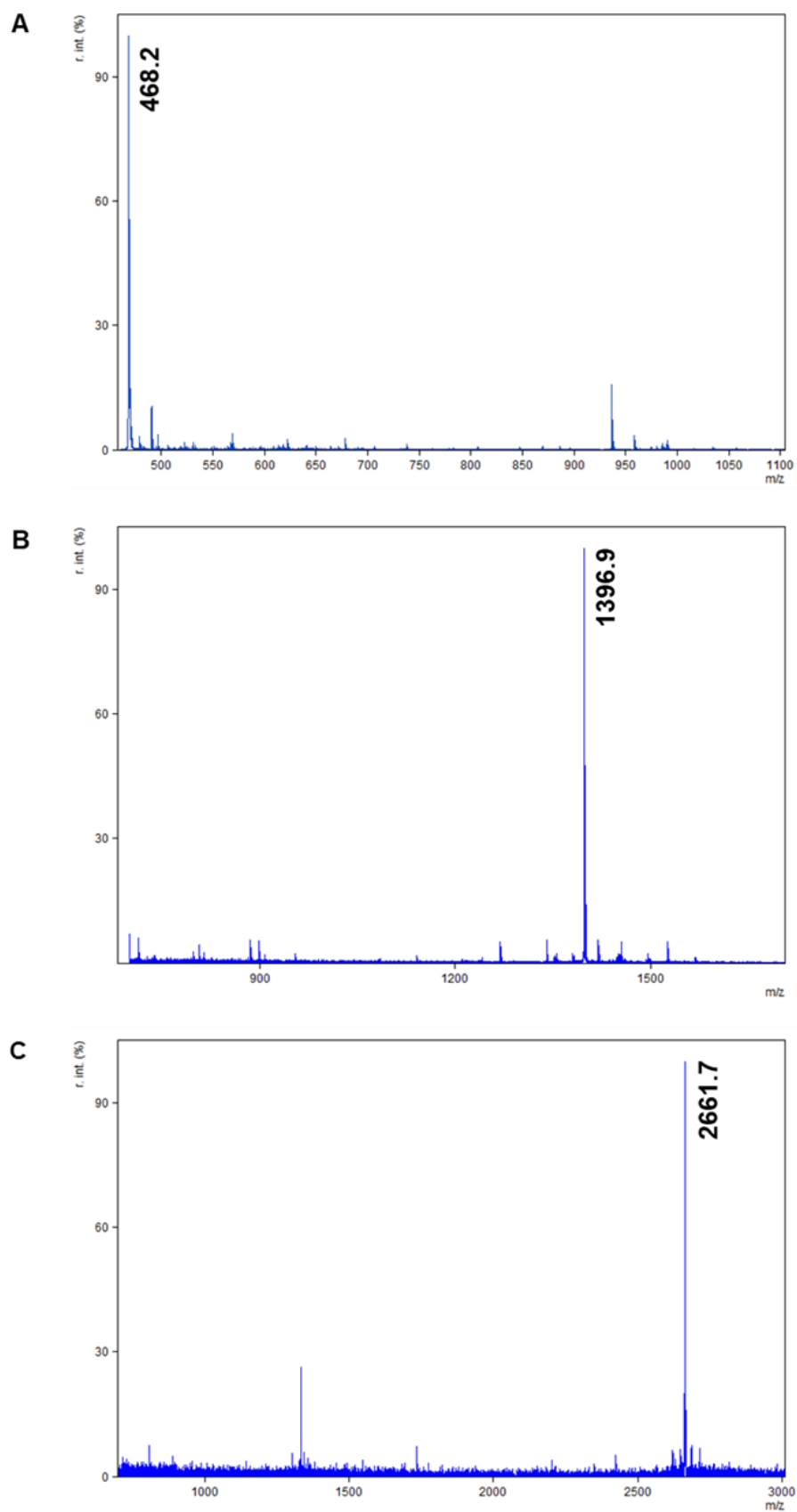


Figure 2.9. Mass spectra of the RRH (A), TAT (B) and bTAT (C) obtained with matrix assisted laser desorption ionisation-time of flight mass spectrometry analysis.

2.4.4 Characterization of PLGA nanoparticles

Unmodified PLGA nanoparticles prepared using the bulk nanoprecipitation method had a significantly larger size compared to PLGA nanoparticles prepared using microfluidics (Table 2.5). PLGA nanoparticles formulated with both methods were monodisperse, but the PDI of the PLGA nanoparticles was higher when prepared with the microfluidics method. Patel *et al.* (2016) reported that a decrease in PDI was obtained with an increasing ratio between the aqueous and organic solutions from 3:1 to 6:1 for the formulation of cromolyn-loaded PLGA using a bulk nanoprecipitation method. A similar observation was made in the present study where the bulk nanoprecipitation method with a higher ratio between the aqueous and organic phase (20:1) yielded nanoparticles with a lower PDI compared to the microfluidics method, where the ratio between the aqueous and organic phase was 6:1. Using a higher ratio between the aqueous and organic phase during the preparation of polymeric nanoparticles results in a greater dilution of the organic polymer solution and the formed nanoparticles are less likely to aggregate. The higher ratio of aqueous to organic phase in the bulk nanoprecipitation method did not reduce the size of PLGA nanoparticles and the formation of nanoparticles > 180 nm might be due to a polymer concentration above the critical polymer concentration (Lepeltier *et al.*, 2014). A concentration above the critical polymer concentration leads to the presence of amorphous polymer aggregates, which influence the size of prepared polymeric nanoparticles (Galindo-Rodríguez *et al.*, 2005). The zeta potential of PLGA nanoparticles prepared with the two methods was similar (Table 2.5) and a negative surface charge below -20 mV suggested the presence of negatively charged carboxyl groups on the surface of the PLGA nanoparticles (Vasconcelos *et al.*, 2015). The TEM micrographs revealed that PLGA nanoparticles with a spherical shape were obtained with both preparation methods (Figure 2.10A and C).

Table 2.5. Characterization of PLGA and TAT-tagged PLGA nanoparticles prepared with the optimized parameters for the bulk nanoprecipitation method and with the microfluidics method (Streck *et al.*, 2019a). Data are means \pm SD ($n = 3$ independent batches). * p -value < 0.05 in comparison to the respective bulk method.

	Size \pm SD (nm)	PDI \pm SD	Zeta potential \pm SD (mV)	Conjugation efficiency (%)
Unmodified PLGA nanoparticles				
Bulk	184.0 \pm 3.9	0.110 \pm 0.007	-23.0 \pm 0.8	N/A
Microfluidics	151.2 \pm 1.2*	0.149 \pm 0.014	-22.2 \pm 0.5	N/A
TAT-tagged PLGA nanoparticles				
Bulk	201.9 \pm 12.5	0.136 \pm 0.057	-6.0 \pm 3.4	55.3 \pm 0.7
Microfluidics	172.4 \pm 2.6*	0.164 \pm 0.014	-4.3 \pm 0.8	56.3 \pm 1.0

The size of TAT-tagged PLGA nanoparticles prepared using a post-bulk and post-microfluidics conjugation approach, increased in comparison to PLGA nanoparticles (Table 2.5), suggesting the presence of the CPP on the surface of the PLGA nanoparticles (Vasconcelos *et al.*, 2015). The TAT-tagged PLGA nanoparticles produced using the microfluidics method were significantly smaller than TAT-tagged PLGA nanoparticles produced using the bulk nanoprecipitation method (Table 2.5). Further, the TAT-tagged PLGA nanoparticles prepared with the bulk nanoprecipitation method showed a size of 200 nm with a standard deviation above ± 10 nm indicating a low batch-to-batch reproducibility (Table 2.5). The zeta potential of TAT-tagged PLGA nanoparticles prepared in this study was between -4 to -6 mV (Table 2.5). Although there was a shift in zeta potential to become less negative after conjugation of TAT, the overall negative zeta potential indicated that negatively charged carboxyl groups of the PLGA polymer were still present on the surface and that the surface density of TAT was not sufficient to achieve a positive surface charge (Gullotti and Yeo, 2012). The surface charge of the TAT-tagged PLGA nanoparticles in the present study was within the range of -7 to +3 mV published in the literature for TAT conjugated to PLGA-PEG or PLGA nanoparticles with a size larger than 200 nm (Gartziandia *et al.*, 2016; Xu *et al.*, 2013a). The conjugation efficiency of TAT to the PLGA nanoparticles was not different after production of the

nanoparticles using the bulk nanoprecipitation or microfluidics methods, with $55.3 \pm 0.7\%$ and $56.3 \pm 1.0\%$ conjugation efficiency, respectively (Table 2.5).

The morphology of the CPP-tagged PLGA nanoparticles did not change with the conjugation of TAT to PLGA nanoparticles prepared using the bulk nanoprecipitation or microfluidics methods (Figure 2.10B and E). Similarly, the conjugation of RRH and bTAT to PLGA nanoparticles prepared using the microfluidics method did not influence the morphology of the nanoparticles (Figure 2.10D and F). The microfluidics method was selected for further investigations of the utility of this method for producing CPP-tagged PLGA nanoparticles due to the smaller nanoparticle size yielded with better reproducibility by this method.

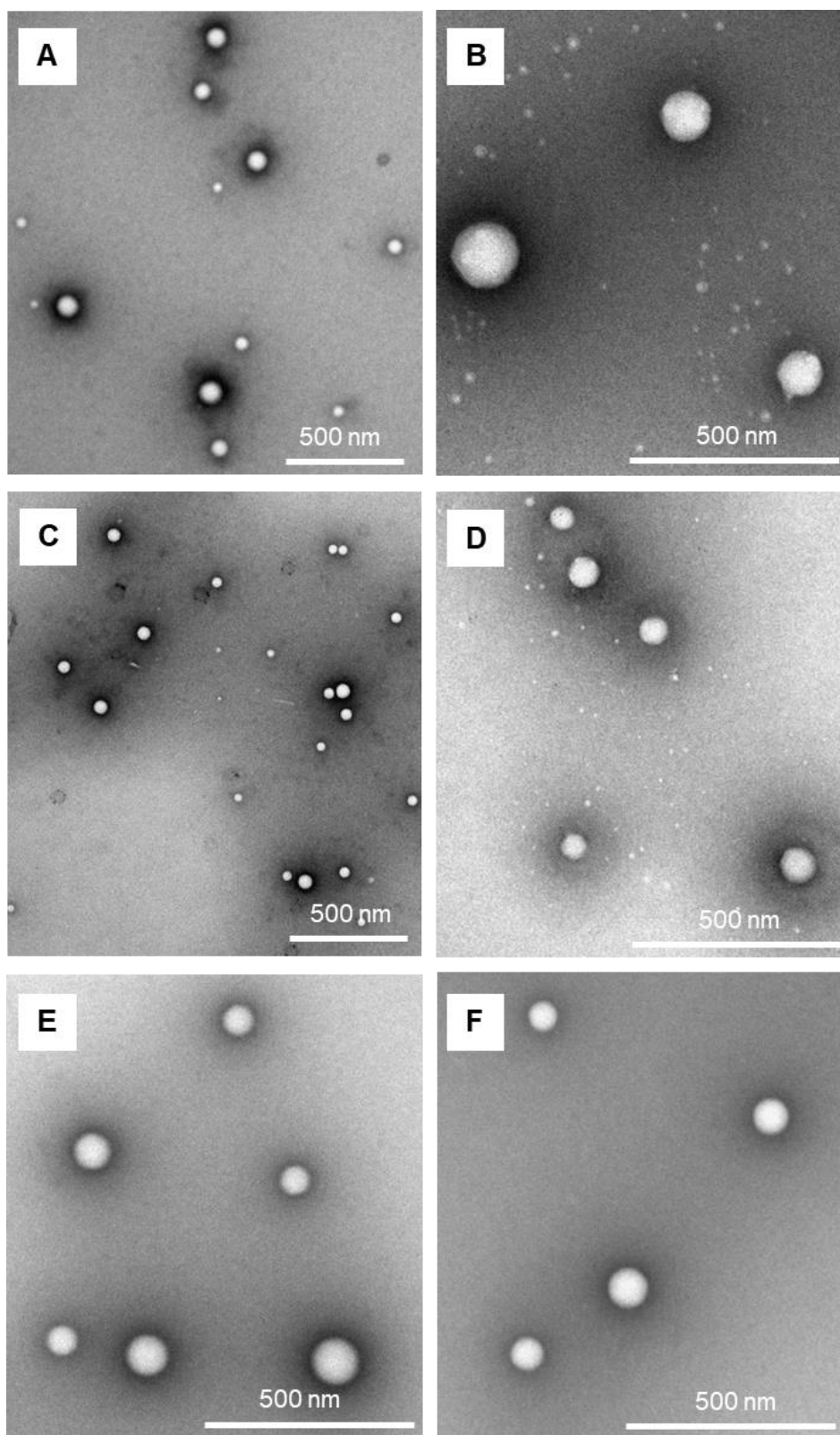


Figure 2.10. Transmission electron micrographs of unmodified PLGA (A) and TAT-tagged PLGA nanoparticles (B) prepared using a bulk nanoprecipitation method and unmodified PLGA (C), RRH- (D), TAT- (E) and bTAT-tagged PLGA nanoparticles (F) prepared using the microfluidics method (Streck *et al.*, 2019a).

2.4.5 Investigation of binding between CPPs and PLGA polymer

FTIR was used for the physicochemical characterization of the PLGA polymer, the three different CPPs and PLGA-CPP conjugates. The FTIR spectrum of the PLGA polymer alone showed the characteristic C=O stretch of the carboxyl group at 1749 cm^{-1} and C-O ester stretches between 1167 and 1086 cm^{-1} (Figure 2.11). The individual CPPs showed bands related to the amide I and II bond vibration at 1667 - 1659 and 1541 - 1560 cm^{-1} , respectively (Figure 2.11). The amide bond I and II vibrations were associated with the C=O stretching and N-H bending of the amide bonds between the individual amino acids of the CPPs (Haris and Severcan, 1999). In addition, C-O ester stretch vibrations from the C-terminal amino acid of the CPPs were observed between 1202 and 1130 cm^{-1} (Figure 2.11).

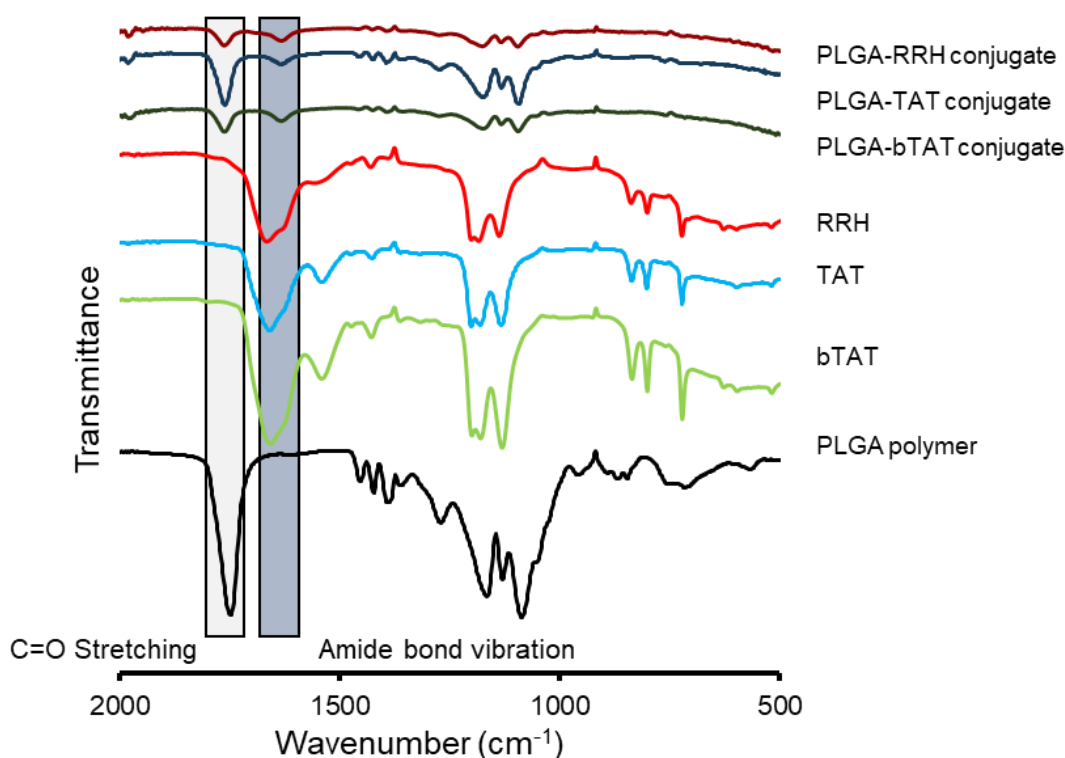


Figure 2.11. Fourier-transform infrared spectra of PLGA polymer, the individual cell-penetrating peptides (RRH, TAT, bTAT) and PLGA-CPP conjugates (Streck *et al.*, 2019a).

PLGA nanoparticles tagged with CPPs were analysed using FTIR, however, the FTIR spectrum showed broad and weak FTIR bands, which made assignment of wavenumbers difficult. Therefore, PLGA-CPP conjugates prepared by covalently attaching CPPs to the PLGA polymer were used to identify any interactions between the PLGA polymer and the CPPs. The carboxyl group of the PLGA polymer and the primary amine of the CPPs were utilized to form a covalent bond using a zero-length crosslinking reaction (Hermanson, 2013c). Conjugation between the CPPs and PLGA polymer was confirmed with the observation of an amide I bond vibration in the CPP-PLGA conjugates at approximately 1635 cm^{-1} . The shift of the amide I bond vibration to a lower wavenumber in comparison to the amide I bond vibration in RRH, TAT and bTAT ($1667\text{-}1659\text{ cm}^{-1}$) provided evidence of the successful formation of a covalent bond between these two components (Figure 2.11). The FTIR spectra of the PLGA-CPP conjugates also showed a C=O stretch at 1763 cm^{-1} for the carboxyl group of the PLGA polymer indicating that there were unconjugated carboxyl groups present.

2.4.6 Characteristics of CPP-tagged PLGA nanoparticles depends on the CPP architecture

The influence of CPP architecture on the characteristics of CPP-tagged PLGA nanoparticles was investigated by conjugating CPPs to the surface of PLGA nanoparticles produced using microfluidics. Unmodified PLGA nanoparticles had an average size of 150 nm and a zeta potential of -19 mV (Figure 2.12A and B). With conjugation of each of the three different CPPs, the size of the nanoparticles increased, but the increase in size was independent of the concentration of CPP (Figure 2.12A). The slight increase in size of the CPP-tagged PLGA nanoparticles could be attributed to the presence of CPPs. Further, nanoparticles may increase in size due to swelling caused by the more hydrophilic surface of the CPP-tagged PLGA nanoparticles compared to unmodified PLGA nanoparticles (Feiner-Gracia *et al.*, 2018).

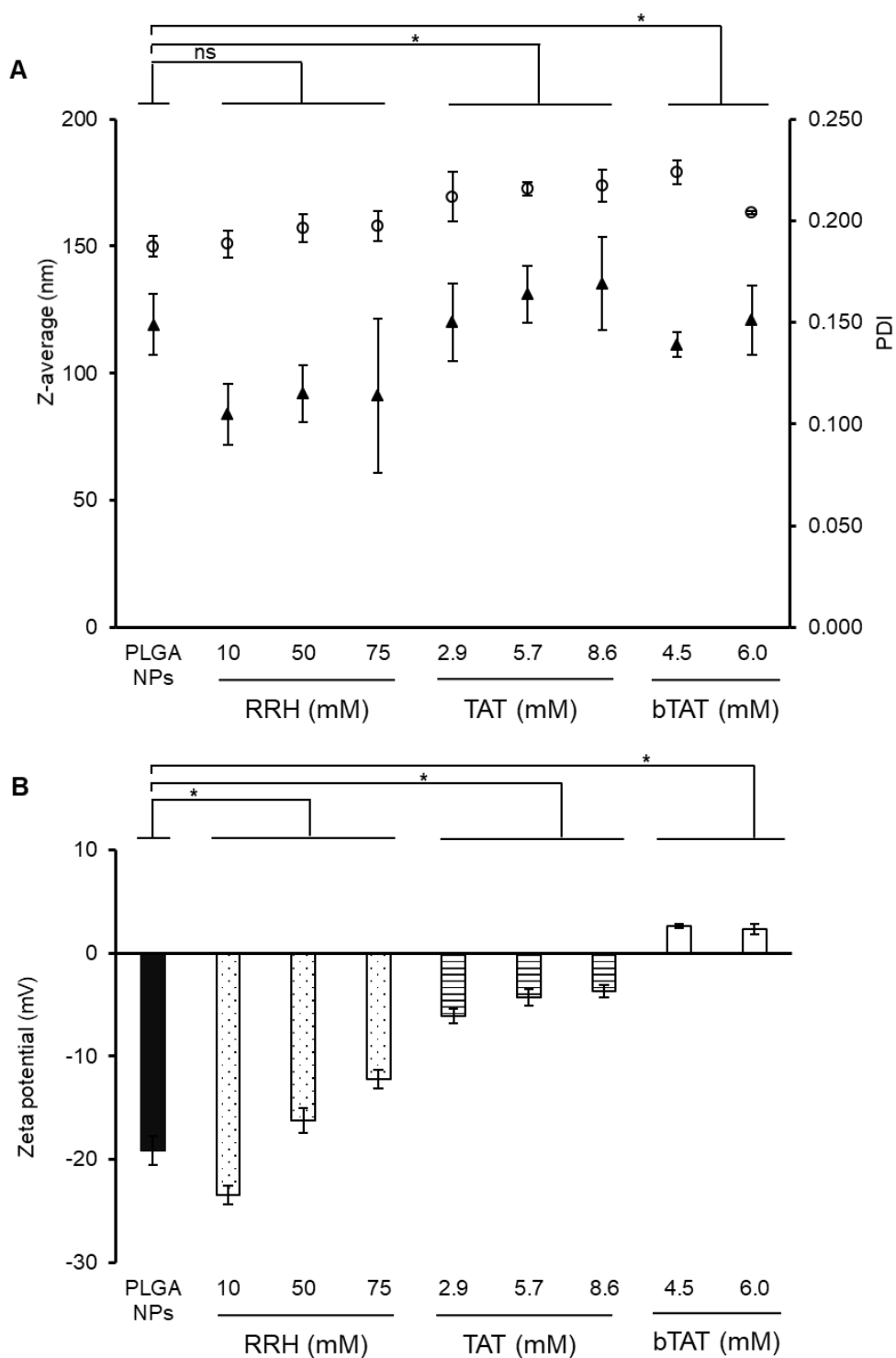


Figure 2.12. Size, polydispersity index (A) and zeta potential (B) of PLGA nanoparticles and CPP-tagged PLGA nanoparticles with different concentrations of CPPs (RRH, TAT, bTAT), prepared using the post-microfluidics conjugation approach. Size is displayed as circles and triangles represent polydispersity (Streck *et al.*, 2019a). Data are means \pm SD ($n = 3$ independent batches). * p -value < 0.05 for the comparison of CPP-tagged PLGA nanoparticles with PLGA nanoparticles, ns = not significant.

The influence of different CPP concentrations on the physicochemical characteristics of CPP-tagged PLGA nanoparticles was evaluated to design nanoformulations with a diameter below 200 nm and a neutral zeta potential to be suitable for future investigations as oral drug delivery systems. Studies have shown that PLGA nanoparticles with a size below 200 nm were taken up by Caco-2 cells to a higher extent compared to larger nanoparticles and that the surface charge of nanoformulations influences the electrostatic interactions with the negatively charged cell membrane (Danhier *et al.*, 2012; Gaumet *et al.*, 2009). In the present study, the zeta potential of RRH-tagged PLGA nanoparticles shifted from -24 to -12 mV with increasing concentrations of RRH (Figure 2.12B). The conjugation of TAT resulted in the formation of slightly negative TAT-tagged PLGA nanoparticles with a surface charge of -4 mV (Figure 2.12B). After conjugation of bTAT to the PLGA nanoparticles the zeta potential was slightly positive (+3 mV, Figure 2.12B). The change in zeta potential can be explained by the architecture of the CPPs. The CPPs are characterized by a short, long linear and branched architecture (Figure 2.5). The number of amino acids and positive charges in the peptide sequence is increased with a longer and more complex architecture. RRH contains two positive charges in the peptide sequence, whereas TAT and bTAT contain eight and twelve positive charges, respectively. The increase in positive charges for RRH > TAT > bTAT resulted in positively charged bTAT-tagged PLGA nanoparticles after the post-microfluidics conjugation approach. According to the PDI values, all CPP-tagged PLGA nanoparticles showed a monodisperse size distribution (Figure 2.12A) and no aggregation was observed. This is in contrast to the literature, where highly negatively or positively charged nanoparticles with a zeta potential below -30 and above +30 mV are believed to be more stable because of stronger repulsion forces than between neutral charged nanoparticles with a zeta potential between -10 and +10 mV (Sonam *et al.*, 2014; Tefas *et al.*, 2015; Vasconcelos *et al.*, 2015). This behaviour was reported for PLGA nanoparticles without surface modifications (Sonam *et al.*, 2014; Tefas

et al., 2015). CPP-tagged PLGA nanoparticles prepared in this study and TAT modified PLGA nanoparticles with a surface charge of above +20 mV (Vasconcelos *et al.*, 2015) did not show aggregation. Therefore, it is likely that the surface modification of PLGA nanoparticles with CPPs caused particle repulsion resulting in no aggregation at neutral surface charges.

2.4.7 Validation of RP-HPLC methods

The RP-HPLC methods for the quantification of the concentration of three CPPs RRH, TAT and bTAT were validated and representative RP-HPLC chromatograms are shown in Figure 2.13. The three CPPs were eluted with TFA containing mobile phases over 25 to 37 min and with an increasing concentration of the organic mobile phase at a rate of 0.5-1% per minute. The slow increase of the organic mobile phase supports the elution of the peptides as recommended in the literature (Scanlon and Finlayson, 2004). Further, no interference between injection peaks, CPP peaks and solvent peaks was observed indicating a good selectivity of the RP-HPLC methods.

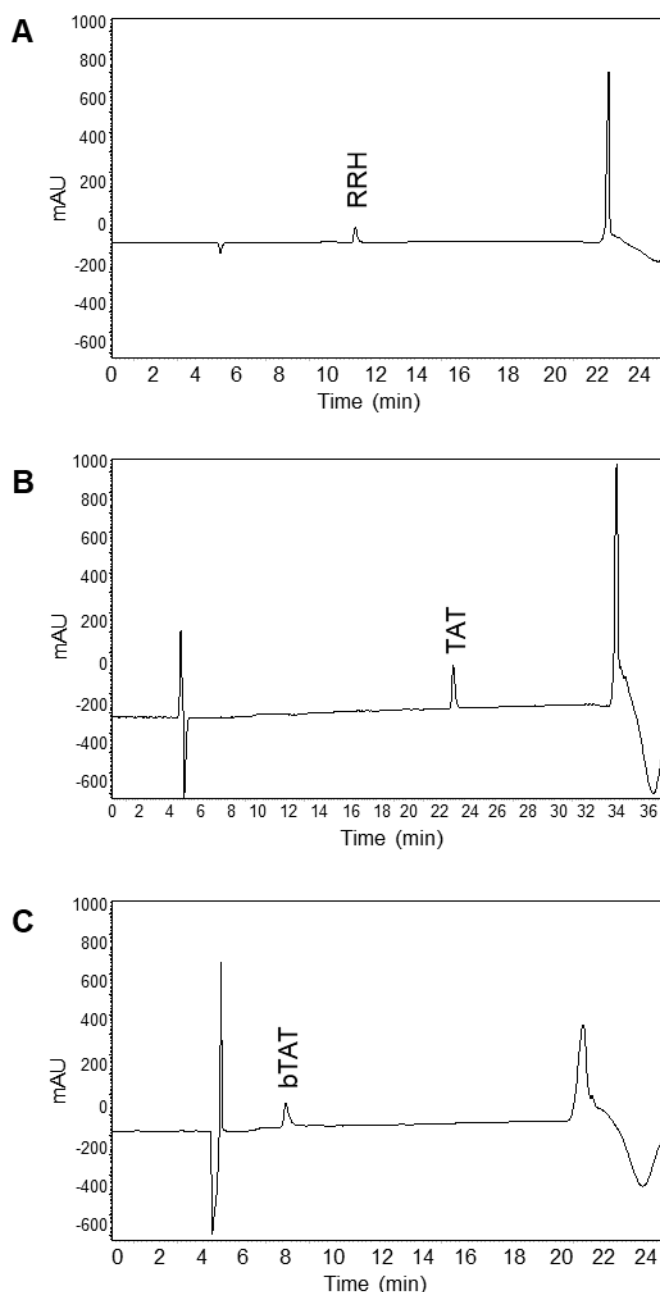


Figure 2.13. Representative RP-HPLC chromatograms of RRH (100 $\mu\text{g}/\text{mL}$) (A), TAT (100 $\mu\text{g}/\text{mL}$) (B) and bTAT (100 $\mu\text{g}/\text{mL}$) (C) eluted with the individual RP-HPLC methods for each CPP.

Standard curves were obtained for five or six different concentrations of RHH, TAT and bTAT after plotting the peak area against the concentration of the peptide. The average standard curve equation (including standard deviation for the slope and y-intercept) for RRH between 50 and 1000 $\mu\text{g}/\text{mL}$ was $y = 13385x (\pm 1153) - 28110 (\pm 7280)$ (Appendix III), for TAT

between 100 and 1000 $\mu\text{g/mL}$ was $y = 40151x (\pm 417) + 84592 (\pm 130705)$ (Appendix III) and for bTAT between 50 and 7500 $\mu\text{g/mL}$ was $y = 17138x (\pm 46) + 383704 (\pm 63462)$ (Appendix III). The average coefficient of regression (R^2) was 1.0000 ± 0.00002 , 0.9994 ± 0.0003 and 0.9999 ± 0.0001 for RRH, TAT and bTAT, respectively. The obtained R^2 showed good linearity between the peak area and the concentration of the CPPs. Overall, the accuracy of the standard curve was not lower than 94% for all three peptides (Table 2.6). The RP-HPLC chromatograms of RRH, TAT and bTAT showed the consistency of the peak shapes, the retention time and resolution over the concentration range used to obtain the standard curve (Appendix IV).

Table 2.6. Measured concentration ($\mu\text{g/mL}$), coefficient of variation (CV, %) and accuracy of standard curves obtained for the validation of RP-HPLC methods for RRH, TAT and bTAT. Data are means \pm SD ($n = 3$).

	Concentration ($\mu\text{g/mL}$)	Measured concentration \pm SD ($\mu\text{g/mL}$)	CV (%)	Accuracy (%)
RRH	50	50.0 ± 1.7	3.4	100.0
	100	100.1 ± 1.2	1.2	100.1
	200	201.2 ± 2.2	1.1	100.6
	300	299.6 ± 2.0	0.7	99.9
	500	498.4 ± 2.1	0.4	99.7
	1000	1000.7 ± 0.5	0.1	100.1
TAT	100	94.0 ± 2.9	3.1	94.0
	300	309.7 ± 9.4	3.0	103.2
	500	509.0 ± 11.0	2.2	101.8
	650	657.9 ± 4.7	0.7	101.2
	800	806.6 ± 8.6	1.1	100.8
	1000	995.4 ± 4.6	0.5	99.5
bTAT	50	52.7 ± 0.7	1.4	105.5
	100	97.5 ± 3.9	4.0	97.5
	250	249.0 ± 4.1	1.6	99.6
	500	500.7 ± 3.3	0.7	100.1
	750	750.0 ± 2.1	0.3	100.0

The precision and accuracy of the RP-HPLC methods for the three CPPs were further evaluated with the measurement of QCs. The QCs were three selected concentrations (low,

medium and high) within the concentration range of the standard curve of each CPP and measurements were repeated three times within one day and on consecutive days to obtain intra- and inter-day variability. Good repeatability and intermediate precision of the RP-HPLC methods for all three CPPs was shown with a coefficient of variation below 2% for the intra-day and inter-day variability, respectively (Table 2.7) (FDA, 2001). The RP-HPLC methods for the three CPPs were accurate as the accuracy was greater than 98% for the intra- and inter-day variability (Table 2.7).

Table 2.7. Measured concentration ($\mu\text{g/mL}$), coefficient of variation (CV, %) and accuracy for intra- and inter-day values of quality control samples of RRH, TAT and bTAT for the validation of RP-HPLC methods. Data are means \pm SD ($n = 3$). QC = quality control sample.

	Concentration QC ($\mu\text{g/mL}$)	Measured concentration \pm SD ($\mu\text{g/mL}$)	CV (%)	Accuracy (%)
RRH intra-day	75	74.7 \pm 1.4	1.8	99.6
	250	250.2 \pm 2.4	0.9	100.1
	750	743.2 \pm 6.1	0.8	99.1
RRH inter-day	75	74.7 \pm 1.0	1.3	99.6
	250	250.2 \pm 2.6	1.0	100.1
	750	743.2 \pm 4.9	0.7	99.1
TAT intra-day	200	196.7 \pm 0.7	0.4	98.3
	450	451.5 \pm 1.5	0.3	100.3
	900	894.0 \pm 1.1	0.1	99.3
TAT inter-day	200	197.4 \pm 2.3	1.2	98.7
	450	451.5 \pm 3.6	0.8	100.3
	900	894.0 \pm 8.8	1.0	99.3
bTAT intra-day	75	74.4 \pm 1.0	1.4	99.2
	350	353.5 \pm 4.7	0.6	101.0
	600	604.9 \pm 2.6	0.4	100.8
bTAT inter-day	75	74.6 \pm 0.9	1.1	99.4
	350	353.5 \pm 3.3	0.9	101.1
	600	604.6 \pm 6.4	1.1	100.8

The sensitivity of the RP-HPLC methods was determined by LOD and LOQ (Table 2.8). All three RP-HPLC methods have shown a high sensitivity and the different CPPs and can be quantified and detected at concentrations below 5.5 $\mu\text{g/mL}$ (Table 2.8).

Table 2.8. The limit of quantification and the limit of detection for the three different RP-HPLC assays to quantify the concentration of each of the CPPs (Streck *et al.*, 2019a).

	Limit of quantification (LOQ) $\mu\text{g/mL}$	Limit of detection (LOD) $\mu\text{g/mL}$
RRH	5.4	1.8
TAT	3.1	1.0
bTAT	2.7	0.9

2.4.8 Conjugation efficiency of CPPs with different architectures on PLGA nanoparticles

The amount of CPPs binding to the surface of PLGA nanoparticles depends on the number of available carboxyl groups and the orientation of the CPP. The number of binding sites on a single PLGA nanoparticle was estimated using the surface area of a PLGA nanoparticle and the Connolly surface area for the lactic acid monomer. The surface area of the lactic acid monomer was calculated from the Connolly surface, which describes the surface area of a molecule that is accessible to a solvent (Connolly, 1983). The surface area of an average spherical PLGA nanoparticle with a diameter of 155 nm was calculated first (Equation 2-6).

$$\text{Surface area} = 4 \times \pi \times r^2 = 4 \times \pi \times 77.5 \text{ nm}^2 = \mathbf{75477 \text{ nm}^2} \quad (2-6)$$

$$\pi = 3.14159 \quad r = \text{radius}$$

Further, it was assumed that 50% of the surface area of a PLGA nanoparticle was occupied by the lactic acid monomer since a PLGA polymer with a monomer ratio of 50:50 (lactic acid:glycolic acid) was used for the preparation of PLGA nanoparticles. Therefore, the surface area occupied by lactic acid monomer was considered to be 37739 nm^2 ($\frac{75477 \text{ nm}^2}{2} = 37739 \text{ nm}^2$). The number of binding sites on a PLGA nanoparticle was estimated by dividing

the surface area of a PLGA nanoparticle occupied by lactic acid by the Connolly surface area of a lactic acid monomer (Equation 2-7) and was estimated to be greater than 16000.

$$\text{Binding sites on PLGA NP} = \frac{\text{Surface area of lactic acid on PLGA nanoparticle}}{\text{Connolly surface area of lactic acid monomer}} \quad (2-7)$$

$$\text{Binding sites on PLGA nanoparticle} = \frac{37739 \text{ nm}^2}{2.328 \text{ nm}^2} = 16211$$

NP = nanoparticle

The three different CPPs have multiple primary amines that are likely to act as a binding site depending on their position in the CPP sequence (Figure 2.5). The estimated amount of CPPs covalently attached to the surface available carboxyl groups of the PLGA nanoparticles was quantified by calculating the conjugation efficiency. The conjugation efficiency for RRH, TAT and bTAT depended on the concentration of the CPPs added (Table 2.9). The amount of RRH conjugated to the PLGA nanoparticles increased by 12-fold when the concentration of RRH was increased from 10 to 50 mM. A further increase in the RRH concentration to 75 mM resulted in only a slight decrease in conjugation efficiency, suggesting that at 50 mM there was a saturation of the surface available carboxyl groups on the PLGA nanoparticles that can react with the primary amines in RRH. The concentration of TAT conjugated to PLGA nanoparticles increased in a linear manner with increasing concentrations of the CPP. The bTAT-tagged PLGA nanoparticles showed a similar concentration of bTAT conjugated to the surface of the PLGA nanoparticles as TAT (Table 2.9). These results can be related to the structure of the CPPs. The short CPP RRH showed the highest concentration of CPP on the surface, which is related to the amount of RRH that was added and the shorter amino acid sequence in comparison to the other two CPPs. The concentrations of TAT and bTAT conjugated to the PLGA

nanoparticles were similar and the amount of CPP that can be conjugated might be limited because of the more complex and branched architectures of the CPPs, which induced steric hindrance between individual CPP molecules. With the conjugation of TAT and bTAT to the surface of PLGA nanoparticles, it is possible that not all available binding sites would be used due to the orientation of the CPPs. TAT has primary amines along the amino acid sequence and can, therefore, bind in an orientation perpendicular to the nanoparticle surface or with a more tangential orientation in relation to the nanoparticle surface. A tangential orientation of the CPP may cover other binding sites on the surface of the PLGA nanoparticles since the tangential orientation covers more surface area. The same applies to the bTAT, which has primary amino acids in the long linear backbone and the short branches.

Table 2.9. Conjugation efficiencies and the equivalent concentrations of the CPPs tagged to PLGA nanoparticles (NPs) using different concentrations of CPPs prepared with a post-microfluidics conjugation approach (Streck *et al.*, 2019a). Data are means \pm SD ($n = 3$ independent batches). * p -value < 0.05 in comparison to the conjugation efficiency of 8.6 mM TAT.

CPP concentration (mM)	Conjugation efficiency \pm SD (%)	CPP concentration \pm SD (μ M)
RRH-tagged PLGA NPs		
10	32.4 ± 0.8	0.25 ± 0.03
50	74.4 ± 4.5	3.10 ± 0.19
75	58.5 ± 6.0	3.66 ± 0.37
TAT-tagged PLGA NPs		
2.9	57.6 ± 0.5	$0.15 \pm < 0.01$
5.7	56.3 ± 1.0	0.29 ± 0.01
8.6	55.5 ± 0.8	0.43 ± 0.01
bTAT-tagged PLGA NPs		
4.5	$79.8 \pm 0.3^*$	$0.33 \pm < 0.01$
6.0	45.4 ± 0.7	$0.25 \pm < 0.01$

2.5 Conclusion

The DoE study of the bulk nanoprecipitation method showed that the PLGA polymer concentration and the surfactant concentration influenced the size and PDI of PLGA nanoparticles. Using the microfluidics method, the DoE revealed that flow rate ratio has an influence on the size resulting in the formulation of smaller PLGA nanoparticles at higher flow rate ratio (aqueous:organic). The successful conjugation of CPPs to the PLGA polymer was shown by the formation of amide bonds. The CPP architecture determined the physicochemical characteristics and in particular, the zeta potential of the CPP-tagged PLGA nanoparticles. The surface charge was tuned from negatively charged RRH- and TAT-tagged PLGA nanoparticles to slightly positively charged bTAT-tagged PLGA nanoparticles with the introduction of a branched CPP architecture. The covalent attachment of CPPs to the PLGA polymer was confirmed with FTIR by identifying the formation of an amide I bond. The amount of CPPs tagged to PLGA nanoparticles increased with higher amounts of CPP added.

Decoration of nanoparticles with CPPs of different architectures showed the ability to tune the surface charge of PLGA nanoparticles and further investigation will focus on the distribution of CPPs on PLGA nanoparticles (Chapter 3) and implication for the interactions with cells at the nano-bio interface (Chapter 4).

Chapter Three

Distribution of cell-penetrating peptides with different architectures on polymeric nanoparticles

Parts of this Chapter have been published as:

S. Streck, A. J. Clulow, H. Mørck Nielsen, T. Rades, B. J. Boyd and A. McDowell (2019). The distribution of cell-penetrating peptides on polymeric nanoparticles prepared using microfluidics and elucidated with light scattering techniques. *Journal of Colloid and Interface Science*, 555, 438-448.

S. Streck, L. Hong, B. J. Boyd and A. McDowell (2019). Microfluidics for the production of nanomedicines: Considerations for polymer and lipid-based systems. *Pharmaceutical Nanotechnology*, 7, 1-21.

3.1 Introduction

Light scattering techniques have been frequently applied for the characterisation of nanoparticles. Dynamic light scattering is commonly used to evaluate the hydrodynamic diameter of nanoparticles and is also a standard technique for the quality control of nanoparticles (Brar and Verma, 2011). To further gain knowledge about the internal structure and morphology of nanoparticles, radiation from other sources such as X-rays and electrons can be utilized and the application of X-ray scattering and electron microscopy for polymeric nanoparticles is further described in this Chapter.

3.1.1 *Characterisation of polymeric nanoparticles using small angle X-ray scattering*

The shape and structure of nanoparticles and biomacromolecules can be probed by the utilization of X-ray techniques (Kikhney and Svergun, 2015; Li *et al.*, 2016). Small angle X-ray scattering (SAXS) is a contrast method that uses X-rays to generate scattering patterns based on the electron density of a sample (Li *et al.*, 2016; Putnam *et al.*, 2007). The applications of SAXS include the structural characterisation of lipid crystalline nanoparticles (Hong *et al.*, 2015), micelles (Sanada *et al.*, 2013), polymeric nanoparticles (Jäger *et al.*, 2018) and proteins (Zhang *et al.*, 2007) in solution. Further, SAXS can be used for time-resolved studies to monitor kinetic processes like the formation of liquid crystalline structures during the digestion of milk (Clulow *et al.*, 2018) or the assembly of nanoparticles in a microfluidic device (Ghazal *et al.*, 2017).

Synchrotron facilities can provide X-rays with higher energy for SAXS and longer sample-to-detector lengths than lab-based instruments, which is important for the investigation of nanoparticles with a diameter larger than 100 nm using SAXS. A high quality of X-ray beam

used at synchrotron facilities is ensured as the radiation is generated by the acceleration of electrons close to the speed of light (Boyd and Rades, 2016). To obtain the scattering profile of a sample, the sample solution is placed in a quartz capillary in the X-ray beam, illuminated with the X-ray beam and the scattered X-rays are recorded using a diode array detector (Figure 3.1A) (Boyd and Rades, 2016). For samples measured in solution, the scattering pattern of the pure solvent is obtained first and subtracted from the scattering pattern of the samples (Kikhney and Svergun, 2015). With this approach, the influence of the solvent is removed and the scattering pattern of the sample remains for further evaluation of the shape and size of the sample (Kikhney and Svergun, 2015; Putnam *et al.*, 2007). Generally, particles are randomly distributed in solution and this behaviour results in an isotropic or radially scattering pattern (Putnam *et al.*, 2007), which is recorded and averaged by the 2D detector and plotted as a 1D scattering curve with the scattering intensity $I(q)$ on the y-axis against the scattering vector, q , on the x-axis (Figure 3.1B) (Kikhney and Svergun, 2015).

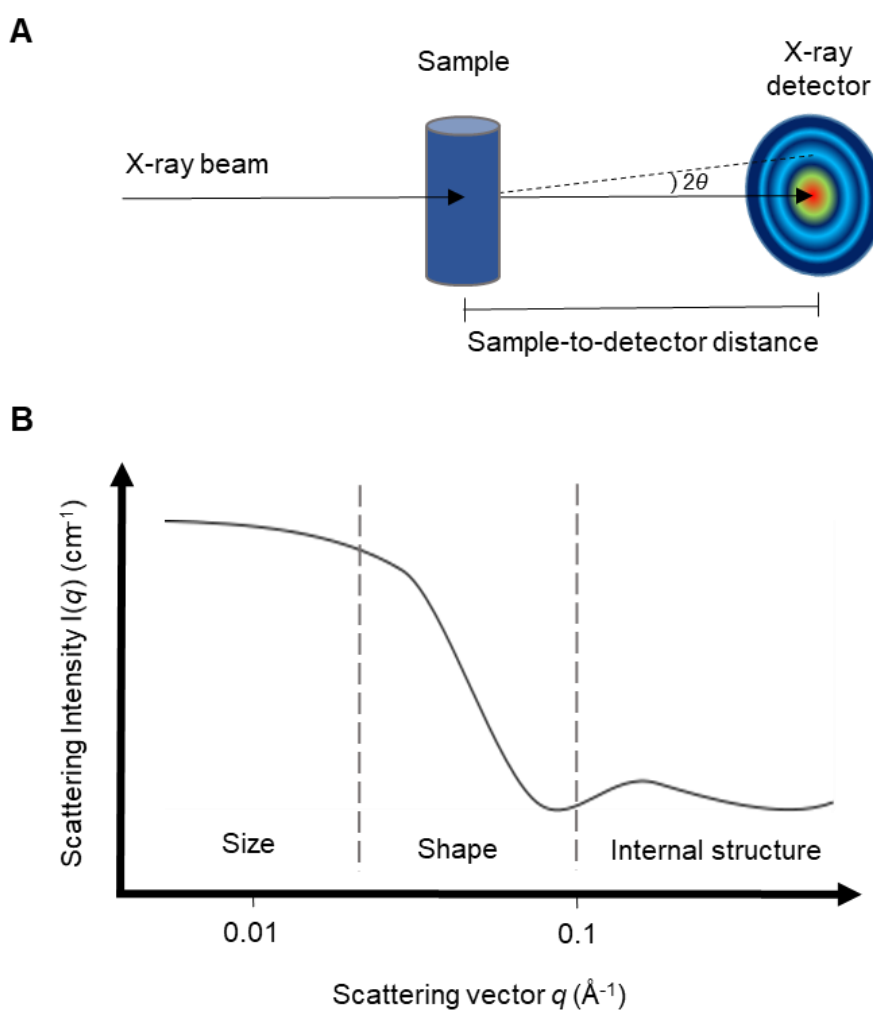


Figure 3.1. Schematic of the sample set up for small angle X-ray scattering with the detection of scattering patterns (A) and a small angle X-ray scattering plot showing information about the sample structure deduced from the scattering curve (B) (Li *et al.*, 2016; Luo *et al.*, 2019b). 2θ = scattering angle, $I(q)$ = scattering intensity, q = scattering vector.

To obtain the scattering curve, each pixel of the recorded isotropic scattering pattern is converted to one scattering angle using the pixel size of the detector and the sample-to-detector distance (Li *et al.*, 2016). The 1D scattering curve contains information about the size, shape and internal structure of the sample (Figure 3.1B) (Augsten *et al.*, 2008; Putnam *et al.*, 2007) as well as molecular weight and particle volume (Kikhney and Svergun, 2015). Analysis of the scattering data can be performed by using the Guinier approximation, which shows a linear relationship in the lower q region between $\log(I(q))$ and q^2 , to determine the radius of gyration

(R_g) as a measurement of particle size (Putnam *et al.*, 2007). In the higher q regions ($q > 0.05 \text{ \AA}^{-1}$), the Porod approximation, where the scattering shows a decay of the scattering curve (q^{-4}), can be observed (Li *et al.*, 2016). The Porod approximation is based on the assumption that the electron density of two compounds in a two-phase system, e.g. particles and buffer, is different (Ruland, 1971). The higher q regions provide information for surface area calculation of particular systems of inorganic, polymeric and porous materials (Li *et al.*, 2016). The pair distribution function $p(r)$ is calculated by Fourier transformation of the scattering data and based on the distance between the electrons of the material within the sample, and information about the diameter and shape e.g. of particles can be obtained (Kikhney and Svergun, 2015; Putnam *et al.*, 2007).

In order to obtain high quality data with SAXS, it is crucial to consider the influence of the X-ray exposure time on the sample and the influence of the concentration of the sample on the scattering profile. Using synchrotron-based SAXS, the exposure time can vary from fractions of a second to minutes, and shorter exposure reduces the risk of radiation damage to the sample (Kikhney and Svergun, 2015). Further, the use of a flow cell instead of a static solution and reduced X-ray energy avoids radiation damage (Jeffries *et al.*, 2015). The concentration of the sample can be increased in SAXS experiments to gain a better signal-to-noise ratio due to higher scattering intensities (Kikhney and Svergun, 2015). One drawback of high sample concentrations, however, is the decrease in the inter-particle distance and therefore the possibility of an unwanted contribution of scattering to the scattering in the low q region, influencing the radius of gyration (Franke *et al.*, 2012; Kikhney and Svergun, 2015).

Small angle neutron scattering (SANS) and SAXS are complementary scattering techniques utilizing either the scattering of neutrons or electrons (Di Cola *et al.*, 2016). Similar to SAXS, SANS is a non-invasive technique that can also be used to investigate structure and interactions of soft matters including liposomes (Hofmann *et al.*, 2010), polymeric nanoparticles (Desgouilles *et al.*, 2003), polymeric micelles (Yang *et al.*, 2015), core-shell nanoparticles with a metallic core and polymeric shell (Luo *et al.*, 2019b) and cyclic peptide-polymer conjugates (Koh *et al.*, 2016). Neutrons interact with the atomic nucleus of elements and result in a scattering contrast that varies greatly between elements and isotopes (Lopez *et al.*, 2018). The significant scattering contrast between hydrogen and its isotope deuterium is particularly important and deuterated solvents are often used in SANS experiments (Grillo, 2008). The contrast of a system, e.g. polymeric nanoparticles in a dispersant, can be varied by deuteration of specific molecules or by changing the amount of D₂O and H₂O in the solvent mixture during preparation (Di Cola *et al.*, 2016; Yang *et al.*, 2015).

The combined application of SANS and SAXS can aid to acquire data on the hydrophobic core and the hydrophilic shell of colloids including micelles (Manet *et al.*, 2011) and liposomes (Di Cola *et al.*, 2016). SANS can provide information about the hydrophobic structure, whereas SAXS is sensitive towards polar groups. Therefore, in this thesis SAXS was used to study the distribution of gold labelled CPPs. The used CPPs contain polar and charged amino acids in their sequence leading to increased hydrophilicity on the surface of polymeric nanoparticles after conjugation.

3.1.2 *Imaging of nanoparticles to reveal morphology*

Imaging of viral particles, nanoparticles and cells is achieved by using microscopic techniques including electron microscopy and atomic force microscopy as both techniques offer nanoscale resolution (Barreto-Vieira and Barth, 2015; Ruozi *et al.*, 2011; Ruozi *et al.*, 2014; Tantra and Knight, 2011; Ye *et al.*, 2015). Scanning and transmission electron microscopes are most commonly used for the visualisation of individual nanoparticles to obtain information about size and shape (Reifarth *et al.*, 2018).

Scanning electron microscopy (SEM) is used for the investigation of shape and morphology of micro- and nanoparticles (Bootz *et al.*, 2004; Dubes *et al.*, 2003; Zhai *et al.*, 2015; Zhou *et al.*, 2019). In particular, the porosity of microparticles and morphological changes of microparticles during drug release (over a period of days to weeks) can be monitored using SEM (Gao *et al.*, 2016; Zhai *et al.*, 2015). Before SEM analysis, the particle samples are dried and sputter coated with metals such as gold or palladium to generate contrast (Bootz *et al.*, 2004; Gao *et al.*, 2016; Zhai *et al.*, 2015). These two preparations steps are required, however also a major disadvantage as changes in the properties of the particles can occur (Bootz *et al.*, 2004).

TEM is used to generate information about the morphology of individual polymeric nanoparticles in a label-free manner (Augsten *et al.*, 2008; Reifarth *et al.*, 2018; Saarinen *et al.*, 2019). Using TEM, the electron beam is focused onto the sample and unscattered electron waves undergo a change in their wave amplitude and phase after passing through the sample (Tantra and Knight, 2011; Winey *et al.*, 2014). The short wavelength electron beam originates from an electron source that is operated under vacuum (de Jonge and Ross, 2011; Miao *et al.*,

1999) and due to the short wavelength of the electron beam, a high resolution below 20 nm and down to 1 nm can be achieved (Pauw, 2013; Winey *et al.*, 2014).

Sample preparation has an influence on the quality of the specimen and it is crucial to obtain high quality images with sufficient contrast between nanoparticles in the sample and the background (Ruozi *et al.*, 2014). Samples for TEM analysis are prepared by spotting a drop of nanoparticle suspension onto copper grids (Bohrey *et al.*, 2016; Winey *et al.*, 2014). Polymers are known to generate a low contrast and therefore, heavy metals like osmium tetroxide (Chelopo *et al.*, 2016), phosphotungstic acid (Bohrey *et al.*, 2016) or uranyl acetate (Chelopo *et al.*, 2016; Ruozi *et al.*, 2014) are used for negative staining of polymeric nanoparticles to enhance the contrast between nanoparticles and background to facilitate the observation of nanoparticle features.

One of the main drawbacks of TEM is the presence of artefacts, which can be caused by drying of the nanoparticles during sample preparation (Franken *et al.*, 2017) and damage of specimen through long exposure time to the electron beam (Tantra and Knight, 2011). Therefore, it is important to critically examine obtained TEM micrographs and incorporate other scattering techniques to complement the TEM data. Further, investigation of nanoparticles with TEM is limited by the fact that not all nanoparticles in the sample are analysed and typically only representative images of the whole sample are reported (Li *et al.*, 2016).

3.1.3 Functionalisation of polymeric nanoparticles using microfluidics

As discussed earlier, functionalisation of nanoparticles with specific moieties for targeted and enhanced delivery of therapeutics to specific cells can be achieved using microfluidics (Kamaly *et al.*, 2016; Kolishetti *et al.*, 2010). Conjugation of the polymer with a functional moiety can occur at different steps in the preparation process, namely before, during or after microfluidics preparation of polymeric nanoparticles (Figure 3.2). The functionalisation of polymeric nanoparticles performed in a pre-microfluidics approach makes use of polymer-ligand conjugates as a starting material (Figure 3.2A) (Kamaly *et al.*, 2016; Liu *et al.*, 2010; Valencia *et al.*, 2013). This approach has been used to achieve decoration of polymeric nanoparticles with targeted ligands including collagen IV (Kamaly *et al.*, 2016), argininyglycyl aspartic acid (RGD) (Liu *et al.*, 2010) and the LIG ligand (Valencia *et al.*, 2013) for different therapeutic conditions including cancer and atherosclerosis. Liu *et al.* (2010) formulated RGD-targeted supramolecular nanoparticles for targeting the $\alpha_v\beta_3$ integrin receptor of tumour cells and an approximately 60% higher uptake was observed in $\alpha_v\beta_3$ receptor positive cells in comparison to $\alpha_v\beta_3$ receptor negative cells. In addition, ligand density has been shown to influence cellular uptake of polymeric nanoparticles in prostate cancer cell lines that overexpress the prostate-specific membrane antigen (Valencia *et al.*, 2013). The use of increasing amounts of PLGA-PEG-LIG conjugates from 14 to 40 mol% of targeted polymeric nanoparticles increased cell uptake by approximately 35% in comparison to non-targeted polymeric nanoparticles (Valencia *et al.*, 2013).

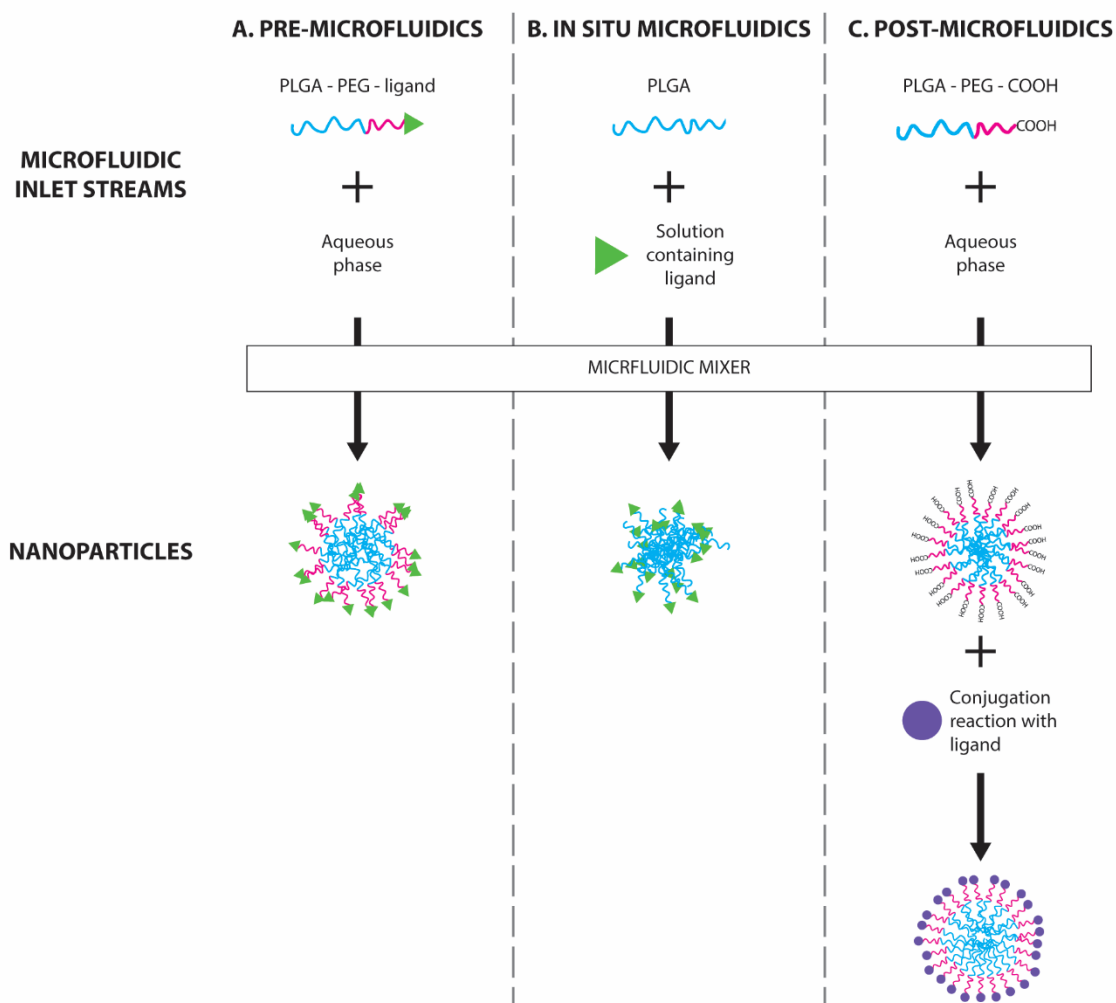


Figure 3.2. Functionalisation of polymeric nanoparticles using a pre-microfluidics (A) (Kamaly *et al.*, 2016; Liu *et al.*, 2010; Valencia *et al.*, 2013), an *in situ* microfluidics (B) or a post-microfluidics (C) (Kolishetti *et al.*, 2010) conjugation approach (Streck *et al.*, 2019c).

The modality for producing functionalised nanoparticles using microfluidics discussed in the literature involves mainly the formation of nanoparticles from functionalised polymer material during the mixing process. An alternative strategy for the formulation of surface-modified polymeric nanoparticles is to functionalise the nanoparticles after production in the microfluidic device in a post-microfluidics conjugation approach (Figure 3.2C). In order to deliver anticancer drugs to prostate cancer cells, Kolishetti *et al.* (2010) functionalised the surface of PLGA-PEG nanoparticles with a targeting ligand (A10-Aptamer) and showed accumulation of the targeted nanoparticles in the endosomes of prostate cancer cells after

endocytosis. The attachment of the targeting ligand was performed using a zero-length crosslinking reaction with a carbodiimide (Kolishetti *et al.*, 2010). Such zero-length crosslinking reactions are commonly used for the surface modification of polymeric nanoparticles (Yadav *et al.*, 2011) and were described in Chapter 2, Section 2.1.4.

The above mentioned studies illustrate that functionalised polymeric nanoparticles have the potential to achieve a targeted delivery approach for therapeutics. The conjugation reaction is commonly performed in pre- and post-microfluidics conjugation approaches and the possibility of microfluidic devices to act as a reaction vessel for functionalisation of polymeric nanoparticles has not yet been fully exploited. Theoretically, the conjugation reaction between the polymer and the moieties used for functionalisation of polymeric nanoparticles can be translated from a pre- or post-microfluidics reaction to an *in situ* microfluidics reaction (Figure 3.2B). For the translation of the conjugation reaction into the microfluidic channel, the conjugation reaction must be first evaluated for its suitability. Performing the conjugation reaction in the microchannel relies on the formation of a covalent bond between the two components and that the formation of nanoparticles can occur simultaneously. The conjugation needs to occur almost immediately since the mixing time in the microchannel is greatly reduced compared to a traditional bulk approach. It is proposed here that with a successful conjugation, the functionalisation moiety will be present on the surface and free functionalisation moieties might be encapsulated in the polymeric matrix of the nanoparticles. In this thesis, the *in situ* functionalisation approach is applied to the preparation of CPP-tagged PLGA nanoparticles for the first time. The formulated CPP-tagged PLGA nanoparticles are evaluated with different advanced characterisation techniques including SAXS to get new insight on the influence of the preparation method on the physicochemical properties of the formulated nanoparticles.

3.1.4 *Chapter aims*

The aims of this study were to determine the utility of microfluidics for the production of CPP-tagged PLGA nanoparticles and the influence and distribution of CPP architecture on the nanoformulations after preparation. PLGA nanoparticles were surface modified with CPPs of three different architectures (short, long linear and branched) using two different conjugation approaches, a post-microfluidics and an *in situ* microfluidics conjugation approach. The influence of the different conjugation approaches on the distribution of CPPs was investigated using imaging techniques and X-ray scattering.

3.2 Materials

Gold nanoparticles (5 nm Gold NanoSpheres, COOH-PEGylated) referred to as AuNPs were supplied by Nanohybrids (Austin, TX, USA). The stock solution of AuNPs used in this work had the following characteristics as quoted by the manufacturer: diameter = 4.7 ± 0.8 nm; surface plasmon resonance peak = 514 nm; particle concentration = 5.3×10^{15} mL⁻¹; Au mass concentration = 6.3 mg mL⁻¹; pH = 7.0; particle surface = Carboxy-PEG 5 kDa, zeta potential = -6.5 mV.

All other ingredients and peptides required for the preparation of the nanoformulations were used as listed in Chapter 2.

3.3 Methods

3.3.1 *In situ microfluidics conjugation for the preparation of CPP-tagged PLGA nanoparticles and Au-labelled CPP-tagged nanoparticles*

For the *in situ* conjugation of CPPs to PLGA nanoparticles, a method was adapted from Karve *et al.* (2011). The organic PLGA solution (10 mg/mL in ACN) was first activated by adding 250 μ L of EDC solution (1.5 mM in ultra-pure water) and 250 μ L of sulfo-NHS solution (2 mM in ultra-pure water) dropwise under gentle stirring, which was continued for 30 min at room temperature. The mixture was precipitated by transfer into ultra-pure water and spun in a centrifuge at 3150 g for 20 min at 8°C. The supernatant was removed and the pellet was dissolved at a concentration of 10 mg/mL in ACN. 100 μ L of CPPs (containing either 75 mM RRH, 8.6 mM TAT or 4.5 mM bTAT) were mixed with 1 mL of 2% (w/v) PVA solution. For the *in situ* microfluidics conjugation approach, a higher concentration of the CPP RRH was

selected due to a higher conjugation efficiency in comparison to the post-microfluidics conjugation approach.

For the preparation of Au-labelled CPP-tagged PLGA nanoparticles, each CPP solution was incubated for 2 h with a 0.016 mM AuNPs solution (equals a 1-360 fold lower concentration than the expected conjugation efficiency of each CPP) prior to the microfluidics preparation. The label-free CPP solutions and the Au-labelled CPP solutions were mixed with the activated organic solution of PLGA using the NanoAssemblr[®] Benchtop Device with a total flow rate of 10 mL/min and a flow rate ratio of 6:1. The Au-labelled CPP-tagged PLGA nanoparticles were kept in the fridge at 4°C until further required (Figure 3.3A, (ii)). The label-free CPP-tagged PLGA nanoparticles (Figure 3.3A, (i)) were separated by ultra-centrifugation at 42800 g for 15 min at 4°C to remove excess of ACN and unconjugated CPPs. The supernatant was kept for RP-HPLC analysis and the nanoparticle pellet was re-suspended in 100 µL of ultra-pure water and stored at 4°C until required.

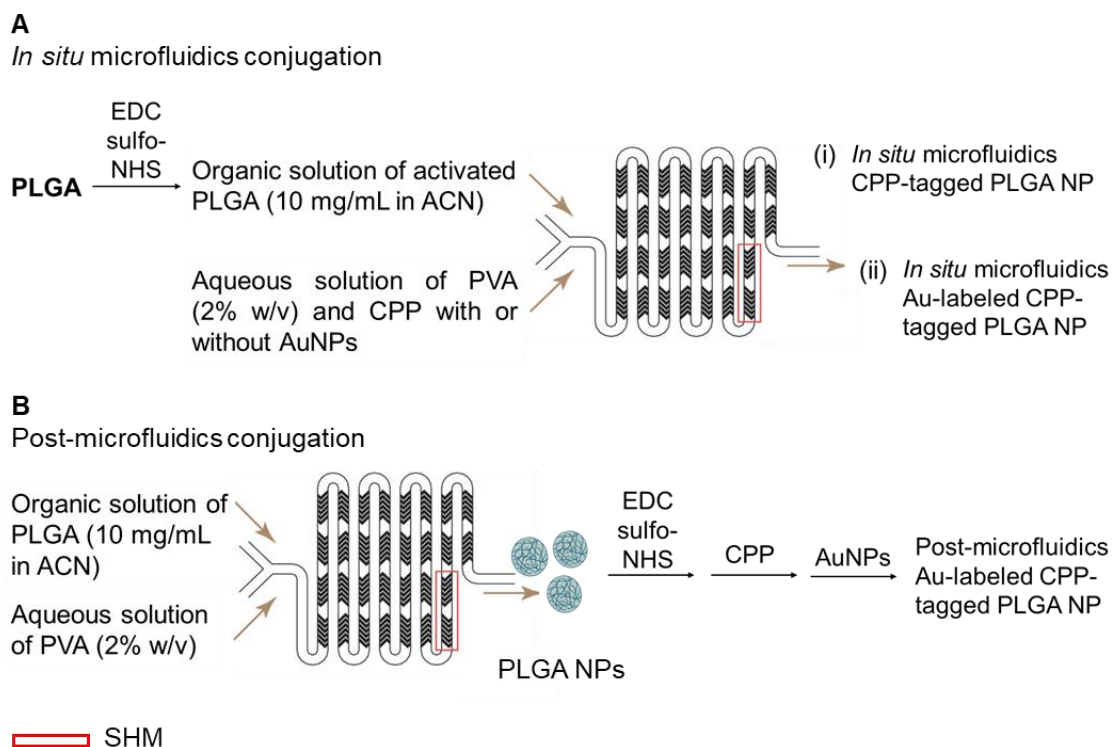


Figure 3.3. Comparison of the *in situ* microfluidics (A) and the post-microfluidics (B) conjugation approaches for the formulation of Au-labelled CPP-tagged PLGA nanoparticles. Label-free CPP-tagged PLGA nanoparticles (i) and Au-labelled CPP-tagged PLGA nanoparticles (ii) were produced using the *in situ* microfluidics (A) conjugation approach. The microchannel diagram, with the red box indicating the herringbone structure, was modified from Belliveau *et al.* (2012) (Streck *et al.*, 2019b). SHM = staggered herringbone mixer, ACN = acetonitrile.

3.3.2 Conjugation efficiency of CPPs after *in situ* microfluidics preparation of CPP-tagged PLGA nanoparticles

The conjugation efficiency of the three CPPs (RRH, TAT and bTAT) to nanoparticles was obtained indirectly from the amount of CPP in the supernatant after preparation of CPP-tagged PLGA nanoparticles using the *in situ* conjugation approach. The supernatant was collected after *in situ* microfluidics preparation as described above for label-free CPP-tagged PLGA nanoparticles. The RP-HPLC methods for the quantification of the CPP concentrations were described in Chapter 2, Section 2.3.9.

3.3.3 *Post-microfluidics conjugation for the preparation of CPP-tagged PLGA nanoparticles and Au-labelled CPP-tagged PLGA nanoparticles*

PLGA nanoparticles were prepared using the NanoAssemblr[®] Benchtop Device and surface modified with RRH (50 mM), TAT (8.6 mM) and bTAT (4.5 mM) as described in Chapter 2, Section 2.3.5 and 2.3.6, respectively. After removal of free CPPs by ultracentrifugation, the nanoparticle pellet was re-suspended and diluted with 1 mL HEPES buffer (0.025 M, pH 6.11). For the preparation of Au-labelled CPP-tagged PLGA nanoparticles, a suspension of the AuNPs was added to the CPP-tagged PLGA nanoparticles at a 1.5-2 fold lower concentration than the expected conjugation efficiency of each CPP (RRH: 1.6 mM AuNPs, TAT: 0.24 mM AuNPs and bTAT: 0.19 mM AuNPs) and incubated overnight with gentle stirring (Figure 3.3B).

3.3.4 *Characterization of nanoformulations*

The Z-average diameter, PDI and zeta potential of the nanoformulations were measured using DLS and laser Doppler electrophoresis as described previously in Chapter 2, Section 2.3.7.

3.3.5 *Transmission electron microscopy*

TEM micrographs were recorded to investigate the morphology of the Au-labelled CPP-tagged PLGA nanoparticles. The Au-labelled CPP-tagged PLGA nanoparticles were prepared using either the post-microfluidics or the *in situ* microfluidics conjugation approach as described in Sections 3.3.1 and 3.3.3. TEM grids (Electron Microscope Science, Hatfield, PA USA) were made hydrophilic by glow discharge in air for 1 min (Aebi and Pollard, 1987).

Solutions of the Au-labelled CPP-tagged PLGA nanoparticles (10 μL) were spotted onto a 300 mesh copper grid and air-dried for 30-60 s before the excess solution was blotted with Whatman filter paper Number 1. The samples were viewed with a Technai F30 (FEI, Eindhoven, The Netherlands) and a Philips CM 100 Bio TWIN TEM (Philips Electron Optics, Eindhoven, The Netherlands).

3.3.6 *Small angle X-ray scattering*

The SAXS/WAXS beamline at the Australian Synchrotron (ANSTO, Clayton, Australia) was used to investigate the distribution of Au-labelled CPPs with different architectures conjugated to PLGA nanoparticles produced using either the post-microfluidics or *in situ* microfluidics conjugation approach. The samples were measured in a quartz capillary mounted in the X-ray beam with a wavelength of the 0.954 \AA (photon energy 13 keV). Sample-to-detector distances of 1.53 m and 7.33 m were used to cover a scattering vector q range of $0.003 < q < 0.665 \text{ \AA}^{-1}$. The scattering vector q is given by $q = \left(\frac{4\pi}{\lambda}\right) \sin \theta$, where λ is the X-ray wavelength and 2θ is the scattering angle. 2D scattering profiles were acquired during X-ray exposures between 0.1-1 s using a Pilatus 1 M detector. The obtained scattering patterns were radially integrated into plots of $I(q)$ versus q using the in-house-developed software package ScatterBrain (Vithani *et al.*, 2017).

3.3.7 *Statistical analysis*

Students t -tests were performed to make a comparison between single groups and obtained p -values were statistically significant at $p < 0.05$.

3.4 Results and Discussion

3.4.1 *Conjugation approaches for preparation of CPP-tagged PLGA nanoparticles*

The main difference between the post-microfluidics and the *in situ* microfluidics conjugation approach to formulate CPP-tagged PLGA nanoparticles is the time point when the PLGA polymer was activated by EDC/sulfo-NHS to enable the conjugation reaction with the CPPs. In the post-microfluidics conjugation approach, the free carboxyl groups of the PLGA polymer were activated after formation of the nanoparticles. Using this approach, the conjugation reaction with the CPPs was limited to the surface available carboxyl groups. In the *in situ* microfluidics conjugation approach, the PLGA polymer was activated before formation of the nanoparticles. The activated carboxyl groups react with the CPPs during mixing within the microchannel and consequently, the CPPs should have been distributed throughout the PLGA nanoparticles.

3.4.2 *Characteristics of CPP-tagged PLGA nanoparticles depends on the CPP architecture*

The *in situ* microfluidics conjugation approach was used to formulate PLGA nanoparticles and CPP-tagged PLGA nanoparticles. Unmodified PLGA nanoparticles were monodisperse and showed an average size of 130 nm and a negative surface charge of -18 mV (Figure 3.4). In comparison to the unmodified PLGA nanoparticles prepared using microfluidics in Chapter 2 (Section 2.4.6), unmodified PLGA nanoparticles prepared using the *in situ* microfluidics conjugation approach showed a smaller size, which might be related to the use of the activated polymer for the preparation of PLGA nanoparticles. A possible explanation is that the reactive sulfo-NHS ester intermediate on the activated PLGA polymer interferes with the nanoprecipitation process. The unmodified PLGA nanoparticles were formulated for control purposes only as the reactive sulfo-NHS ester intermediate may lead to unwanted

reactions. CPP-tagged PLGA nanoparticles had a size between 159 and 174 nm, depending on the CPP used, and showed a monodisperse size distribution with a PDI < 0.155 after preparation with the *in situ* microfluidics conjugation approach (Figure 3.4A). Both preparation methods resulted in CPP-tagged PLGA nanoparticles with a similar size and polydispersity (Chapter 2, Section 2.4.6). The bTAT-tagged PLGA nanoparticles were only tested using one concentration of bTAT (4.5 mM) for the *in situ* microfluidics conjugation approach as the results from the post-microfluidics conjugation approach with 4.5 and 6 mM bTAT did not reveal a difference in size or zeta potential (Chapter 2, Figure 2.12).

The zeta potential of RRH-tagged PLGA nanoparticles decreased from -18 to -8 mV with increasing concentrations of RRH (Figure 3.4B). The conjugation of TAT resulted in slightly negatively charged PLGA nanoparticles with a surface charge between -4 to -2 mV (Figure 3.4B). The CPP-tagged PLGA nanoparticles prepared with the branched CPP, bTAT, showed a positive zeta potential of +4 mV after preparation using the *in situ* microfluidics conjugation approach (Figure 3.4B). A similar change in zeta potential after preparation of CPP-tagged PLGA nanoparticles was also observed using the post-microfluidics conjugation approach in Chapter 2, Section 2.4.6 and can be explained by the incorporation of more positive charges in the CPP sequence with a more complex architecture of the CPPs.

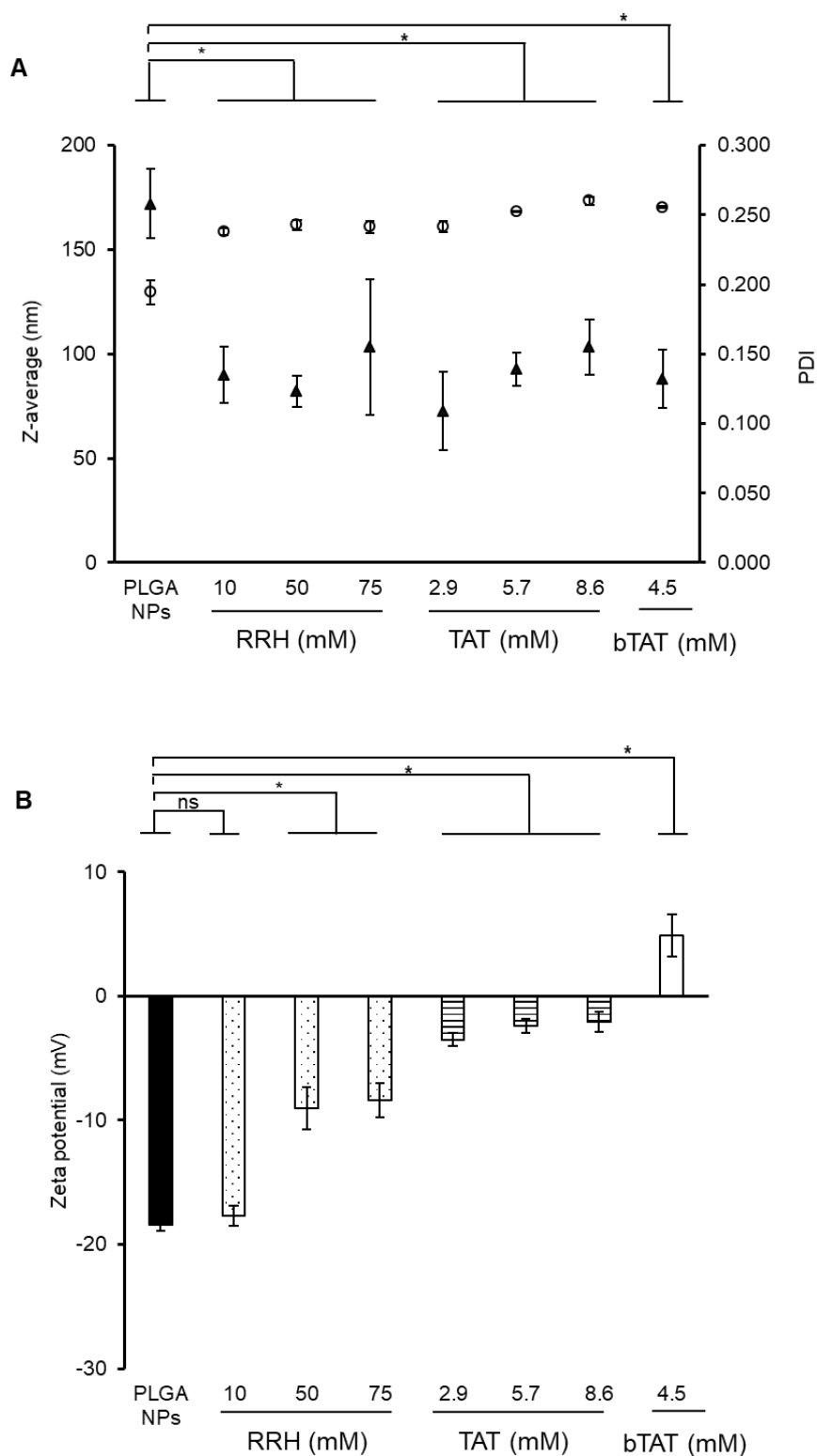


Figure 3.4. Size, polydispersity (A) and zeta potential (B) of PLGA nanoparticles and CPP-tagged PLGA nanoparticles with different concentrations of the CPPs (RRH, TAT and bTAT), prepared using the *in situ* microfluidics conjugation approach. Size is displayed as circles and triangles represent polydispersity. Data are means \pm SD ($n = 3$ independent batches). * p -value < 0.05 for the comparison of CPP-tagged PLGA nanoparticles with PLGA nanoparticles, ns = not significant.

3.4.3 Conjugation efficiency of CPPs with different architecture on PLGA nanoparticles

The conjugation efficiency of CPPs tagged to PLGA nanoparticles using the *in situ* microfluidics conjugation approach was dependent on the concentration of CPP added (Table 3.1). Conjugation efficiencies of RRH increased from 73% to 91% with higher amounts of RRH added. For RRH-tagged PLGA nanoparticles, the amount of RRH associated to the nanoformulation was almost double using the *in situ* microfluidics conjugation approach in comparison to the post-microfluidics conjugation approach at a RRH concentration of 75 mM (Chapter 2, Section 2.4.8). The bTAT-tagged PLGA nanoparticles showed a high conjugation efficiency (> 80%) using the *in situ* microfluidics conjugation approach. The conjugation efficiency and the amount of bTAT conjugated to the PLGA nanoparticles using the *in situ* microfluidics approach were similar compared to the post-microfluidics conjugation (Chapter 2, Section 2.4.8). The higher conjugation efficiencies for RRH- and bTAT-tagged PLGA nanoparticles prepared using the *in situ* microfluidics conjugation approach compared to the post-microfluidics conjugation approach suggested encapsulation of RRH and bTAT within the formulated CPP-tagged PLGA nanoparticles. Higher conjugation efficiencies were observed as RRH and bTAT were encapsulated as well as present on the surface of the PLGA nanoparticles. The conjugation efficiency of TAT using the *in situ* microfluidics conjugation approach increased with higher amounts of TAT added, but was overall low and ranged between 15% to 29%. The conjugation efficiency of TAT was lower, compared to the post-microfluidics conjugation approach (Chapter 2, Section 2.4.8) and the other CPPs investigated. One possible reason for the low conjugation efficiency of TAT could be related to the amino acids present in the peptide sequence of the investigated CPPs. RRH and bTAT both contain the amino acid histidine in their peptide sequence and histidine has been shown to bind to ethylcyanoacrylate monomer units during preparation of PECA nanoparticles (Kafka *et al.*, 2009). The lack of histidine in the TAT peptide sequence might be a reason for the lower conjugation

efficiency as fewer interactions with the PLGA polymer occur during the formulation of the nanoparticles in the microchannel.

Table 3.1 Conjugation efficiencies and the equivalent concentration of the CPPs tagged to PLGA nanoparticles (NPs) using different concentrations of CPPs prepared with the *in situ* microfluidics conjugation approach. Data are means \pm SD ($n = 3$ independent batches). * $p < 0.05$ in comparison to the CPP concentration of 10 and 50 mM RRH, ^a $p < 0.05$ in comparison to the CPP concentration of 2.9 and 5.7 mM TAT, ^b $p < 0.05$ in comparison to the CPP concentration of 8.6 mM TAT.

CPP concentration (mM)	Conjugation efficiency (%) \pm SD	CPP concentration (μ M) \pm SD
RRH-tagged PLGA NPs		
10	73.2 \pm 3.5	0.67 \pm 0.03
50	83.2 \pm 1.1	3.78 \pm 0.05
75	91.0 \pm < 0.1	6.20 \pm < 0.01*
TAT-tagged PLGA NPs		
2.9	14.7 \pm 3.3	0.04 \pm 0.01
5.7	17.5 \pm 1.6	0.09 \pm 0.01
8.6	28.7 \pm 0.5	0.22 \pm < 0.01 ^a
bTAT-tagged PLGA NPs		
4.5	84.2 \pm 0.3	0.35 \pm < 0.01 ^b

3.4.4 Characterization of Au-labelled CPP-tagged PLGA nanoparticles

CPP-tagged PLGA nanoparticles were labelled with gold nanoparticles (AuNPs) to facilitate subsequent structural analysis using TEM and SAXS. The spherical AuNPs had a nominal diameter of 4.7 nm and had a zeta potential of -6.5 mV due to the surface decoration with PEG groups. The Au-labelled CPP-tagged PLGA nanoparticles were produced using each of the different conjugation approaches previously described. The addition of AuNPs to CPP-tagged PLGA nanoparticles did not change the average size (Table 3.2) as it remained between 140-180 nm, which was comparable with the size range of the Au label-free CPP-tagged PLGA nanoparticles prepared using post-microfluidics and *in situ* microfluidics conjugation approach (Figure 3.4 and Chapter 2, Figure 2.12). The addition of AuNPs to CPP-tagged PLGA nanoparticles prepared using the post-microfluidics and the *in situ* microfluidics conjugation

approach resulted in an increase in polydispersity, which might be related to the presence of free AuNPs. The zeta potential of the CPP-tagged PLGA nanoparticles was, however, influenced by the addition of AuNPs and resulted in a negative surface charge between -12 and 0 mV (Table 3.1 and Table 3.2) indicating electrostatic interactions between the positively charged CPPs and the negatively charged AuNPs. Using the *in situ* microfluidics conjugation approach, the surface charge of the Au-labelled CPP-tagged PLGA nanoparticles was less negative due to the encapsulation of the AuNPs within the polymeric nanoparticles, which cannot contribute to the overall surface charge.

Table 3.2. Characterization of Au-labelled CPP-tagged PLGA nanoparticles used for transmission electron microscopy and small angle X-ray scattering analysis prepared using the *in situ* microfluidics or post-microfluidics conjugation approach (Streck *et al.*, 2019b). Data are means \pm SD ($n = 3$). * $p < 0.05$ in comparison to bTAT-tagged PLGA NPs prepared with the *in situ* microfluidics conjugation approach.

Sample	Size \pm SD (nm)	PDI	Zeta potential \pm SD (mV)
<i>In situ</i> microfluidics conjugation approach for Au-labelled nanoformulations			
RRH-tagged PLGA NPs (75 mM)	140.6 \pm 18.4	0.235 \pm 0.034	0.2 \pm 4.4
TAT-tagged PLGA NPs (8.6 mM)	168.1 \pm 14.3	0.224 \pm 0.039	-2.4 \pm 3.7
bTAT-tagged PLGA NPs (4.5 mM)	142.4 \pm 2.9	0.190 \pm 0.043	-0.2 \pm 6.3
Post-microfluidics conjugation approach for Au-labelled nanoformulations			
RRH-tagged PLGA NPs (50 mM)	163.9 \pm 3.2	0.225 \pm 0.060	-12.3 \pm 7.6
TAT-tagged PLGA NPs (8.6 mM)	180.7 \pm 19.6	0.187 \pm 0.067	-5.2 \pm 0.3
bTAT-tagged PLGA NPs (4.5 mM)	156.9 \pm 6.1*	0.162 \pm 0.038	-4.6 \pm 7.0

3.4.5 TEM micrographs show the distribution of CPP on PLGA nanoparticles

Visualisation of Au-labelled CPP-tagged PLGA nanoparticles prepared with both conjugation approaches showed individual nanoparticles with a regular spherical shape and a smooth surface of the CPP-tagged PLGA nanoparticles independent of the conjugation approach, (Figure 3.5 and Figure 3.7). The AuNPs were attached to the RRH-tagged PLGA nanoparticles prepared using the post-microfluidics and *in situ* microfluidics conjugation approach (Figure 3.5). The observed size of the polymeric nanoparticles after preparation on the TEM grids was smaller compared to DLS, which is related to the shrinkage of the polymer during the drying step during sample preparation (Luque-Michel *et al.*, 2016).

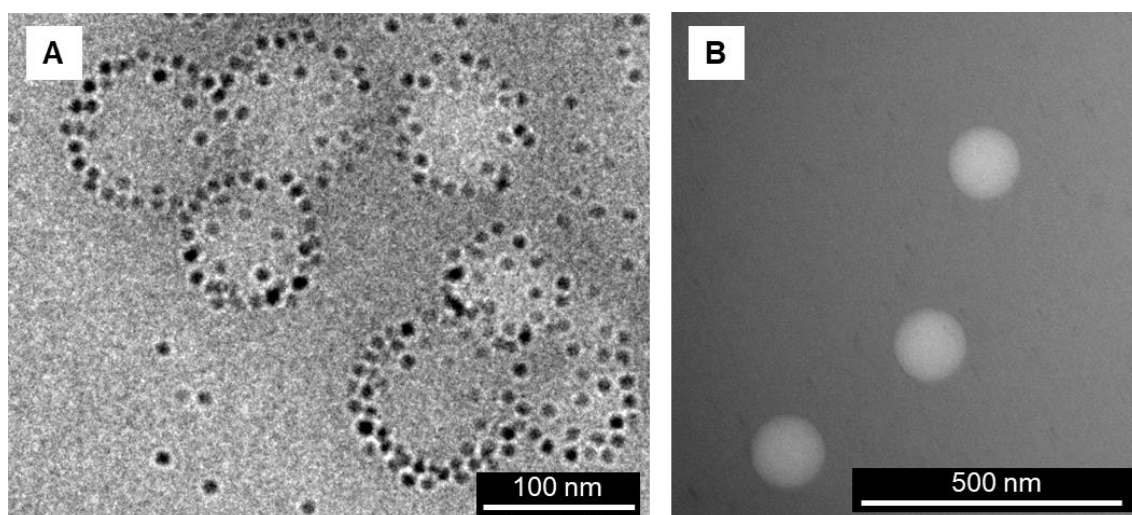


Figure 3.5. Representative micrographs of Au-labelled RRH-tagged PLGA nanoparticles prepared using the post-microfluidics (A) and the *in situ* microfluidics conjugation approach (B) (Streck *et al.*, 2019b).

The AuNPs formed mono- and/or bi-layers around the RRH-tagged PLGA nanoparticles (Figure 3.5A) suggesting an interaction of the negatively charged AuNPs with the positively charged RRH on the PLGA nanoparticle surface. Further, the RRH-tagged PLGA nanoparticles showed a surface saturation with AuNPs (Figure 3.5A). It was also

possible to observe an apparent depletion zone around the Au-labelled RRH-tagged PLGA nanoparticles with free AuNPs also being observed (Figure 3.6A). The interaction between the CPPs and AuNPs, as well as the behaviour of free AuNPs, is dependent on the surface charge of the respective particles. The negatively charged AuNPs can electrostatically bind to the positive charges within the CPP sequence. RRH contains positively charged guanidinium groups and here, the guanidinium groups are likely to act as binding sites for AuNPs. An evenly spaced arrangement of free AuNPs was observed here, where the nanoparticles adopted a hexagonal lattice pattern (Figure 3.6, Insert 1) with an average distance of 27.6 ± 4.0 nm ($n = 100$, number of free AuNPs) between the AuNPs. The free AuNPs are expected to repel each other because of their negative charge and the resulting electrostatic forces between the individual AuNPs. Interestingly, it was observed that the average distance between AuNPs was significantly shorter when associated with the RRH-tagged PLGA nanoparticles (Figure 3.6, Insert 2) compared to the distance between free AuNPs. The average distance between AuNPs surface-bound to RRH-tagged PLGA nanoparticles was 12.1 ± 2.5 nm ($n = 6$, number of Au-labelled RRH-tagged PLGA nanoparticles). The shorter distance can be explained by a reduction of electrostatic forces between AuNPs due to the binding to RRH.

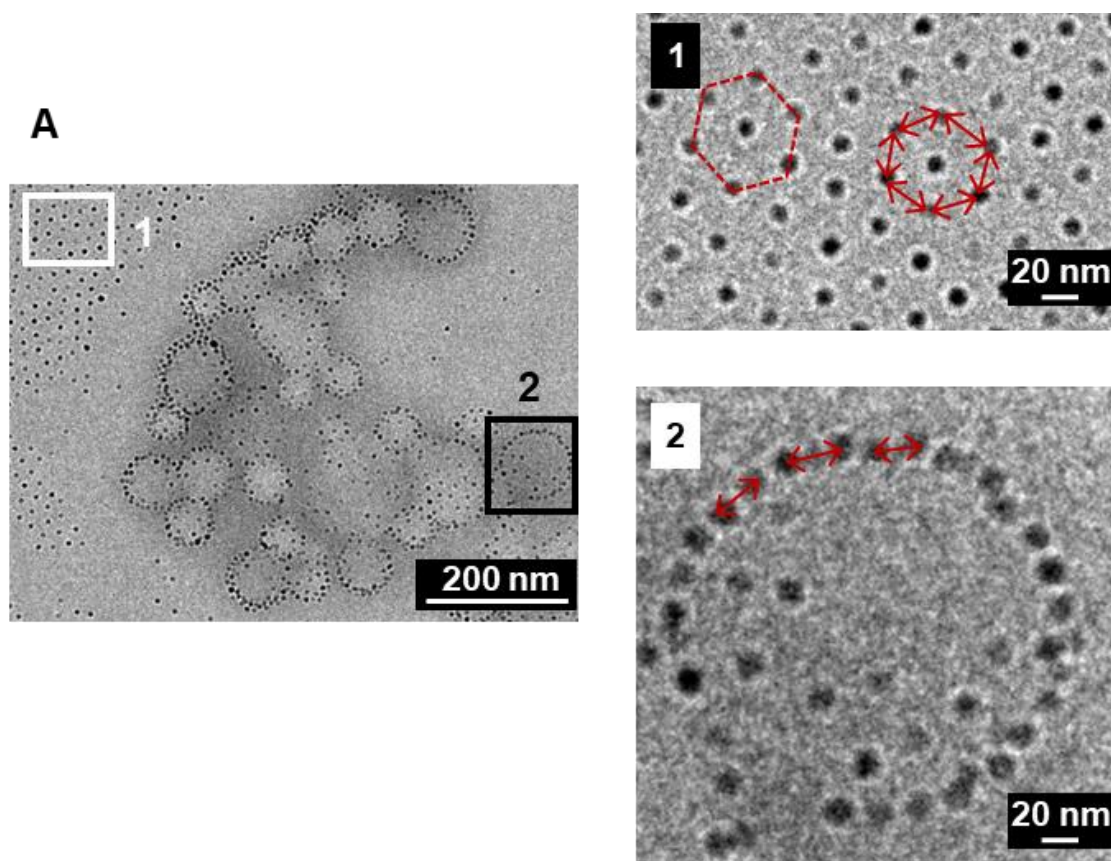


Figure 3.6. Transmission electron micrograph of Au-labelled RRH-tagged PLGA nanoparticles (A) and inserts of free individual AuNPs (1) and a RRH-tagged PLGA nanoparticle with surface-bound AuNPs (2). The hexagonal formation of the AuNPs is indicated by the red dashed line and the red arrows indicate how the distance between AuNPs was measured (Streck *et al.*, 2019b).

Au-labelled TAT-tagged PLGA nanoparticles prepared using the post-microfluidics conjugation approach showed an arrangement of AuNPs around individual TAT-tagged PLGA nanoparticles (Figure 3.7A). The AuNPs did not cover the surface completely and showed a space between individual AuNPs, which might be due to steric hindrance introduced by the longer TAT sequence compared to the short CPP sequence of RRH. Further, in Chapter 2 (Section 2.4.8) the available binding sites for CPPs on a PLGA nanoparticle were estimated to be 16000 and it is possible that not all binding sites were occupied by TAT and therefore, no complete surface saturation with AuNPs was observed. A similar observation was made for

Au-labelled bTAT-tagged PLGA nanoparticles, were the AuNPs arrange around bTAT-tagged PLGA nanoparticles with a regular distance between each other (Figure 3.7C).

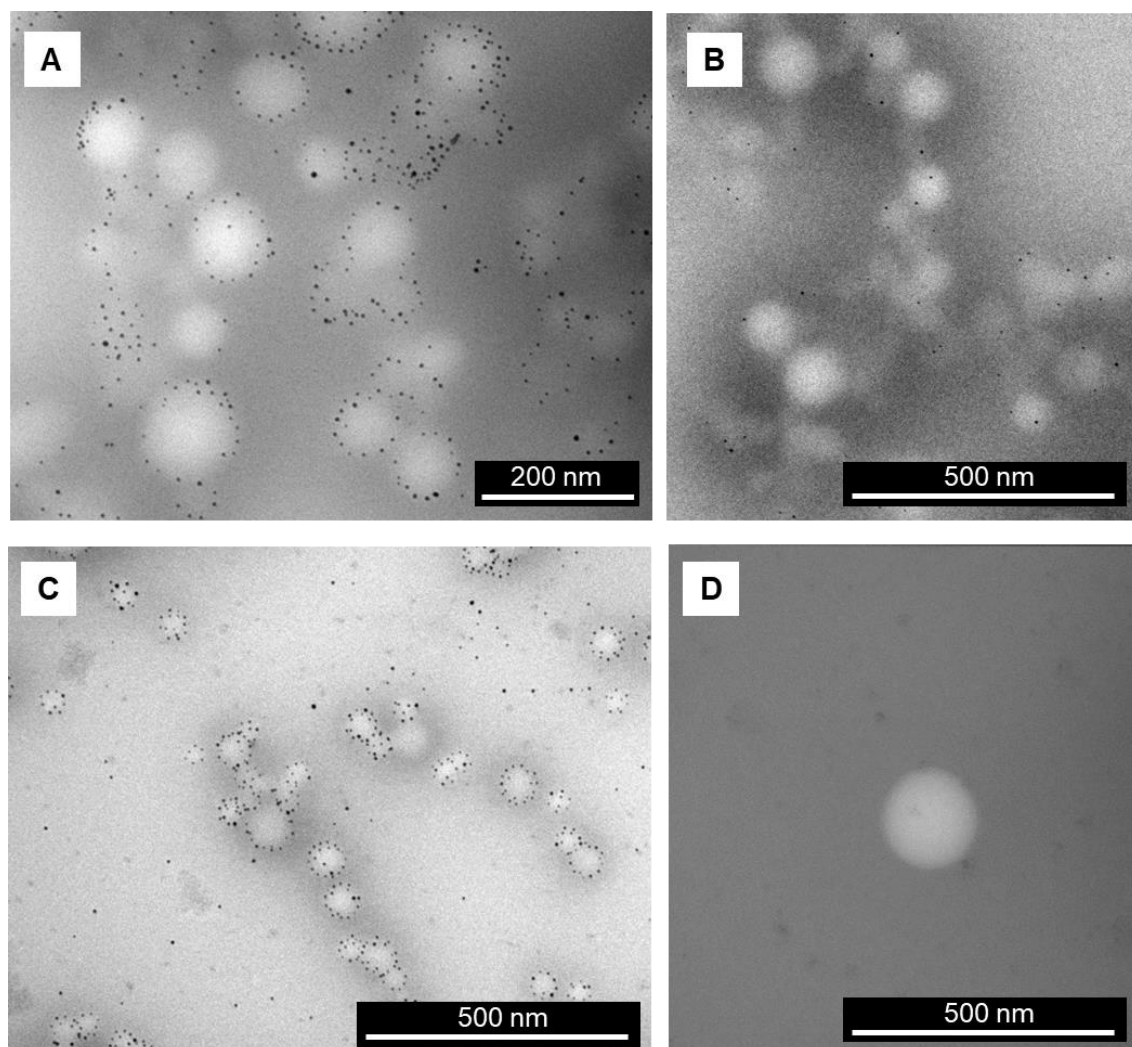


Figure 3.7. Representative micrographs of Au-labelled TAT- and bTAT-tagged PLGA nanoparticles prepared using the post-microfluidics (A, C) and the *in situ* microfluidics conjugation approach (B, D).

The TEM micrographs obtained for Au-labelled CPP-tagged PLGA nanoparticles prepared using the *in situ* microfluidics conjugation approach did not give conclusive results about the AuNPs distribution and therefore, the CPP distribution (Figure 3.5B and Figure 3.7B and D). In comparison to the Au-labelled CPP-tagged PLGA nanoparticles prepared using the post-microfluidics conjugation approach, fewer AuNPs were observed in using TEM for the

Au-labelled CPP-tagged PLGA nanoparticles prepared with the *in situ* microfluidics conjugation approach and individual AuNPs seemed to generate less contrast and appeared grey in the TEM micrographs making the imaging more difficult to interpret.

Since the aim of this study was to investigate the distribution of the CPPs on the PLGA nanoparticles another technique, namely SAXS, was used to examine how the CPPs were distributed after preparation of Au-labelled CPP-tagged PLGA nanoparticles using the post-microfluidics and the *in situ* microfluidics conjugation approach.

3.4.6 Investigation of CPP distribution on PLGA nanoparticles using SAXS

The distribution of CPPs conjugated to PLGA nanoparticles prepared using the two different conjugation approaches was investigated using SAXS. The SAXS profiles were obtained by radial integration of 2D scattering patterns into plots of the scattered X-ray intensity $I(q)$ versus the scattering vector q . The scattering profiles of the three different Au-labelled CPP-tagged PLGA nanoparticles prepared using either the post-microfluidics or the *in situ* microfluidics conjugation approach are presented in Figure 3.8. A suspension of AuNPs alone was used as a reference to determine the SAXS scattering pattern of the label used in this study (Appendix V and black data points in Figure 3.8A-F). The manufacturer's specifications for the AuNPs provided an average particle diameter of 4.7 ± 0.8 nm. The high q portion of the scattering profile for the AuNPs above $q = 0.10 \text{ \AA}^{-1}$ could be fitted with the sphere form factor for a sphere with a radius of 2.2 nm and a polydispersity of 0.17 (Polydispersity = $\frac{\text{Standard deviation}}{\text{Mean}}$) and was therefore consistent with the information supplied by the manufacturer. However, the model did not account for some additional low q scattering intensity observed and this is suggestive of the presence of a small fraction of larger

AuNPs. The full scattering profile was fitted by incorporating a second sphere form factor into the fitting model with a radius of 4.4 nm and a modelled volume fraction an order of magnitude lower than the AuNPs fitted with a sphere radius of 2.2 nm (Appendix V). This suggested that the commercially obtained AuNPs contained a subpopulation of around 1% of AuNPs with diameters of 8.8 ± 1.5 nm in addition to those of the specified diameter of 4.4 ± 0.7 nm, consistent with the manufacturer's specifications.

The flat-plateau (Guinier region) below $q = 0.02 \text{ \AA}^{-1}$ revealed that there were no structure factor perturbations to the form factor and indicated that the AuNPs were at a sufficiently low concentration in the dispersion not to be interacting with one another. In addition, the scattering profiles of CPP-tagged PLGA nanoparticles prepared using the post-microfluidics conjugation approach were obtained as a reference for both conjugation approaches since a similar size was measured with DLS. These references account for the scattering caused by the Au-label free CPP-tagged PLGA nanoparticles themselves. Given the large average diameter of the PLGA nanoparticles (> 150 nm), the Guinier plateau at low q was not observable within the measurable q -range of the instrument. The lowest observable q value of 0.0026 \AA^{-1} gave a maximum observable particle radius of $\sim 500 \text{ \AA}$ ($\sqrt{5/3} \times 1/q_{\min}$) and thereby a maximum observable diameter of ~ 100 nm. However, scattering intensity indicated scattering length density (SLD) contrast between the nanoparticles and the dispersant and surface (Porod) scattering from the PLGA nanoparticles was observed at higher q that reached the incoherent background intensity at $q \approx 0.02 \text{ \AA}^{-1}$ (Figure 3.8, red data points).

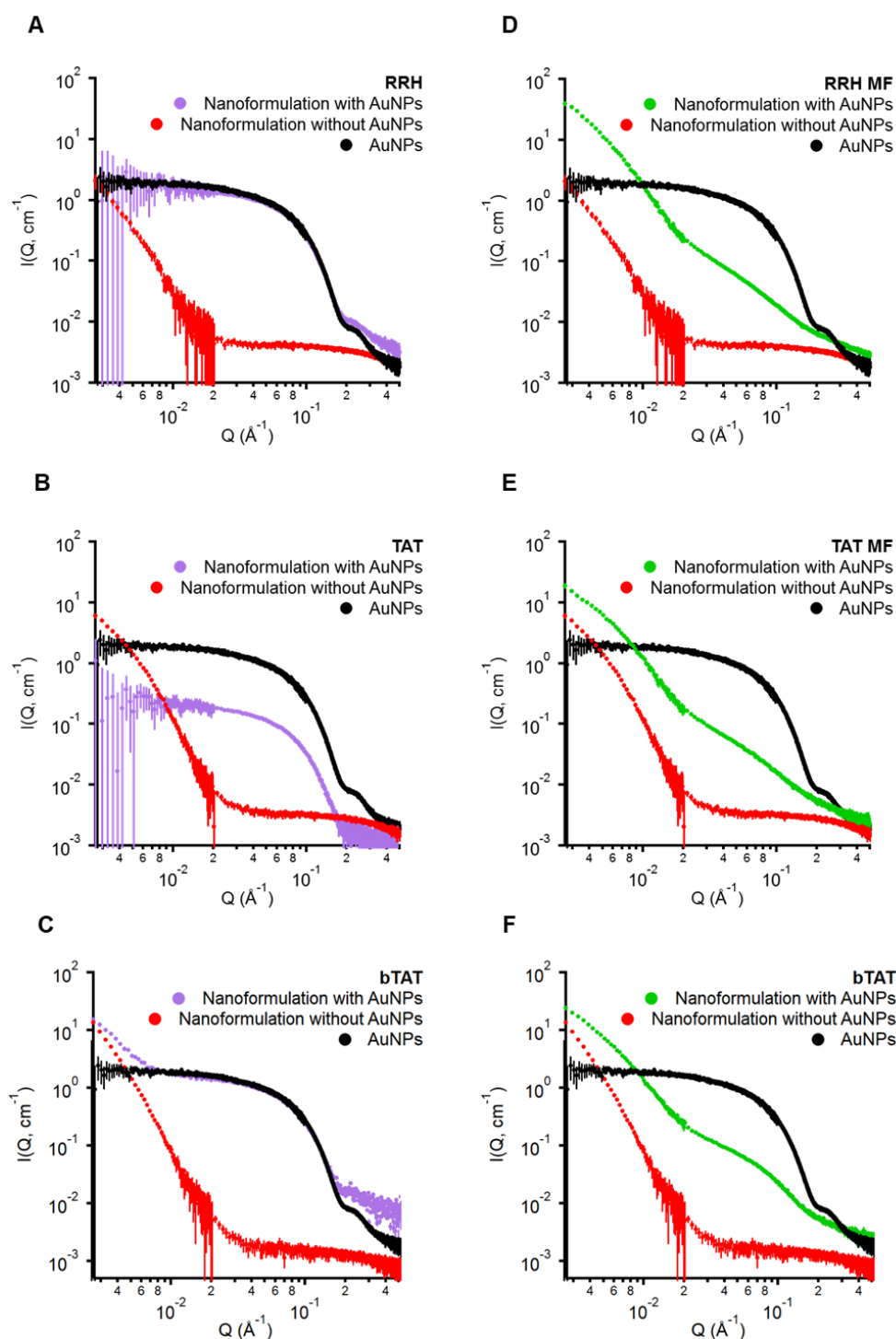


Figure 3.8. Small angle X-ray scattering profiles of AuNPs (black data points) and PLGA nanoparticles tagged with CPPs of different architectures (RRH, TAT and bTAT) (red data points). Panels A-C show Au-labelled CPP-tagged PLGA nanoparticles prepared with the post-microfluidics conjugation approach (purple data points) and panels D-F were produced using the *in situ* microfluidics conjugation approach (green data points) (Streck *et al.*, 2019b). AuNPs = gold nanoparticles and MF = microfluidics.

The Au-labelled CPP-tagged PLGA nanoparticles prepared using the post-microfluidics conjugation approach had scattering profiles that showed features from the scattering profiles of the label-free CPP-tagged PLGA nanoparticles and the scattering profile of the AuNPs. Examining the Au-labelled CPP-tagged PLGA nanoparticles that were tagged *in situ* in the microfluidic channel, a low q scattering feature was observed (Figure 3.8D-F). The scattering feature at low q was consistent with the scattering of the larger PLGA nanoparticles alongside a high q shoulder commensurate with the presence of a lower concentration of AuNPs than that used in the post-microfluidics conjugation approach. The shape of the low q scattering feature of the Au-labelled CPP-tagged PLGA nanoparticles prepared with the *in situ* microfluidics conjugation approach was similar to the scattering profile of the label-free CPP-tagged PLGA nanoparticles in the cases of RRH and TAT, indicating PLGA nanoparticles with a similar size. The corresponding feature for the bTAT-tagged PLGA nanoparticles prepared with the *in situ* microfluidics conjugation approach was broader, extending to higher q scattering intensity than the corresponding nanoparticles not labelled with AuNPs. This indicated that the Au-labelled bTAT-tagged PLGA particles were, in fact, smaller than their unlabelled counterparts. The diameters of the Au-labelled CPP-tagged PLGA nanoparticles prepared using the *in situ* microfluidics conjugation approach measured by DLS were between 142 and 168 nm and similar to the label-free CPP-tagged PLGA nanoparticles (Table 3.2, Figure 3.4 and Chapter 2, Figure 2.10). The primary difference between unmodified and CPP-tagged PLGA nanoparticles in the low q scattering feature was that for each CPP-tagged PLGA nanoparticle formulation there was an increase in the absolute scattering intensity by up to an order of magnitude when CPPs were pre-conjugated to AuNPs and incorporated into the polymerization mixture inside the microfluidic channel. In contrast to the PLGA nanoparticles, the AuNPs are strong X-ray scatterers with higher SLDs because they have a greater electron density than the aqueous dispersant (Clara-Rahola *et al.*, 2018). These observations led to the conclusion that

the strongly scattering AuNPs were incorporated uniformly throughout the CPP-tagged PLGA nanoparticles when the *in situ* microfluidics conjugation approach was used. With the incorporation of the AuNPs, the SLD contrast of the CPP-tagged PLGA nanoparticles increased without significantly changing their size as observed by the similar shapes and positions of the scattering profiles. Similar binding behaviour has been shown previously for superparamagnetic iron oxide nanoparticles inside PLGA nanoparticles (Wassel *et al.*, 2007).

The scattering profiles obtained from the Au-labelled CPP-tagged PLGA nanoparticles prepared with the post-microfluidics conjugation approach (Figure 3.8A-C) were somewhat different to scattering profiles obtained with the *in situ* microfluidics conjugation approach, containing primarily the features of the AuNPs alone. It is likely that the absence of prominent features from the PLGA nanoparticles at low q was obscured by the strong scattering from the AuNPs in this region. For all three Au-labelled CPP-tagged PLGA nanoparticles, the scattering from the native PLGA nanoparticles was weaker than the scattering of the AuNPs at most observable q values. It is also possible that binding of AuNPs to the surface of the PLGA nanoparticles, as observed by TEM (Figure 3.5A and Figure 3.7A and C), led to a measurable increase in the overall size of the PLGA nanoparticles, which would push the scattering feature to lower q values and outside of the observable range of the instrument. However, a significant increase in the scattering intensity from the PLGA nanoparticles was not observed when AuNPs were bound to CPP-tagged PLGA nanoparticles after the post-microfluidics conjugation approach and this supports the hypothesis that the post-microfluidics conjugation approach did not lead to the conjugation of the PLGA polymer with CPPs inside the nanoparticles. The only case where scattering from the CPP-tagged PLGA nanoparticles was observed with the post-microfluidics conjugation approach was in the case of bTAT-tagged PLGA nanoparticles and in this case, the measured scattering intensity was the same as the sum of the scattering observed

from bTAT conjugated PLGA nanoparticles and the AuNPs used to label them (Figure 3.8C). As such, the location of any binding of the AuNPs by the CPPs could not be deduced directly from the SAXS data for the Au-labelled CPP-tagged PLGA nanoparticles prepared with the post-microfluidics conjugation approach. Any feature that represents a polymer core and AuNPs-shell arrangement, which would typically appear as a side-maximum at higher q values, were obscured by the strong scattering from the AuNPs. Lastly, it should be noted that SAXS experiments were performed using a bulk nanoparticle suspension and therefore the obtained data displays an average of the CPP distribution in the nanoparticle population.

3.4.7 Structural distribution of CPPs

A model is proposed for the selective conjugation of CPPs to PLGA nanoparticles using different microfluidic approaches. Based on the SAXS, DLS and TEM data the distribution of the CPPs depends on the conjugation approach. The AuNPs were electrostatically bound to the positively charged CPPs and acted as a label to increase the scattering intensity of the PLGA nanoparticles. TEM micrographs for the post-microfluidics conjugation approach indicated a core-shell like arrangement of the AuNPs around the PLGA nanoparticles. Using the post-microfluidics conjugation approach the CPPs were apparently initially conjugated to the available carboxyl groups on the surface of the PLGA nanoparticles (Figure 3.9A). A potential movement of the CPPs towards the inside of the nanoparticles due to pores in the polymer matrix could not be observed with SAXS as the scattering contrast of the CPPs on their own is very low. The presence of pores in PLGA nanoparticles is not clearly stated in the literature and a porous structure is mainly reported for larger PLGA microparticles prepared using a double emulsion solvent evaporation technique in the presence of ammonium bicarbonate (Chen *et al.*, 2019b). Even if pores are present in the PLGA nanoparticles, it is possible that

the AuNPs (with a size of approximately 4.4 nm) could not penetrate through those pores into the internal space of the nanoparticles.

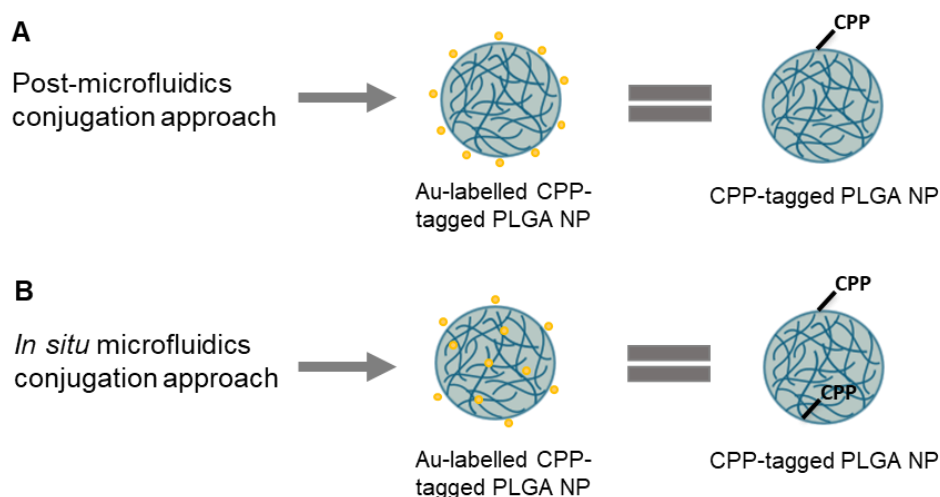


Figure 3.9. Schematic overview of proposed CPP distribution of Au-labelled CPP-tagged PLGA nanoparticles and the corresponding distribution of label-free CPP-tagged PLGA nanoparticles prepared using a post-microfluidics conjugation (A) or an *in situ* microfluidics conjugation (B) approach (Streck *et al.*, 2019b). NP = nanoparticle.

The scattering curves of the Au-labelled CPP-tagged PLGA nanoparticles prepared with the *in situ* microfluidics conjugation approach showed an enhanced scattering contrast between the nanoparticles and the dispersant and thereby a distribution of the strongly scattering Au-labelled CPPs throughout the polymeric PLGA nanoparticles (Figure 3.9B). When using the *in situ* microfluidics conjugation approach, the PLGA polymer was activated prior to the formulation of the nanoparticles and AuNPs/CPPs could bind to the PLGA polymer during the polymer matrix formation, both being encapsulated inside the PLGA nanoparticles and present on their surfaces (Figure 3.9B). To further elucidate the dynamic distribution of CPPs during nanoparticle formation, future work could incorporate microfluidics coupled with SANS to study *in situ* scattering of soft matters over time (Adamo *et al.*, 2018).

3.5 Conclusion

The CPP-tagged PLGA nanoparticles prepared using the *in situ* microfluidics approach showed an influence of the CPP architecture on the physicochemical characteristics, in particular, the tuneability of the surface charge. The amount of CPP tagged to PLGA nanoparticles was concentration dependent and increased with higher concentrations of CPPs added. Further, the distribution of ligands on and within nanoparticles is critical to their utilization *in vivo* but is not often understood. Here, PLGA nanoparticles were tagged with variants of the cationic CPP, TAT, known to enhance cell uptake (Trehin *et al.*, 2004) and prepared using different microfluidics-based conjugation approaches to probe the impact of architecture and preparation method on the structure of the resulting nanoparticles. TAT has been previously conjugated to polymer nanoparticles (Vasconcelos *et al.*, 2015; Zhu *et al.*, 2016a), but the distribution of the ligand on and within the particles was not explored, nor was their preparation by microfluidic techniques. In the present study, for the first time, the utilization of microfluidics to produce CPP-tagged PLGA nanoparticles has been demonstrated. It has also been shown that the distribution of the CPPs within the nanoparticle delivery system was influenced by the preparation method. CPPs were distributed throughout the PLGA nanoparticles when prepared using the *in situ* microfluidics conjugation approach. In contrast, for CPP-tagged PLGA nanoparticles prepared using post-microfluidics conjugation, the results were consistent with the CPPs being distributed on the surface of the nanoparticles. This finding has important implications for the use of such nanoparticles, where the density of CPPs on the surface is important in dictating biological interactions or alternatively when using an ion pairing strategy to localize labile drugs to the inside of the nanoparticles. Future studies exploring the impact of the nanoparticle preparation method on interactions with cells will test this implication.

Chapter Four

Interaction of cell-penetrating peptide modified polymeric nanoparticles with
cells

4.1 Introduction

Interactions of nanoparticles with cell membranes are widely investigated, but still not completely understood. Different cell lines such as HeLa and Caco-2 cells have been utilized as *in vitro* cell culture models to study nanoparticle-cell interactions and cellular uptake of nanoparticles (Czuba *et al.*, 2018; Morimoto *et al.*, 2016; Nam *et al.*, 2002; Sheng *et al.*, 2015). The human cervical cancer cell line HeLa cells is a well-established cell line for uptake studies of CPPs (Masters, 2002; Ramaker *et al.*, 2018), whereas Caco-2 cells are used as a cell culture model for the intestinal epithelium (Hidalgo *et al.*, 1989). In this Chapter, the focus is on the influences of surface modification of polymeric nanoparticles on nanoparticle-cell interactions in different *in vitro* cell culture models.

4.1.1 *Interactions of nanoparticles at the nano-bio interface*

The nano-bio interface is described as the space between nanomaterials and biological systems, and processes occurring at the nano-bio interface determine the uptake of nanoparticles (Nel *et al.*, 2009; Shang and Nienhaus, 2013). Dynamic interactions at the nano-bio interface include both long- and short-range forces (Nel *et al.*, 2009; Shang and Nienhaus, 2013). Long-range forces include van der Waals and repulsive electrostatic interactions with the cell membrane, whereas short-range forces arise from surface charges or combine steric, depletion and solvent interactions (Nel *et al.*, 2009; Shang and Nienhaus, 2013). These forces influence the formation of a protein corona around nanoparticles, determine cellular contact and subsequent endocytosis and intracellular transport (Shang and Nienhaus, 2013). A protein corona is formed around positively and negatively charged nanoparticles when they enter biological fluids, with albumin being the main protein component (Fleischer and Payne, 2014; Nel *et al.*, 2009). Adherence to the cell membrane involves either specific or non-specific

binding and CPPs are an example of surface modifications that can induce non-specific binding to cells (Nel *et al.*, 2009). Other factors that influence interactions at the nano-bio interface are hydrophobicity of the nanoparticles, the surface roughness of the cells and size and shape of the nanoparticles (Nel *et al.*, 2009). To better understand the time frame for particles to arrive at the nano-bio interface and their distribution within *in vitro* and *in vivo* systems, mathematical modelling is used to predict the kinetic behaviour of particles (Li *et al.*, 2012; Thomas *et al.*, 2018).

Kinetic studies of particle distribution can be either used for understanding the fate of nanoparticles in the human body (Li *et al.*, 2010) or to estimate the delivered dose to the cell in an *in vitro* cell culture (Ahmad Khanbeigi *et al.*, 2012). The former is used for the evaluation of nanoparticles in the relevant compartments of the ADME (Absorption, Distribution, Metabolism and Excretion) system after administered to the human body (Li *et al.*, 2017). The latter is used for the improvement of *in vitro* cell culture systems and will be discussed further. The biological response of a system to an administered drug is dose dependent and particokinetics is used as a computational tool to estimate the behaviour of nanoparticles in *in vitro* cell culture systems (Price *et al.*, 2019). Knowledge of the delivered dose is important as there is a great difference between the administered amount and the amount of nanoparticles that reached the cell surface (Faria *et al.*, 2019). Ahmad Khanbeigi *et al.* (2012) reported that only 0.03-0.33% of the administered dose of polystyrene microspheres reached the cell surface of macrophages *in vitro* and the findings were supported by particokinetic estimations.

The biological effects between nanoparticles and the cell membrane occur primarily via interactions of the nanoparticles with the cell components (Thomas *et al.*, 2018). In *in vitro*

cell culture media or buffer, particles can sediment, diffuse and agglomerate according to their physicochemical characteristics including size, charge and density (Hinderliter *et al.*, 2010). Hinderliter *et al.* (2010) used a computational model called the ISDD model (*In vitro* Sedimentation, Diffusion and Dosimetry model) to describe the dynamics of particles in liquids. The model can be used for the estimation of the amount of nanoparticles reaching the cell surface, but a weakness of the ISDD model is that it does not describe changes in size during degradation of the nanoparticles in the physiological environment (Hinderliter *et al.*, 2010; Thomas *et al.*, 2018). The ISD3 model (*In vitro* Sedimentation, Diffusion, Dissolution, and Dosimetry model) developed by Thomas *et al.* (2018) includes dissolution and was tested with silver nanoparticles as model nanoparticles in buffer with 10% fetal bovine serum and macrophages as model cells. Theoretically, the concept of the ISD3 model can also be applied to polymeric nanoparticles in *in vitro* cell culture system. During incubation, the polymeric nanoparticles diffuse and sediment towards the cell surface. At the same time, dissolution of the polymer is occurring and subsequent drug release is triggered by interactions with the cell culture media before and whilst the polymeric nanoparticles reach and interact with the cell surface (Figure 4.1).

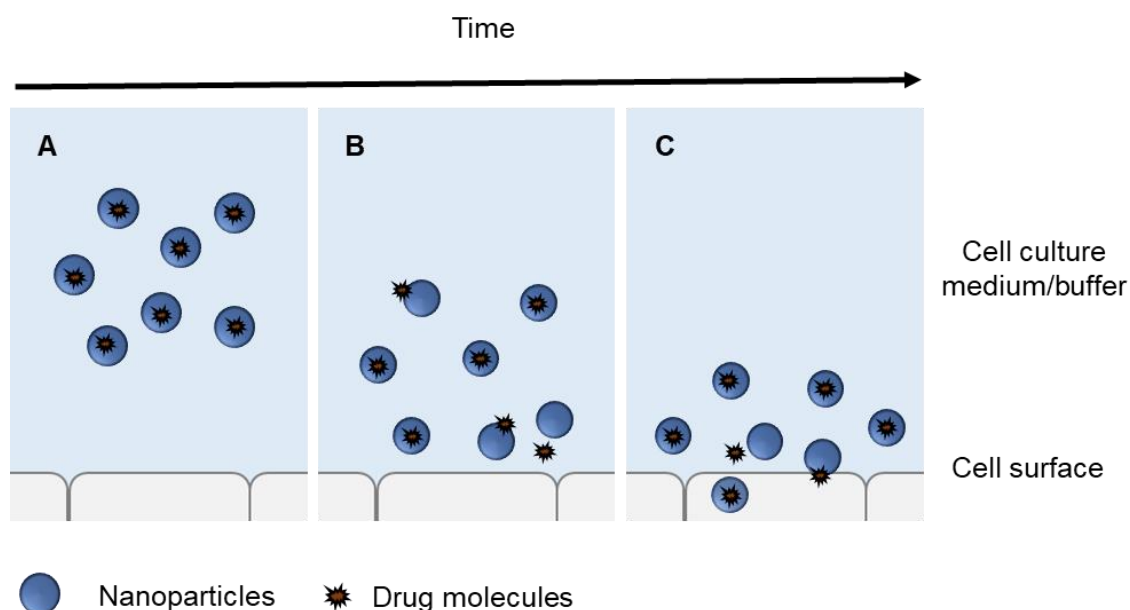


Figure 4.1. Schematic representation of the *in vitro* Sedimentation, Diffusion, Dissolution, and Dosimetry model applied to polymeric nanoparticles including the sedimentation and diffusion of the drug-loaded polymeric nanoparticles (A), the dissolution of the polymer and drug release (B) and the interaction/uptake of drug/nanoparticles at the cell surface (C) (Thomas *et al.*, 2018).

In addition to the delivered dose, the association of nanoparticles with cells can be included in mathematical modelling (Faria *et al.*, 2019). There are a number of different assumptions about nanoparticle-cell interactions that should be incorporated into these mathematical models. These include assuming that all nanoparticles reach the cells and interact with the cells, cell association of nanoparticles is directly proportional to their concentration, cell association is directly proportional to concentration of nanoparticles at cell surface until saturation is reached, and cell association with nanoparticles occurs until association capacity is achieved (Faria *et al.*, 2019). Based on these assumptions Faria *et al.* (2019) proposed a dosimetric-kinetic model for nanoparticle-cell interactions and showed a good fit between theoretical and experimental data when the assumption of saturation of cells with nanoparticles was considered for the kinetic behaviour of the nanoparticles. Using a dosimetric-kinetic model the comparison of data between cell lines is possible and it was found that the choice of cell

line mainly influences the cell-association rate of nanoparticles rather than nanoparticle size (Faria *et al.*, 2019).

4.1.2 *The intestinal epithelium as a barrier for nanoparticle uptake*

Specialized epithelial cells, such as the intestinal epithelium, separates the internal contents of the human body from the environment in the lumen of the gut (Peterson and Artis, 2014). Epithelial cells are highly polarized cells with an apical and basolateral side and the cells are connected to each other by tight junctions to increase tissue integrity and for protection from ingested pathogens (Cartiera *et al.*, 2009). The intestinal epithelium consists of different cell types including absorptive enterocytes, mucus-producing goblet cells and M cells as part of Peyer-patches that have been reported to play a crucial role in the uptake of polymeric nanoparticles through the epithelium (Beduneau *et al.*, 2014; Boegh *et al.*, 2014; Caldorera-Moore *et al.*, 2019; Rieux *et al.*, 2005; Tariq *et al.*, 2015). Caco-2 cells are well-established as an *in vitro* cell culture model for the human intestinal epithelium since this human cancer adenocarcinoma cell line has similarities with normal intestinal cells (Gaumet *et al.*, 2009). Hidalgo *et al.* (1989) reported morphological changes and endocytic differentiation of Caco-2 cells cultured in permeable filter inserts in *in vitro* cultures after 16 days. Caco-2 cell monolayers are morphologically similar to the columnar epithelium found in the small intestine and show the formation of domes, which are described as aggregations of transporting and polarized epithelial cells (Hidalgo *et al.*, 1989). Further, tight junctions are expressed and localized between cells in the Caco-2 cell monolayer, and metabolic enzymes like phosphatase and sucrase-isomaltase are produced at bio-relevant levels (Birch *et al.*, 2018a; Pinto *et al.*, 1983). A reason for Caco-2 cells being a popular *in vitro* cell culture model includes the

simplicity of the system and culturing of the cell line in a reproducible and rapid way (Beduneau *et al.*, 2014; Lea, 2015).

Despite the properties of Caco-2 cells that promote their suitability as an intestinal epithelium cell model, there are some limitations to the use of Caco-2 cells. Variations in characteristics of Caco-2 cells occur with increasing passage numbers, due to the expression of differentiation markers, increase in transepithelial electrical resistance (TEER) and proliferation rate (Lea, 2015). Therefore, making a direct comparison of Caco-2 cell results obtained with earlier or later passage numbers between laboratories is difficult (Lea, 2015). The main limitation of Caco-2 cells as a model for the intestinal epithelium is the differentiation into one particular cell type, namely enterocytes, and the absence of a mucus layer on top the cells (Beduneau *et al.*, 2014; Birch *et al.*, 2018a). Mucus mainly consists of water (95%) but other components including mucin, proteins and lipids (Boegh *et al.*, 2013) are responsible for the intestinal mucus being a rate-limiting step for the absorption of nanoparticles after oral delivery (Boegh *et al.*, 2014). In particular, mucin, which consists of glycosylated polymeric proteins that form a mesh on top of epithelial cells, represents a significant barrier for the uptake of nanoparticles across the epithelial lining. *In vitro* co-culture of Caco-2 cells with HT-29 cells (Beduneau *et al.*, 2014) or the addition of biosimilar mucus on the Caco-2 cell monolayer (Birch *et al.*, 2018a) are strategies to overcome the limitation of the Caco-2 cell culture model lacking mucus. The co-culture of Caco-2 and HT-29 cells combines absorptive enterocyte-like cells and mucus-secreting cells to mimic the intestinal epithelium (Fan *et al.*, 2014). Intestinal mucus is a steric barrier for the interaction and uptake of compounds like small molecules, lipophilic drugs, biomacromolecules and nanoparticles by the epithelium (Birch *et al.*, 2018a; Boegh *et al.*, 2014). Biosimilar mucus has similar rheological properties compared to mucus originating

from pig and can be used on Caco-2 cell monolayers or alone for the evaluation of particle movement and mucoadhesive formulations (Birch *et al.*, 2018a; Boegh *et al.*, 2014).

Polymeric nanoparticles can be used as a controlled release drug delivery system to enhance oral absorption and protect the encapsulated drug against degradation in the GIT (Gaumet *et al.*, 2009). However, to achieve high drug absorption, the designed drug delivery system requires a controlled burst release of the drug at the surface of the epithelium and constant drug release while the nanoparticles are in close proximity to the cell surface. It has been suggested that nanoparticles intended for oral drug delivery need to be (i) resistant to the GIT environment and (ii) penetrate mucus to localize at the cell surface (Du *et al.*, 2018; He *et al.*, 2013).

The uptake mechanisms proposed for nanoparticles include endocytosis via clathrin-dependent and caveolae-dependent pathways, and macropinocytosis (Dausend *et al.*, 2008). The types of endocytic pathways were described in Chapter 1. The uptake of PLGA nanoparticles into Caco-2 cells is reported to occur in a concentration- and time-dependent manner (Alqahtani *et al.*, 2015; Cartiera *et al.*, 2009; He *et al.*, 2013; Tariq *et al.*, 2015). For identification of uptake mechanisms involved in the internalization of nanoparticles, *in vitro* cell experiments can be performed at a lower temperature to distinguish between active and passive uptake or inhibitors can be applied prior to the nanoparticle incubation of cells (Table 4.1). Endocytosis is an energy-dependent uptake pathway and a decrease in temperature to 4°C reduces the ATP synthesis and subsequently inhibits endocytosis due to low ATP levels, which can hinder endocytic uptake pathways (Cartiera *et al.*, 2009; Morimoto *et al.*, 2016). In the literature, a reduction in nanoparticle uptake is reported of up to 50% at 4°C for PLGA, CPP-

modified PLGA and PEG-PLA nanoparticles (Liu *et al.*, 2013; Sheng *et al.*, 2015; Siu *et al.*, 2018; Win and Feng, 2005). These reports show that endocytosis is crucial for the uptake of nanoparticles in *in vitro* cell culture systems. The application of specific endocytosis inhibitors shows that clathrin- and caveolae-dependent endocytosis are the main active uptake mechanisms (He *et al.*, 2013; Siu *et al.*, 2018; Tariq *et al.*, 2015; Xu *et al.*, 2013a). Further, macropinocytosis is also involved in nanoparticle uptake depending on the properties of the nanoparticles, including their size (Elsner *et al.*, 2015; Siu *et al.*, 2018; Zhu *et al.*, 2016b).

Table 4.1. Chemical inhibitors of *in vitro* uptake pathways categorized based on their influence on polymeric nanoparticle internalization. +, ++, and +++ represent low, medium and high influence on nanoparticle internalization.

Inhibitor	Mechanism	Cell line	Influence on nanoparticle uptake	References
Methyl-β-cyclodextrin	Caveolae-dependent endocytosis	HeLa, Caco-2	++ to +++	(He <i>et al.</i> , 2013; Morimoto <i>et al.</i> , 2016; Sheng <i>et al.</i> , 2015)
Filipin	Caveolae-dependent endocytosis	Caco-2	++	(Siu <i>et al.</i> , 2018; Tariq <i>et al.</i> , 2015; Xu <i>et al.</i> , 2013a)
Nystatin	Caveolae-dependent endocytosis	HeLa, Caco-2	+	(He <i>et al.</i> , 2013; Morimoto <i>et al.</i> , 2016)
Genistein	Caveolae-dependent endocytosis	Caco-2	+	(He <i>et al.</i> , 2013)
Phenylarsine oxide	Clathrin-dependent endocytosis	Caco-2	++	(He <i>et al.</i> , 2013)
Sucrose	Clathrin-dependent endocytosis	HeLa, Caco-2	+	(Morimoto <i>et al.</i> , 2016; Siu <i>et al.</i> , 2018)
Chlorpromazine	Clathrin-dependent endocytosis	Caco-2	+ to ++	(Sheng <i>et al.</i> , 2015; Siu <i>et al.</i> , 2018; Tariq <i>et al.</i> , 2015; Xu <i>et al.</i> , 2013a; Zhu <i>et al.</i> , 2016b)
5-N-ethyl-N-isoproamiloride	Macropinocytosis	Caco-2	+ to ++	(He <i>et al.</i> , 2013; Siu <i>et al.</i> , 2018; Zhu <i>et al.</i> , 2016b)
Sodium azide	Active transport	Caco-2	++	(Sheng <i>et al.</i> , 2015; Tariq <i>et al.</i> , 2015)

Uptake of nanoparticles is also influenced by their size and surface chemistry. The size of nanoparticles is crucial for their interactions with and adhesion to cells (Win and Feng, 2005). With the increase in nanoparticle size from 50 to 1000 nm lower amounts of polystyrene nanoparticles, expressed as fluorophore concentration ($\leq 0.05 \mu\text{g}/\mu\text{g}$ protein), were found to be taken up in Caco-2 cells (Banerjee *et al.*, 2016). Using confocal microscopy, PLGA nanoparticles with a size of > 300 nm were found to be located in the cell membrane of Caco-2 cells after 4 h, whereas smaller PLGA nanoparticles with a size of 100 nm were found in the

intracellular space of the cells and in the cell nucleus (Gaumet *et al.*, 2009). Most studies reported in the literature have used PLGA nanoparticles with a size between 100 and 240 nm for uptake studies (Cartiera *et al.*, 2009; Czuba *et al.*, 2018; Guo *et al.*, 2019; Joshi *et al.*, 2016; Tariq *et al.*, 2015). The characteristics of the nanoparticle surface, including surface charge and hydrophilicity, are crucial for interactions of the nanoparticles with cells leading to potential cellular uptake (Gaumet *et al.*, 2009). The uptake of PLGA nanoparticles with a slightly negative surface charge between -9 to -2 mV was reported to be lower in comparison to surface-modified PLGA nanoparticles with CPPs or chitosan and a surface charge above $> +8$ mV (Alqahtani *et al.*, 2015; Czuba *et al.*, 2018; Sheng *et al.*, 2015; Zhu *et al.*, 2016a).

Uptake of nanoparticles is mostly stated qualitatively by fluorescence and confocal images (Alqahtani *et al.*, 2015; Cartiera *et al.*, 2009) and quantitatively by flow cytometry or measurement of drug and fluorophore concentration (Czuba *et al.*, 2018; Guo *et al.*, 2019). Methods for the quantitative measurement of drug or fluorophore concentration include the bicinchoninic acid (BCA) assay, fluorescence and HPLC analysis and results are reported as the concentration of drug in cells after cell lysis (Guo *et al.*, 2019; Sheng *et al.*, 2015; Siu *et al.*, 2018). Flow cytometry is used to analyse fluorescence within individual cells, but results are often reported as the mean fluorescence intensity (Czuba *et al.*, 2018) or as a peak shift (Tariq *et al.*, 2015) making comparison with other studies difficult. In general, biological materials such as cells are prone to show a variation in their response and to ensure comparison between studies, more details of protocols should be shared within the research community. A standardisation as suggested by Faria *et al.* (2018) can aid to overcome the limited comparability of *in vitro* cell culture data. MIRIBEL, minimum information reporting in bio-nano experimental literature, combines information about the material characteristics, biological characteristics and experimental protocol that will promote the four principles of

reusability, quantification, practicality and quality to ensure the comparison of results (Faria *et al.*, 2018).

4.1.3 Chapter aims

The aim of the work presented in this Chapter is to investigate the interactions between CPP-tagged PLGA nanoparticles and cells at the nano-bio interface. Therefore, a fluorophore-labelled PLGA was used for the preparation of CPP-tagged PLGA-FPR nanoparticles to enable the detection of the vehicle using flow cytometry and confocal laser scanning microscopy (CLSM). PLGA-FPR and CPP-tagged PLGA-FPR nanoparticles were prepared using the post-microfluidics and the *in situ* microfluidics conjugation approach and characterised for their physicochemical properties. Nanoparticle-cell interactions of the nanoformulations prepared with both preparation methods were tested in HeLa cells to investigate the influence of the preparation method and the architecture of the CPPs on the nano-bio interface. In order to evaluate the potential of the CPP-tagged PLGA-FPR nanoparticles as an oral drug delivery system, cell interaction of the nanoformulations with Caco-2 cells was investigated.

4.2 Materials

HeLa cells (human cervical cells) were purchased from American Type Culture Collection (ATCC, Manassas, VA, USA) and Caco-2 cells (carcinogenic human colonic cells) were provided by Prof. Ian Tucker as a kind gift. Poly(lactide-*co*-glycolide)-FPR648 (PLGA-FPR, 50:50, FPR648 fluorescent end-capped, MW 23,240 Da) was supplied by PolySciTech (West Lafayette, IN, USA). MEM non-essential amino acids solution (NEAA, 100×, cell culture grade), Hanks' Balanced salts (powder, cell culture grade), bovine serum albumin (BSA, $\geq 98\%$), propidium iodide ($\geq 97\%$), phenazine methosulfate (PMS, $\geq 90\%$), ethylenediaminetetraacetic acid (EDTA, cell culture grade) and cell culture flasks were purchased from Sigma-Aldrich (St. Louis, MO, USA). Penicillin-streptomycin (10,000 units/mL penicillin, 10 mg/mL streptomycin, cell culture grade), Hoechst 33342 (purity $\geq 99\%$, final concentration 1 mg/mL) and CellMask™ Orange plasma membrane stain (5 mg/mL in DMSO, final concentration 5 μ g/mL) were purchased from Thermo Fisher Scientific Australia Pty (Scoresby, Australia). Dulbecco's Modified Eagle Medium, (DMEM, 4.5 g/L glucose, L-glutamine, phenol red, cell culture grade), Dulbecco's Phosphate Buffered Saline powder (DPBS, cell culture grade), Trypan Blue Stain 0.4% and TrypLE Express (no phenol red) were supplied by Gibco® Life Technologies (Grand Island, NE, USA). 3-(4,5-Dimethylthiazol-2-yl)-5-(3-carboxymethoxyphenyl)-2-(4-sulfophenyl)-2H-tetrazolium (MTS) and CellTiter 96® AQueous One Solution were purchased from Promega (Madison, WI, USA). Cover glasses No. 1 (circular, 13 mm) were from Lab Supply (Dunedin, New Zealand). Ibidi μ -slides were obtained from Ibidi (Gräfelfing, Germany). HyClone fetal bovine serum (FBS) was sourced from GE Healthcare Life Sciences (Tauranga, New Zealand). Cell culture plates and Falcon® cell culture inserts (0.4 μ m pore size) were sourced from BD Biosciences (San Jose, CA, USA). Nylon syringe filters (0.45 μ m) were obtained from MicroAnalytix Pty Ltd (Auckland, New Zealand).

The cell culture buffer used in this study was HBSS supplemented with 10 mM HEPES and 0.05 % (w/v) BSA and is referred to below as hHBSS.

All other ingredients and peptides required for the preparation of the nanoformulations used are listed in Chapter 2.

4.3 Methods

4.3.1 *Preparation of CPP-tagged PLGA-FPR nanoparticles using microfluidics*

CPP-tagged PLGA-FPR nanoparticles were prepared using the post-microfluidics and *in situ* microfluidics conjugation approach as previously described in Chapters 2 and 3 with some modifications. The PLGA polymer was exchanged with the PLGA-FPR polymer, which is a fluorophore-labelled PLGA polymer. Further, either the NanoAssemblr[®] Benchtop device (flow rate ratio 6:1, total flow rate 10 mL/min) or NanoAssemblr[®] Cartridges were used in combination with a syringe pump (Pump 11 Elite (Harvard Apparatus, Cambridge, MA, USA), flow rate ratio 6:1 and total flow rate 2.5 mL/min).

4.3.2 *Characterization of CPP-tagged PLGA-FPR nanoparticles*

The Z-average diameter, PDI and the zeta potential of the nanoformulations were measured using DLS and laser Doppler electrophoresis as described in Chapter 2. The nanoformulations were prepared in hHBSS or in ultra-pure water and for size and zeta potential measurements further diluted with ultra-pure water.

The conjugation efficiencies of the three CPPs on CPP-tagged PLGA-FPR nanoparticles prepared using the post-microfluidics and *in situ* microfluidics conjugation approach were determined using RP-HPLC. The RP-HPLC methods were described in Chapter 2 and samples of supernatants were filtered through a 0.45 μm nylon membrane prior to RP-HPLC analysis.

4.3.3 *Culturing of HeLa and Caco-2 cells*

HeLa cells were cultured in 75 cm^2 cell culture flasks with Eagle's Minimal Essential Medium (EMEM) supplemented with 100 IU/mL penicillin, 100 $\mu\text{g}/\text{mL}$ streptomycin, 2 mM L-glutamine, 0.01 mM non-essential amino acids, 1 mM sodium pyruvate and 10% (v/v) FBS at 37°C and 5% CO_2 . At a confluence of 80-90% in the culturing flasks, HeLa cells were detached by trypsin-EDTA treatment (5 mg/mL trypsin and 2 mg/mL EDTA in DPBS, pH 7.4) and seeded for subsequent experiments. HeLa cells were seeded at a density of 1.5×10^4 cells/well in 96-well plates for cell viability assay, 1.5×10^5 cells/well in 12-well plates for flow cytometry, and 4.5×10^5 cells/well in ibidi μ -slides for CLSM, 24 or 48 h prior to the experiments using passages 2 to 9.

Caco-2 cells were routinely cultured in 75 cm^2 cell culture flask with Dulbecco's Modified Eagle Medium (DMEM) containing 4 mM L-glutamine and supplemented with 1% (v/v) penicillin-streptomycin, 1% (v/v) non-essential amino acids and 10% (v/v) FBS at 37°C and 5% CO_2 . Caco-2 cells were weekly sub-cultured in a 1:5 ratio at a confluence of around 50% and monitored using an Olympus CKX41 microscope (Auckland, New Zealand) with phase contrast to evaluate confluence. For the cell viability assay, Caco-2 cells were seeded in 96-well plate at a density of 5×10^3 cells/well for 7-12 days until they reached confluence.

Caco-2 cells were seeded at a density of 1×10^5 cells/cm² in Falcon[®] cell culture inserts (diameter, 0.4 μ m pores) and grown for 22 days for the cell integrity study. Caco-2 cells were seeded for 21 days in 12-well plates at a density of 3×10^4 cells/well or on cover glasses in 12-well plates at a density of 5×10^3 cells/well for flow cytometry and CLSM analysis, respectively. The medium was replaced every two to three days and passage 59 to 73 were used for experiments.

4.3.4 Toxicity of nanoformulations in HeLa and Caco-2 cells

HeLa cells were washed with hHBSS (pH 7.4) and incubated with 100 μ L PLGA-FPR or CPP-tagged PLGA-FPR nanoparticles (0.09-0.90 mg/mL) and CPP solutions (1-100 μ M) for 1 h before the test solutions were removed and HeLa cells were washed twice with hHBSS (pH 7.4). Subsequently, HeLa cells were incubated with a MTS/PMS solution containing 240 μ g/mL MTS and 2.4 μ g/mL PMS in hHBSS (pH 7.4) for 4 h at 37°C and 5% CO₂. Absorbance was measured at 490 nm using microplate reader POLARstar OPTIMA (BMG Labtech, Ortenberg, Germany).

Caco-2 cells were washed with hHBSS (pH 7.4) and incubated with 100 μ L PLGA-FPR or CPP-tagged PLGA-FPR nanoparticles (0.07-0.72 mg/mL) and CPP solutions (0.05-20 μ M) for 2 h. Afterwards, the test solutions were removed and Caco-2 cells were washed twice with hHBSS (pH 7.4) before incubation with the CellTiter96[®] AQueous One Solution Reagent containing 90 μ g/mL MTS and 4.8 μ g/mL μ M phenazine ethosulfate (PES) for 1 h at 37°C and 5% CO₂. Absorbance was measured at 490 nm using the POLARstar OMEGA microplate reader (BMG Labtech, Ortenberg, Germany).

Both cell lines were treated with hHBSS (pH 7.4) only and 0.2 % (w/v) SDS in HBSS as negative and positive controls, respectively. Cell viability for both cell lines was calculated with the absorbance of the test solutions and positive and negative controls as described in Equation (4-1).

$$\text{Cell viability (\%)} = \frac{\text{Absorbance}_{(\text{test solutions})} - \text{Absorbance}_{(\text{pos. control})}}{\text{Absorbance}_{(\text{neg. control})} - \text{Absorbance}_{(\text{pos. control})}} \times 100 \quad (4-1)$$

4.3.5 Cell integrity of Caco-2 cell monolayer

Caco-2 cells were washed and equilibrated with hHBSS (pH 7.4) for 20 min at 37°C and 5% CO₂ before TEER was measured using Millicell[®] ERS Voltohmmeter (EMD Millipore, Billerica, MA, USA) with a chopstick electrode. The reported TEER values (TEER_{Caco-2 cell monolayer}) were obtained from the resistance of the tissue (Equation 4-2) and multiplication with the semipermeable membrane area (Equation 4-3).

$$R_{\text{Tissue}}(\Omega) = R_{\text{Caco-2 monolayer}} - R_{\text{blank insert}} \quad (4-2)$$

$$\text{TEER}_{\text{Caco-2 cell monolayer}}(\Omega \times \text{cm}^2) = R_{\text{Tissue}} - M_{\text{Area}} \quad (4-3)$$

4.3.6 Uptake of nanoparticles using flow cytometry for HeLa and Caco-2 cells

HeLa cells were washed with hHBSS (pH 7.4) and incubated with 500 µL of PLGA-FPR or CPP-tagged PLGA-FPR nanoparticles (0.09-0.90 mg/mL) for 1 h at 37°C and 5% CO₂. The nanoformulations were removed and the HeLa cells were washed with ice-cold DPBS (pH 7.4). For the trypsinization of HeLa cells, 500 µL of trypsin (0.05% (v/v) in DPBS, pH 7.4)

was added to the HeLa cells and incubated for 5 min at 37°C and 5% CO₂. The plate was slightly agitated before 800 µL complete medium (hHBSS (pH 7.4) with 10% (v/v) FBS) was added to terminate the trypsinization process. HeLa cells were collected and separated by centrifugation at 270 g for 3 min, prior to a second wash with 400 µL ice-cold heparin (20 µg/mL in DPBS, pH 7.4) and again separated by centrifugation as above. Finally, HeLa cells were re-suspended in 500 µL complete medium and 10,000 viable cells were analysed and gated for forward/sideways light scattering using a Gallios Flow Cytometer (Beckman Coulter, Brea, CA, USA) and obtained data were analysed using FlowJo V10 analysis software (BD, Franklin Lakes, NJ, USA).

Caco-2 cells were washed once with hHBSS (pH 7.4) and incubated with 500 µL PLGA-FPR or CPP-tagged PLGA-FPR nanoparticles (0.07-0.72 mg/mL) at 37°C and 5% CO₂ for 0.5, 2 and 6 h. The nanoformulations were discarded and Caco-2 cells were washed twice with DPBS (pH 7.4) at room temperature. For the trypsinization of Caco-2 cells, 400 µL TrypLE Express was added and incubated at 37°C and 5% CO₂ for 10 min. To stop the trypsinization process, 1 mL of complete medium (hHBSS (pH 7.4) with 1% (v/v) FBS) was added. Caco-2 cells were separated by centrifugation at 330 g for 5 min, re-suspended and washed with 400 µL of ice-cold DPBS (pH 7.4) containing heparin (20 µg/mL). For the quantification of internalized and surface-bound nanoparticles, no heparin treatment was applied and Caco-2 cells were washed with ice-cold DPBS (pH 7.4) only. Caco-2 cells were separated by centrifugation as above and re-suspend with 500 µL of DPBS (pH 7.4). Cell viability was evaluated by adding 5 µL of propidium iodide (0.025 mg/mL) before analysis. 30,000 viable cells were analysed with FACS Canto™ II flow cytometry (BD Biosciences, San Jose, CA, USA), gated for forward/sideways light scattering and obtained data were analysed using FlowJo V10 analysis software.

4.3.7 *Qualitative cell uptake study using confocal laser scanning microscopy for HeLa and Caco-2 cells*

HeLa cells were washed with hHBSS (pH 7.4) before incubation with 200 μ L of PLGA-FPR or CPP-tagged PLGA-FPR nanoparticles (0.90 mg/mL) for 1 h. After the incubation, HeLa cells were washed with hHBSS (pH 7.4) and first incubated with 2 μ L of Hoechst 33342 (1 mg/mL) in 200 μ L hHBSS (pH 7.4) for 15 to 30 min at 37°C and 5% CO₂ to stain the cell nucleus. HeLa cells were washed with hHBSS (pH 7.4) and incubated with 1 μ L of CellMask orange (5 μ g/mL) in 200 μ L hHBSS (pH 7.4) for another 15 to 30 min at 37°C and 5% CO₂. Finally, the cells were washed again with hHBSS (pH 7.4) and live cell images were taken using the LSM 780 Zeiss inverted confocal microscope equipped with a 63 \times /1.4 numerical aperture oil medium DIC III objective (Carl Zeiss, Oberkochen, Germany).

Similarly, Caco-2 cells were washed with hHBSS (pH 7.4) and incubated with 400 μ L of PLGA-FPR or CPP-tagged PLGA-FPR (0.72 mg/mL) nanoparticles for 2 h at 37°C and 5% CO₂. After the incubation Caco-2 cells were washed twice with hHBSS (pH 7.4) and further incubated with 2 μ L of Hoechst 33342 (1 mg/mL) in 500 μ L hHBSS (pH 7.4) for 10 min at 37°C and 5% CO₂ to stain the cell nucleus. Caco-2 cells were washed with hHBSS (pH 7.4) and incubated with 1 μ L of CellMask orange (5 μ g/mL) in 500 μ L hHBSS (pH 7.4) for another 10 min at 37°C and 5% CO₂. Finally, the cells were washed again with hHBSS (pH 7.4) before the cover glass was removed from the well with tweezers and carefully placed onto a drop of Fluoromount-G™ to reduce fluorescence bleaching. Caco-2 cells were investigated using the Nikon A1+ Inverted Confocal Scanning Microscope equipped with a 60 \times /1.4 numerical aperture PlanApo oil objective (Nikon Instruments, Melville, NY, USA).

4.3.8 *Statistical analysis*

Experiments for the characterisation of the PLGA-FPR and CPP-tagged PLGA-FPR nanoparticles were performed at least in triplicate of independent batches and results are presented as mean \pm SD. *In vitro* cell culture experiments were performed as biological replicates with at least three repeats and results are presented as mean \pm standard error of the mean (SEM). Student's *t*-test was performed to make a comparison between single groups and obtained *p*-values were considered statistically significant at $p < 0.05$.

4.4 Results and Discussion

4.4.1 Characterization of CPP-tagged PLGA-FPR nanoparticles

For the *in vitro* investigation of CPP-tagged PLGA nanoparticles, the PLGA polymer was replaced by a fluorescent PLGA labelled with the fluorophore FPR 648, which emits red fluorescence (λ_{ex} wavelength = 648 nm, λ_{em} wavelength = 672 nm). The fluorescent PLGA polymer is hereafter referred to as PLGA-FPR. The CPP-tagged PLGA-FPR nanoparticles were characterized for their physicochemical properties and conjugation efficiencies of CPPs were determined before investigating *in vitro* interactions with HeLa and Caco-2 cells.

4.4.1.1 Physicochemical properties of nanoparticles in ultra-pure water

PLGA-FPR and CPP-tagged PLGA-FPR nanoparticles were characterized in ultra-pure water to obtain their native size and charge. The nanoformulations were monodisperse and showed a size between 140 and 180 nm for PLGA-FPR and CPP-tagged PLGA-FPR nanoparticles produced using the post-microfluidics or the *in situ* microfluidics conjugation approach (Table 4.2). The surface charge of the CPP-tagged PLGA-FPR nanoparticles prepared with both conjugation approaches changed from a negative zeta potential of -16 mV to a positive zeta potential of +8 mV depending on the conjugated CPP (Table 4.2). The influence of the CPP architecture on the surface charge was discussed earlier in Chapters 2 and 3. Fluorophore-labelled PLGA and CPP-tagged PLGA nanoparticles prepared using the post-microfluidics and *in situ* microfluidics conjugation approach had a size below 200 nm, a similar size distribution, and a similar zeta potential in comparison to PLGA and CPP-tagged PLGA nanoparticles prepared with the non-labelled PLGA polymer as a precursor material (Table 4.2 and Chapter 3, Figure 3.4 and Chapter 2, Figure 2.12).

Table 4.2. Characterization of PLGA-FPR and CPP-tagged PLGA-FPR nanoparticles in ultra-pure water prepared using the post-microfluidics or the *in situ* microfluidics conjugation approach. Data are mean \pm SD ($n = 3$).

Nanoparticles	Size \pm SD (nm)	PDI \pm SD	Zeta potential \pm SD (mV)
Post-microfluidics conjugation approach			
PLGA-FPR	176.9 \pm 4.5	0.131 \pm 0.013	-22.9 \pm 0.9
RRH-tagged PLGA-FPR	178.1 \pm 1.2	0.130 \pm 0.008	-16.3 \pm 0.4
TAT-tagged PLGA-FPR	182.5 \pm 5.2	0.137 \pm 0.017	-2.3 \pm 1.2
bTAT-tagged PLGA-FPR	185.1 \pm 6.1	0.164 \pm 0.017	8.8 \pm 0.6
<i>In situ</i> microfluidics conjugation approach			
PLGA-FPR	137.4 \pm 16.0	0.150 \pm 0.021	-13.2 \pm 3.1
RRH-tagged PLGA-FPR	139.7 \pm 4.6	0.177 \pm 0.032	-5.7 \pm 3.2
TAT-tagged PLGA-FPR	139.3 \pm 1.2	0.172 \pm 0.023	-3.1 \pm 0.4
bTAT-tagged PLGA-FPR	142.1 \pm 7.2	0.161 \pm 0.017	1.5 \pm 0.3

Further, the conjugation efficiency of each CPP was determined to estimate the amount of CPP covalently bound to PLGA-FPR nanoparticles formulated with the post-microfluidics or the *in situ* microfluidic conjugation approach. Details of the conjugation reaction and theoretical considerations were discussed earlier in Chapters 2 and 3. Using the fluorophore-labelled PLGA polymer, the CPP conjugation efficiency was lower compared to the non-labelled PLGA polymer (Table 4.3). The conjugation efficiencies were 74%, 56% and 80% for the post-microfluidics conjugation approach and 91%, 29% and 85% for the *in situ* microfluidics conjugation approach using RRH, TAT and bTAT, respectively (Chapter 3, Table 3.1 and Chapter 2, Table 2.9). The lower conjugation efficiencies of the three CPPs can be attributed to the presence of the fluorescent FPR molecules, which were conjugated to the PLGA polymer to obtain the fluorophore-labelled PLGA polymer. For the conjugation of the fluorescent dye and the CPPs, the carboxyl groups of the PLGA polymer were utilized and therefore a lower number of carboxyl groups remained available for conjugation of CPPs. One

exception was the conjugation efficiency of TAT-tagged PLGA-FPR nanoparticles prepared using the *in situ* microfluidics conjugation approach, which showed a higher conjugation efficiency with the fluorophore-labelled PLGA polymer in comparison to the non-labelled PLGA polymer (Table 4.3 and Chapter 3, Table 3.1). This might be related to a higher encapsulation of TAT, since a distinction between the encapsulated amount and the amount on the surface of the PLGA-FPR nanoparticles cannot be made using the RP-HPLC method to determine the amount of CPP.

Table 4.3. Conjugation efficiencies and the equivalent concentration of CPPs tagged to PLGA-FPR nanoparticles using the post-microfluidics and the *in situ* microfluidics conjugation approach. Data are mean \pm SD ($n = 3$).

Nanoparticles	Conjugation efficiency \pm SD (%)	CPP concentration \pm SD (μ M)
Post-microfluidics conjugation approach		
RRH-tagged PLGA-FPR	8.9 \pm 4.3	0.32 \pm 0.15
TAT-tagged PLGA-FPR	19.4 \pm 12.4	0.14 \pm 0.08
bTAT-tagged PLGA-FPR	5.5 \pm 5.1	0.02 \pm 0.02
<i>In situ</i> microfluidics conjugation approach		
RRH-tagged PLGA-FPR	9.4 \pm 4.8	0.62 \pm 0.31
TAT-tagged PLGA-FPR	47.3 \pm 7.0	0.36 \pm 0.05
bTAT-tagged PLGA-FPR	11.7 \pm 6.9	0.05 \pm 0.03

4.4.1.2 Physicochemical properties of nanoparticles in cell culture buffer

For the *in vitro* investigation of PLGA-FPR and CPP-tagged PLGA-FPR nanoparticles in cell culture systems, nanoformulations formulated with both preparation methods were re-suspended in cell culture buffer to maintain physiological conditions for the cells during incubation. The size of PLGA-FPR and CPP-tagged PLGA-FPR nanoparticles in cell culture

buffer was found to be between 175 and 245 nm with a PDI below 0.250 indicating that the nanoformulations were monodisperse (Table 4.4 and Table 4.5). Similarly, the size and surface charge of OVA-loaded chitosan nanoparticles was influenced by their suspension in HBSS in comparison to ultra-pure water with a size increase from 126 to 196 nm and a decrease in the surface charge from +38 to +10 mV when HBSS was the suspending media (Cole *et al.*, 2018). Here, the surface charge of the nanoformulations was between -8 and -2 mV, which showed the influence of the cell culture buffer (hHBBS) (Table 4.4 and Table 4.5). Due to the presence of salts and proteins in the cell culture buffer, it is likely that an electrostatic reaction between the positively charged CPPs and negatively charged ions leads to the formation of a salt/protein corona around the nanoparticles and an increase in the hydrodynamic diameter. In addition, it is likely that the salts and proteins present in the cell culture buffer also influenced the surface charge of the CPP-tagged PLGA-FPR nanoparticles and therefore positive charged induced by CPP architecture were shielded and did not contribute to the overall surface charge. Since the zeta potential for all formulations was similar, the surface charge as a factor for enhancing cellular uptake of nanoparticles could be excluded and any difference in cellular uptake can be related to the CPP architecture used for the conjugation with PLGA-FPR nanoparticles.

Table 4.4. Characterization of PLGA-FPR and CPP-tagged PLGA-FPR nanoparticles in cell culture buffer for *in vitro* studies in HeLa cells prepared using the post-microfluidics and the *in situ* microfluidics conjugation approach. Data are mean \pm SD ($n = 6$).

Nanoparticles	Size \pm SD (nm)	PDI \pm SD	Zeta potential \pm SD (mV)
Post-microfluidics conjugation approach			
PLGA-FPR	204.3 \pm 10.6	0.165 \pm 0.032	-8.2 \pm 0.7
RRH-tagged PLGA-FPR	210.2 \pm 5.8	0.176 \pm 0.037	-8.1 \pm 0.6
TAT-tagged PLGA-FPR	213.6 \pm 3.0	0.151 \pm 0.044	-3.5 \pm 0.5
bTAT-tagged PLGA-FPR	210.7 \pm 12.4	0.169 \pm 0.006	-3.2 \pm 1.2
<i>In situ</i> microfluidics conjugation approach			
PLGA-FPR	216.9 \pm 15.2	0.194 \pm 0.073	-5.3 \pm 2.2
RRH-tagged PLGA-FPR	241.8 \pm 15.3	0.253 \pm 0.028	-6.6 \pm 1.9
TAT-tagged PLGA-FPR	245.4 \pm 6.7	0.238 \pm 0.018	-5.0 \pm 0.4
bTAT-tagged PLGA-FPR	240.5 \pm 30.8	0.236 \pm 0.064	-4.6 \pm 1.2

Table 4.5. Characterization of PLGA-FPR and CPP-tagged PLGA-FPR nanoparticles in cell culture buffer for *in vitro* studies in Caco-2 cells prepared using the post-microfluidics conjugation approach. Data are mean \pm SD ($n = 6$).

Nanoparticles	Size \pm SD (nm)	PDI \pm SD	Zeta potential \pm SD (mV)
Post-microfluidics conjugation approach			
PLGA-FPR	175.4 \pm 7.2	0.165 \pm 0.037	-4.0 \pm 1.0
RRH-tagged PLGA-FPR	176.6 \pm 4.6	0.164 \pm 0.022	-3.8 \pm 2.2
TAT-tagged PLGA-FPR	185.1 \pm 10.1	0.199 \pm 0.054	-2.0 \pm 1.2
bTAT-tagged PLGA-FPR	194.4 \pm 14.1	0.234 \pm 0.065	-4.1 \pm 2.8

4.4.2 Interaction of nanoformulations with HeLa cells

The interactions between CPP-tagged PLGA-FPR nanoparticles and the nano-bio interface of cells were first investigated with HeLa cells. For the *in vitro* cell experiments with HeLa cells, PLGA-FPR and CPP-tagged PLGA-FPR nanoparticles were prepared using the post-microfluidics or the *in situ* microfluidics conjugation approach. The CPPs used in the study are described by their distinct architecture including a short (RRH), a long linear (TAT) and a branched peptide sequence (bTAT) (Chapter 2, Figure 2.5).

4.4.2.1 Cell viability of HeLa cells

The effect of nanoformulations on the cell viability of HeLa cells was investigated using the MTS assay. The MTS assay is an end-point assay for the determination of viable cells and utilizes an electron transfer reaction from the electron coupling reagent (PMS or PES) to the tetrazolium salt (MTS) (Jacobsen *et al.*, 1996). The electron transfer can only occur if viable cells are present and the absorbance of the resulting coloured formazan product can be directly related to the viability of the cells (Cory *et al.*, 1991). Cell viability of HeLa cells was investigated after incubation with PLGA-FPR and CPP-tagged PLGA-FPR nanoparticles for 1 h (Figure 4.2A and B). The nanoformulations were tested at three different concentrations and the negative control was set to 100% as indicated by the black line in the cell viability graphs (Figure 4.2). HeLa cells were viable after incubation with PLGA-FPR and CPP-tagged PLGA-FPR nanoparticles, indicating that the nanoformulations in different concentrations had no toxic effect on the cells. As reported in the literature, unmodified PLGA nanoparticles with concentrations between 0.625 and 2.5 mg/mL were non-toxic to HeLa cells after 48 h of incubation (Egusquiaguirre *et al.*, 2015). In contrast, a decrease in cell viability of HeLa cells incubated with PLGA nanoparticles for 48 h to below 70% was reported at a concentration

of ≥ 0.2 mg/mL (Chen *et al.*, 2017a). In the present study, the nanoparticle concentrations ranged between 0.09 and 0.9 mg/mL for PLGA-FPR nanoparticles and did not show a negative influence on cell viability. An influence on the cell viability was not expected since the PLGA polymer is biocompatible and no toxicity was induced by the fluorescent label of the PLGA polymer. RRH-tagged PLGA-FPR nanoparticles formulated with both preparation methods showed a decrease in cell viability to 84%, which was lower, compared to other CPP-tagged PLGA-FPR nanoparticles, but the cell viability was acceptable for using a concentration of 0.90 mg/mL in further *in vitro* experiments. CPP-modified PLGA nanoparticles (0.625-2.5 mg/mL) were reported to maintain moderate viability levels in HeLa cells and cell viability decreased with higher concentrations of nanoparticles administered (Egusquiaguirre *et al.*, 2015). Feiner-Gracia *et al.* (2018) found a reduction in cell viability to about 60% when TAT-modified nanoparticles were used in a concentration of 3 mg/mL in comparison to 0.3 mg/mL after 24 h incubation in HeLa cells and the toxicity was attributed to the positive charges of TAT-modified PLGA nanoparticles. Further, HeLa cells were incubated with five different concentrations of the three CPPs, RRH, TAT and bTAT, ranging from 1 to 100 μ M. For all concentrations, HeLa cells showed a cell viability of above 91% indicating that the CPPs were non-toxic (Figure 4.2C). This is in alignment with a study by Trehin *et al.* (2004) that showed that TAT (47-57) was non-toxic to lung cancer (Calu-3 cells) and buccal mucosa cells (TR146) at concentrations between 10 and 100 μ M.

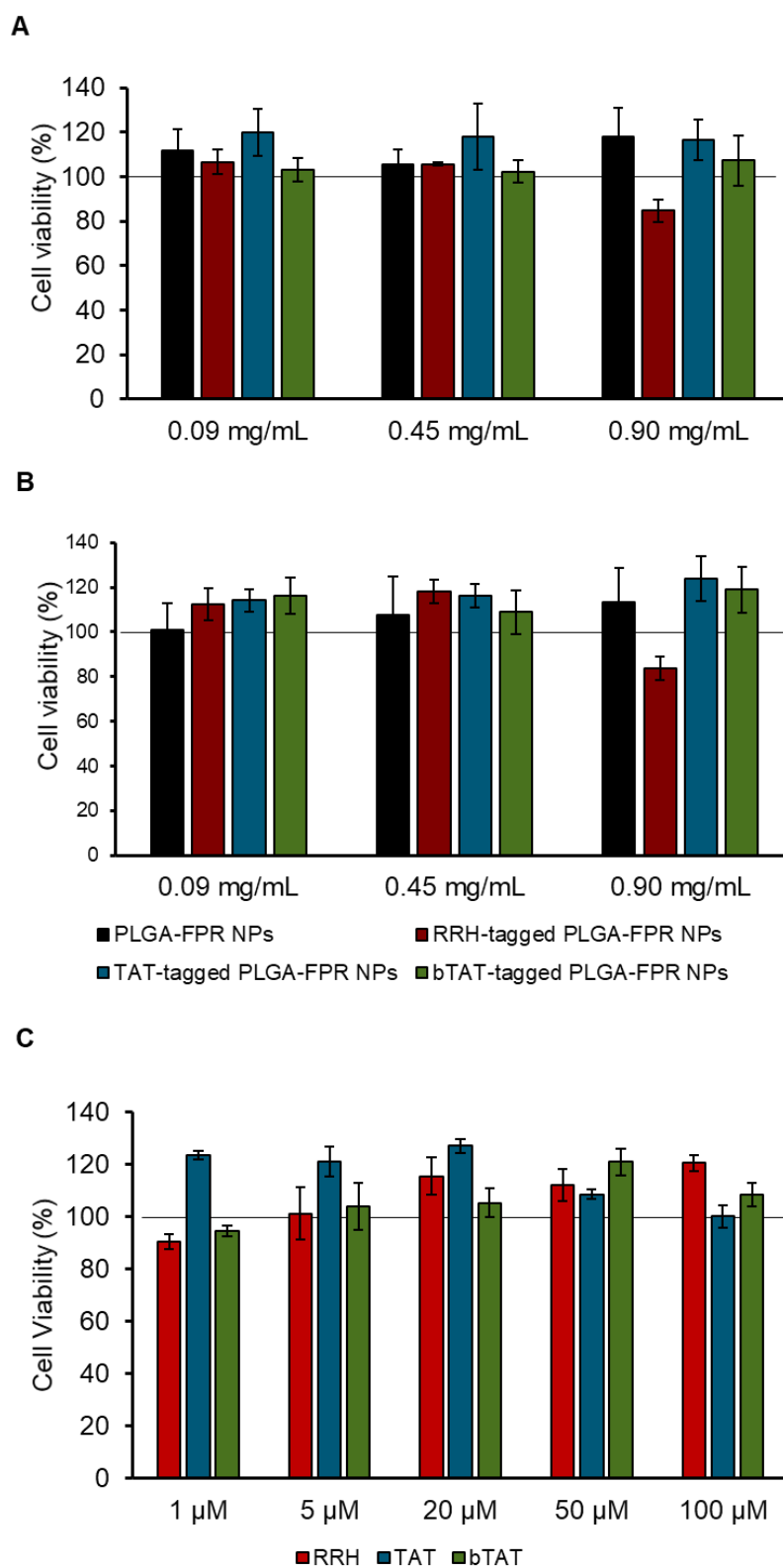


Figure 4.2. Cell viability of HeLa cells after 1 h incubation with PLGA-FPR and CPP-tagged PLGA-FPR nanoparticles prepared using the post-microfluidics (A) or *in situ* microfluidics (B) conjugation approach and CPP solutions with different concentrations (C). The black line indicates 100% as negative control. Data are means \pm SEM ($n = 3$). NPs = nanoparticles.

4.4.2.2 Quantification of cellular uptake of nanoparticles in HeLa cells

Flow cytometry was used to quantify the cellular uptake of PLGA-FPR and CPP-tagged PLGA-FPR nanoparticles prepared using the post-microfluidics and the *in situ* microfluidics conjugation approach in HeLa cells (Figure 4.3). By using flow cytometry analysis, individual cells are analysed for their fluorescence intensity using forward/sideward light scattering. Flow cytometry analysis revealed that the mean fluorescence intensity of HeLa cells incubated with PLGA-FPR and CPP-tagged PLGA-FPR nanoparticles was similar to the control, HeLa cells incubated with cell culture buffer, or approximately up to 1.7-fold higher. The low increase in fluorescence intensity between control cells and HeLa cells treated with nanoformulations indicates a low internalization efficiency of the nanoformulations (Figure 4.3). PLGA-FPR and CPP-tagged PLGA-FPR nanoparticles were applied to HeLa cells in different concentrations ranging between 0.05 and 0.90 mg/mL, but a concentration-dependent uptake of the nanoformulations was not observed. Further, higher cellular uptake was expected for the branched CPP bTAT, but this was not observed. Arginine-rich dendrimers based on TAT showed 10-15 times higher fluorescence after incubation with HeLa cells for 1 h in comparison to the linear TAT (Eggimann *et al.*, 2014). The addition of the branched CPP to a polymeric carrier might influence the penetration abilities of the branched CPP as in the literature, uptake of sequence-modified CPPs were reported for the CPPs only (Brock *et al.*, 2018; Hoyer *et al.*, 2012; Zhao *et al.*, 2014a). One exception was the TAT-tagged PLGA-FPR nanoparticles prepared with the post-microfluidics conjugation approach, which showed a 1.8 and 1.6-fold higher uptake in comparison to PLGA-FPR nanoparticles when a concentration of 0.90 mg/mL or the 1:2 dilution of that concentration was used, respectively (Figure 4.3A). The increase in uptake was significant for the 1:2 dilution in comparison to the PLGA-FPR nanoparticles. HeLa cells were washed with heparin to remove membrane-associated nanoformulations (Iwasa *et al.*, 2006; Patel *et al.*, 2019) and therefore a contribution of membrane-associated nanoparticles

to the fluorescence intensity was unlikely. Spider silk protein nanoparticles modified with TAT or R₈ and with a size below 300 nm showed that after incubation for 24 or 48 h up to 60% of cultured HeLa cells contained nanoparticles (Elsner *et al.*, 2015). Cellular uptake of lyophilisomes, hollow micro- or nano-meter capsules made of albumin, with a size below 1 μm was investigated with flow cytometry and trypan blue was used to quench the fluorescence of membrane-associated lyophilisomes (van Bracht *et al.*, 2014). Double the amount of lyophilisome positive cells in the HeLa cell population were observed over 4 h for TAT-conjugated lyophilisomes in comparison to unmodified lyophilisomes (van Bracht *et al.*, 2014). These two studies claim that HeLa cells were able to take up nanoparticles with a size > 200 nm as fluorescence was tested with flow cytometry after trypan blue treatment (Elsner *et al.*, 2015; van Bracht *et al.*, 2014). The main difference to the present study was the time selected for the incubation with HeLa cells. The literature reports suggest that longer incubation times between 4 to 48 h may be required for the efficient internalization of CPP-tagged PLGA-FPR nanoparticles in HeLa cells. In the present study, a shorter incubation time of 1 h was selected to investigate the likelihood of the initial contact between the CPPs with different architectures and the cells. Further, the internalization of CPP solutions including penetratin and branched peptides is reported in the literature after 1 h in HeLa cells (Birch *et al.*, 2017; Monreal *et al.*, 2015; Saleh *et al.*, 2010) indicating that cell interactions occur within a short time.

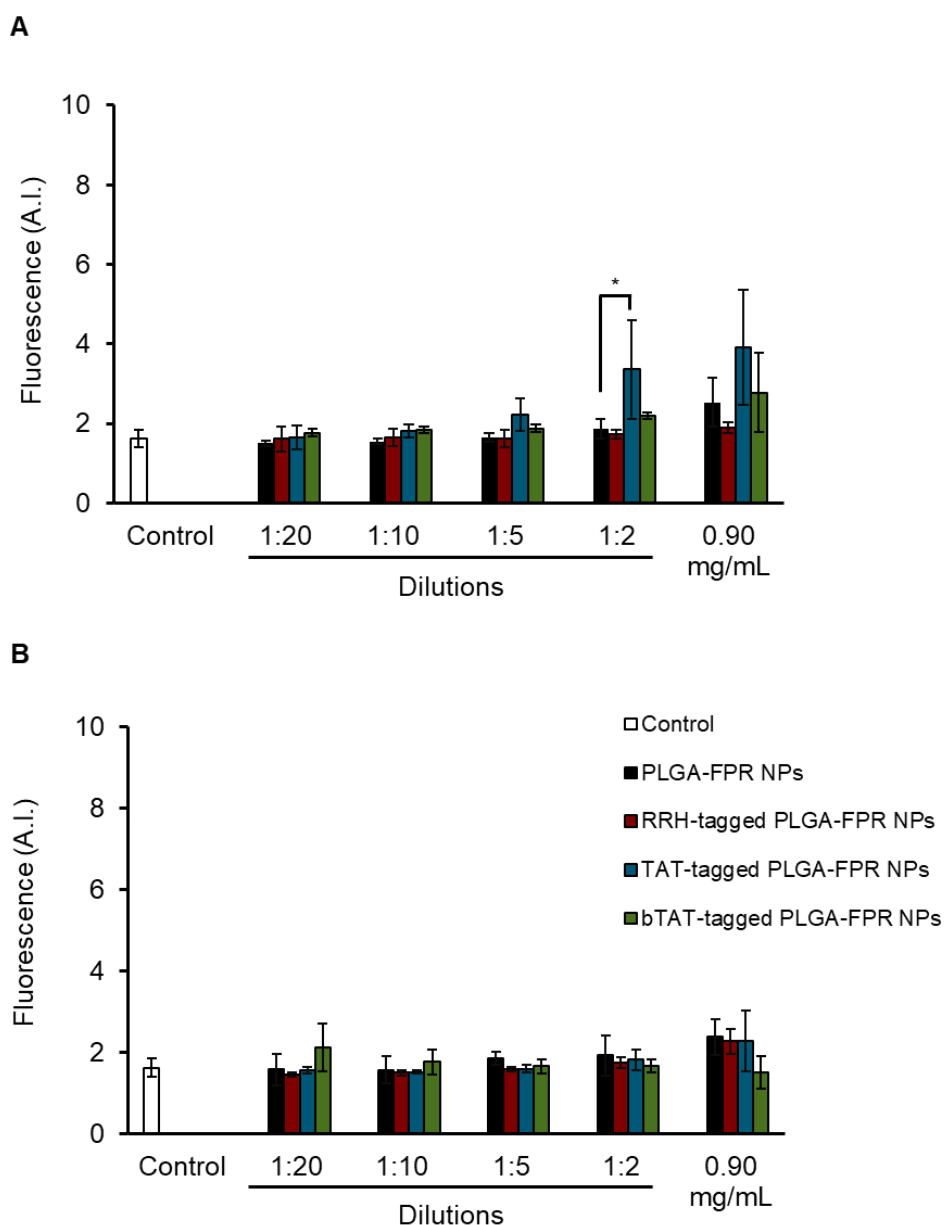


Figure 4.3. Fluorescence intensity measured in HeLa cells after 1 h incubation with different dilutions of PLGA-FPR and CPP-tagged PLGA-FPR nanoparticles prepared using the post-microfluidics (A) or the *in situ* microfluidics (B) conjugation approach. Control cells were incubated with cell culture buffer. Data are means \pm SEM ($n = 3$). * p -value < 0.05 for comparison between PLGA-FPR and TAT-tagged PLGA-FPR nanoparticles. NPs = nanoparticles.

4.4.2.3 Qualification of cellular uptake of nanoparticles in HeLa cells

For qualitative microscopic analysis, HeLa cells were incubated with PLGA-FPR and CPP-tagged PLGA-FPR nanoparticles prepared using the post-microfluidics or the *in situ*

microfluidics conjugation approach. In order to observe the HeLa cells under the microscope, the cell nucleus was stained with Hoechst 33342 and the cell membrane was stained with CellMask™ Orange plasma membrane stain appearing in blue and green, respectively.

Confocal images showed association of the PLGA-FPR and CPP-tagged PLGA-FPR nanoparticles to the cell membrane of HeLa cells after incubation for 1 h. This observation was made for nanoparticles prepared using the post-microfluidics (Figure 4.4) and the *in situ* microfluidics conjugation approach (Figure 4.5). A study by Chen *et al.* (2017a) showed overlapping fluorescence of doxorubicin-loaded PLGA-PEG-folic acid nanoparticles with the nucleus after 4 and 24 h of incubation indicating that a longer incubation time was needed for the uptake of polymeric nanoparticles in HeLa cells. No difference in cellular interactions of PLGA-FPR nanoparticles tagged with the three CPPs: RRH, TAT and bTAT nor a difference between preparation methods was observed. For example, confocal images of TAT-tagged PLGA-FPR nanoparticles prepared using the post-microfluidics and the *in situ* microfluidics conjugation approach showed a similar even distribution of the nanoparticles and association of the nanoparticles with the cell membrane of HeLa cells (Figure 4.4C and Figure 4.5C). The larger cluster of TAT-tagged PLGA-FPR nanoparticles prepared using the *in situ* microfluidics conjugation can be related to aggregation of the nanoparticles (Figure 4.4C). Improvement of internalization was reported in the literature for PLGA nanoparticles modified with fluorophore-labelled CPPs at a concentration of 5 mg/mL after incubation in HeLa cells for 4 to 72 h, whereas no efficient internalization of PLGA nanoparticles on their own was observed (Egusquiaguirre *et al.*, 2015). Another study also observed uptake after incubation in HeLa cells for 4 h with TAT-modified lyophilisomes in comparison to unmodified lyophilisomes (van Bracht *et al.*, 2014). As for PLGA-FPR nanoparticles, the incubation time is crucial for CPP-modified nanoparticles to show efficient uptake into HeLa cells.

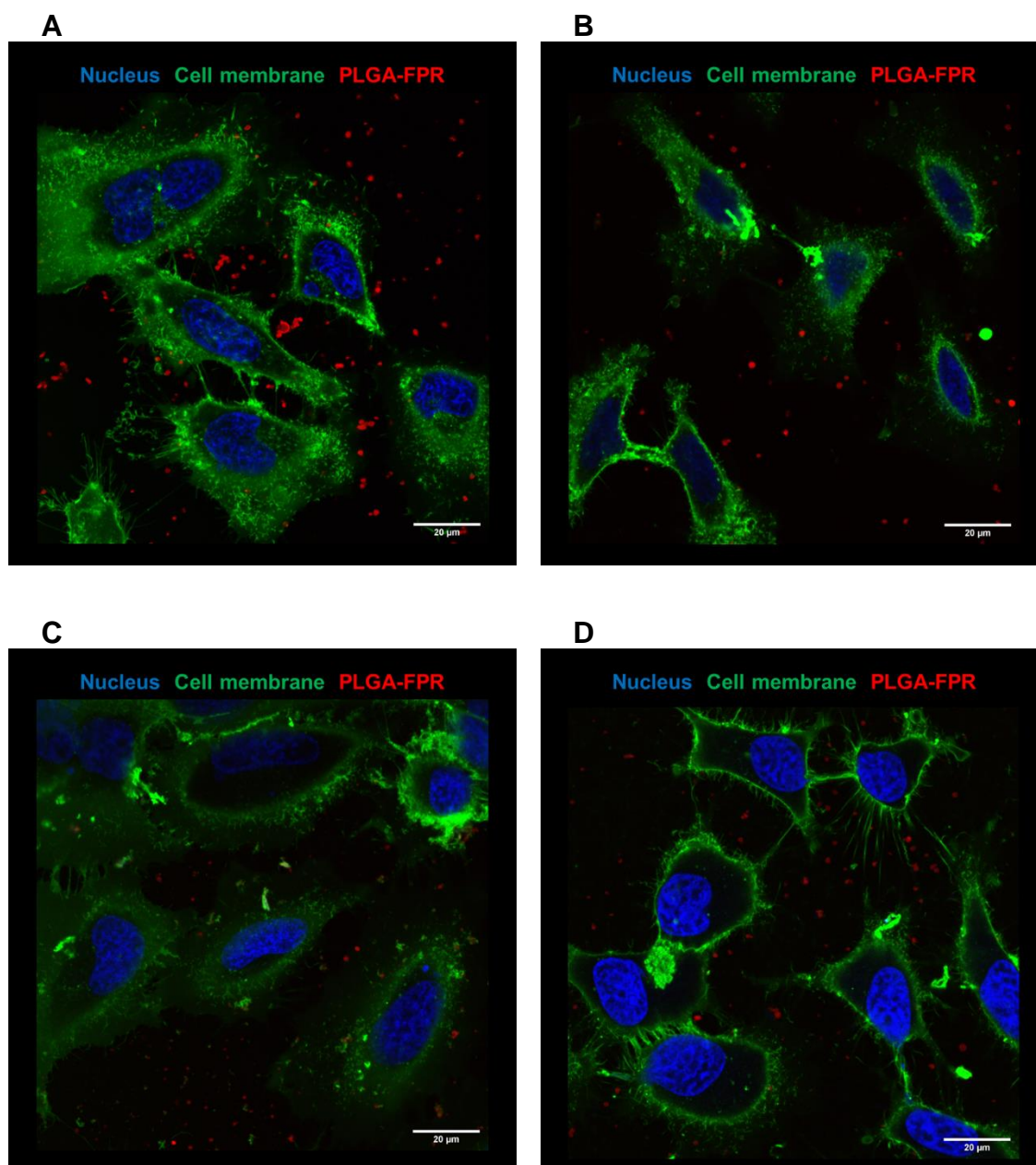


Figure 4.4. Confocal images of HeLa cells incubated for 1 h with PLGA-FPR (A), RRH- (B), TAT- (C) and bTAT-tagged PLGA-FPR nanoparticles (D) prepared using the post-microfluidics conjugation approach.

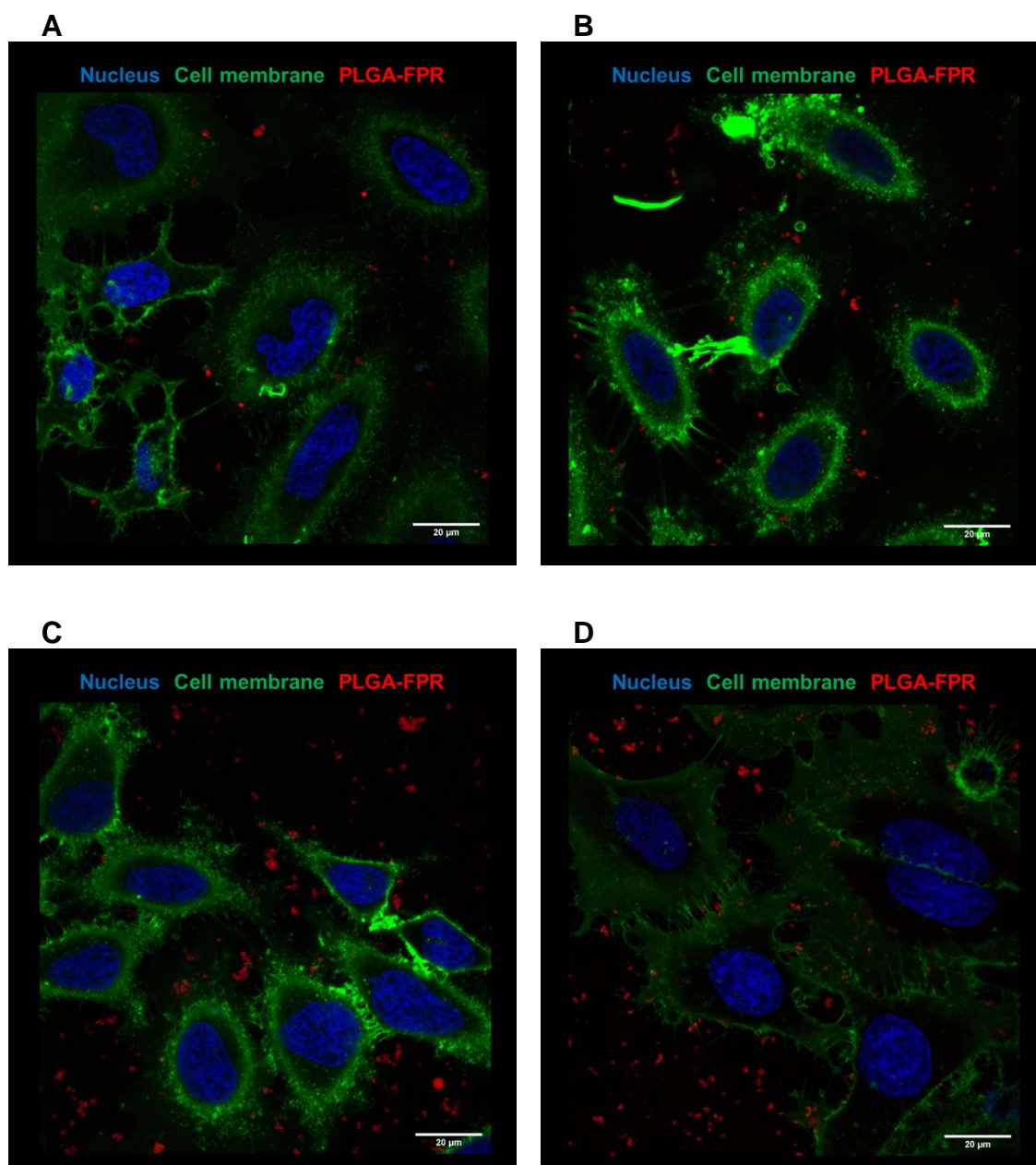


Figure 4.5. Confocal images of HeLa cells incubated for 1 h with PLGA-FPR (A), RRH- (B), TAT- (C) and bTAT-tagged PLGA-FPR nanoparticles (D) prepared using the *in situ* microfluidics conjugation approach.

As observed from the confocal images for PLGA-FPR and CPP-tagged PLGA-FPR nanoparticles, the cell membrane appeared intact after incubation with the nanoformulations. Further, as red fluorescence can be observed between the HeLa cells, an interaction of PLGA-FPR or CPP-tagged PLGA-FPR nanoparticles with the coating of the cell culture μ -slides

cannot be excluded. The μ -slides were coated with collagen IV displaying a neutral charge at physiological pH and HeLa cells were not confluent leaving space between them and the possibility of interactions between the nanoformulations and the coating.

4.4.3 *Interaction of nanoformulations with Caco-2 cells*

Caco-2 cell monolayers are frequently used as a model for the intestinal epithelium and the cell line was selected to evaluate the potential of CPP-tagged PLGA-FPR nanoparticles as an oral drug delivery system. Based on the similar results obtained with HeLa cells for PLGA-FPR and CPP-tagged PLGA-FPR nanoparticles prepared using both conjugation approaches, further experiments were performed with CPP-tagged PLGA-FPR nanoparticles prepared using the post-microfluidics conjugation approach only. The CPPs are present on the surface of PLGA-FPR nanoparticles after post-microfluidics conjugation (Streck *et al.*, 2019b) and therefore interactions between CPPs and the cell surface are more likely. The *in situ* microfluidics conjugation approach also encapsulates the CPPs, which cannot contribute to cell interactions. In this thesis, Caco-2 cells were grown as cell monolayers and for analysis of cell viability and uptake of nanoparticles with CLSM an intact cell monolayer was used, whereas for analysis of uptake using flow cytometry the cell monolayer was suspended into single cells.

4.4.3.1 *Cell viability and cell integrity of Caco-2 cells*

The influence of PLGA-FPR and CPP-tagged PLGA-FPR nanoparticles on the viability of Caco-2 cells was evaluated after incubation for 2 h (Figure 4.6). The PLGA-FPR and CPP-tagged PLGA nanoparticles were non-toxic to Caco-2 cells and the cell viability was above 90%. Previous studies reported that surface-modified and drug-loaded PLGA nanoparticles were non-toxic to Caco-2 cells at concentrations between 2 mg/mL to 5 mg/well after

incubation for 2-4 h (Czuba *et al.*, 2018; Sheng *et al.*, 2016). TAT- and R₈-modified PLGA and R₈-modified PLGA-PEG nanoparticles showed cell viability above 80% after 2-6 h incubation in Caco-2 cells (Liu *et al.*, 2013; Zhu *et al.*, 2016a). Further, CPP solutions with concentrations ranging between 0.05 and 20 μ M were non-toxic to Caco-2 cells and showed a cell viability of around 100% (Figure 4.6B). In the present study, no toxicity of the CPPs was found and the concentrations used were lower compared to the concentration used in HeLa cells (Section 4.4.2.1) and in other cell lines as described in the literature (Section 4.4.2.1).

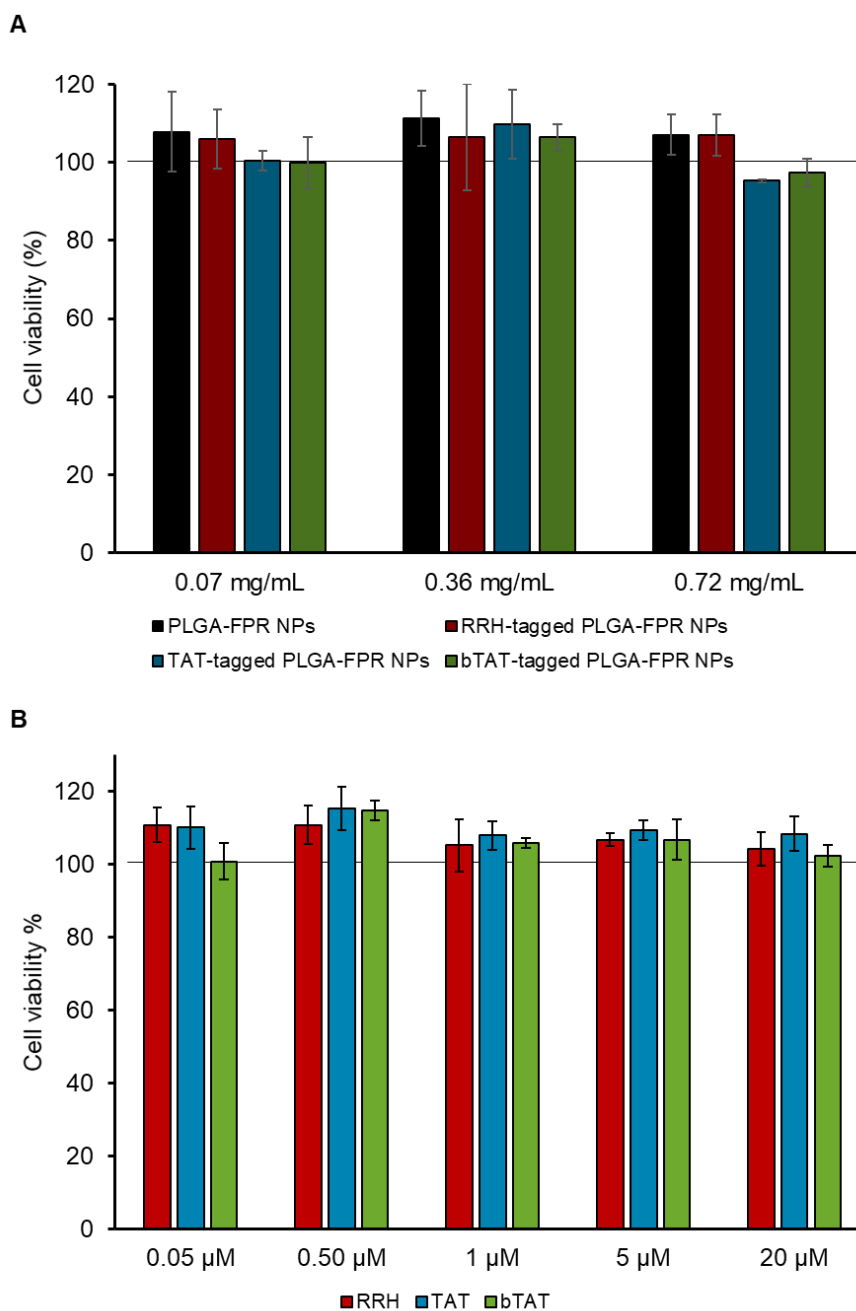


Figure 4.6. Cell viability graphs of Caco-2 cells after 2 h incubation with PLGA-FPR and CPP-tagged PLGA-FPR nanoparticles prepared using the post-microfluidics conjugation approach (A) and CPP solutions with different concentrations (B). The black line indicates 100% as negative control. Data are means \pm SEM ($n = 3$). NPs = nanoparticles.

The TEER value is the main measurement of epithelial integrity and primarily reflects the tightness of the tight junctions between cells (Mukherjee *et al.*, 2004). During the culturing of Caco-2 cells on permeable filter inserts, the TEER value increases as the cells grow into a

monolayer (Mukherjee *et al.*, 2004). The TEER value of the Caco-2 cell monolayer was monitored between day 17 and day 22 after seeding the Caco-2 cells on cell culture inserts with a permeable membrane and a TEER_{Caco-2 cell monolayer} value of $352 \Omega \times \text{cm}^2$ was reached by day 20 showing the presence of a tight cell monolayer (Appendix VI). Minimum TEER values between 200 and $450 \Omega \times \text{cm}^2$ have been reported in the literature as a threshold for a Caco-2 cell monolayer to be used as a model for intestinal epithelium (Banerjee *et al.*, 2016; Beduneau *et al.*, 2014; Birch *et al.*, 2018a; Faralli *et al.*, 2019; Mu *et al.*, 2019).

4.4.3.2 Quantification of cellular uptake of nanoparticles in Caco-2 cells

The cellular uptake of PLGA-FPR and CPP-tagged PLGA-FPR nanoparticles was measured at different time points to investigate the time-dependent behaviour of the nanoformulations with Caco-2 cells. Before flow cytometry analysis, the Caco-2 cells were washed with heparin to remove any membrane-associated nanoformulations (Iwasa *et al.*, 2006; Patel *et al.*, 2019). The cellular uptake of the nanoformulations was expressed as percentage fluorescence and was found to be between 2.5 to 5% after 2 h incubation (Figure 4.7A). PLGA-FPR nanoparticles showed the highest uptake into Caco-2 cells, but without being significantly different from the uptake of the CPP-tagged PLGA nanoparticles. After 6 h incubation, there was no increase in cellular uptake, indicating that a longer incubation time was not necessarily beneficial for the uptake of nanoformulations into Caco-2 cells (Figure 4.7A). Overall, the findings showed very low uptake of the PLGA-FPR and CPP-tagged PLGA-FPR nanoparticles in Caco-2 cells. Reports from the literature showed internalisation due to the increase or shift of mean fluorescence intensity of PLGA nanoparticles in Caco-2 cells in comparison to control formulations or dye solutions after incubation times between 1 and 4 h (Czuba *et al.*, 2018; Joshi *et al.*, 2016). CPP-modified proliposomes, reconstituted from dry liposomal formulations

before use, showed an initial higher uptake at 2 h, but at a time point of 4 h the mean fluorescence intensity for different proliposome formulations, with and without CPPs showed similar levels (Tunsirikongkon *et al.*, 2019). The study was performed with individual Caco-2 cells that were allowed to adhere overnight and mean fluorescence intensity of control cells without treatment for comparison was not reported.

The cell viability of Caco-2 cells was assessed over the time of the kinetic experiment using propidium iodide. The Caco-2 cells were viable and no toxicity was induced by the nanoformulations over the incubation period of 6 h (Figure 4.7B). Propidium iodide is taken up by dead cells and intercalates with DNA resulting in a red fluorescence and detection of propidium iodide-positive cell with flow cytometry indicates toxicity (Totterman *et al.*, 1997).

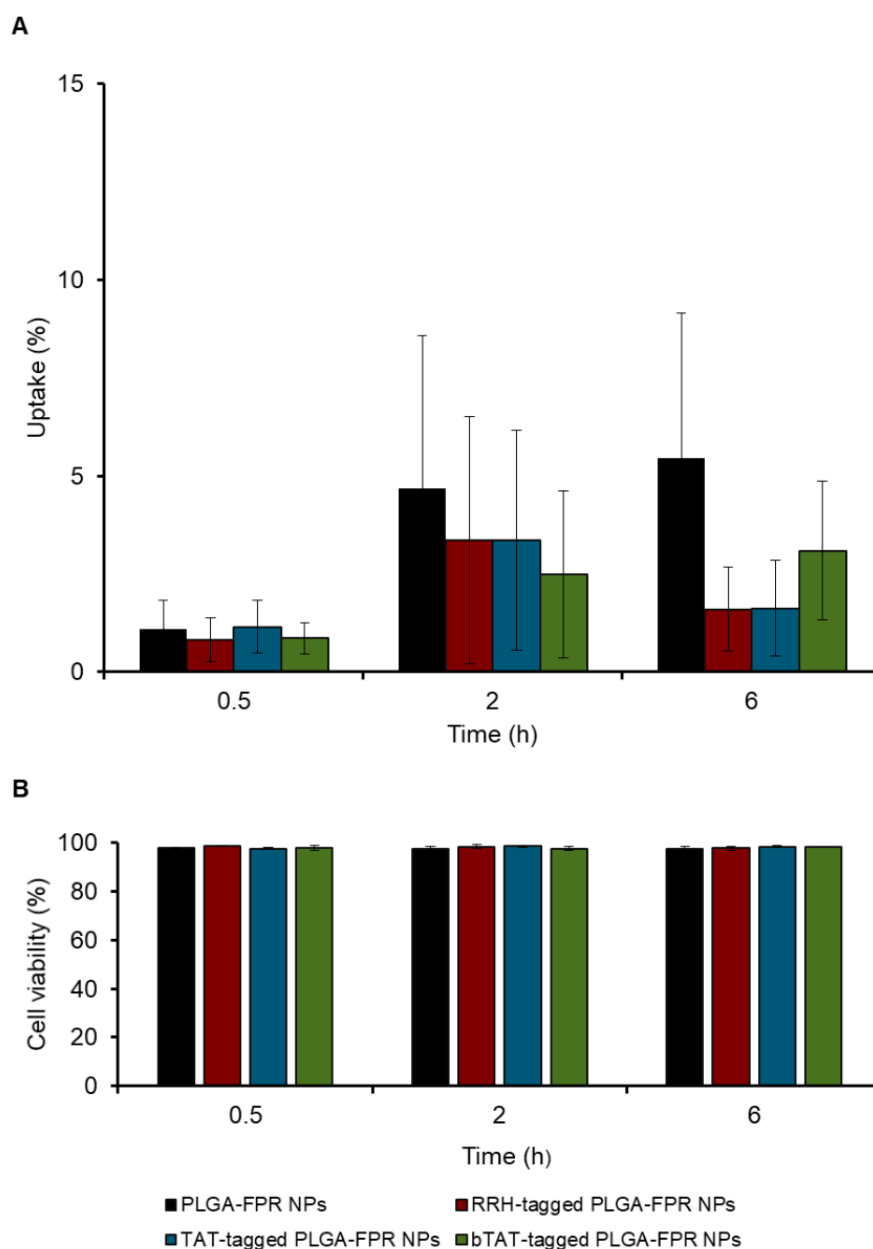


Figure 4.7. Uptake of PLGA-FPR and CPP-tagged PLGA-FPR nanoparticles prepared using the post-microfluidics conjugation approach in Caco-2 cells after incubation for different time points (0.5, 2 and 6 h) (A) and cell viability assessed with propidium iodide staining (B). Data are means \pm SEM ($n = 3$). NPs = nanoparticles.

Possible reasons for the low uptake found in the present study can be related to the Caco-2 cells and to the used nanoformulations. The Caco-2 cells were grown as a monolayer for 21 days before the quantitative and qualitative uptake experiments to generate cells that represent similar characteristics to the intestinal epithelium. With longer culturing times (> 14 days) the

Caco-2 cell monolayer represents a tight barrier due to fully developed tight junctions and internalisation of nanoparticles less favourable. Further, the conjugation efficiencies of the CPPs using the post-microfluidics conjugation approach were below 20% and therefore, the amount of CPP present might have been too low to enhance interactions with the cell surface.

In the literature, evidence of cellular uptake is found for unmodified and surface-modified nanoparticles including polymeric nanoparticles and liposomal formulations (Czuba *et al.*, 2018; Joshi *et al.*, 2016; Tunsirikongkon *et al.*, 2019), but transport across epithelia is often reported to be low. Reasons for low transport include possible exocytosis of nanoparticles towards the apical and basolateral side of the Caco-2 cell monolayer after internalization and during incubation for longer time points (Zhuang *et al.*, 2018). Also, the culturing times for Caco-2 cells used for uptake studies vary greatly between 24 h (Joshi *et al.*, 2016; Tunsirikongkon *et al.*, 2019) and 14 and 21 days (Czuba *et al.*, 2018; Zhuang *et al.*, 2018) of culturing, making the comparison of results difficult.

Since the ability of CPP-tagged PLGA-FPR nanoparticles to penetrate into Caco-2 cell monolayers was low, an association of the CPP-tagged PLGA-FPR nanoparticles was investigated. Flow cytometry data presented in Figure 4.8 shows the percent uptake of nanoformulations into Caco-2 cells after the cells were treated with heparin during sample preparation for the removal of membrane-associated nanoparticles. In order to discriminate between uptake and membrane-associated nanoparticles, a heparin treatment can be applied to cells (Iwasa *et al.*, 2006; Patel *et al.*, 2019). For evaluating the relative amount of membrane-associated nanoformulations, Caco-2 cells were incubated for 2 h with PLGA-FPR and CPP-tagged PLGA-FPR nanoparticles and analysed without heparin treatment. The comparison

between heparin treatment and no heparin treatment indicated that the amount of membrane-associated nanoformulation was low since the uptake, including membrane-associated nanoformulations, remained below 10% without heparin treatment (Figure 4.8). There was a 2 and 2.5-fold increase in percent uptake for PLGA-FPR and bTAT-tagged PLGA-FPR nanoparticles, respectively, when no heparin treatment was applied. The percent uptake for RRH- and TAT-tagged PLGA-FPR nanoparticles showed no difference between heparin treatment and no heparin treatment. Overall, this indicates that the increase in apparent uptake is related to the membrane-associated nanoparticles, which could be taken up into cells with longer incubation times.

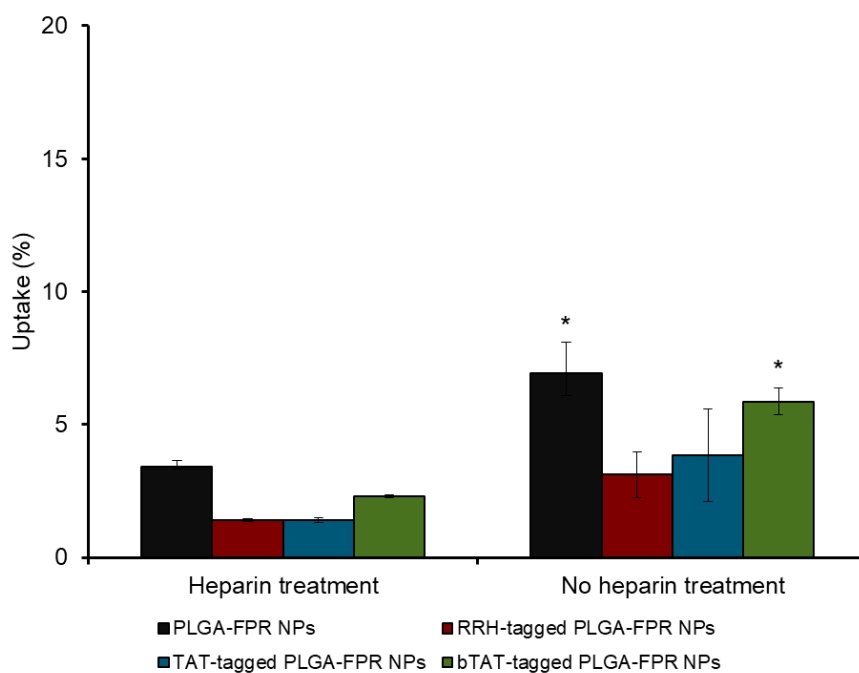


Figure 4.8. Comparison of uptake of PLGA-FPR and CPP-tagged PLGA-FPR nanoparticles after heparin treatment and no heparin treatment in Caco-2 cells after incubation for 2 h. Cells were either washed with heparin (20 $\mu\text{g}/\text{mL}$ in DPBS, pH 7.4) or washed with DPBS (pH 7.4) without heparin. Data are means \pm SEM ($n = 3$). * p -value < 0.05 for comparison between samples prepared with or without heparin treatment. NPs = nanoparticles.

4.4.3.3 Qualification of cellular uptake in Caco-2 cells

CLSM was applied for the qualitative assessment of the cellular uptake of PLGA-FPR and CPP-tagged PLGA-FPR nanoparticles in Caco-2 cells. In order to observe the Caco-2 cell monolayer under the microscope, the cell nucleus and the cell membrane were stained as described for HeLa cells. After incubation of the Caco-2 cell monolayer with PLGA-FPR nanoparticles, a red fluorescence of PLGA-FPR nanoparticles was observed within the monolayer (Figure 4.9A). TAT-tagged PLGA-FPR nanoparticles showed some red fluorescence in the Caco-2 cell monolayer indicating little uptake of the nanoparticles (Figure 4.9C). Uptake studies of nanoparticles containing PLGA are well-reported in the literature. A study by Cartiera *et al.* (2009) found that uptake of rhodamine-loaded PLGA nanoparticles with a size below 100 nm was low and after 24 h of incubation, an association to the Caco-2 cell monolayer with an age between 14 to 21 days was observed. Further, PLGA nanoparticles were found to accumulate in the cell cytoplasm and nucleus of Caco-2 cells (Win and Feng, 2005) and the observed fluorescence intensity was time- and concentration-dependent (He *et al.*, 2013; Joshi *et al.*, 2016; Katsikari *et al.*, 2009). Other studies using confocal microscopy showed that positively charged, lipid-modified PLA-PEG nanoparticles had a better uptake after 0.5 h incubation in Caco-2 cells compared to neutral and negatively charged lipid-modified PLA-PEG nanoparticles (Du *et al.*, 2018). Also, chitosan-coated PLGA nanoparticles with a positive surface charge showed stronger fluorescence than uncoated nanoparticles after 2 h incubation in Caco-2 cell monolayer (Sheng *et al.*, 2015). Uptake studies with CPP-modified nanoparticles showed stronger fluorescence of TAT- and R₈-modified nanoparticles in comparison to unmodified nanoparticles after incubation with Caco-2 cells for 1 h to 4 h (Chen *et al.*, 2017b; Koch *et al.*, 2005; Tunsirikongkon *et al.*, 2019; Zhu *et al.*, 2016a). In contrast to the literature, in this study very little evidence was found that PLGA-FPR and TAT-tagged PLGA-FPR nanoparticles are taken up by Caco-2 cells.

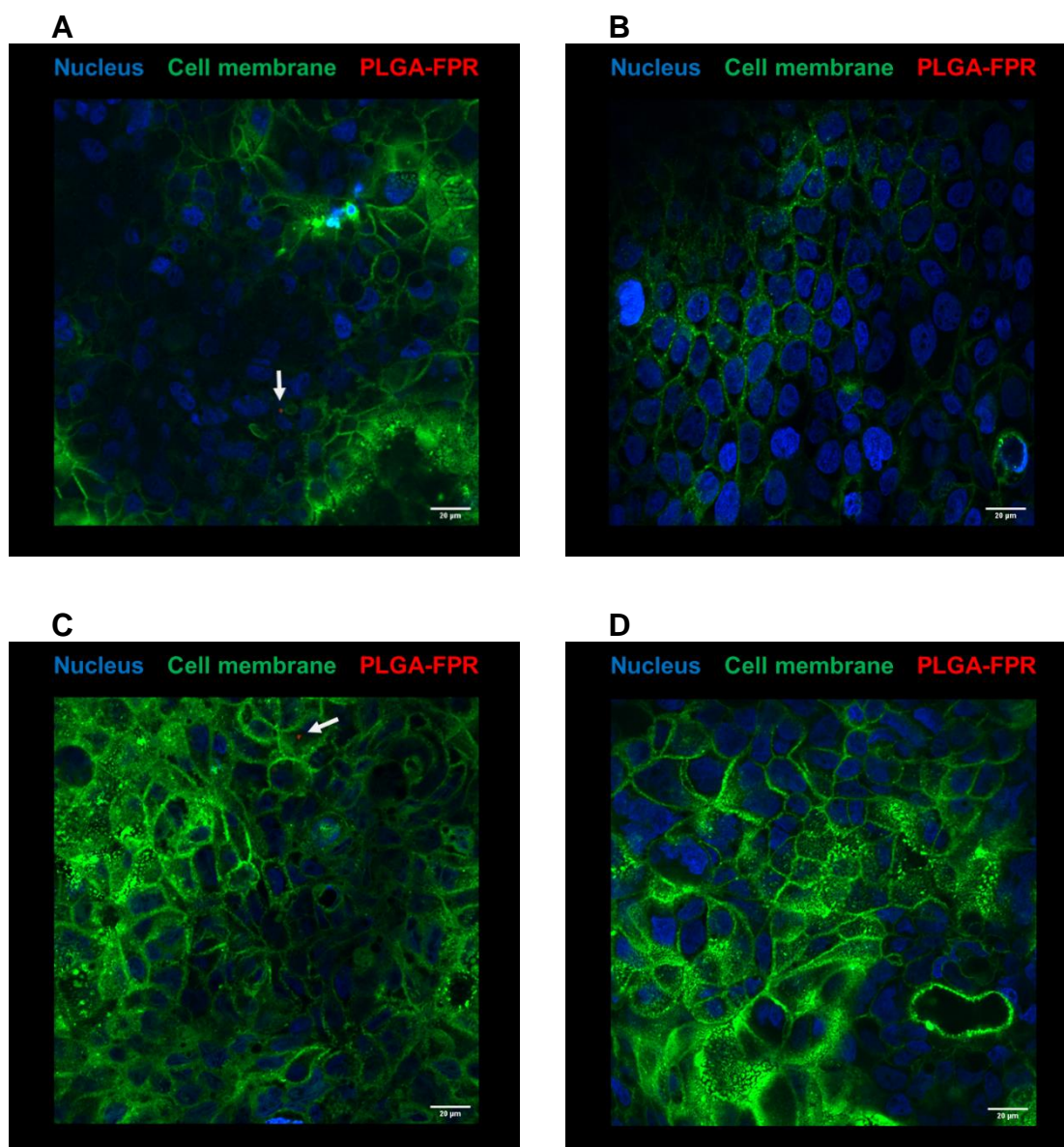


Figure 4.9. Representative confocal images of Caco-2 cell monolayer incubated for 2 h with PLGA-FPR (A), RRH- (B), TAT- (C) and bTAT-tagged PLGA-FPR nanoparticles (D) prepared using the post-microfluidics conjugation approach. The white arrow is pointing towards red fluorescence of PLGA-FPR nanoparticles or CPP-tagged PLGA-FPR nanoparticles.

In contrast to TAT-tagged PLGA-FPR nanoparticles, no uptake of RRH- and bTAT-tagged PLGA-FPR nanoparticles was observed within the Caco-2 cell monolayer (Figure 4.9B and D). To further evaluate the localization of the CPP-tagged PLGA-FPR nanoparticles z-stack images of Caco-2 cells were taken. The red fluorescence related to the CPP-tagged PLGA-FPR nanoparticles was observed towards the top layer of the Caco-2 cell monolayer indicating

an association with the cell membrane (Appendix VII). This association might be rather weak since little red fluorescence was seen. A difference in the behaviour of the CPP-tagged PLGA-FPR nanoparticles depending on the CPP architecture was not observed (Figure 4.9B, C and D). The confocal images of the Caco-2 cell monolayer showed the integrity of the cell membrane after incubation with the nanoformulations.

As discussed earlier, a comparison between the results published in the literature and results presented in this thesis is difficult as culturing times and analysis protocols vary greatly. In the literature, Caco-2 cells were of different ages (Cartiera *et al.*, 2009; Katsikari *et al.*, 2009; Sheng *et al.*, 2015; Tunsirikongkon *et al.*, 2019; Win and Feng, 2005), had a confluence of 70-85% (Cartiera *et al.*, 2009; Chen *et al.*, 2017b; Du *et al.*, 2018; He *et al.*, 2013; Joshi *et al.*, 2016), were fixed during sample preparation and either cell nucleus or cell membrane were stained (Cartiera *et al.*, 2009; Joshi *et al.*, 2016; Katsikari *et al.*, 2009; Koch *et al.*, 2005; Sheng *et al.*, 2015). In the present study, Caco-2 cells were cultured for 21 days to obtain a tight monolayer comparable with the small intestine. Culturing times of Caco-2 cells in literature are often less than 21 days and therefore no tight Caco-2 cell monolayer has developed and nanoparticles can penetrate easier into cells. In addition, the Caco-2 cells in the present study were not fixed to avoid artefacts introduced by the fixation process and cell compartments such as cell nucleus and membrane were stained to distinguish between the compartments. In particular, the age of Caco-2 cells has an influence on cellular uptake and the observation of no uptake might be related to the tight monolayer formed after 21 days.

The observation of no uptake for CPP-tagged PLGA nanoparticles in Caco-2 cells can also be related to little interaction between the CPPs and cells and a low concentration of CPP-

tagged PLGA-FPR nanoparticles reaching the cell surface. As discussed earlier, the amount of CPPs on PLGA-FPR nanoparticles was below 20% and in order to increase the amount of CPP, the fluorophore-labelled PLGA polymer can be spiked with non-labelled PLGA polymer. The addition of non-labelled PLGA will increase the amount of available carboxyl groups used for the conjugation of CPPs and thus the concentration of CPPs on the polymeric nanoparticles can be increased. Further, calculations to estimate the delivered dose can be applied to optimise the amount of nanoparticles that are actually reaching the cell surface. Increasing the nanoparticle concentration at the cell surface is crucial to ensure interactions between the cells and nanoparticles.

4.5 Conclusion

The physiochemical characteristics of CPP-tagged PLGA-FPR nanoparticles were controlled by the CPP architecture as previously observed for non-fluorescent PLGA. Changing the media from ultra-pure water to cell culture buffer resulted in larger PLGA-FPR and CPP-tagged PLGA-FPR nanoparticles (up to 250 nm) with a slightly negative surface charge. Further, the conjugation efficiency of CPPs to the fluorophore-labelled PLGA was low as binding sites for CPP conjugation were partly occupied by the fluorophore. The PLGA-FPR and CPP-tagged PLGA-FPR were non-toxic to HeLa and Caco-2 cells and showed low uptake in both HeLa cells and Caco-2 cells. An influence of CPP architecture on the uptake of CPP-tagged PLGA-FPR nanoparticles was not found, but CPP-tagged PLGA-FPR nanoparticles prepared using the post-microfluidics conjugation approach showed a slightly higher uptake in HeLa in comparison to CPP-tagged PLGA-FPR nanoparticles prepared using the *in situ* microfluidics conjugation approach. There was a trend for increased uptake in Caco-2 cells with longer incubations time of the nanoformulations. The low cellular uptake observed with

flow cytometry was supported by the confocal images for the nanoformulations in both cell lines. In addition, the confocal images indicated an association rather than uptake of the PLGA-FPR and CPP-tagged PLGA-FPR nanoparticles.

Chapter Five

General discussion and future directions

5.1 Introduction and general summary

Nanoparticulate drug delivery systems are of great interest to assist in the treatment of a range of different diseases that require biomacromolecules, such as proteins and peptides, as the therapeutic agent. Efficient delivery of drugs in nanoparticles after oral administration depends on the ability of the nanoparticles to shield and deliver the drug to the site of action. Encapsulation of biomacromolecules in nanoparticles protects the fragile drug against the harsh environment in the GIT following oral ingestion. One strategy to enhance nanoparticle-cell interactions after oral administration is the surface modification of polymeric nanoparticles with cell-penetrating peptides (CPPs) to increase interaction of the delivery system with the intestinal epithelium. Cellular internalisation of nanoparticles decorated with CPPs, such as TAT, is reported in the literature (Feiner-Gracia *et al.*, 2018; van Bracht *et al.*, 2014), however the surface modification of polymeric nanoparticles with CPPs of different architectures has not yet been explored. In this thesis, the hypothesis is that the CPP architecture influences nanoparticle-cell interactions and therefore novel surface-modified polymeric nanoparticles were designed as an oral drug delivery system to test this hypothesis. PLGA nanoparticles were surface-modified with CPPs of different architectures and the physicochemical properties of CPP-tagged PLGA nanoparticles were tuned by using CPPs of different architectures (Chapters 2 and 3). The distribution of CPPs on PLGA nanoparticles depends on the conjugation approach used for the preparation of CPP-tagged PLGA nanoparticles (Chapter 3). Association instead of uptake was found as between CPP-tagged PLGA nanoparticles and two different cell lines in *in vitro* cell culture studies (Chapter 4). The *in vitro* study with Caco-2 cells was used to evaluate the nanoparticle-cell interactions using a cell culture model representing the human intestinal epithelium. The *in vitro* study indicated association of the CPP-tagged PLGA nanoparticles with the cell membrane, in particular of nanoparticles surface-modified with the branched CPP. The observed nanoparticle-cell interactions represent the initial step before

internalisation of nanoparticles into Caco-2 cells. The presented results are valuable for a better understanding of nanoparticle-cell interactions of CPP-tagged PLGA nanoparticles utilizing the oral route of administration. Therefore, the title displays the crucial parts of the thesis including CPPs, the use of nanoformulations and the aim of oral administration in a broad context. The present Chapter firstly discusses the relevance of the results obtained in each Chapter in a broader context and then gives future direction for the further development of the nanoformulations.

5.2 Application of research in the wider research area

Surface modification of nanoparticles is a prudent approach to increase interactions between nanoparticles and the epithelium in the small intestine. Generally, nanoparticles are surface-modified to increase blood circulation time and avoid opsonisation by macrophages (Partikel *et al.*, 2019), for the targeting of specific cell-receptors on the cell surface (Bartheldyova *et al.*, 2018) and to introduce positive charges on the nanoparticle surface (Feiner-Gracia *et al.*, 2018). For these purposes, specific groups such as PEG, receptor-specific ligands and CPPs can be used, respectively. In this thesis, three CPPs with a distinct architecture were used namely the short RRH, the long linear TAT and the branched TAT (Chapter 2). The results presented in Chapter 2 show that after surface modification with CPPs, the surface of PLGA nanoparticles was tuned from slightly negative to slightly positive values depending on the CPP architecture. Of particular interest was the suitability of the branched CPP for surface modification of polymeric nanoparticles. To the best of my knowledge branched CPPs has not yet been conjugated to polymeric nanoparticles before. Further, modifications of the CPP sequence have been of great interest and an increase in positive charges in the CPP sequence was reported to enhance cellular uptake (Brock *et al.*, 2018). In this thesis, the novel branched

CPP, bTAT, was designed based on the known peptides TAT and RRH. As demonstrated in Chapter 2, the branched CPP can be conjugated to polymeric nanoparticles, demonstrating that surface decoration of nanoparticles with ligands of complex shape and architecture is feasible. Surface-modification of nanoparticles with complex ligands might be beneficial to increase cell interactions and improve the efficiency of drug delivery systems. In addition, the branched architecture of the CPP sequence is considered to cover more surface area of the cell as the amino acids in the branches can reach over a wider area and can potentially enhance interactions between CPP-tagged PLGA nanoparticles and cells.

The use of CPPs for the surface modification of polymeric nanoparticles results in a tuneability of the surface charge of polymeric nanoparticles. Further, the use of covalent bonds between the polymeric nanoparticles and the CPPs leads to well-defined systems in comparison to non-covalent bound CPPs as the amount of CPPs on covalent modified nanoparticles can be quantified and optimised. Pre- and post-conjugation approaches are well-described in the literature and require either the synthesis of polymer-ligand conjugates before formulation of nanoparticles or the performance of a conjugation reaction after formulation of nanoparticles (Kamaly *et al.*, 2016; Valencia *et al.*, 2013). In this thesis, the preparation of surface-modified polymeric nanoparticles using the *in situ* microfluidics conjugation approach was described for the first time. The *in situ* conjugation approach aims to utilize the benefits of microfluidics such as a rapid and controlled mixing of precursor materials for the formulation of surface-modified nanoparticles. The preparation time of the CPP-tagged PLGA nanoparticles was greatly reduced, as the post-microfluidics conjugation approach takes 2 days due to an overnight incubation, whereas the *in situ* microfluidics conjugation approach takes only 3 to 4 hours (Chapter 3). The innovative approach of gold labelling and the application of small angle X-ray scattering in this thesis proofed evidence that the CPP distribution depended on the

preparation method. Therefore, the *in situ* microfluidic conjugation approach is a time efficient and well-characterised approach that can be applied to the surface-modification of other nanoparticulate systems e.g. liposomes.

Following formulation, *in vitro* cell culture studies can elucidate nanoparticle-cell interactions to collect information about toxicity, cell response and efficacy of drug delivery. The testing of nanoparticles in different cell lines allows the identification of cell-specific interactions. HeLa cells are a well-known cell line for the investigation of cell interactions and uptake of CPPs, whereas Caco-2 cells are an *in vitro* model for the intestinal barrier offering the possibility to evaluate the suitability of nanoparticles as oral drug delivery systems. The initial contact between CPP-tagged PLGA nanoparticles and HeLa cells did not result in an efficient internalization of nanoformulations, which might be related to the limited incubation time of 1 h (Chapter 4). The analysis of CPP-tagged PLGA nanoparticles exposed to Caco-2 cells for different time points showed an association to the epithelial cells rather than localisation of the nanoformulations within cells in the Caco-2 cell monolayer (Chapter 4). A slight advantage of the nanoformulations prepared with the branched CPP was observed in Caco-2 cells indicating the potential of the branched CPP to be further investigated for oral drug delivery systems.

The minimal observed interactions observed between the CPP-tagged PLGA nanoparticles and HeLa or Caco-2 cells might be due to method-related limitations. As with most *in vitro* cell culture studies described in the literature, the *in vitro* cell culture studies in this thesis were performed in multiwell plates and this set up might not sufficiently represent the environment of the human GIT. As an example, a lack of similarity between the small

intestine and *in vitro* cell culture model relates to a difference in cell structure and differentiation, cell organisation, exposed surface area and flow conditions (Beduneau *et al.*, 2014; Guo *et al.*, 2000; Wang *et al.*, 2018). Further, when using multiwell plates, washing steps are compulsory for analysis and detachment of cells from the wells is thus possible. The forces used in these washing steps might be stronger compared to the flow of fluids *in vivo* resulting in the removal of non-tightly bound nanoparticles, which could have taken up by the cells eventually in an *in vivo* situation.

Formulation related-limitations identified in *in vitro* cell culture studies performed in this thesis were associated with the influence of the cell culture buffer on the measured surface charge of the CPP-tagged PLGA nanoparticles. Independent of the surface modification with CPPs of different architecture or no surface modification, the nanoformulations displayed net zeta potentials close to neutral. To achieve cellular uptake, negatively charged nanoparticles have to overcome an electrostatic repulsion barrier due to the same charge of nanoparticles and cells. This repulsion barrier is less difficult to overcome for slightly negatively charged nanoparticles (Reix *et al.*, 2012) and net neutral nanoparticles. Thus, the low interaction of the overall net neutral CPP-tagged PLGA nanoparticles presented in Chapter 4 might arise from formulation- and method-related limitations.

5.3 Future direction: Defining the surface of nanoparticles

Future direction should be aimed at specific improvements for the formulation of nanoparticles and analytical methods to overcome the described formulation- and method-related limitations. In order to improve the functionality of the CPP-tagged PLGA nanoparticles presented in this study, the surface coverage of the PLGA nanoparticles with

CPPs and the CPP orientation can be optimised. The used CPPs, in particular, the long linear TAT and the branched TAT, have multiple primary amines in their sequence and binding to the surface of PLGA nanoparticles can occur in multiple directions. Without controlling the orientation of the CPPs on the nanoparticle surface, the surface coverage is non-uniform and this results in variation of how individual CPP molecules are present on the PLGA nanoparticle surface. To achieve uniform coverage of the surface of PLGA nanoparticles with CPPs, protective groups could be added to the CPPs prior to the conjugation reaction. The addition of protective groups limits the amount of available primary amines in the CPP sequence and facilitates the arrangement of the CPPs in a defined orientation on the surface of PLGA nanoparticles. It should be noted that the protection groups have to be removed before the nanoformulations can be used for further studies. Application of this approach results in specific amino acid sequences pointing towards the cell membrane to trigger nanoparticle-cell interaction. The targeting-specificity of modified nanoparticles is increased with the conjugation of the sdAb protein to the nanoparticle surface if the protein remains in its native structure and the orientation of the protein favours interaction with the targeted receptors (Yong *et al.*, 2019).

A recent advance in the area of surface modification for nanoparticles is the use of crystal structure to identify protein binding sites and the binding of proteins to the surface of nanoparticles utilizing chemical modification and reactions to achieve a desired surface orientation (Yong *et al.*, 2019). An example of innovative surface modifications is molecular imprinting for the design of polymeric nanoparticles with receptor specific ligands. The principle behind molecular imprinting is that functionalized monomers polymerize with cross-linkers around a template molecule e.g. a cell ligand (Chen *et al.*, 2016). After removing the template, the formulated nanoparticles include the shape and size of the ligands, which are

embedded in the rigid polymer (Gagliardi *et al.*, 2017). An example for molecular imprinting of polymeric nanoparticles was shown by Gagliardi *et al.* (2017). They imprinted PLGA nanoparticles towards the biotin-receptor, which is overexpressed on cancer cells. The analysis of HeLa cells showed an increase in fluorescence for molecular imprinted PLGA nanoparticles in comparison to control nanoparticles over 30 min indicating the receptor-mediated uptake of the biotin imprinted PLGA nanoparticles (Gagliardi *et al.*, 2017).

Work extending from this thesis can aim to optimise the conjugation reaction between polymer and ligand within the microfluidics channel for the formulation of surface-modified nanoparticles. This could be investigated using techniques such as microfluidic-small angle neutron scattering. To enable real time neutron scattering, the microfluidic device needs to fulfil certain requirements including high transmission for neutrons, low background scattering and little neutron-induced radioactivity (Adamo *et al.*, 2018; Lopez *et al.*, 2015). With the introduction of the microchannel into the scattering beam, the kinetics of *in situ* microfluidic conjugation reactions can be followed and used for an optimisation of the process-related parameters. Further, the *in situ* microfluidics conjugation approach is of interest for the potential encapsulation of protein drugs, as surface modification should be avoided after protein encapsulation to prevent unwanted release (Zhu *et al.*, 2016b). Generally, a bulk surface modification approach after preparation of nanoparticles is a time-intensive process and nanoparticles are exposed to buffered solutions. A possible issue is that degradation of the nanoparticles and unwanted release of encapsulated drug can occur due to the exposure of the nanoparticles to a buffer with reagents and pH necessary to maintain ideal conditions for the conjugation reaction, but not ideal for the storage of nanoparticles. Thus, for drug-loaded nanoparticles, simultaneous drug-loading and surface modification is advantageous to ensure the retention of the drug within the nanoparticles until use.

5.4 Future direction: Elucidating nanoparticle-cell interactions

Future experiments to improve current cell culture methods can be facilitated by both, microscopic techniques and microfluidic-based cell experiments. Static and dynamic changes in the membrane of live cells can be monitored with scanning ion conductance microscopy (Chen *et al.*, 2019a). Topographical changes in the cell membrane can be recorded after incubation with nanoparticles (Chen *et al.*, 2019a) to elucidate interactions between nanoparticles and cells. To explore details of interactions between individual nanoparticles and cells, the technique of single particle tracking can be utilized. The mobility of fluorophore-labelled nanoparticles is tracked using an optical microscope to generate a trajectory of the nanoparticle mobility as a function of time and space (Manzo and Garcia-Parajo, 2015). Tracking individual nanoparticles aids in understanding the physical behaviour of nanoparticles including sedimentation and diffusion during incubation with cells. Luo *et al.* (2019a) showed that internalisation of CPP-modified semiconductive polymer dots in HeLa cells occurred in three stages, namely the movement of nanoparticles towards the cell membrane, crossing of cell membrane and movement of the nanoparticles within the cytosol. Single particle tracking is a promising technique and can be exploited in future studies to gain more insight into how the architecture of CPPs influences interactions with cells. The main advantage of single particle tracking over other methods such as confocal laser scanning microscopy is that the dynamics of the interactions between nanoparticles and cells are captured. Traditional static images of nanoparticles and cells are not able to visualise the movement of nanoparticles during incubation, which generates useful information about the timeframe and kind of interactions. Lastly, microfluidic devices can be fabricated to accommodate a membrane within the microchannel to accommodate a Caco-2 cell monolayer, which is surrounded by media flowing on the apical and basolateral side (Tan *et al.*, 2018). In this modified microfluidic device, drug

transport studies can be tested under flow conditions with similar fluid shear stresses found in the human gut (Tan *et al.*, 2018) making the results more biologically-relevant.

Future *in vitro* experiments looking at the kinetics of interaction over a longer time period may profit from taking the delivered dose of nanoparticles into consideration to ensure that nanoparticles reach the cell surface and interactions between surface ligands such as CPPs and cells can occur. The design of future experiments is recommended to follow the guidelines for minimum information reporting in bio-nano experimental literature (MIRIBEL) to obtain results that are based on standardised protocols and easily comparable with other studies following the guidelines. Further, an underestimation of interactions between CPP-tagged PLGA nanoparticles and cells due to the analytical methods is possible and therefore, the utilization of microfluidics for uptake studies and visualization of nanoparticle-cell interactions with single particle tracking in future studies has the potential to add crucial information.

In conclusion, this thesis demonstrates that polymeric nanoparticles can be modified with CPPs of different architecture to tune the surface characteristics of PLGA nanoparticles. Microfluidics has been shown for the first time to be suitable for the conjugation of CPPs to the PLGA polymer and the formation of surface-modified polymeric nanoparticles. The well-characterised nanoformulations presented in this thesis can be further exploited to elucidate interactions at the nano-bio interface that govern cellular interactions and therefore the efficacy of delivered therapeutics.

References

- Abouelmagd, S.A., Ku, Y.J., Yeo, Y., 2015. Low molecular weight chitosan-coated polymeric nanoparticles for sustained and pH-sensitive delivery of paclitaxel. *Journal of Drug Targeting*, 23 (7-8), 725-35.
- Adamo, M., Poulos, A.S., G. Lopez, C., Martel, A., Porcar, L., Cabral, J.T., 2018. Droplet microfluidic SANS. *Soft Matter*, 14 (10), 1759-70.
- Aebi, U., Pollard, T.D., 1987. A glow discharge unit to render electron microscope grids and other surfaces hydrophilic. *Journal of Electron Microscopy Technique*, 7 (1), 29-33.
- Ahmad Khanbeigi, R., Kumar, A., Sadouki, F., Lorenz, C., Forbes, B., Dailey, L.A., Collins, H., 2012. The delivered dose: Applying particokinetics to in vitro investigations of nanoparticle internalization by macrophages. *Journal of Controlled Release*, 162 (2), 259-66.
- Alexander-Bryant, A.A., Vanden Berg-Foels, W.S., Wen, X., 2013. Bioengineering strategies for designing targeted cancer therapies. *Advances in Cancer Research*, 118, 1-59.
- Allemann, E., Leroux, J.C., Gurny, R., Doelker, E., 1993. In vitro extended-release properties of drug-loaded poly(DL-lactic acid) nanoparticles produced by a salting-out procedure. *Pharmaceutical Research*, 10 (12), 1732-7.
- Alqahtani, S., Simon, L., Astete, C.E., Alayoubi, A., Sylvester, P.W., Nazzal, S., Shen, Y., Xu, Z., Kaddoumi, A., Sabliov, C.M., 2015. Cellular uptake, antioxidant and antiproliferative activity of entrapped alpha-tocopherol and gamma-tocotrienol in poly (lactic-co-glycolic) acid (PLGA) and chitosan covered PLGA nanoparticles (PLGA-Chi). *Journal of Colloid and Interface Science*, 445, 243-51.
- Alves, I.D., Goasdoue, N., Correia, I., Aubry, S., Galanth, C., Sagan, S., Lavielle, S., Chassaing, G., 2008. Membrane interaction and perturbation mechanisms induced by two cationic cell penetrating peptides with distinct charge distribution. *Biochimica et Biophysica Acta*, 1780 (7-8), 948-59.
- Amoura, M., Illien, F., Joliot, A., Guitot, K., Offer, J., Sagan, S., Burlina, F., 2019. Head to tail cyclisation of cell-penetrating peptides: Impact on GAG-dependent internalisation and direct translocation. *Chemical Communications*, 55 (31), 4566-69.
- Amoyav, B., Benny, O., 2018. Controlled and tunable polymer particles' production using a single microfluidic device. *Applied Nanoscience*, 8 (4), 905-14.
- Angeles-Boza, A.M., Erazo-Oliveras, A., Lee, Y.J., Pellois, J.P., 2010. Generation of endosomolytic reagents by branching of cell-penetrating peptides: Tools for the delivery of bioactive compounds to live cells in cis or trans. *Bioconjugate Chemistry*, 21 (12), 2164-7.
- Arshad, A., Yang, B., Bienemann, A.S., Barua, N.U., Wyatt, M.J., Woolley, M., Johnson, D.E., Edler, K.J., Gill, S.S., 2015. Convection-enhanced delivery of carboplatin PLGA nanoparticles for the treatment of glioblastoma. *PLoS One*, 10 (7), e0132266.
- Augsten, C., Kiselev, M.A., Gehrke, R., Hause, G., Mäder, K., 2008. A detailed analysis of biodegradable nanospheres by different techniques--a combined approach to detect particle sizes and size distributions. *Journal of Pharmaceutical and Biomedical Analysis*, 47 (1), 95-102.
- Avgoustakis, K., 2008. Poly lactide-co-glycolic acid (PLGA), in: Mishra, M. (Ed.), *Encyclopedia of Biomaterials and Biomedical Engineering*, 1st ed. Taylor & Francis pp. 2259-69.
- Babos, G., Biró, E., Meiczinger, M., Feczko, T., 2018. Dual drug delivery of sorafenib and doxorubicin from PLGA and PEG-PLGA polymeric nanoparticles. *Polymers*, 10 (8), 895.

- Baby, T., Liu, Y., Middelberg, A.P.J., Zhao, C.-X., 2017. Fundamental studies on throughput capacities of hydrodynamic flow-focusing microfluidics for producing monodisperse polymer nanoparticles. *Chemical Engineering Science*, 169, 128-39.
- Bahnsen, J.S., Franzyk, H., Sandberg-Schaal, A., Nielsen, H.M., 2013. Antimicrobial and cell-penetrating properties of penetratin analogs: Effect of sequence and secondary structure. *Biochimica et Biophysica Acta*, 1828 (2), 223-32.
- Bailey, B.A., Desai, K.H., Ochyl, L.J., Ciotti, S.M., Moon, J.J., Schwendeman, S.P., 2017. Self-encapsulating poly(lactic-co-glycolic acid) (PLGA) microspheres for intranasal vaccine delivery. *Molecular Pharmaceutics*, 14 (9), 3228-37.
- Bairagi, U., Mittal, P., Singh, J., Mishra, B., 2018. Preparation, characterization, and in vivo evaluation of nano formulations of ferulic acid in diabetic wound healing. *Drug Development and Industrial Pharmacy*, 44 (11), 1783-96.
- Banerjee, A., Qi, J., Gogoi, R., Wong, J., Mitragotri, S., 2016. Role of nanoparticle size, shape and surface chemistry in oral drug delivery. *Journal of Controlled Release*, 238, 176-85.
- Banik, B.L., Fattahi, P., Brown, J.L., 2016. Polymeric nanoparticles: The future of nanomedicine. *Wiley Interdisciplinary Reviews: Nanomedicine and Nanobiotechnology*, 8 (2), 271-99.
- Barreto-Vieira, D.F., Barth, O.M., 2015. Negative and positive staining in transmission electron microscopy for virus diagnosis, in: Maitama, Y. (Ed.), *Microbiology in Agriculture and Human Health*, 1st ed. Intech, pp. 45-56.
- Bartczak, D., Kanaras, A.G., 2011. Preparation of peptide-functionalized gold nanoparticles using one pot EDC/sulfo-NHS coupling. *Langmuir*, 27 (16), 10119-23.
- Bartheldyova, E., Effenberg, R., Masek, J., Prochazka, L., Knotigova, P.T., Kulich, P., Hubatka, F., Velinska, K., Zelnickova, J., Zouharova, D., Fojtikova, M., Hrebik, D., Plevka, P., Mikulik, R., Miller, A.D., Macaulay, S., Zyka, D., Droz, L., Raska, M., Ledvina, M., Turanek, J., 2018. Hyaluronic acid surface modified liposomes prepared via orthogonal aminoxy coupling: Synthesis of nontoxic aminoxylipids based on symmetrically alpha-branched fatty acids, preparation of liposomes by microfluidic mixing, and targeting to cancer cells expressing CD44. *Bioconjugate Chemistry*, 29 (7), 2343-56.
- Beduneau, A., Tempesta, C., Fimbel, S., Pellequer, Y., Jannin, V., Demarne, F., Lamprecht, A., 2014. A tunable Caco-2/HT29-MTX co-culture model mimicking variable permeabilities of the human intestine obtained by an original seeding procedure. *European Journal of Pharmaceutics and Biopharmaceutics*, 87 (2), 290-8.
- Belliveau, N.M., Huft, J., Lin, P.J., Chen, S., Leung, A.K., Leaver, T.J., Wild, A.W., Lee, J.B., Taylor, R.J., Tam, Y.K., Hansen, C.L., Cullis, P.R., 2012. Microfluidic synthesis of highly potent limit-size lipid nanoparticles for in vivo delivery of siRNA. *Molecular Therapy Nucleic Acids*, 1, e37.
- Bilati, U., Pasquarello, C., Corthals, G.L., Hochstrasser, D.F., Allemann, E., Doelker, E., 2005. Matrix-assisted laser desorption/ionization time-of-flight mass spectrometry for quantitation and molecular stability assessment of insulin entrapped within PLGA nanoparticles. *Journal of Pharmaceutical Sciences*, 94 (3), 688-94.
- Binder, H., Lindblom, G., 2003. Charge-dependent translocation of the Trojan peptide penetratin across lipid membranes. *Biophysical Journal*, 85 (2), 982-95.
- Birch, D., Christensen, M.V., Staerk, D., Franzyk, H., Nielsen, H.M., 2017. Fluorophore labeling of a cell-penetrating peptide induces differential effects on its cellular distribution and affects cell viability. *Biochimica et Biophysica Acta (BBA) - Biomembranes*, 1859 (12), 2483-94.

- Birch, D., Diedrichsen, R.G., Christophersen, P.C., Mu, H., Nielsen, H.M., 2018a. Evaluation of drug permeation under fed state conditions using mucus-covered Caco-2 cell epithelium. *European Journal of Pharmaceutical Sciences*, 118, 144-53.
- Birch, D., Christensen, M.V., Staerk, D., Franzyk, H., Nielsen, H.M., 2018b. Stereochemistry as a determining factor for the effect of a cell-penetrating peptide on cellular viability and epithelial integrity. *Biochemical Journal*, 475 (10), 1773-88.
- Bobo, D., Robinson, K.J., Islam, J., Thurecht, K.J., Corrie, S.R., 2016. Nanoparticle-based medicines: A review of FDA-approved materials and clinical trials to date. *Pharmaceutical Research*, 33 (10), 2373-87.
- Boegh, M., Foged, C., Müllertz, A., Nielsen, H.M., 2013. Mucosal drug delivery: Barriers, in vitro models and formulation strategies. *Journal of Drug Delivery Science and Technology*, 23 (4), 383-91.
- Boegh, M., Baldursdottir, S.G., Müllertz, A., Nielsen, H.M., 2014. Property profiling of biosimilar mucus in a novel mucus-containing in vitro model for assessment of intestinal drug absorption. *European Journal of Pharmaceutics and Biopharmaceutics*, 87 (2), 227-35.
- Bohrey, S., Chourasiya, V., Pandey, A., 2016. Factorial design based preparation, optimization, characterization and in vitro drug release studies of olanzapine loaded PLGA nanoparticles. *Materials Research Express*, 3 (12), 125403.
- Bootz, A., Vogel, V., Schubert, D., Kreuter, J., 2004. Comparison of scanning electron microscopy, dynamic light scattering and analytical ultracentrifugation for the sizing of poly(butyl cyanoacrylate) nanoparticles. *European Journal of Pharmaceutics and Biopharmaceutics*, 57 (2), 369-75.
- Borrelli, A., Tornesello, A.L., Tornesello, M.L., Buonaguro, F.M., 2018. Cell penetrating peptides as molecular carriers for anti-cancer agents. *Molecules*, 23 (2).
- Bourganis, V., Karamanidou, T., Kammona, O., Kiparissides, C., 2017. Polyelectrolyte complexes as prospective carriers for the oral delivery of protein therapeutics. *European Journal of Pharmaceutics and Biopharmaceutics*, 111, 44-60.
- Boyd, B.J., Rades, T., 2016. Applications of small angle X-ray scattering in pharmaceutical science, in: Müllertz, A., Perrie, Y., Rades, T. (Eds.), *Analytical techniques in the pharmaceutical sciences*. Springer, pp. 339-60.
- Bozkir, A., Saka, O.M., 2005. Formulation and investigation of 5-FU nanoparticles with factorial design-based studies. *Il Farmaco*, 60 (10), 840-46.
- Bramosanti, M., Chronopoulou, L., Grillo, F., Valletta, A., Palocci, C., 2017. Microfluidic-assisted nanoprecipitation of antiviral-loaded polymeric nanoparticles. *Colloids and Surfaces A: Physicochemical and Engineering Aspects*, 532, 369-76.
- Brar, S.K., Verma, M., 2011. Measurement of nanoparticles by light-scattering techniques. *TrAC Trends in Analytical Chemistry*, 30 (1), 4-17.
- Brock, D.J., Kustigian, L., Jiang, M., Graham, K., Wang, T.Y., Erazo-Oliveras, A., Najjar, K., Zhang, J., Rye, H., Pellois, J.P., 2018. Efficient cell delivery mediated by lipid-specific endosomal escape of supercharged branched peptides. *Traffic*, 19 (6), 421-35.
- Brock, R., 2014. The uptake of arginine-rich cell-penetrating peptides: Putting the puzzle together. *Bioconjugate Chemistry*, 25 (5), 863-8.
- Bu, X., Zhu, T., Ma, Y., Shen, Q., 2015. Co-administration with cell penetrating peptide enhances the oral bioavailability of docetaxel-loaded nanoparticles. *Drug Development and Industrial Pharmacy*, 41 (5), 764-71.
- Cai, H., Liang, Z., Huang, W., Wen, L., Chen, G., 2017. Engineering PLGA nano-based systems through understanding the influence of nanoparticle properties and cell-penetrating peptides for cochlear drug delivery. *International Journal of Pharmaceutics*, 532 (1), 55-65.

- Caldero, G., Garcia-Celma, M.J., Solans, C., 2011. Formation of polymeric nano-emulsions by a low-energy method and their use for nanoparticle preparation. *Journal of Colloid and Interface Science*, 353 (2), 406-11.
- Caldorera-Moore, M., Vela Ramirez, J.E., Peppas, N.A., 2019. Transport and delivery of interferon-alpha through epithelial tight junctions via pH-responsive poly(methacrylic acid-grafted-ethylene glycol) nanoparticles. *Journal of Drug Targeting*, 27 (5-6), 582-89.
- Capretto, L., Mazzitelli, S., Brognara, E., Lampronti, I., Carugo, D., Hill, M., Zhang, X., Gambari, R., Nastruzzi, C., 2012. Mithramycin encapsulated in polymeric micelles by microfluidic technology as novel therapeutic protocol for beta-thalassemia. *International Journal of Nanomedicine*, 7, 307-24.
- Capretto, L., Carugo, D., Mazzitelli, S., Nastruzzi, C., Zhang, X., 2013. Microfluidic and lab-on-a-chip preparation routes for organic nanoparticles and vesicular systems for nanomedicine applications. *Advanced Drug Delivery Reviews*, 65 (11), 1496-532.
- Cardoso, A.M.S., Trabulo, S., Cardoso, A.L., Lorents, A., Morais, C.M., Gomes, P., Nunes, C., Lúcio, M., Reis, S., Padari, K., Pooga, M., Pedroso de Lima, M.C., Jurado, A.S., 2012. S4(13)-PV cell-penetrating peptide induces physical and morphological changes in membrane-mimetic lipid systems and cell membranes: Implications for cell internalization. *Biochimica et Biophysica Acta*, 1818 (3), 877-88.
- Cartiera, M.S., Johnson, K.M., Rajendran, V., Caplan, M.J., Saltzman, W.M., 2009. The uptake and intracellular fate of PLGA nanoparticles in epithelial cells. *Biomaterials*, 30 (14), 2790-8.
- Chelopo, M.P., Kalombo, L., Wesley-Smith, J., Grobler, A., Hayeshi, R., 2016. The fabrication and characterization of a PLGA nanoparticle–Pheroid® combined drug delivery system. *Journal of Materials Science*, 52 (6), 3133-45.
- Chen, F., Manandhar, P., Ahmed, M.S., Chang, S., Panday, N., Zhang, H., Moon, J.H., He, J., 2019a. Extracellular surface potential mapping by scanning ion conductance microscopy revealed transient transmembrane pore formation induced by conjugated polymer nanoparticles. *Macromolecular Bioscience*, 19 (2), e1800271.
- Chen, J., Wu, Q., Luo, L., Wang, Y., Zhong, Y., Dai, H.B., Sun, D., Luo, M.L., Wu, W., Wang, G.X., 2017a. Dual tumor-targeted poly(lactic-co-glycolic acid)-polyethylene glycol-folic acid nanoparticles: A novel biodegradable nanocarrier for secure and efficient antitumor drug delivery. *International Journal of Nanomedicine*, 12, 5745-60.
- Chen, L., Wang, X., Lu, W., Wu, X., Li, J., 2016. Molecular imprinting: Perspectives and applications. *Chemical Society Reviews*, 45 (8), 2137-211.
- Chen, Q., Gou, S., Ma, P., Song, H., Zhou, X., Huang, Y., Kwon Han, M., Wan, Y., Kang, Y., Xiao, B., 2019b. Oral administration of colitis tissue-accumulating porous nanoparticles for ulcerative colitis therapy. *International Journal of Pharmaceutics*, 557, 135-44.
- Chen, S., Guo, F., Deng, T., Zhu, S., Liu, W., Zhong, H., Yu, H., Luo, R., Deng, Z., 2017b. Eudragit S100-coated chitosan nanoparticles co-loading Tat for enhanced oral colon absorption of insulin. *AAPS PharmSciTech*, 18 (4), 1277-87.
- Chiesa, E., Dorati, R., Modena, T., Conti, B., Genta, I., 2018. Multivariate analysis for the optimization of microfluidics-assisted nanoprecipitation method intended for the loading of small hydrophilic drugs into PLGA nanoparticles. *International Journal of Pharmaceutics*, 536 (1), 165-77.
- Chiu, J.Z., Tucker, I.G., McLeod, B.J., McDowell, A., 2015. Arginine-tagging of polymeric nanoparticles via histidine to improve cellular uptake. *European Journal of Pharmaceutics and Biopharmaceutics*, 89, 48-55.
- Clara-Rahola, J., Moscoso, A., Belén Ruiz-Muelle, A., Laurenti, M., Formanek, P., Lopez-Romero, J.M., Fernández, I., Diaz, J.F., Rubio-Retama, J., Fery, A., Contreras-Cáceres,

- R., 2018. Au@p4VP core@shell pH-sensitive nanocomposites suitable for drug entrapment. *Journal of Colloid and Interface Science*, 514, 704-14.
- Clayton, A.H.A., Atcliffe, B.W., Howlett, G.J., Sawyer, W.H., 2006. Conformation and orientation of penetratin in phospholipid membranes. *Journal of Peptide Science*, 12 (3), 233-38.
- Clulow, A.J., Salim, M., Hawley, A., Boyd, B.J., 2018. A closer look at the behaviour of milk lipids during digestion. *Chemistry and Physics of Lipids*, 211, 107-16.
- Cole, H., Bryan, D., Lancaster, L., Mawas, F., Vllasaliu, D., 2018. Chitosan nanoparticle antigen uptake in epithelial monolayers can predict mucosal but not systemic in vivo immune response by oral delivery. *Carbohydrate Polymers*, 190, 248-54.
- Connolly, M., 1983. Solvent-accessible surfaces of proteins and nucleic acids. *Science*, 221 (4612), 709-13.
- Coolen, A.L., Lacroix, C., Mercier-Gouy, P., Delaune, E., Monge, C., Exposito, J.Y., Verrier, B., 2019. Poly(lactic acid) nanoparticles and cell-penetrating peptide potentiate mRNA-based vaccine expression in dendritic cells triggering their activation. *Biomaterials*, 195, 23-37.
- Cory, A.H., Owen, T.C., Barltrop, J.A., Cory, J.G., 1991. Use of an aqueous soluble tetrazolium/formazan assay for cell growth assays in culture. *Cancer Communications*, 3 (7), 207-12.
- Cox, A., Vinciguerra, D., Re, F., Magro, R.D., Mura, S., Masserini, M., Couvreur, P., Nicolas, J., 2019. Protein-functionalized nanoparticles derived from end-functional polymers and polymer prodrugs for crossing the blood-brain barrier. *European Journal of Pharmaceutics and Biopharmaceutics*, 142, 70-82.
- Crucho, C.I.C., Barros, M.T., 2017. Polymeric nanoparticles: A study on the preparation variables and characterization methods. *Materials Science and Engineering: C Materials for Biological Applications*, 80, 771-84.
- Czuba, E., Diop, M., Mura, C., Schaschkow, A., Langlois, A., Bietiger, W., Neidl, R., Virgiglio, A., Auberval, N., Julien-David, D., Maillard, E., Frere, Y., Marchioni, E., Pinget, M., Sigrist, S., 2018. Oral insulin delivery, the challenge to increase insulin bioavailability: Influence of surface charge in nanoparticle system. *International Journal of Pharmaceutics*, 542 (1-2), 47-55.
- Danhier, F., Ansorena, E., Silva, J.M., Coco, R., Le Breton, A., Preat, V., 2012. PLGA-based nanoparticles: An overview of biomedical applications. *Journal of Controlled Release*, 161 (2), 505-22.
- Date, A.A., Hanes, J., Ensign, L.M., 2016. Nanoparticles for oral delivery: Design, evaluation and state-of-the-art. *Journal of Controlled Release*, 240, 504-26.
- Dausend, J., Musyanovych, A., Dass, M., Walther, P., Schrezenmeier, H., Landfester, K., Mailander, V., 2008. Uptake mechanism of oppositely charged fluorescent nanoparticles in HeLa cells. *Macromolecular Bioscience*, 8 (12), 1135-43.
- de Jonge, N., Ross, F.M., 2011. Electron microscopy of specimens in liquid. *Nature Nanotechnology*, 6, 695-704.
- Derakhshandeh, K., Erfan, M., Dadashzadeh, S., 2007. Encapsulation of 9-nitrocamptothecin, a novel anticancer drug, in biodegradable nanoparticles: Factorial design, characterization and release kinetics. *European Journal of Pharmaceutics and Biopharmaceutics*, 66 (1), 34-41.
- Derossi, D., Calvet, S., Trembleau, A., Brunissen, A., Chassaing, G., Prochiantz, A., 1996. Cell internalization of the third helix of the Antennapedia homeodomain is receptor-independent. *The Journal of Biological Chemistry*, 271 (30), 18188-93.

- Desgouilles, S., Vauthier, C., Bazile, D., Vacus, J., Grossiord, J.-L., Veillard, M., Couvreur, P., 2003. The design of nanoparticles obtained by solvent evaporation: A comprehensive study. *Langmuir*, 19 (22), 9504-10.
- Di Cola, E., Grillo, I., Ristori, S., 2016. Small angle X-ray and neutron scattering: Powerful tools for studying the structure of drug-loaded liposomes. *Pharmaceutics*, 8 (2).
- Dong, Y.D., Tchung, E., Nowell, C., Kaga, S., Leong, N., Mehta, D., Kaminskas, L.M., Boyd, B.J., 2019. Microfluidic preparation of drug-loaded PEGylated liposomes, and the impact of liposome size on tumour retention and penetration. *Journal of Liposome Research*, 29 (1), 1-9.
- Donno, R., Gennari, A., Lallana, E., De La Rosa, J.M.R., d'Arcy, R., Treacher, K., Hill, K., Ashford, M., Tirelli, N., 2017. Nanomanufacturing through microfluidic-assisted nanoprecipitation: Advanced analytics and structure-activity relationships. *International Journal of Pharmaceutics*, 534 (1), 97-107.
- Draheim, C., de Crecy, F., Hansen, S., Collnot, E.M., Lehr, C.M., 2015. A design of experiment study of nanoprecipitation and nano spray drying as processes to prepare PLGA nano- and microparticles with defined sizes and size distributions. *Pharmaceutical Research*, 32 (8), 2609-24.
- Du, X.J., Wang, J.L., Iqbal, S., Li, H.J., Cao, Z.T., Wang, Y.C., Du, J.Z., Wang, J., 2018. The effect of surface charge on oral absorption of polymeric nanoparticles. *Biomaterials Science*, 6 (3), 642-50.
- Du, Y., Zhang, Z., Yim, C., Lin, M., Cao, X., 2010. A simplified design of the staggered herringbone micromixer for practical applications. *Biomicrofluidics*, 4 (2), 024105.
- Dubes, A., Parrot-Lopez, H., Abdelwahed, W., Degobert, G., Fessi, H., Shahgaldian, P., Coleman, A.W., 2003. Scanning electron microscopy and atomic force microscopy imaging of solid lipid nanoparticles derived from amphiphilic cyclodextrins. *European Journal of Pharmaceutics and Biopharmaceutics*, 55 (3), 279-82.
- Eggimann, G.A., Blattes, E., Buschor, S., Biswas, R., Kammer, S.M., Darbre, T., Reymond, J.-L., 2014. Designed cell penetrating peptide dendrimers efficiently internalize cargo into cells. *Chemical Communications*, 50 (55), 7254-57.
- Egusquiaguirre, S.P., Manguan-Garcia, C., Pintado-Berninches, L., Iarriccio, L., Carbajo, D., Albericio, F., Royo, M., Pedraz, J.L., Hernandez, R.M., Perona, R., Igartua, M., 2015. Development of surface modified biodegradable polymeric nanoparticles to deliver GSE24.2 peptide to cells: A promising approach for the treatment of defective telomerase disorders. *European Journal of Pharmaceutics and Biopharmaceutics*, 91, 91-102.
- Elsner, M.B., Herold, H.M., Muller-Herrmann, S., Bargel, H., Scheibel, T., 2015. Enhanced cellular uptake of engineered spider silk particles. *Biomaterials Science*, 3 (3), 543-51.
- Erazo-Oliveras, A., Najjar, K., Dayani, L., Wang, T.Y., Johnson, G.A., Pellois, J.P., 2014. Protein delivery into live cells by incubation with an endosomolytic agent. *Nature Methods*, 11 (8), 861-7.
- Fan, T., Chen, C., Guo, H., Xu, J., Zhang, J., Zhu, X., Yang, Y., Zhou, Z., Li, L., Huang, Y., 2014. Design and evaluation of solid lipid nanoparticles modified with peptide ligand for oral delivery of protein drugs. *European Journal of Pharmaceutics and Biopharmaceutics*, 88 (2), 518-28.
- Faralli, A., Shekarforoush, E., Mendes, A.C., Chronakis, I.S., 2019. Enhanced transepithelial permeation of gallic acid and (-)-epigallocatechin gallate across human intestinal Caco-2 cells using electrospun xanthan nanofibers. *Pharmaceutics*, 11 (4).
- Faria, M., Bjornmalm, M., Thurecht, K.J., Kent, S.J., Parton, R.G., Kavallaris, M., Johnston, A.P.R., Gooding, J.J., Corrie, S.R., Boyd, B.J., Thordarson, P., Whittaker, A.K., Stevens, M.M., Prestidge, C.A., Porter, C.J.H., Parak, W.J., Davis, T.P., Crampin, E.J.,

- Caruso, F., 2018. Minimum information reporting in bio-nano experimental literature. *Nature Nanotechnology*, 13 (9), 777-85.
- Faria, M., Noi, K.F., Dai, Q., Björnmalm, M., Johnston, S.T., Kempe, K., Caruso, F., Crampin, E.J., 2019. Revisiting cell-particle association in vitro: A quantitative method to compare particle performance. *Journal of Controlled Release*, 307, 355-67.
- Farkhani, S.M., Valizadeh, A., Karami, H., Mohammadi, S., Sohrabi, N., Badrzadeh, F., 2014. Cell penetrating peptides: Efficient vectors for delivery of nanoparticles, nanocarriers, therapeutic and diagnostic molecules. *Peptides*, 57, 78-94.
- Farokhzad, O.C., Langer, R., 2009. Impact of nanotechnology on drug delivery. *ACS Nano*, 3 (1), 16-20.
- FDA, 1997. *Guidance for industry: Q2B validation of analytical procedures: Methology*. Food and Drug Administration, Center for Drug Evaluation and Research and Center for Veterinary Medicine.
- FDA, 2001. *Guidance for Industry: Bioanalytical Method Validation*. Food and Drug Administration, Center for Drug Evaluation and Research and Center for Veterinary Medicine.
- Feiner-Gracia, N., Dols-Perez, A., Royo, M., Solans, C., Garcia-Celma, M.J., Fornaguera, C., 2018. Cell penetrating peptide grafting of PLGA nanoparticles to enhance cell uptake. *European Polymer Journal*, 108, 429-38.
- Feng, Q., Liu, J., Li, X., Chen, Q., Sun, J., Shi, X., Ding, B., Yu, H., Li, Y., Jiang, X., 2017. One-step microfluidic synthesis of nanocomplex with tunable rigidity and acid-switchable surface charge for overcoming drug resistance. *Small*, 13 (9), 1603109.
- Fenton, O.S., Olafson, K.N., Pillai, P.S., Mitchell, M.J., Langer, R., 2018. Advances in biomaterials for drug delivery. *Advanced Materials*, e1705328.
- Fessi, H., Puisieux, F., Devissaguet, J.P., Ammoury, N., Benita, S., 1989. Nanocapsule formation by interfacial polymer deposition following solvent displacement. *International Journal of Pharmaceutics*, 55 (1), R1-R4.
- Fischer, R., Kohler, K., Fotin-Mlecsek, M., Brock, R., 2004. A stepwise dissection of the intracellular fate of cationic cell-penetrating peptides. *The Journal of Biological Chemistry*, 279 (13), 12625-35.
- Fleischer, C.C., Payne, C.K., 2014. Nanoparticle-cell interactions: Molecular structure of the protein corona and cellular outcomes. *Accounts of Chemical Research*, 47 (8), 2651-9.
- Foerg, C., Ziegler, U., Fernandez-Carneado, J., Giralt, E., Merkle, H.P., 2007. Differentiation restricted endocytosis of cell penetrating peptides in MDCK cells corresponds with activities of Rho-GTPases. *Pharmaceutical Research*, 24 (4), 628-42.
- Fornaguera, C., Dols-Perez, A., Caldero, G., Garcia-Celma, M.J., Camarasa, J., Solans, C., 2015. PLGA nanoparticles prepared by nano-emulsion templating using low-energy methods as efficient nanocarriers for drug delivery across the blood-brain barrier. *Journal of Controlled Release*, 211, 134-43.
- Franke, D., Kikhney, A.G., Svergun, D.I., 2012. Automated acquisition and analysis of small angle X-ray scattering data. *Nuclear Instruments and Methods in Physics Research Section A: Accelerators, Spectrometers, Detectors and Associated Equipment*, 689, 52-59.
- Frankel, A.D., Pabo, C.O., 1988. Cellular uptake of the tat protein from human immunodeficiency virus. *Cell*, 55 (6), 1189-93.
- Franken, L.E., Boekema, E.J., Stuart, M.C.A., 2017. Transmission electron microscopy as a tool for the characterization of soft materials: Application and interpretation. *Advanced Science*, 4 (5), 1600476.
- Frohlich, E., 2016. Cellular elimination of nanoparticles. *Environmental Toxicology and Pharmacology*, 46, 90-94.

- Futaki, S., Suzuki, T., Ohashi, W., Yagami, T., Tanaka, S., Ueda, K., Sugiura, Y., 2001. Arginine-rich peptides. An abundant source of membrane-permeable peptides having potential as carriers for intracellular protein delivery. *The Journal of Biological Chemistry*, 276 (8), 5836-40.
- Gagliardi, M., Bertero, A., Bifone, A., 2017. Molecularly imprinted biodegradable nanoparticles. *Scientific Reports*, 7, 40046.
- Galindo-Rodríguez, S.A., Puel, F., Briançon, S., Allémann, E., Doelker, E., Fessi, H., 2005. Comparative scale-up of three methods for producing ibuprofen-loaded nanoparticles. *European Journal of Pharmaceutical Sciences*, 25 (4), 357-67.
- Gao, X., Hong, S., Liu, Z., Yue, T., Dobnikar, J., Zhang, X., 2019. Membrane potential drives direct translocation of cell-penetrating peptides. *Nanoscale*, 11 (4), 1949-58.
- Gao, Y., Zhao, D., Chang, M.-W., Ahmad, Z., Li, J.-S., 2016. Optimising the shell thickness-to-radius ratio for the fabrication of oil-encapsulated polymeric microspheres. *Chemical Engineering Journal*, 284, 963-71.
- Gartziandia, O., Egusquiaguirre, S.P., Bianco, J., Pedraz, J.L., Igartua, M., Hernandez, R.M., Pr at, V., Beloqui, A., 2016. Nanoparticle transport across in vitro olfactory cell monolayers. *International Journal of Pharmaceutics*, 499 (1), 81-89.
- Gaumet, M., Gurny, R., Delie, F., 2009. Localization and quantification of biodegradable particles in an intestinal cell model: The influence of particle size. *European Journal of Pharmaceutical Sciences*, 36 (4), 465-73.
- Ghazal, A., Gontsarik, M., Kutter, J.P., Lafleur, J.P., Ahmadvand, D., Labrador, A., Salentinig, S., Yagmur, A., 2017. Microfluidic platform for the continuous production and characterization of multilamellar vesicles: A synchrotron small-angle X-ray scattering (SAXS) study. *The Journal of Physical Chemistry Letters*, 8 (1), 73-79.
- Green, M., Loewenstein, P.M., 1988. Autonomous functional domains of chemically synthesized human immunodeficiency virus tat trans-activator protein. *Cell*, 55 (6), 1179-88.
- Griffin, B.T., Guo, J., Presas, E., Donovan, M.D., Alonso, M.J., O'Driscoll, C.M., 2016. Pharmacokinetic, pharmacodynamic and biodistribution following oral administration of nanocarriers containing peptide and protein drugs. *Advanced Drug Delivery Reviews*, 106, 367-80.
- Grillo, I., 2008. Small-angle neutron scattering and applications in soft condensed matter, Springer, pp. 723-82.
- Guidotti, G., Brambilla, L., Rossi, D., 2017. Cell-penetrating peptides: From basic research to clinics. *Trends in Pharmacological Sciences*, 38 (4), 406-24.
- Gullotti, E., Yeo, Y., 2012. Beyond the imaging: Limitations of cellular uptake study in the evaluation of nanoparticles. *Journal of Controlled Release*, 164 (2), 170-76.
- Gump, J.M., June, R.K., Dowdy, S.F., 2010. Revised role of glycosaminoglycans in TAT protein transduction domain-mediated cellular transduction. *The Journal of Biological Chemistry*, 285 (2), 1500-7.
- Guo, F., Ouyang, T., Peng, T., Zhang, X., Xie, B., Yang, X., Liang, D., Zhong, H., 2019. Enhanced oral absorption of insulin using colon-specific nanoparticles co-modified with amphiphilic chitosan derivatives and cell-penetrating peptides. *Biomaterials Science*, 7 (4), 1493-506.
- Guo, P., Weinstein, A.M., Weinbaum, S., 2000. A hydrodynamic mechanosensory hypothesis for brush border microvilli. *American Journal of Physiology-Renal Physiology*, 279 (4), F698-F712.
- Habault, J., Poyet, J.L., 2019. Recent advances in cell penetrating peptide-based anticancer therapies. *Molecules*, 24 (5).

- Haggag, Y.A., Faheem, A.M., Tambuwala, M.M., Osman, M.A., El-Gizawy, S.A., O'Hagan, B., Irwin, N., McCarron, P.A., 2018. Effect of poly(ethylene glycol) content and formulation parameters on particulate properties and intraperitoneal delivery of insulin from PLGA nanoparticles prepared using the double-emulsion evaporation procedure. *Pharmaceutical Development and Technology*, 23 (4), 370-81.
- Hanrahan, G., Lu, K., 2006. Application of factorial and response surface methodology in modern experimental design and optimization. *Critical Reviews in Analytical Chemistry*, 36 (3-4), 141-51.
- Haque, S., Boyd, B.J., McIntosh, M.P., Pouton, C.W., Kaminskas, L.M., Whittaker, M., 2018. Suggested procedures for the reproducible synthesis of poly(D,L-lactide-co-glycolide) nanoparticles using the emulsification solvent diffusion platform. *Current Nanoscience*, 14 (5), 448-53.
- Haris, P.I., Severcan, F., 1999. FTIR spectroscopic characterization of protein structure in aqueous and non-aqueous media. *Journal of Molecular Catalysis B: Enzymatic*, 7 (1), 207-21.
- He, B., Lin, P., Jia, Z., Du, W., Qu, W., Yuan, L., Dai, W., Zhang, H., Wang, X., Wang, J., Zhang, X., Zhang, Q., 2013. The transport mechanisms of polymer nanoparticles in Caco-2 epithelial cells. *Biomaterials*, 34 (25), 6082-98.
- He, C., Hu, Y., Yin, L., Tang, C., Yin, C., 2010. Effects of particle size and surface charge on cellular uptake and biodistribution of polymeric nanoparticles. *Biomaterials*, 31 (13), 3657-66.
- He, C., Yin, L., Tang, C., Yin, C., 2012. Size-dependent absorption mechanism of polymeric nanoparticles for oral delivery of protein drugs. *Biomaterials*, 33 (33), 8569-78.
- Herce, H.D., Garcia, A.E., Cardoso, M.C., 2014. Fundamental molecular mechanism for the cellular uptake of guanidinium-rich molecules. *Journal of the American Chemical Society*, 136 (50), 17459-67.
- Hermanson, G.T., 2013a. Introduction to bioconjugation, in: Audet, J., Preap, M. (Eds.), *Bioconjugate Techniques*, 3rd ed. Academic Press, pp. 1-125.
- Hermanson, G.T., 2013b. (Strept)avidin–biotin systems, in: Audet, J., Preap, M. (Eds.), *Bioconjugate Techniques*, 3rd ed. Academic Press, pp. 465-505.
- Hermanson, G.T., 2013c. Zero-length crosslinkers, in: Audet, J., Preap, M. (Eds.), *Bioconjugate Techniques*, 3rd ed. Academic Press, pp. 259-73.
- Hidalgo, I.J., Raub, T.J., Borchardt, R.T., 1989. Characterization of the human colon carcinoma cell line (Caco-2) as a model system for intestinal epithelial permeability. *Gastroenterology*, 96 (3), 736-49.
- Hinderliter, P.M., Minard, K.R., Orr, G., Chrisler, W.B., Thrall, B.D., Pounds, J.G., Teeguarden, J.G., 2010. ISDD: A computational model of particle sedimentation, diffusion and target cell dosimetry for in vitro toxicity studies. *Particle and Fibre Toxicology*, 7 (1), 36.
- Hofmann, A.M., Wurm, F., Hühn, E., Nawroth, T., Langguth, P., Frey, H., 2010. Hyperbranched polyglycerol-based lipids via oxyanionic polymerization: Toward multifunctional stealth liposomes. *Biomacromolecules*, 11 (3), 568-74.
- Homs, M., Calderó, G., Monge, M., Morales, D., Solans, C., 2018. Influence of polymer concentration on the properties of nano-emulsions and nanoparticles obtained by a low-energy method. *Colloids and Surfaces A: Physicochemical and Engineering Aspects*, 536, 204-12.
- Hong, L., Salentinig, S., Hawley, A., Boyd, B.J., 2015. Understanding the mechanism of enzyme-induced formation of lyotropic liquid crystalline nanoparticles. *Langmuir*, 31 (24), 6933-41.

- Hoyer, J., Schatzschneider, U., Schulz-Siegmund, M., Neundorf, I., 2012. Dimerization of a cell-penetrating peptide leads to enhanced cellular uptake and drug delivery. *Beilstein Journal of Organic Chemistry*, 8, 1788-97.
- Hu, J., Lou, Y., Wu, F., 2019. Improved intracellular delivery of polyarginine peptides with cargoes. *The Journal of Physical Chemistry B*, 123 (12), 2636-44.
- Huang, Y., Jiang, Y., Wang, H., Wang, J., Shin, M.C., Byun, Y., He, H., Liang, Y., Yang, V.C., 2013. Curb challenges of the "Trojan Horse" approach: Smart strategies in achieving effective yet safe cell-penetrating peptide-based drug delivery. *Advanced Drug Delivery Reviews*, 65 (10), 1299-315.
- Huang, Y.W., Lee, H.J., Tolliver, L.M., Aronstam, R.S., 2015. Delivery of nucleic acids and nanomaterials by cell-penetrating peptides: Opportunities and challenges. *BioMed Research International*, 2015, 834079.
- Hyrup Møller, L., Bahnsen, J.S., Nielsen, H.M., Ostergaard, J., Sturup, S., Gammelgaard, B., 2015. Selenium as an alternative peptide label - comparison to fluorophore-labelled penetratin. *European Journal of Pharmaceutical Sciences*, 67, 76-84.
- Iwasa, A., Akita, H., Khalil, I., Kogure, K., Futaki, S., Harashima, H., 2006. Cellular uptake and subsequent intracellular trafficking of R8-liposomes introduced at low temperature. *Biochimica et Biophysica Acta*, 1758 (6), 713-20.
- Jacobsen, J., Pedersen, M., Rassing, M.R., 1996. TR146 cells as a model for human buccal epithelium: II. Optimisation and use of a cellular sensitivity MTS/PMS assay. *International Journal of Pharmaceutics*, 141 (1), 217-25.
- Jafari, S., Maleki Dizaj, S., Adibkia, K., 2015. Cell-penetrating peptides and their analogues as novel nanocarriers for drug delivery. *BioImpacts*, 5 (2), 103-11.
- Jafarifar, E., Hajialyani, M., Akbari, M., Rahimi, M., Shokoohinia, Y., Fattahi, A., 2017. Preparation of a reproducible long-acting formulation of risperidone-loaded PLGA microspheres using microfluidic method. *Pharmaceutical Development and Technology*, 22 (6), 836-43.
- Jäger, A., Jäger, E., Giacomelli, F.C., Nallet, F., Steinhart, M., Putaux, J.-L., Konefał, R., Špěváček, J., Ulbrich, K., Štěpánek, P., 2018. Structural changes on polymeric nanoparticles induced by hydrophobic drug entrapment. *Colloids and Surfaces A: Physicochemical and Engineering Aspects*, 538, 238-49.
- Jahn, A., Vreeland, W.N., Gaitan, M., Locascio, L.E., 2004. Controlled vesicle self-assembly in microfluidic channels with hydrodynamic focusing. *Journal of the American Chemical Society*, 126 (9), 2674-5.
- Jaimes-Aguirre, L., Morales-Avila, E., Ocampo-Garcia, B.E., Medina, L.A., Lopez-Tellez, G., Gibbens-Bandala, B.V., Izquierdo-Sanchez, V., 2017. Biodegradable poly(D,L-lactide-co-glycolide)/poly(L-gamma-glutamic acid) nanoparticles conjugated to folic acid for targeted delivery of doxorubicin. *Materials Science and Engineering: C Materials for Biological Applications*, 76, 743-51.
- Jain, A., Jain, S.K., 2015. L-Valine appended PLGA nanoparticles for oral insulin delivery. *Acta Diabetologica*, 52 (4), 663-76.
- Jara, M.O., Catalan-Figueroa, J., Landin, M., Morales, J.O., 2018. Finding key nanoprecipitation variables for achieving uniform polymeric nanoparticles using neurofuzzy logic technology. *Drug Delivery and Translational Research*, 8 (6), 1797-806.
- Jeevanandam, J., Chan, Y.S., Danquah, M.K., 2016. Nano-formulations of drugs: Recent developments, impact and challenges. *Biochimie*, 128-129, 99-112.
- Jeffries, C.M., Graewert, M.A., Svergun, D.I., Blanchet, C.E., 2015. Limiting radiation damage for high-brilliance biological solution scattering: Practical experience at the EMBL P12 beamline PETRAIII. *Journal of Synchrotron Radiation*, 22 (2), 273-9.

- Jeong, C., Yoo, J., Lee, D., Kim, Y.C., 2016. A branched TAT cell-penetrating peptide as a novel delivery carrier for the efficient gene transfection. *Biomaterials Research*, 20 (1), 28.
- Jones, A.T., 2007. Macropinocytosis: Searching for an endocytic identity and role in the uptake of cell penetrating peptides. *Journal of Cellular and Molecular Medicine*, 11 (4), 670-84.
- Jones, S.W., Christison, R., Bundell, K., Voyce, C.J., Brockbank, S.M.V., Newham, P., Lindsay, M.A., 2005. Characterisation of cell-penetrating peptide-mediated peptide delivery. *British Journal of Pharmacology*, 145 (8), 1093-102.
- Joshi, G., Kumar, A., Sawant, K., 2016. Bioavailability enhancement, Caco-2 cells uptake and intestinal transport of orally administered lopinavir-loaded PLGA nanoparticles. *Drug Delivery*, 23 (9), 3492-504.
- Kafka, A.P., Kleffmann, T., Rades, T., McDowell, A., 2009. Histidine residues in the peptide D-Lys6-GnRH: Potential for copolymerization in polymeric nanoparticles. *Molecular Pharmaceutics*, 6 (5), 1483-91.
- Kafka, A.P., Kleffmann, T., Rades, T., McDowell, A., 2011. The application of MALDI TOF MS in biopharmaceutical research. *International Journal of Pharmaceutics*, 417 (1-2), 70-82.
- Kalani, M., Yunus, R., 2012. Effect of supercritical fluid density on nanoencapsulated drug particle size using the supercritical antisolvent method. *International Journal of Nanomedicine*, 7, 2165-72.
- Kamaly, N., Fredman, G., Fojas, J.J., Subramanian, M., Choi, W.I., Zepeda, K., Vilos, C., Yu, M., Gadde, S., Wu, J., Milton, J., Carvalho Leitao, R., Rosa Fernandes, L., Hasan, M., Gao, H., Nguyen, V., Harris, J., Tabas, I., Farokhzad, O.C., 2016. Targeted interleukin-10 nanotherapeutics developed with a microfluidic chip enhance resolution of inflammation in advanced atherosclerosis. *ACS Nano*, 10 (5), 5280-92.
- Kamei, N., Morishita, M., Takayama, K., 2009. Importance of intermolecular interaction on the improvement of intestinal therapeutic peptide/protein absorption using cell-penetrating peptides. *Journal of Controlled Release*, 136 (3), 179-86.
- Kaneko, K., McDowell, A., Ishii, Y., Hook, S., 2018. Characterization and evaluation of stabilized particulate formulations as therapeutic oral vaccines for allergy. *Journal of Liposome Research*, 28 (4), 296-304.
- Kang, H., DeLong, R., Fisher, M.H., Juliano, R.L., 2005. Tat-conjugated PAMAM dendrimers as delivery agents for antisense and siRNA oligonucleotides. *Pharmaceutical Research*, 22 (12), 2099-106.
- Kang, X., Luo, C., Wei, Q., Xiong, C., Chen, Q., Chen, Y., Ouyang, Q., 2013. Mass production of highly monodisperse polymeric nanoparticles by parallel flow focusing system. *Microfluidics and Nanofluidics*, 15 (3), 337-45.
- Karnik, R., Gu, F., Basto, P., Cannizzaro, C., Dean, L., Kyei-Manu, W., Langer, R., Farokhzad, O.C., 2008. Microfluidic platform for controlled synthesis of polymeric nanoparticles. *Nano Letters*, 8 (9), 2906-12.
- Karve, S., Werner, M.E., Cummings, N.D., Sukumar, R., Wang, E.C., Zhang, Y.-A., Wang, A.Z., 2011. Formulation of diblock polymeric nanoparticles through nanoprecipitation technique. *Journal of Visualized Experiments* (55), e3398.
- Kastner, E., Kaur, R., Lowry, D., Moghaddam, B., Wilkinson, A., Perrie, Y., 2014. High-throughput manufacturing of size-tuned liposomes by a new microfluidics method using enhanced statistical tools for characterization. *International Journal of Pharmaceutics*, 477 (1-2), 361-8.

- Kastner, E., Verma, V., Lowry, D., Perrie, Y., 2015. Microfluidic-controlled manufacture of liposomes for the solubilisation of a poorly water soluble drug. *International Journal of Pharmaceutics*, 485 (1-2), 122-30.
- Katsikari, A., Patronidou, C., Kiparissides, C., Arsenakis, M., 2009. Uptake and cytotoxicity of poly(d,l-lactide-co-glycolide) nanoparticles in human colon adenocarcinoma cells. *Materials Science and Engineering: B*, 165 (3), 160-64.
- Khan, I.U., Serra, C.A., Anton, N., Vandamme, T.F., 2015. Production of nanoparticle drug delivery systems with microfluidics tools. *Expert Opinion on Drug Delivery*, 12 (4), 547-62.
- Kikhney, A.G., Svergun, D.I., 2015. A practical guide to small angle X-ray scattering (SAXS) of flexible and intrinsically disordered proteins. *FEBS Letters*, 589 (19), 2570-7.
- Kim, Y., Lee Chung, B., Ma, M., Mulder, W.J., Fayad, Z.A., Farokhzad, O.C., Langer, R., 2012. Mass production and size control of lipid-polymer hybrid nanoparticles through controlled microvortices. *Nano Letters*, 12 (7), 3587-91.
- Klein, M.J., Schmidt, S., Wadhvani, P., Burck, J., Reichert, J., Afonin, S., Berditsch, M., Schober, T., Brock, R., Kansy, M., Ulrich, A.S., 2017. Lactam-stapled cell-penetrating peptides: Cell uptake and membrane binding properties. *Journal of Medicinal Chemistry*, 60 (19), 8071-82.
- Koch, A.M., Reynolds, F., Merkle, H.P., Weissleder, R., Josephson, L., 2005. Transport of surface-modified nanoparticles through cell monolayers. *ChemBioChem*, 6 (2), 337-45.
- Koh, M.L., FitzGerald, P.A., Warr, G.G., Jolliffe, K.A., Perrier, S., 2016. Study of (cyclic peptide)-polymer conjugate assemblies by small-angle neutron scattering. *Chemistry*, 22 (51), 18419-28.
- Kolishetti, N., Dhar, S., Valencia, P.M., Lin, L.Q., Karnik, R., Lippard, S.J., Langer, R., Farokhzad, O.C., 2010. Engineering of self-assembled nanoparticle platform for precisely controlled combination drug therapy. *Proceedings of the National Academy of Sciences of the United States of America*, 107 (42), 17939-44.
- Kong, J., Yu, S., 2007. Fourier transform infrared spectroscopic analysis of protein secondary structures. *Acta Biochimica et Biophysica Sinica*, 39 (8), 549-59.
- Koren, E., Torchilin, V.P., 2012. Cell-penetrating peptides: Breaking through to the other side. *Trends in Molecular Medicine*, 18 (7), 385-93.
- Kostag, M., Köhler, S., Liebert, T., Heinze, T., 2010. Pure cellulose nanoparticles from trimethylsilyl cellulose. *Macromolecular Symposia*, 294 (2), 96-106.
- Kristensen, M., de Groot, A.M., Berthelsen, J., Franzyk, H., Sijts, A., Nielsen, H.M., 2015. Conjugation of cell-penetrating peptides to parathyroid hormone affects its structure, potency, and transepithelial permeation. *Bioconjugate Chemistry*, 26 (3), 477-88.
- Kristensen, M., Nielsen, H.M., 2016. Cell-penetrating peptides as carriers for oral delivery of biopharmaceuticals. *Basic & Clinical Pharmacology & Toxicology*, 118 (2), 99-106.
- Künnapuu, K., Veiman, K.-L., Porosk, L., Rammul, E., Kiisholts, K., Langel, Ü., Kurrikoff, K., 2019. Tumor gene therapy by systemic delivery of plasmid DNA with cell-penetrating peptides. *FASEB BioAdvances*, 1 (2), 105-14.
- Laulicht, B., Cheifetz, P., Mathiowitz, E., Tripathi, A., 2008. Evaluation of continuous flow nanosphere formation by controlled microfluidic transport. *Langmuir*, 24 (17), 9717-26.
- Lea, T., 2015. Caco-2 cell line, in: Verhoeckx, K., Cotter, P., Lopez-Exposito, I., Kleiveland, C., Lea, T., Mackie, A., Requena, T., Swiatecka, D., Wichers, H. (Eds.), *The Impact of Food Bioactives on Health: In vitro and ex vivo models*, ed. Springer, pp. 103-11.
- Lee, S.Y., Jung, E., Park, J.H., Park, J.W., Shim, C.K., Kim, D.D., Yoon, I.S., Cho, H.J., 2016. Transient aggregation of chitosan-modified poly(d,l-lactic-co-glycolic) acid

- nanoparticles in the blood stream and improved lung targeting efficiency. *Journal of Colloid and Interface Science*, 480, 102-08.
- Lepeltier, E., Bourgaux, C., Couvreur, P., 2014. Nanoprecipitation and the "Ouzo effect": Application to drug delivery devices. *Advanced Drug Delivery Reviews*, 71, 86-97.
- Leung, M.H.M., Shen, A.Q., 2018. Microfluidic assisted nanoprecipitation of PLGA nanoparticles for curcumin delivery to leukemia Jurkat cells. *Langmuir*, 34 (13), 3961-70.
- Li, M., Al-Jamal, K.T., Kostarelos, K., Reineke, J., 2010. Physiologically based pharmacokinetic modeling of nanoparticles. *ACS Nano*, 4 (11), 6303-17.
- Li, M., Panagi, Z., Avgoustakis, K., Reineke, J., 2012. Physiologically based pharmacokinetic modeling of PLGA nanoparticles with varied mPEG content. *International Journal of Nanomedicine*, 7, 1345-56.
- Li, M., Zou, P., Tyner, K., Lee, S., 2017. Physiologically based pharmacokinetic (PBPK) modeling of pharmaceutical nanoparticles. *The AAPS Journal*, 19 (1), 26-42.
- Li, T., Senesi, A.J., Lee, B., 2016. Small angle X-ray scattering for nanoparticle research. *Chemical Reviews*, 116 (18), 11128-80.
- Lim, J.M., Bertrand, N., Valencia, P.M., Rhee, M., Langer, R., Jon, S., Farokhzad, O.C., Karnik, R., 2014a. Parallel microfluidic synthesis of size-tunable polymeric nanoparticles using 3D flow focusing towards in vivo study. *Nanomedicine*, 10 (2), 401-9.
- Lim, J.M., Swami, A., Gilson, L.M., Chopra, S., Choi, S., Wu, J., Langer, R., Karnik, R., Farokhzad, O.C., 2014b. Ultra-high throughput synthesis of nanoparticles with homogeneous size distribution using a coaxial turbulent jet mixer. *ACS Nano*, 8 (6), 6056-65.
- Lince, F., Marchisio, D.L., Barresi, A.A., 2008. Strategies to control the particle size distribution of poly- ϵ -caprolactone nanoparticles for pharmaceutical applications. *Journal of Colloid and Interface Science*, 322 (2), 505-15.
- Liu, K., Wang, H., Chen, K.J., Guo, F., Lin, W.Y., Chen, Y.C., Phung, D.L., Tseng, H.R., Shen, C.K., 2010. A digital microfluidic droplet generator produces self-assembled supramolecular nanoparticles for targeted cell imaging. *Nanotechnology*, 21 (44), 445603.
- Liu, K., Zhu, Z., Wang, X., Gonçalves, D., Zhang, B., Hierlemann, A., Hunziker, P., 2015. Microfluidics-based single-step preparation of injection-ready polymeric nanosystems for medical imaging and drug delivery. *Nanoscale*, 7 (40), 16983-93.
- Liu, X., Liu, C., Zhang, W., Xie, C., Wei, G., Lu, W., 2013. Oligoarginine-modified biodegradable nanoparticles improve the intestinal absorption of insulin. *International Journal of Pharmaceutics*, 448 (1), 159-67.
- Lonn, P., Dowdy, S.F., 2015. Cationic PTD/CPP-mediated macromolecular delivery: Charging into the cell. *Expert Opinion on Drug Delivery*, 12 (10), 1627-36.
- Lopes, M., Shrestha, N., Correia, A., Shahbazi, M.A., Sarmiento, B., Hirvonen, J., Veiga, F., Seica, R., Ribeiro, A., Santos, H.A., 2016. Dual chitosan/albumin-coated alginate/dextran sulfate nanoparticles for enhanced oral delivery of insulin. *Journal of Controlled Release*, 232, 29-41.
- Lopez, C.G., Watanabe, T., Martel, A., Porcar, L., Cabral, J.T., 2015. Microfluidic-SANS: Flow processing of complex fluids. *Scientific Reports*, 5, 7727.
- Lopez, C.G., Watanabe, T., Adamo, M., Martel, A., Porcar, L., Cabral, J.T., 2018. Microfluidic devices for small-angle neutron scattering. *Journal of Applied Crystallography*, 51, 570-83.
- Lukanowska, M., Howl, J., Jones, S., 2013. Bioportides: Bioactive cell-penetrating peptides that modulate cellular dynamics. *Biotechnology Journal*, 8 (8), 918-30.

- Lundquist, P., Artursson, P., 2016. Oral absorption of peptides and nanoparticles across the human intestine: Opportunities, limitations and studies in human tissues. *Advanced Drug Delivery Reviews*, 106, 256-76.
- Luo, Y., Han, Y., Hu, X., Yin, M., Wu, C., Li, Q., Chen, N., Zhao, Y., 2019a. Live-cell imaging of octaarginine-modified polymer dots via single particle tracking. *Cell Proliferation*, 52 (2), e12556.
- Luo, Z., Yang, Y., Radulescu, A., Kohlbrecher, J., Darwish, T.A., Ong, Q.K., Guldin, S., Stellacci, F., 2019b. Multidimensional characterization of mixed ligand nanoparticles using small angle neutron scattering. *Chemistry of Materials*.
- Luque-Michel, E., Larrea, A., Lahuerta, C., Sebastian, V., Imbuluzqueta, E., Arruebo, M., Blanco-Prieto, M.J., Santamaria, J., 2016. A simple approach to obtain hybrid Au-loaded polymeric nanoparticles with a tunable metal load. *Nanoscale*, 8 (12), 6495-506.
- Makadia, H.K., Siegel, S.J., 2011. Poly lactic-co-glycolic acid (PLGA) as biodegradable controlled drug delivery carrier. *Polymers*, 3 (3), 1377-97.
- Malhaire, H., Gimel, J.C., Roger, E., Benoit, J.P., Lagarce, F., 2016. How to design the surface of peptide-loaded nanoparticles for efficient oral bioavailability? *Advanced Drug Delivery Reviews*, 106, 320-36.
- Mandenius, C.F., Brundin, A., 2008. Bioprocess optimization using design-of-experiments methodology. *Biotechnology Progress*, 24 (6), 1191-203.
- Manet, S., Lecchi, A., Imperor-Clerc, M., Zholobenko, V., Durand, D., Oliveira, C.L., Pedersen, J.S., Grillo, I., Meneau, F., Rochas, C., 2011. Structure of micelles of a nonionic block copolymer determined by SANS and SAXS. *The Journal of Physical Chemistry B*, 115 (39), 11318-29.
- Mante, A., Heider, M., Zlomke, C., Mader, K., 2016. PLGA nanoparticles for peroral delivery: How important is pancreatic digestion and can we control it? *European Journal of Pharmaceutics and Biopharmaceutics*, 108, 32-40.
- Manzo, C., Garcia-Parajo, M.F., 2015. A review of progress in single particle tracking: From methods to biophysical insights. *Reports on Progress in Physics*, 78 (12), 124601.
- Masood, F., 2016. Polymeric nanoparticles for targeted drug delivery system for cancer therapy. *Materials Science and Engineering: C Materials for Biological Applications*, 60, 569-78.
- Masters, J.R., 2002. HeLa cells 50 years on: The good, the bad and the ugly. *Nature Reviews Cancer*, 2 (4), 315-19.
- Miao, J., Charalambous, P., Kirz, J., Sayre, D., 1999. Extending the methodology of X-ray crystallography to allow imaging of micrometre-sized non-crystalline specimens. *Nature*, 400 (6742), 342-44.
- Min, K.I., Im, D.J., Lee, H.J., Kim, D.P., 2014. Three-dimensional flash flow microreactor for scale-up production of monodisperse PEG-PLGA nanoparticles. *Lab on a Chip*, 14 (20), 3987-92.
- Mitchell, D.J., Kim, D.T., Steinman, L., Fathman, C.G., Rothbard, J.B., 2000. Polyarginine enters cells more efficiently than other polycationic homopolymers. *The Journal of Peptide Research*, 56 (5), 318-25.
- Moku, G., Layek, B., Trautman, L., Putnam, S., Panyam, J., Prabha, S., 2019. Improving payload capacity and anti-tumor efficacy of mesenchymal stem cells using TAT peptide functionalized polymeric nanoparticles. *Cancers*, 11 (4).
- Monreal, I.A., Liu, Q., Tyson, K., Bland, T., Dalisay, D.S., Adams, E.V., Wayman, G.A., Aguilar, H.C., Saludes, J.P., 2015. Branched dimerization of Tat peptide improves permeability to HeLa and hippocampal neuronal cells. *Chemical Communication*, 51 (25), 5463-6.

- Montrose, K., Yang, Y., Krissansen, G.W., 2014a. The tetrapeptide core of the carrier peptide Xentry is cell-penetrating: Novel activatable forms of Xentry. *Scientific Reports*, 4, 4900.
- Montrose, K., Yang, Y., Krissansen, G.W., 2014b. X-pep, a novel cell-penetrating peptide motif derived from the hepatitis B virus. *Biochemical and Biophysical Research Communications*, 453 (1), 64-8.
- Morikawa, Y., Tagami, T., Hoshikawa, A., Ozeki, T., 2018. The use of an efficient microfluidic mixing system for generating stabilized polymeric nanoparticles for controlled drug release. *Biological and Pharmaceutical Bulletin*, 41 (6), 899-907.
- Morimoto, N., Wakamura, M., Muramatsu, K., Toita, S., Nakayama, M., Shoji, W., Suzuki, M., Winnik, F.M., 2016. Membrane translocation and organelle-selective delivery steered by polymeric zwitterionic nanospheres. *Biomacromolecules*, 17 (4), 1523-35.
- Mu, Y., Fu, Y., Li, J., Yu, X., Li, Y., Wang, Y., Wu, X., Zhang, K., Kong, M., Feng, C., Chen, X., 2019. Multifunctional quercetin conjugated chitosan nano-micelles with P-gp inhibition and permeation enhancement of anticancer drug. *Carbohydrate Polymers*, 203, 10-18.
- Mukherjee, T., Squillante, E., Gillespie, M., Shao, J., 2004. Transepithelial electrical resistance is not a reliable measurement of the Caco-2 monolayer integrity in Transwell. *Drug Delivery*, 11 (1), 11-8.
- Nam, Y.S., Park, J.Y., Han, S.-H., Chang, I.-S., 2002. Intracellular drug delivery using poly(D,L-lactide-co-glycolide) nano-particles derivatized with a peptide from a transcriptional activator protein of HIV-1. *Biotechnology Letters*, 24 (24), 2093-98.
- Nel, A.E., Mädler, L., Velegol, D., Xia, T., Hoek, E.M.V., Somasundaran, P., Klaessig, F., Castranova, V., Thompson, M., 2009. Understanding biophysicochemical interactions at the nano-bio interface. *Nature Materials*, 8, 543.
- Ortiz de Solorzano, I., Uson, L., Larrea, A., Miana, M., Sebastian, V., Arruebo, M., 2016. Continuous synthesis of drug-loaded nanoparticles using microchannel emulsification and numerical modeling: Effect of passive mixing. *International Journal of Nanomedicine*, 11, 3397-416.
- Othman, R., Vladislavljević, G.T., Hemaka Bandulasena, H.C., Nagy, Z.K., 2015. Production of polymeric nanoparticles by micromixing in a co-flow microfluidic glass capillary device. *Chemical Engineering Journal*, 280, 316-29.
- Ou, Z.Q., Schmierer, D.M., Strachan, C.J., Rades, T., McDowell, A., 2014. Influence of postharvest processing and storage conditions on key antioxidants in puha (*Sonchus oleraceus* L.). *The Journal of Pharmacy and Pharmacology*, 66 (7), 998-1008.
- Pan, R., Xu, W., Ding, Y., Lu, S., Chen, P., 2016. Uptake mechanism and direct translocation of a new CPP for siRNA delivery. *Molecular Pharmaceutics*, 13 (4), 1366-74.
- Park, K., Skidmore, S., Hadar, J., Garner, J., Park, H., Otte, A., Soh, B.K., Yoon, G., Yu, D., Yun, Y., Lee, B.K., Jiang, X., Wang, Y., 2019. Injectable, long-acting PLGA formulations: Analyzing PLGA and understanding microparticle formation. *Journal of Controlled Release*, 304, 125-34.
- Park, T.G., 1995. Degradation of poly(lactic-co-glycolic acid) microspheres: Effect of copolymer composition. *Biomaterials*, 16 (15), 1123-30.
- Partikel, K., Korte, R., Stein, N.C., Mulac, D., Herrmann, F.C., Humpf, H.-U., Langer, K., 2019. Effect of nanoparticle size and PEGylation on the protein corona of PLGA nanoparticles. *European Journal of Pharmaceutics and Biopharmaceutics*, 141, 70-80.
- Patel, L.N., Wang, J., Kim, K.J., Borok, Z., Crandall, E.D., Shen, W.C., 2009. Conjugation with cationic cell-penetrating peptide increases pulmonary absorption of insulin. *Molecular Pharmaceutics*, 6 (2), 492-503.

- Patel, R.R., Chaurasia, S., Khan, G., Chaubey, P., Kumar, N., Mishra, B., 2016. Cromolyn sodium encapsulated PLGA nanoparticles: An attempt to improve intestinal permeation. *International Journal of Biological Macromolecules*, 83, 249-58.
- Patel, S.G., Sayers, E.J., He, L., Narayan, R., Williams, T.L., Mills, E.M., Allemann, R.K., Luk, L.Y.P., Jones, A.T., Tsai, Y.-H., 2019. Cell-penetrating peptide sequence and modification dependent uptake and subcellular distribution of green fluorescent protein in different cell lines. *Scientific Reports*, 9 (1), 6298.
- Pauw, B.R., 2013. Everything SAXS: Small-angle scattering pattern collection and correction. *Journal of Physics: Condensed Matter*, 25 (38), 383201.
- Pelaz, B., del Pino, P., Maffre, P., Hartmann, R., Gallego, M., Rivera-Fernández, S., de la Fuente, J.M., Nienhaus, G.U., Parak, W.J., 2015. Surface functionalization of nanoparticles with polyethylene glycol: Effects on protein adsorption and cellular uptake. *ACS Nano*, 9 (7), 6996-7008.
- Pelkmans, L., Helenius, A., 2002. Endocytosis via caveolae. *Traffic*, 3 (5), 311-20.
- Peterson, L.W., Artis, D., 2014. Intestinal epithelial cells: Regulators of barrier function and immune homeostasis. *Nature Reviews Immunology*, 14, 141.
- Pinto, M., Robine, S., Appay, M.D., Lacroix, B., Assmann, P.F., Fogh, J., Zweibaum, A., 1983. Enterocyte-like differentiation and polarization of the human-colon carcinoma cell-line Caco-2 in culture. *Biology of the Cell*, 47, 323-30.
- Pooga, M., Hallbrink, M., Zorko, M., Langel, Ü., 1998. Cell penetration by transportan. *FASEB Journal*, 12 (1), 67-77.
- Price, S.R., Kinnear, C., Balog, S., 2019. Particokinetics and in vitro dose of high aspect ratio nanoparticles. *Nanoscale*, 11 (12), 5209-14.
- Putnam, C.D., Hammel, M., Hura, G.L., Tainer, J.A., 2007. X-ray solution scattering (SAXS) combined with crystallography and computation: Defining accurate macromolecular structures, conformations and assemblies in solution. *Quarterly Reviews of Biophysics*, 40 (3), 191-285.
- Quintanar-Guerrero, D., Allemann, E., Fessi, H., Doelker, E., 1998. Preparation techniques and mechanisms of formation of biodegradable nanoparticles from preformed polymers. *Drug Development and Industrial Pharmacy*, 24 (12), 1113-28.
- Ramaker, K., Henkel, M., Krause, T., Rockendorf, N., Frey, A., 2018. Cell penetrating peptides: A comparative transport analysis for 474 sequence motifs. *Drug Delivery*, 25 (1), 928-37.
- Reifarth, M., Hoepfener, S., Schubert, U.S., 2018. Uptake and intracellular fate of engineered nanoparticles in mammalian cells: Capabilities and limitations of transmission electron microscopy—polymer-based nanoparticles. *Advanced Materials*, 30 (9), 1703704.
- Reix, N., Parat, A., Seyfritz, E., Van der Werf, R., Epure, V., Ebel, N., Danicher, L., Marchioni, E., Jeandidier, N., Pinget, M., Frere, Y., Sigrist, S., 2012. In vitro uptake evaluation in Caco-2 cells and in vivo results in diabetic rats of insulin-loaded PLGA nanoparticles. *International Journal of Pharmaceutics*, 437 (1-2), 213-20.
- Rieux, A.d., Ragnarsson, E.G.E., Gullberg, E., Pr at, V., Schneider, Y.-J., Artursson, P., 2005. Transport of nanoparticles across an in vitro model of the human intestinal follicle associated epithelium. *European Journal of Pharmaceutical Sciences*, 25 (4), 455-65.
- Ruczyński, J., Rusiecka, I., Turecka, K., Kozłowska, A., Alenowicz, M., Ga ało, I., Kawiak, A., Rekowski, P., Waleron, K., Koci , I., 2019. Transportan 10 improves the pharmacokinetics and pharmacodynamics of vancomycin. *Scientific Reports*, 9 (1), 3247.
- Ruland, W., 1971. Small-angle scattering of two-phase systems: Determination and significance of systematic deviations from Porod's law. *Journal of Applied Crystallography*, 4 (1), 70-73.

- Ruozi, B., Belletti, D., Tombesi, A., Tosi, G., Bondioli, L., Forni, F., Vandelli, M.A., 2011. AFM, ESEM, TEM, and CLSM in liposomal characterization: A comparative study. *International Journal of Nanomedicine*, 6, 557-63.
- Ruozi, B., Belletti, D., Vandelli, M.A., Pederzoli, F., Veratti, P., Forni, F., Tosi, G., Tonelli, M., Zapparoli, M., 2014. AFM/TEM complementary structural analysis of surface-functionalized nanoparticles. *Journal of Physical Chemistry & Biophysics*, 4 (4).
- Ryser, H.J., Hancock, R., 1965. Histones and basic polyamino acids stimulate the uptake of albumin by tumor cells in culture. *Science*, 150 (3695), 501-3.
- Saarinen, J., Gutter, F., Lindman, M., Agopov, M., Fraser-Miller, S.J., Scherliess, R., Jokitalo, E., Santos, H.A., Peltonen, L., Isomaki, A., Strachan, C.J., 2019. Cell-nanoparticle interactions at (sub)-nanometer resolution analyzed by electron microscopy and correlative coherent anti-Stokes Raman scattering. *Biotechnology Journal*, 14 (4), e1800413.
- Saleh, A.F., Arzumanov, A., Abes, R., Owen, D., Lebleu, B., Gait, M.J., 2010. Synthesis and splice-redirecting activity of branched, arginine-rich peptide dendrimer conjugates of peptide nucleic acid oligonucleotides. *Bioconjugate Chemistry*, 21 (10), 1902-11.
- Sanada, Y., Akiba, I., Sakurai, K., Shiraishi, K., Yokoyama, M., Mylonas, E., Ohta, N., Yagi, N., Shinohara, Y., Amemiya, Y., 2013. Hydrophobic molecules infiltrating into the poly(ethylene glycol) domain of the core/shell interface of a polymeric micelle: Evidence obtained with anomalous small-angle X-ray scattering. *Journal of the American Chemical Society*, 135 (7), 2574-82.
- Scanlon, D.B., Finlayson, J., 2004. Prep/semiprep separation of peptides, in: Aguilar, M.-I. (Ed.), *Methods in Molecular Biology*, ed. Humana Press Inc.
- Scott, A.J., Penlidis, A., 2017. Copolymerization, in: *Reference Module in Chemistry, Molecular Sciences and Chemical Engineering*, ed.
- Shahbazi, S., Bolhassani, A., 2018. Comparison of six cell penetrating peptides with different properties for in vitro and in vivo delivery of HPV16 E7 antigen in therapeutic vaccines. *International Immunopharmacology*, 62, 170-80.
- Shai, Y., 2013. ATR-FTIR studies in pore forming and membrane induced fusion peptides. *Biochimica et Biophysica Acta*, 1828 (10), 2306-13.
- Shang, L., Nienhaus, G.U., 2013. Small fluorescent nanoparticles at the nano-bio interface. *Materials Today*, 16 (3), 58-66.
- Sharma, G., Sharma, A.R., Nam, J.-S., Doss, G.P.C., Lee, S.-S., Chakraborty, C., 2015. Nanoparticle based insulin delivery system: The next generation efficient therapy for Type 1 diabetes. *Journal of Nanobiotechnology*, 13 (1), 74.
- Sharma, N., Mishra, S., Sharma, S., Deshpande, R.D., Sharma, R.K., 2013. Preparation and optimization of nanoemulsions for targeting drug delivery. *International Journal of Drug Development and Research*, 5 (4), 37-48.
- Sharma, S., Parmar, A., Kori, S., Sandhir, R., 2016. PLGA-based nanoparticles: A new paradigm in biomedical applications. *TrAC Trends in Analytical Chemistry*, 80, 30-40.
- Sheng, J., Han, L., Qin, J., Ru, G., Li, R., Wu, L., Cui, D., Yang, P., He, Y., Wang, J., 2015. N-trimethyl chitosan chloride-coated PLGA nanoparticles overcoming multiple barriers to oral insulin absorption. *ACS Applied Materials & Interfaces*, 7 (28), 15430-41.
- Sheng, J., He, H., Han, L., Qin, J., Chen, S., Ru, G., Li, R., Yang, P., Wang, J., Yang, V.C., 2016. Enhancing insulin oral absorption by using mucoadhesive nanoparticles loaded with LMWP-linked insulin conjugates. *Journal of Controlled Release*, 233, 181-90.
- Shi, J., Guo, S., Wu, Y., Chen, G., Lai, J., Xu, X., 2019. Behaviour of cell penetrating peptide TAT-modified liposomes loaded with salvianolic acid B on the migration, proliferation, and survival of human skin fibroblasts. *Journal of Liposome Research*, 1-14.

- Siafaka, P.I., Ustundag Okur, N., Karavas, E., Bikiaris, D.N., 2016. Surface modified multifunctional and stimuli responsive nanoparticles for drug targeting: Current status and uses. *International Journal of Molecular Sciences*, 17 (9).
- Silva, S., Almeida, A.J., Vale, N., 2019. Combination of cell-penetrating peptides with nanoparticles for therapeutic application: A review. *Biomolecules*, 9 (1), 22.
- Singh, B., Bhatowa, R., Tripathi, C.B., Kapil, R., 2011a. Developing micro-/nanoparticulate drug delivery systems using "design of experiments". *International Journal of Pharmaceutical Investigation*, 1 (2), 75-87.
- Singh, B., Kapil, R., Nandi, M., Ahuja, N., 2011b. Developing oral drug delivery systems using formulation by design: Vital precepts, retrospect and prospects. *Expert Opinion on Drug Delivery*, 8 (10), 1341-60.
- Siu, F.Y., Ye, S., Lin, H., Li, S., 2018. Galactosylated PLGA nanoparticles for the oral delivery of resveratrol: enhanced bioavailability and in vitro anti-inflammatory activity. *International Journal of Nanomedicine*, 13, 4133-44.
- Solans, C., Solé, I., 2012. Nano-emulsions: Formation by low-energy methods. *Current Opinion in Colloid & Interface Science*, 17 (5), 246-54.
- Sonam, Chaudhary, H., Kumar, V., 2014. Taguchi design for optimization and development of antibacterial drug-loaded PLGA nanoparticles. *International Journal of Biological Macromolecules*, 64, 99-105.
- Steinbach, J.M., Seo, Y.E., Saltzman, W.M., 2016. Cell penetrating peptide-modified poly(lactic-co-glycolic acid) nanoparticles with enhanced cell internalization. *Acta Biomaterialia*, 30, 49-61.
- Streck, S., Neumann, H., Nielsen, H.M., Rades, T., McDowell, A., 2019a. Comparison of bulk and microfluidics methods for the formulation of poly-lactic-co-glycolic acid (PLGA) nanoparticles modified with cell-penetrating peptides of different architectures. *International Journal of Pharmaceutics: X*, 1, 100030.
- Streck, S., Clulow, A.J., Nielsen, H.M., Rades, T., Boyd, B.J., McDowell, A., 2019b. The distribution of cell-penetrating peptides on polymeric nanoparticles prepared using microfluidics and elucidated with small angle X-ray scattering. *Journal of Colloid and Interface Science*, 555, 438-48.
- Streck, S., Hong, L., Boyd, B.J., McDowell, A., 2019c. Microfluidics for the production of nanomedicines: Considerations for polymer and lipid-based systems. *Pharmaceutical Nanotechnology*, 7 (6), 1-21.
- Stroock, A.D., Dertinger, S.K., Ajdari, A., Mezic, I., Stone, H.A., Whitesides, G.M., 2002. Chaotic mixer for microchannels. *Science*, 295 (5555), 647-51.
- Su, Y., Doherty, T., Waring, A.J., Ruchala, P., Hong, M., 2009. Roles of arginine and lysine residues in the translocation of a cell-penetrating peptide from ¹³C, ³¹P, and ¹⁹F solid-state NMR. *Biochemistry*, 48 (21), 4587-95.
- Sun, J., Zhang, L., Wang, J., Feng, Q., Liu, D., Yin, Q., Xu, D., Wei, Y., Ding, B., Shi, X., Jiang, X., 2015. Tunable rigidity of (polymeric core)–(lipid shell) nanoparticles for regulated cellular uptake. *Advanced Materials*, 27 (8), 1402-07.
- Tan, H.Y., Trier, S., Rahbek, U.L., Dufva, M., Kutter, J.P., Andresen, T.L., 2018. A multi-chamber microfluidic intestinal barrier model using Caco-2 cells for drug transport studies. *PLoS One*, 13 (5), e0197101.
- Tantra, R., Knight, A., 2011. Cellular uptake and intracellular fate of engineered nanoparticles: A review on the application of imaging techniques. *Nanotoxicology*, 5 (3), 381-92.
- Tariq, M., Alam, M.A., Singh, A.T., Iqbal, Z., Panda, A.K., Talegaonkar, S., 2015. Biodegradable polymeric nanoparticles for oral delivery of epirubicin: In vitro, ex vivo, and in vivo investigations. *Colloids and Surfaces B: Biointerfaces*, 128, 448-56.

- Tefas, L.R., Tomuta, I., Achim, M., Vlase, L., 2015. Development and optimization of quercetin-loaded PLGA nanoparticles by experimental design. *Clujul Medical*, 88 (2), 214-23.
- Thomas, D.G., Smith, J.N., Thrall, B.D., Baer, D.R., Jolley, H., Munusamy, P., Kodali, V., Demokritou, P., Cohen, J., Teeguarden, J.G., 2018. ISD3: A particokinetic model for predicting the combined effects of particle sedimentation, diffusion and dissolution on cellular dosimetry for in vitro systems. *Particle and Fibre Toxicology*, 15 (1), 6.
- Thwala, L.N., Preat, V., Csaba, N.S., 2017. Emerging delivery platforms for mucosal administration of biopharmaceuticals: A critical update on nasal, pulmonary and oral routes. *Expert Opinion on Drug Delivery*, 14 (1), 23-36.
- Torchilin, V.P., 2014. Multifunctional, stimuli-sensitive nanoparticulate systems for drug delivery. *Nature Reviews Drug Discovery*, 13 (11), 813-27.
- Totaro, K.A., Liao, X., Bhattacharya, K., Finneman, J.I., Sperry, J.B., Massa, M.A., Thorn, J., Ho, S.V., Pentelute, B.L., 2016. Systematic investigation of EDC/sNHS-mediated bioconjugation reactions for carboxylated peptide substrates. *Bioconjugate Chemistry*, 27 (4), 994-1004.
- Toth, M.J., Kim, T., Kim, Y., 2017. Robust manufacturing of lipid-polymer nanoparticles through feedback control of parallelized swirling microvortices. *Lab on a Chip*, 17 (16), 2805-13.
- Totterman, A.M., Schipper, N.G., Thompson, D.O., Mannermaa, J.P., 1997. Intestinal safety of water-soluble beta-cyclodextrins in paediatric oral solutions of spironolactone: Effects on human intestinal epithelial Caco-2 cells. *The Journal of Pharmacy and Pharmacology*, 49 (1), 43-8.
- Trehin, R., Krauss, U., Beck-Sickinger, A.G., Merkle, H.P., Nielsen, H.M., 2004. Cellular uptake but low permeation of human calcitonin-derived cell penetrating peptides and Tat(47-57) through well-differentiated epithelial models. *Pharmaceutical Research*, 21 (7), 1248-56.
- Tunsirikongkon, A., Pyo, Y.C., Kim, D.H., Lee, S.E., Park, J.S., 2019. Optimization of polyarginine-conjugated PEG lipid grafted proliposome formulation for enhanced cellular association of a protein drug. *Pharmaceutics*, 11 (6).
- Utada, A.S., Chu, L.Y., Fernandez-Nieves, A., Link, D.R., Holtze, C., Weitz, D.A., 2007. Dripping, jetting, drops, and wetting: The magic of microfluidics. *MRS Bulletin*, 32 (9), 702-08.
- Vaidya, B., Parvathaneni, V., Kulkarni, N.S., Shukla, S.K., Damon, J.K., Sarode, A., Kanabar, D., Garcia, J.V., Mitragotri, S., Muth, A., Gupta, V., 2019. Cyclodextrin modified erlotinib loaded PLGA nanoparticles for improved therapeutic efficacy against non-small cell lung cancer. *International Journal of Biological Macromolecules*, 122, 338-47.
- Valencia, P.M., Basto, P.A., Zhang, L., Rhee, M., Langer, R., Farokhzad, O.C., Karnik, R., 2010. Single-step assembly of homogenous lipid-polymeric and lipid-quantum dot nanoparticles enabled by microfluidic rapid mixing. *ACS Nano*, 4 (3), 1671-9.
- Valencia, P.M., Farokhzad, O.C., Karnik, R., Langer, R., 2012. Microfluidic technologies for accelerating the clinical translation of nanoparticles. *Nature Nanotechnology*, 7, 623.
- Valencia, P.M., Pridgen, E.M., Rhee, M., Langer, R., Farokhzad, O.C., Karnik, R., 2013. Microfluidic platform for combinatorial synthesis and optimization of targeted nanoparticles for cancer therapy. *ACS Nano*, 7 (12), 10671-80.
- van Bracht, E., Versteegden, L.R., Stolle, S., Verdurmen, W.P., Woestenenk, R., Raave, R., Hafmans, T., Oosterwijk, E., Brock, R., van Kuppevelt, T.H., Daamen, W.F., 2014. Enhanced cellular uptake of albumin-based lyophilisomes when functionalized with cell-penetrating peptide TAT in HeLa cells. *PLoS One*, 9 (11), e110813.

- van Oppen, L.M.P.E., Pille, J., Stuu, C., van Stevendaal, M., van der Vorm, L.N., Smeitink, J.A.M., Koopman, W.J.H., Willems, P.H.G.M., van Hest, J.C.M., Brock, R., 2019. Octa-arginine boosts the penetration of elastin-like polypeptide nanoparticles in 3D cancer models. *European Journal of Pharmaceutics and Biopharmaceutics*, 137, 175-84.
- Vasconcelos, A., Vega, E., Perez, Y., Gomara, M.J., Garcia, M.L., Haro, I., 2015. Conjugation of cell-penetrating peptides with poly(lactic-co-glycolic acid)-polyethylene glycol nanoparticles improves ocular drug delivery. *International Journal of Nanomedicine*, 10, 609-31.
- Vithani, K., Hawley, A., Jannin, V., Pouton, C., Boyd, B.J., 2017. Inclusion of digestible surfactants in solid SMEDDS formulation removes lag time and influences the formation of structured particles during digestion. *The AAPS Journal*, 19 (3), 754-64.
- Vives, E., Brodin, P., Lebleu, B., 1997. A truncated HIV-1 Tat protein basic domain rapidly translocates through the plasma membrane and accumulates in the cell nucleus. *The Journal of Biological Chemistry*, 272 (25), 16010-7.
- von Roemeling, C., Jiang, W., Chan, C.K., Weissman, I.L., Kim, B.Y.S., 2017. Breaking down the barriers to precision cancer nanomedicine. *Trends in Biotechnology*, 35 (2), 159-71.
- Vuddanda, P.R., Mishra, A., Singh, S.K., Singh, S., 2015. Development of polymeric nanoparticles with highly entrapped herbal hydrophilic drug using nanoprecipitation technique: An approach of quality by design. *Pharmaceutical Development and Technology*, 20 (5), 579-87.
- Wang, J.T., Wang, J., Han, J.J., 2011. Fabrication of advanced particles and particle-based materials assisted by droplet-based microfluidics. *Small*, 7 (13), 1728-54.
- Wang, Y., Kim, R., Hinman, S.S., Zwarycz, B., Magness, S.T., Allbritton, N.L., 2018. Bioengineered systems and designer matrices that recapitulate the intestinal stem cell niche. *Cellular and Molecular Gastroenterology and Hepatology*, 5 (3), 440-53.e1.
- Wassel, R.A., Grady, B., Kopke, R.D., Dormer, K.J., 2007. Dispersion of super paramagnetic iron oxide nanoparticles in poly(d,l-lactide-co-glycolide) microparticles. *Colloids and Surfaces A: Physicochemical and Engineering Aspects*, 292 (2), 125-30.
- Water, J.J., Kim, Y., Maltesen, M.J., Franzyk, H., Foged, C., Nielsen, H.M., 2015. Hyaluronic acid-based nanogels produced by microfluidics-facilitated self-assembly Improves the safety profile of the cationic host defense peptide novicidin. *Pharmaceutical Research*, 32 (8), 2727-35.
- Whitesides, G.M., 2006. The origins and the future of microfluidics. *Nature*, 442 (7101), 368-73.
- Williams, M.S., Longmuir, K.J., Yager, P., 2008. A practical guide to the staggered herringbone mixer. *Lab on a Chip*, 8 (7), 1121-29.
- Win, K.Y., Feng, S.S., 2005. Effects of particle size and surface coating on cellular uptake of polymeric nanoparticles for oral delivery of anticancer drugs. *Biomaterials*, 26 (15), 2713-22.
- Winey, M., Meehl, J.B., O'Toole, E.T., Giddings, T.H., Jr., 2014. Conventional transmission electron microscopy. *Molecular Biology of the Cell*, 25 (3), 319-23.
- Wu, X.S., Wang, N., 2001. Synthesis, characterization, biodegradation, and drug delivery application of biodegradable lactic/glycolic acid polymers. Part II: Biodegradation. *Journal of Biomaterials Science Polymer Edition*, 12 (1), 21-34.
- Xia, H., Gao, X., Gu, G., Liu, Z., Hu, Q., Tu, Y., Song, Q., Yao, L., Pang, Z., Jiang, X., Chen, J., Chen, H., 2012. Penetratin-functionalized PEG-PLA nanoparticles for brain drug delivery. *International Journal of Pharmaceutics*, 436 (1-2), 840-50.
- Xie, H., Smith, J.W., 2010. Fabrication of PLGA nanoparticles with a fluidic nanoprecipitation system. *Journal of Nanobiotechnology*, 8, 18.

- Xu, H., Kona, S., Su, L.-C., Tsai, Y.-T., Dong, J.-F., Brilakis, E.S., Tang, L., Banerjee, S., Nguyen, K.T., 2013a. Multi-ligand poly(L-lactic-co-glycolic acid) nanoparticles inhibit activation of endothelial cells. *Journal of Cardiovascular Translational Research*, 6 (4), 570-78.
- Xu, J., Zhang, S., Machado, A., Lecommandoux, S., Sandre, O., Gu, F., Colin, A., 2017. Controllable microfluidic production of drug-loaded PLGA nanoparticles using partially water-miscible mixed solvent microdroplets as a precursor. *Scientific Reports*, 7 (1), 4794.
- Xu, S., Olenyuk, B.Z., Okamoto, C.T., Hamm-Alvarez, S.F., 2013b. Targeting receptor-mediated endocytotic pathways with nanoparticles: Rationale and advances. *Advanced Drug Delivery Reviews*, 65 (1), 121-38.
- Yadav, K.S., Sawant, K.K., 2010. Modified nanoprecipitation method for preparation of cytarabine-loaded PLGA nanoparticles. *AAPS PharmSciTech*, 11 (3), 1456-65.
- Yadav, S.C., Kumari, A., Yadav, R., 2011. Development of peptide and protein nanotherapeutics by nanoencapsulation and nanobioconjugation. *Peptides*, 32 (1), 173-87.
- Yang, B., Lowe, J.P., Schweins, R., Edler, K.J., 2015. Small angle neutron scattering studies on the internal structure of poly(lactide-co-glycolide)-block-poly(ethylene glycol) nanoparticles as drug delivery vehicles. *Biomacromolecules*, 16 (2), 457-64.
- Ye, D., Dawson, K.A., Lynch, I., 2015. A TEM protocol for quality assurance of in vitro cellular barrier models and its application to the assessment of nanoparticle transport mechanisms across barriers. *The Analyst*, 140 (1), 83-97.
- Yong, K.W., Yuen, D., Chen, M.Z., Porter, C.J.H., Johnston, A.P.R., 2019. Pointing in the right direction: Controlling the orientation of proteins on nanoparticles improves targeting efficiency. *Nano Letters*, 19 (3), 1827-31.
- Yoo, J., Lee, D., Gujrati, V., Rejinold, N.S., Lekshmi, K.M., Uthaman, S., Jeong, C., Park, I.K., Jon, S., Kim, Y.C., 2017. Bioreducible branched poly(modified nona-arginine) cell-penetrating peptide as a novel gene delivery platform. *Journal of Controlled Release*, 246, 142-54.
- Zabihi, F., Xin, N., Li, S., Jia, J., Cheng, T., Zhao, Y., 2014. Polymeric coating of fluidizing nano-curcumin via anti-solvent supercritical method for sustained release. *The Journal of Supercritical Fluids*, 89, 99-105.
- Zhai, P., Chen, X.B., Schreyer, D.J., 2015. PLGA/alginate composite microspheres for hydrophilic protein delivery. *Materials Science and Engineering: C Materials for Biological Applications*, 56, 251-59.
- Zhang, C., Ren, W., Liu, Q., Tan, Z., Li, J., Tong, C., 2019. Transportan-derived cell-penetrating peptide delivers siRNA to inhibit replication of influenza virus in vivo. *Drug Design, Development and Therapy*, 13, 1059-68.
- Zhang, D., Wang, J., Xu, D., 2016. Cell-penetrating peptides as noninvasive transmembrane vectors for the development of novel multifunctional drug-delivery systems. *Journal of Controlled Release*, 229, 130-39.
- Zhang, F., Skoda, M.W.A., Jacobs, R.M.J., Martin, R.A., Martin, C.M., Schreiber, F., 2007. Protein interactions studied by SAXS: Effect of ionic strength and protein concentration for BSA in aqueous solutions. *The Journal of Physical Chemistry B*, 111 (1), 251-59.
- Zhang, L., Feng, Q., Wang, J., Zhang, S., Ding, B., Wei, Y., Dong, M., Ryu, J.-Y., Yoon, T.-Y., Shi, X., Sun, J., Jiang, X., 2015. Microfluidic synthesis of hybrid nanoparticles with controlled lipid layers: Understanding flexibility-regulated cell-nanoparticle interaction. *ACS Nano*, 9 (10), 9912-21.

- Zhang, Z., Tsai, P.C., Ramezanli, T., Michniak-Kohn, B.B., 2013. Polymeric nanoparticles-based topical delivery systems for the treatment of dermatological diseases. *Wiley Interdisciplinary Reviews: Nanomedicine and Nanobiotechnology*, 5 (3), 205-18.
- Zhao, J., Zhou, R., Fu, X., Ren, W., Ma, L., Li, R., Zhao, Y., Guo, L., 2014a. Cell-penetrable lysine dendrimers for anti-cancer drug delivery: Synthesis and preliminary biological evaluation. *Archiv der Pharmazie*, 347 (7), 469-77.
- Zhao, Z., Li, Y., Zhang, Y., Chen, A.-Z., Li, G., Zhang, J., Xie, M.-B., 2014b. Development of silk fibroin modified poly(l-lactide)-poly(ethylene glycol)-poly(l-lactide) nanoparticles in supercritical CO₂. *Powder Technology*, 268, 118-25.
- Zhigaltsev, I.V., Belliveau, N., Hafez, I., Leung, A.K., Huft, J., Hansen, C., Cullis, P.R., 2012. Bottom-up design and synthesis of limit size lipid nanoparticle systems with aqueous and triglyceride cores using millisecond microfluidic mixing. *Langmuir*, 28 (7), 3633-40.
- Zhou, X., Chen, Q., Ma, Y., Huang, Y., Gou, S., Xiao, B., 2019. Porous polymeric microparticles as an oral drug platform for effective ulcerative colitis treatment. *Journal of Pharmaceutical Sciences*, 108 (7), 2238-42.
- Zhu, S., Chen, S., Gao, Y., Guo, F., Li, F., Xie, B., Zhou, J., Zhong, H., 2016a. Enhanced oral bioavailability of insulin using PLGA nanoparticles co-modified with cell-penetrating peptides and Engrailed secretion peptide (Sec). *Drug Delivery*, 23 (6), 1980-91.
- Zhu, X., Wu, J., Shan, W., Tao, W., Zhao, L., Lim, J.-M., D'Ortenzio, M., Karnik, R., Huang, Y., Shi, J., Farokhzad, O.C., 2016b. Polymeric nanoparticles amenable to simultaneous installation of exterior targeting and interior therapeutic proteins. *Angewandte Chemie*, 55 (10), 3309-12.
- Zhu, X., Lu, N., Zhou, Y., Xuan, S., Zhang, J., Giampieri, F., Zhang, Y., Yang, F., Yu, R., Battino, M., Wang, Z., 2019. Targeting pancreatic cancer cells with peptide-functionalized polymeric magnetic nanoparticles. *International Journal of Molecular Sciences*, 20 (12).
- Zhuang, J., Wang, D., Li, D., Yang, Y., Lu, Y., Wu, W., Wu, W., Qi, J., 2018. The influence of nanoparticle shape on bilateral exocytosis from Caco-2 cells. *Chinese Chemical Letters*, 29 (12), 1815-18.
- Zu, M., Ma, L., Zhang, X., Xie, D., Kang, Y., Xiao, B., 2019. Chondroitin sulfate-functionalized polymeric nanoparticles for colon cancer-targeted chemotherapy. *Colloids and Surfaces B: Biointerfaces*, 177, 399-406.

Appendix

Appendix I

Input factors and output responses for the individual runs of the bulk nanoprecipitation method from the design of experiments study. Data obtained for the centre point is shown as mean \pm SD ($n = 3$).

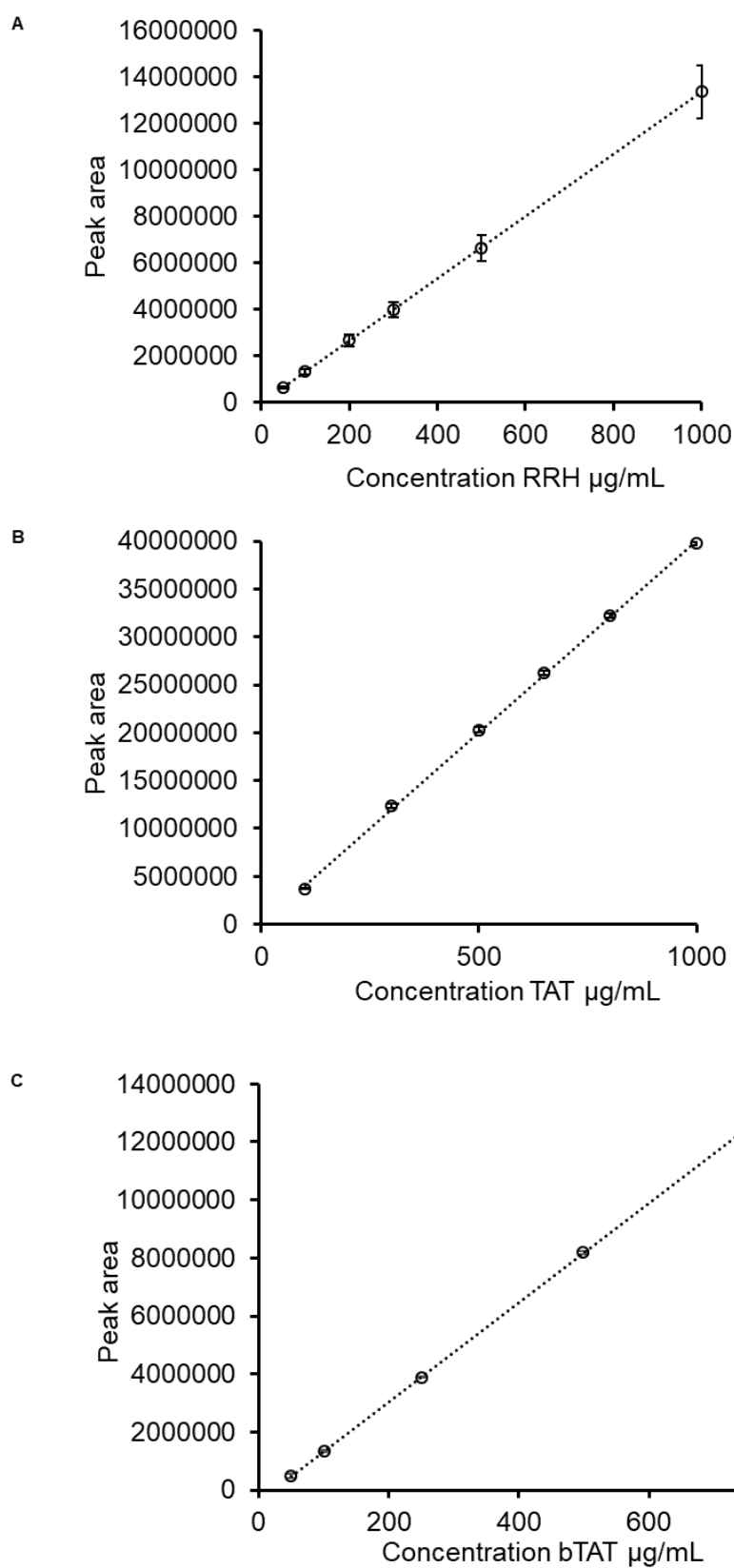
PLGA Concentration (mg/mL) Level			PVA Concentration (%) Level			Time (h) Level			Size (nm)	PDI
-1	0	1	-1	0	1	-1	0	1		
2			0.5			0.5			103.7	0.205
2			0.5				4		107.5	0.335
2					5	0.5			188.5	0.204
2					5		4		235.1	0.225
	13.5			2.75			2.25		154.8 \pm 6.1	0.149 \pm 0.024
		25	0.5				0.5		149.4	0.187
		25	0.5				4		153.9	0.167
		25			5		0.5		174.2	0.173
		25			5		4		193.6	0.171

Appendix II

Input factors and output responses for the individual runs of the microfluidics method from the design of experiments study. Data obtained for the centre point is shown as mean \pm SD ($n = 6$).

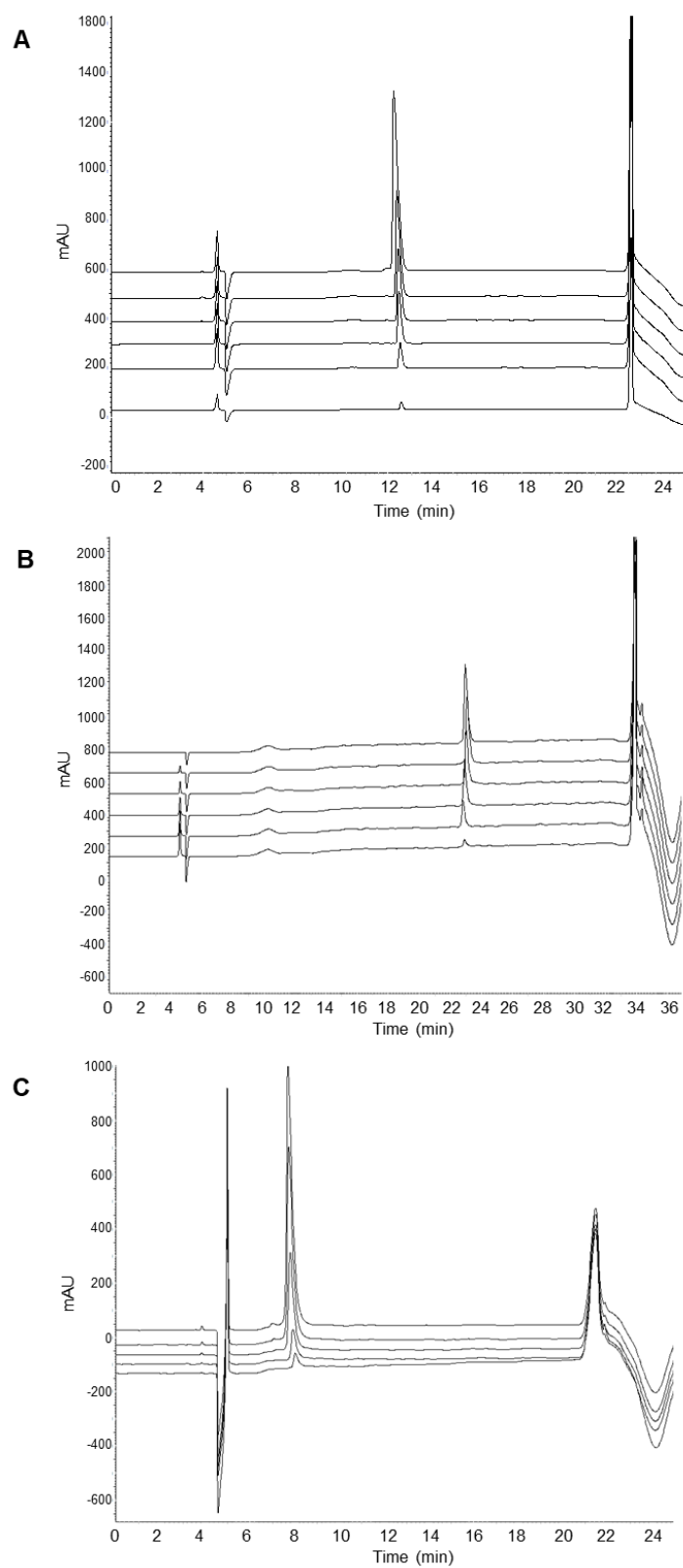
Total Flow Rate (TFR) mL/min Level			Flow Rate Ratio (FRR) Level			Size (nm)	PDI
-1	0	1	-1	0	1		
2			1 : 1			194.8	0.055
2			1 : 1			196.8	0.080
2					12 : 1	136.4	0.165
2					12 : 1	135.0	0.168
	7			6.5 : 1		172.7 \pm 1.5	0.143 \pm 0.014
		12	1 : 1			194.2	0.056
		12	1 : 1			192.2	0.060
		12			12 : 1	137.8	0.163
		12			12 : 1	139.8	0.155

Appendix III



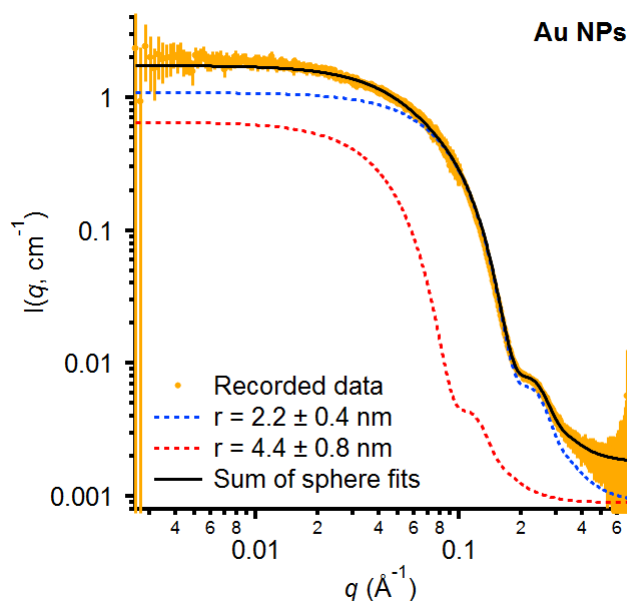
Standard curves of RP-HPLC methods for RRH (50-1000 $\mu\text{g/mL}$) (A), TAT (100-1000 $\mu\text{g/mL}$) (B) and bTAT (50-750 $\mu\text{g/mL}$) (C). Data are means \pm SD ($n = 3$).

Appendix IV



Stacked RP-HPLC chromatograms of the RRH standards (50-1000 $\mu\text{g/mL}$) (A), TAT standards (100-1000 $\mu\text{g/mL}$) (B) and bTAT standards (50-750 $\mu\text{g/mL}$) (C).

Appendix V



Small angle X-ray scattering profile of the AuNPs used in this study along with the fitting of the spherical structure factors. The dashed blue and red lines indicate the fitting models for spheres with radii of 2.2 and 4.4 nm, respectively. Polydispersity of 0.17 (standard deviation in radius over the mean radius) was incorporated into the two sphere models according to the manufacturers specified standard deviation in mean radius. The black line is the sum of the two models. Note that the background for each individual sphere model is half of the observed background in the recorded data. SASView fitting software was used for the data modelling and the following fitting parameters were used:

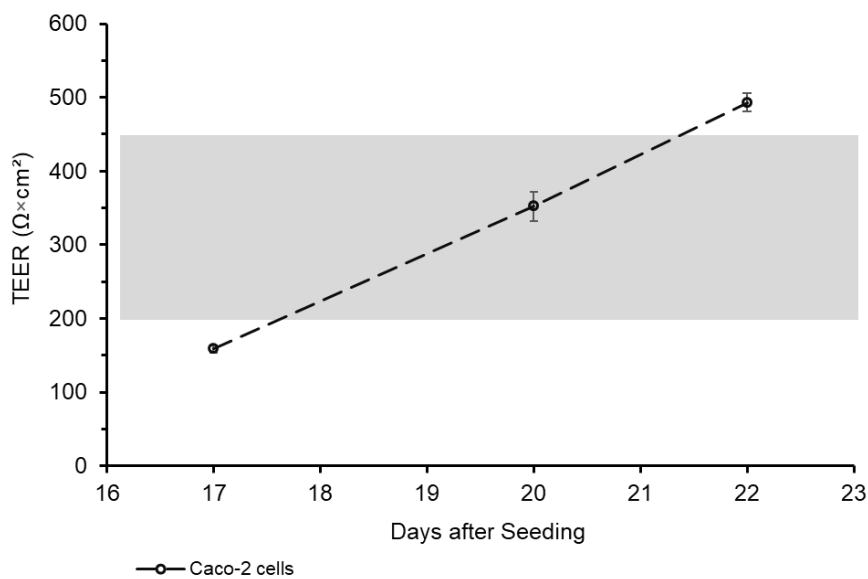
$$I(q) = \frac{\phi}{V} \left[3V(\Delta\rho) \frac{\sin(qr) - qr \cos(qr)}{(qr)^3} \right]^2 + \text{background}$$

where ϕ = particle volume fraction, V = particle volume, $\Delta\rho$ = SLD contrast, r = particle radius.

Sphere 1 – radius = 22 Å (fixed), polydispersity = 0.17 (fixed), particle SLD = $1.23 \times 10^{-4} \text{ \AA}^{-2}$ (for Au, fixed), solvent SLD = $9.47 \times 10^{-6} \text{ \AA}^{-2}$ (for water, fixed), background = 0.0009 cm^{-1} (fixed) and volume fraction of particles = $(1.41 \pm 0.01) \times 10^{-5}$.

Sphere 2 – radius = 44 Å (fixed), polydispersity = 0.17 (fixed), particle SLD = $1.23 \times 10^{-4} \text{ \AA}^{-2}$ (for Au, fixed), solvent SLD = $9.47 \times 10^{-6} \text{ \AA}^{-2}$ (for water, fixed), background = 0.0009 cm^{-1} (fixed) and volume fraction of particles = $(1.06 \pm 0.01) \times 10^{-6}$.

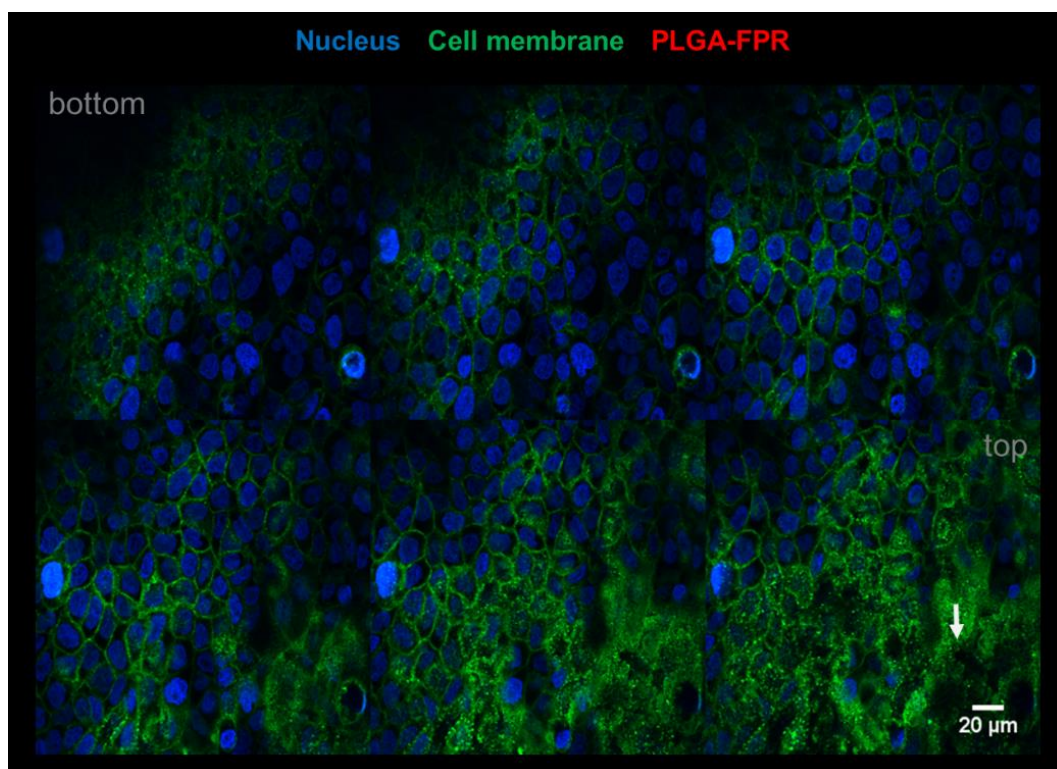
Appendix VI



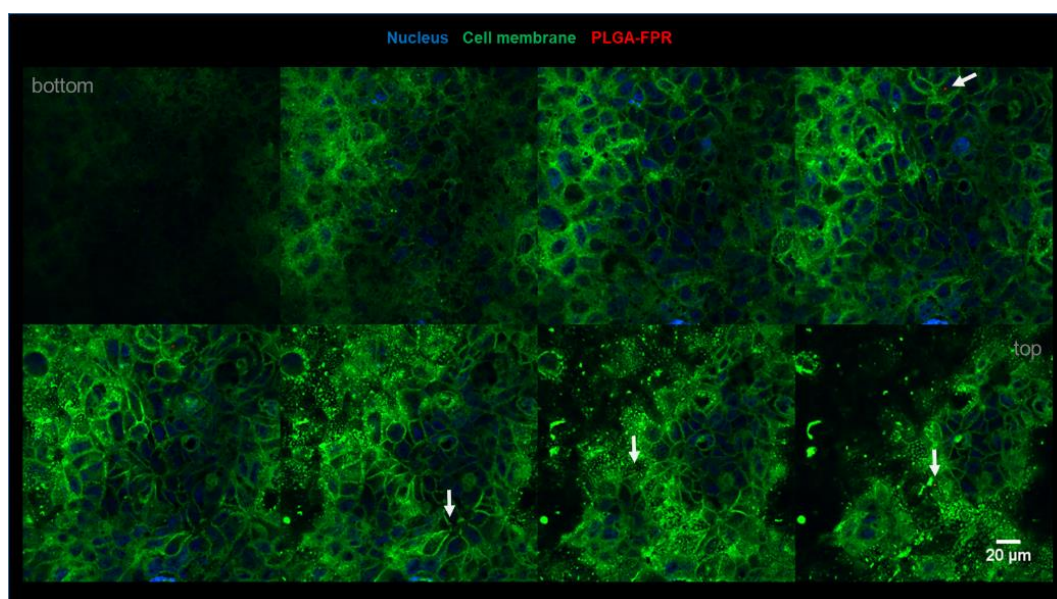
Monitoring of transepithelial electrical resistance (TEER) value of Caco-2 cell monolayer between day 17 and day 22 after seeding on cell culture inserts with a permeable membrane. Data are means \pm SEM ($n = 3$).

Appendix VII

A



B



Confocal images of Caco-2 cell monolayer incubated for 2 h with RRH- (A), TAT- (B) and bTAT-tagged PLGA-FPR nanoparticles (C) prepared using the post-microfluidics conjugation approach. The z-stack images of Caco-2 cells with CPP-tagged PLGA have had a slice thickness of 0.75 µm or 1.25 µm for RRH- or TAT- and bTAT-tagged PLGA-FPR nanoparticles, respectively. The white arrow is pointing towards red fluorescence of PLGA-FPR nanoparticles or CPP-tagged PLGA-FPR nanoparticles.

Appendix VII cont'.

C

